Unique Characteristics of Voids in a Complex Universe

Nico Schuster

München 2023

Unique Characteristics of Voids in a Complex Universe

Nico Schuster

Dissertation
an der Fakultät für Physik
der Ludwig–Maximilians–Universität
München

vorgelegt von
Nico Schuster
aus Neustadt an der Waldnaab

München, den 29. August 2023

Erstgutachter: PD Dr. Nico Hamaus
Zweitgutachter: Prof. Dr. Klaus Dolag
Tag der mündlichen Prüfung: 19. Oktober 2023

Zusammenfassung

Das ΛCDM Modell ermöglicht eine erfolgreiche Beschreibung unseres Universums und seinen Strukturen vom Urknall bis zur heutigen Zeit. Dabei setzt es zwei Arten von Materie bzw. Energie voraus, deren genaue Natur noch unbekannt ist. Laut diesem Modell besteht der größte Teil der Materie aus kalter dunkler Materie (CDM) und baryonische Materie macht nur einen geringen Teil aus, obwohl daraus alle sichtbaren Strukturen bestehen. Zusätzlich gibt es die dunkle Energie, welche die beschleunigte Expansion des Universums antreibt und sich durch eine kosmologische Konstante Λ äußerst gut erklären lässt.

Die dichtesten Strukturen in unserem Universum wurden ausgiebig erforscht und deren Beobachtungen ermöglichten das ΛCDM Modell. Im Gegensatz dazu wurden die größten und leersten Regionen in unserem Universum, bekannt als kosmische Leerräume bzw. Voids, erst seit kurzem genauer untersucht. Kosmologische Tests mittels Voids werden immer häufiger benutzt, dennoch gibt es einige Aspekte dieser Regionen, die detaillierter erforscht und verstanden werden können. Dazu zählt die Struktur und Dynamik von Materie um Voids, als auch die Überprüfung theoretischer Vorhersagen in diesen Regionen.

Diese Doktorarbeit beschäftigt sich mit dem Erforschen dieser Aspekte mittels modernster hydrodynamischer Simulationen. Die Untersuchung von Voids ist an und für sich interessant, zusätzlich können unsere Ergebnisse helfen, kosmologische Tests zu verfeinern und den Nutzen von Voids über große Zeiträume und Skalen zu erweitern.

Zuerst stellen wir das Thema und die Grundlagen der Kosmologie in Kapitel 1 und 2 vor und erklären unsere Methoden sowie die benutzten Simulationen in Kapitel 3 und 4. Nachdem die Grundlagen etabliert wurden, betrachten wir allgemeine Eigenschaften von Voids in Kapitel 5, wo wir eine Konvergenz ihrer Radien auf großen Skalen finden. Danach erforschen wir allgemeine Aspekte der Struktur und Dynamik von Materie um Voids in Kapitel 6, was unterschiedliche Grenzen der herkömmlichen Methodik aufdeckt. In Kapitel 7 zeigen wir eine Übereinstimmung zwischen theoretischen Vorhersagen zur Dynamik von Materie und den Simulationen auf ‘kleinen’ Skalen von wenigen Megaparsec auf. Kapitel 8 untersucht die Notwendigkeit von hydrodynamischen Simulationen und wir finden nur geringe Einflüsse von Baryonen auf beobachtbare Void-Statistiken im Vergleich zu vereinfachten Simulationen ohne Baryonen. Schließlich erkunden wir die Entwicklung von Voids über nahezu das gesamte Alter des Universums in Kapitel 9, wo wir verschiedenste Statistiken sowie theoretische Vorhersagen zum Wachstum von Strukturen analysieren. Weiterhin entdecken wir eine einzigartige Eigenschaft von Voids, die ihre Entwicklung trivial erscheinen lässt, obwohl die Gründe dafür höchstwahrscheinlich sehr komplex sind.

Abstract

The ΛCDM model is quite successful in the phenomenological description of the evolution of our Universe and the structures within, even though it relies on two as of yet unknown forms of matter and energy. According to this model, most of the matter in our Universe is in the form of cold dark matter (CDM) and visible structures made up of baryonic matter contain significantly less mass than CDM. The other unknown quantity that drives the late-time accelerated expansion of our Universe is referred to as dark energy. A cosmological constant Λ for this type of energy is so far consistent with observations.

The most overdense structures in our Universe have been studied extensively and through their use in observations the ΛCDM model was built. In contrast, the study of the largest and most underdense regions of the cosmic web, known as cosmic voids, emerged only in recent years. While their use as cosmological probes is already well established, there is still a vast space to explore various aspects of their structure and dynamics, as well as to test the validity of predictions from linear theory in these underdense environments.

The subject of this dissertation is to test both of these aspects by using state-of-the-art hydrodynamical N-body simulations. The detailed study of voids is not only interesting in its own right, but our results can additionally help in improving current methods employed in cosmological tests with voids, as well as maximize their use across both time and scale.

After introducing the topic and summarizing the basics of cosmology in chapters 1 and 2, we describe our methods and simulations in chapters 3 and 4. As the background of this work is covered, we investigate general aspects of void properties and find an alignment of their size distributions on large scales in chapter 5, before exploring the structure and dynamics of tracers around voids through their profiles in chapter 6, where we identify new biases in estimators. These chapters form the foundations for more detailed studies and we find a validity of linear theory predictions on velocities around voids down to scales of only a few megaparsecs in chapter 7. Subsequently, in chapter 8 we explore the necessity of complex hydrodynamical simulations and discover small impacts of baryons on observable void statistics compared to more simple dark matter only simulations. Moreover, we examine the different distributions of CDM and baryons around voids. Lastly, we follow the evolution of voids over nearly the entire age of the Universe in chapter 9, where we analyze the evolution of their common statistics in matter and biased tracers, as well as test theoretical predictions on the growth of structures. Furthermore, we uncover a unique characteristic of voids that makes their evolution appear quite trivial, although reasons for this seem to be rather complex.

Contents

List of Figures

List of Tables

"That is the beginning of knowledge –
the discovery of something we do not understand."

Frank Herbert,
God Emperor of Dune

Chapter 1

Introduction

The ultimate goal of cosmology is quite ambitious. Its aim is to understand and describe the evolution of our Universe in its entirety. This includes the evolution of its matter and energy contents, starting from the beginning of the Universe close to 14 billion years ago up to current time, as well as ultimately determine its fate in the far future. So far the earliest observations of our Universe start with the first observable light, the cosmic microwave background (CMB) radiation, which revealed the presence of extremely small fluctuations in both density and temperature at a time when the Universe was still relatively young, with an age of only 380 000 years [1, 2]. While tiny, these fluctuations already provide the necessary seeds for the cosmic structures we observe today, as small initial overdensities were amplified under the influence of gravity by many orders of magnitude and steadily built up what is now known as the *cosmic web*, an intricate system of gravitationally bound structures residing in our cosmos. This cosmic web consists of a network of sheets, connected by long filaments, which are in turn connected by nodes of high density [3]. As matter most strongly clusters in these overdense regions, the remaining space becomes more devoid of matter and expands in time as the Universe evolves, thus creating enormous underdensities, referred to as cosmic voids [4–9].

With past and upcoming surveys of the sky we are able to map out significant fractions of the observable Universe and the structures of the cosmic web therein in ever increasing detail ([e.g., 10–20]), at least indirectly via surveys that map out luminous tracers, such as galaxies and clusters. However, the dominant fraction of the matter content in our Universe is not directly observable and is assumed to be some form of *cold dark matter* (CDM), a type of matter that is solely affected by gravity and no other known forces, but its particle nature is still unclear and remains one of the most important questions in both cosmology and particle physics. In addition, a late-time accelerated expansion of space has been first observed around 25 years ago using supernovae data and revealed the presence of what is now referred to as *dark energy*. While its exact nature is unknown, observations are so far consistent with a cosmological constant Λ [21, 22]. These unknown components of matter and energy make up the current standard model of cosmology, the ΛCDM model. At present time around 95% of the energy content in the Universe is contained in the form of CDM and dark energy, while baryonic matter accounts for the remaining 5%, yet it

makes up all the visible structures we observe. Despite the still to be determined nature of both CDM and dark energy, simulations allow us to study the ΛCDM universe in great detail and help us investigate the formation and evolution of cosmic structures [e.g., 23, 24].

In recent years the study of cosmic voids in both simulations and observations emerged and gained traction (see e.g. references [25–28] for reviews), as it was discovered that voids can be utilized as very efficient cosmological probes [27–35]. For example, using voids as probes for dark energy originates from their underdense nature, as the interior of voids can be thought of as small and independent 'pocket universes' of low density, in which dark energy became of relevancy at much earlier times compared to the rest of our Universe [33, 36, 37]. While the expansion of voids distinguishes them from collapsed objects that decoupled from the Hubble flow, voids still exhibit universal characteristics, similarly to halos, like the shapes of their radial density profiles [38, 39]. These density profiles have become a focus of interest in a number of recent studies, both in the context of analyzing ΛCDM cosmology [e.g., 40–49], testing modifications of general relativity (GR) [e.g., 50–60], as well as exploring models of dark matter [e.g., 61–65] and the influence of massive neutrinos [e.g., 66–73].

Moreover, the study of their radial velocity profiles has become of importance for modeling redshift-space distortions (RSD) and the observable void shapes in redshift space [e.g., 74–83]. As it proves difficult to measure the velocities of tracers directly, local mass conservation is used to relate their density with the velocity of tracers. While voids themselves are nonlinear objects with densities at their boundaries on the level of the mean background density and above, the relationship between velocity and density can be described remarkably well by the linearized continuity equation [38]. This unique property of voids has been key in the success of RSD models around these underdense environments.

While voids are already well established cosmological probes, there is still more to learn about their internal structures and dynamics through the use of simulations. This thesis aims to study the fundamental properties of voids in great detail across vast ranges in resolution and scale with the help of hydrodynamical simulations of a ΛCDM Universe. A simulation study across scales can help us improve current observational applications, such as RSD, determine the necessity for inclusion of baryonic effects on void statistics and can unveil some new fundamental properties of voids. In this work we compare different estimators for the velocity and density around averaged (stacked) voids and explore the effects of weighting schemes, subsamplings and mass cuts of the underlying tracer distributions on their profiles. Furthermore, we examine the limits of linear mass conservation around both stacked and individual voids, we study the impact of baryonic physics on their statistics, and explore their statistical evolution over cosmic time. Parts of this thesis are based on the publication *Why cosmic voids matter: nonlinear structure & linear dynamics* [84] by N. Schuster, N. Hamaus, K. Dolag and J. Weller, as well as manuscripts currently in preparation for publication.

The outline of this thesis is as follows: In chapter 2 we provide an introduction to the theoretical foundations of ΛCDM cosmology and cosmic voids. Chapter 3 introduces the watershed void finder that is applied to the tracer catalogs extracted from simulations and provides definitions for commonly used properties of voids. Furthermore, we explain details

on the different estimators for density and velocity profiles of both individual and stacked voids, as well as their interrelation via the linearized continuity equation. Chapter 4 provides details on the hydrodynamical simulations from the `Magneticum` suite, which contains cosmological simulations across a variety of different resolutions in mass and scale, and we discuss our selection of halos as tracers for the void identification and calculation of void profiles. The presentation of novel results starts in chapter 5, where we describe halo and void catalogs obtained from the `Magneticum` simulations, in addition to discussing general insights on the scale and tracer dependence of void properties and their correlation. In chapter 6 we investigate various properties of both density and velocity around voids for a variety of tracers. We discuss the impact of merging of voids and mass weights on the density, how common void properties are reflected in their profiles and the different effects of subsamplings and mass cuts. These investigations reveal the bias of the different estimators. While not feasible in observations, we additionally explore the splitting of profiles in inflowing and outflowing tracers samples. Chapter 7 tests the validity of the application of linear mass conservation across a wide range in scale for both individual and stacked density profiles by comparing results with the measured velocities. Next, chapter 8 explores the impact of baryonic physics on common void statistics, for voids identified in both CDM and baryons, along with comparing statistics of halo defined voids between hydrodynamical and dark matter only simulations for a variety of cases. Furthermore, we examine differences in the structure and dynamics of baryons and CDM around voids identified in halos and are able to place an upper limit on these deviations through a resolution study. In chapter 9 we investigate the evolution of voids over a vast amount of time as the Universe ages, for fixed subsamplings of CDM in order to explore how matter clusters over time, and for halos identified at fixed mass cuts, which reveals the impact of halo formation on the statistics of voids. Furthermore, we test how well linear theory can predict the growth of structures and we identify a way of investigating void density profiles that is universal across time and a wide range in mass and scale. Finally, in chapter 10 we conclude and summarize the overall results from this work and discuss potential open questions, as well as applications in observational studies.

For a comprehensive understanding of this thesis, chapters 2 to 6 should be read first and in order of appearance. Chapters 7 to 9 can be read out of order, as they only rely on the more general discussions from chapters 2 to 6.

Chapter 2

Basics of cosmology

As the ΛCDM model works very well for the phenomenological description of our Universe and is the basis of modern cosmology, we will use this chapter to briefly introduce some of its underlying concepts. We first provide an overview on cosmology in a homogeneous ΛCDM universe in section 2.1, including its foundations in general relativity. We then cover the evolution of inhomogeneities under the force of gravity in section 2.2 and the evolution of spherical underdensities, i.e. voids, in section 2.3. The summaries of topics covered in these sections are based on references [85–89]. Throughout this chapter we adopt the following conventions:

- We use natural units $c = \hbar = 1$
- Greek indices α, β etc. cover the 4 space-time indices with $x^0 = t$, e.g. $\alpha = 0, 1, 2, 3$
- Latin indices j, k etc. denote spatial components 1, 2, 3
- Einstein summation convention is adopted, i.e. if any index appears in both upper and lower position, one sums over this index without explicit writing of the sum, e.g. $j_i k^i = \sum_{i=1}^{3} j_i k^i = j_1 k^1 + j_2 k^2 + j_3 k^3$
- We adopt the metric signature $(-, +, +, +)$
- Dots on top of functions indicate derivatives with respect to physical time, e.g. $\dot{a} \equiv \frac{\mathrm{d}a}{\mathrm{d}t}$
- Lengths and distances are usually given in units of Mpc/h, with h defined as: $h \equiv \frac{H_0}{100\,\mathrm{km\,s^{-1}\,Mpc^{-1}}}$, where H_0 is the Hubble constant
- Masses are given in units of $M_\odot/h$, where $M_\odot$ is the solar mass.
- Numerical values of selected physical constants are given by [90]:
  - speed of light in vacuum: $c = 299\,792\,458\,\mathrm{m\,s^{-1}}$
  - gravitational constant: $G = 6.674\,30(15) \times 10^{-11}\,\mathrm{m^3\,kg^{-1}\,s^{-2}}$
  - parsec: $1\mathrm{pc} = 3.085\,677\,581\,49... \times 10^{16}\,\mathrm{m}$
  - Solar mass: $M_\odot = 1.988\,41(4) \times 10^{30}\,\mathrm{kg}$

2.1 The ΛCDM Universe

The ΛCDM model assumes the *cosmological principle*, which describes the Universe as spatially homogeneous and isotropic on large enough scales, typically larger than a few hundred megaparsecs. It further assumes that on these large scales, gravity is the only relevant interaction and can be adequately described by general relativity. The other fundamental forces like electromagnetism solely affect baryonic matter and not CDM. Furthermore, these other forces are only relevant at significantly smaller scales compared to gravity.

The equations that describe the intricate connection between the geometrical properties of spacetime and the energy contents of the Universe are the Einstein field equations:

$$G_{\mu\nu} = R_{\mu\nu} - \frac{1}{2} R\, g_{\mu\nu} = 8\pi G\, T_{\mu\nu}\,, \tag{2.1}$$

where the right side contains Newton's gravitational constant G and the energy contents of the Universe are described by the energy-momentum tensor $T_{\mu\nu}$. The cosmological constant Λ can be either included in the energy-momentum tensor or can be added to the left side of equation (2.1) as a term $\Lambda\, g_{\mu\nu}$. Furthermore, $g_{\mu\nu}$ are the components of the metric, $R_{\mu\nu}$ is the Ricci tensor and $R \equiv R^{\mu}_{\mu}$ the Ricci scalar. The Ricci tensor itself is given by:

$$R_{\mu\nu} = \frac{\partial \Gamma^{\alpha}_{\mu\nu}}{\partial x^{\alpha}} - \frac{\partial \Gamma^{\alpha}_{\mu\alpha}}{\partial x^{\nu}} + \Gamma^{\alpha}_{\beta\alpha}\Gamma^{\beta}_{\mu\nu} - \Gamma^{\alpha}_{\beta\nu}\Gamma^{\beta}_{\mu\alpha}\,, \tag{2.2}$$

with the Christoffel symbols Γ in terms of the metric:

$$\Gamma^{\mu}_{\alpha\beta} = \frac{1}{2}\, g^{\mu\nu} \left(\frac{\partial g_{\alpha\nu}}{\partial x^{\beta}} + \frac{\partial g_{\beta\nu}}{\partial x^{\alpha}} - \frac{\partial g_{\alpha\beta}}{\partial x^{\nu}} \right) . \tag{2.3}$$

Equation (2.1) shows the connection between the metric and the energy contents, where the geometry of spacetime is determined by the right hand side of this equation. The metric tensor $g_{\mu\nu}$ itself defines the line element:

$$\mathrm{d}s^2 = g_{\mu\nu}\, \mathrm{d}x^{\mu} \mathrm{d}x^{\nu}\,. \tag{2.4}$$

As the cosmological principle assumes a spatially homogeneous and isotropic universe, the metric of such a universe has to share these qualities. Hence, the spatial components of the metric have to be invariant against translations and rotations. The Friedmann-Lemaître-Robertson-Walker (FLRW) metric fulfills such requirements and is given in the form of the line element as :

$$\mathrm{d}s^2 = -\,\mathrm{d}t^2 + a^2(t) \left[\frac{\mathrm{d}r^2}{1 - \mathrm{K}\, r^2} + r^2 \left(\mathrm{d}\theta^2 + \sin^2\theta\, \mathrm{d}\phi^2 \right) \right] , \tag{2.5}$$

where (comoving) spatial polar coordinates (r, θ, ϕ) are used. The quantity $a(t)$ is known as the *scale factor* and it determines the scaling of spatial distances with respect to

the distance at a chosen initial time t_0. By convention this time is chosen as present time and $a(t_0) \equiv a_0 = 1$. This scale factor defines the relation between physical coordinates $\boldsymbol{x}_{\text{phys}}$ and comoving coordinates $\boldsymbol{q}_{\text{com}}$ as $\boldsymbol{x}_{\text{phys}} = a(t)\,\boldsymbol{q}_{\text{com}}$. Hence, if two objects experience no net force between them and simply follow the expansion of the Universe, their comoving distance remains constant, while their physical distance evolves with a. Lastly, the constant K in equation (2.5) represents the spatial curvature and overall geometry of the Universe:

$$\mathrm{K} = \begin{cases} 1 & \text{closed universe ; spherical geometry} \\ 0 & \text{flat universe ; Euclidean geometry} \\ -1 & \text{open universe ; hyperbolic geometry.} \end{cases} \tag{2.6}$$

From now on we will assume a spatially flat universe for the rest of this work, though we will keep K in some equations. Flatness ($\mathrm{K} = 0$) is in accordance with theoretical arguments from inflation [86], and consistent with recent measurements [91].

The components of the FLRW metric $g_{\mu\nu}$ can be read from equations (2.4) and (2.5). With these components, the left hand side of equation (2.1) can be calculated. Of course as the metric has to fulfill homogeneity and isotropy, so do the matter and energy components that fill our Universe. On large scales, these can be approximated as perfect fluids. In the frame of a comoving observer, the energy-momentum tensor of perfect fluids reads as:

$$T^{\mu}_{\nu} = \mathrm{diag}(-\rho,\, p,\, p,\, p)\,, \tag{2.7}$$

where ρ is the energy density and p the pressure of the given fluids. The Universe obviously contains more than one type of matter and energy, but the total energy density and pressure for multiple fluids are simply given be the sums of the respective properties of the individual components. Using this energy-momentum tensor combined with the FLRW metric in the Einstein equations (2.1) we ultimately get the two Friedmann equations:

$$\left(\frac{\dot{a}}{a}\right)^2 = H^2 = \frac{8\pi G}{3}\,\rho - \frac{\mathrm{K}}{a^2}\,, \tag{2.8}$$

$$\frac{\ddot{a}}{a} = \dot{H} + H^2 = -\frac{4\pi G}{3}\,(\rho + 3\,p)\,, \tag{2.9}$$

where $H \equiv \frac{\dot{a}}{a}$ is the Hubble parameter and spatial curvature K is included for the sake of completeness. A further time derivative of the first Friedmann equation (2.8) and using the second Friedmann equation (2.9) results in the continuity equation:

$$\dot{\rho} + 3H\,(\rho + p) = 0\,, \tag{2.10}$$

which describes local conservation of energy and momentum. Typically the energy density and pressure are not independent, but are related by an equation of state:

$$p = w\,\rho\,, \tag{2.11}$$

which connects the density and pressure for different types of matter and energy. Combining this general equation of state with the continuity equation (2.10) reveals the scaling of density with respect to the scale factor:

$$\rho \propto a^{-3(1+w)} \,. \tag{2.12}$$

Radiation and relativistic particles have $w_\mathrm{r} = \frac{1}{3}$, while non-relativistic matter is treated as dust with zero pressure, i.e. $w_\mathrm{m} = 0$, and the cosmological constant has $w_\Lambda = -1$. Hence, their energy densities evolve as:

$$\rho_\mathrm{r} \propto a^{-4} \;\;,\;\; \rho_\mathrm{m} \propto a^{-3} \;\;,\;\; \rho_\Lambda = \text{const.} \tag{2.13}$$

This evolution of different densities already indicates that radiation and other relativistic particles were more relevant at early times, or equivalently small scale factors a, while matter can dominate at intermediate time. The impact of the cosmological constant Λ to the energy densities becomes of more importance at late times, when other densities become smaller due to their dependence on a. Of course these arguments come solely from the scaling with a of different densities, ignoring the percentages each type of energy contributes to the total energy at a fixed time.

In a flat universe ($\mathrm{K} = 0$) the first Friedmann equation (2.8) at time $t = t_0$ defines a *critical density* $\rho_{\mathrm{crit},0}$:

$$\rho_{\mathrm{crit},0} \equiv \frac{3H_0^2}{8\pi G} \,. \tag{2.14}$$

This critical density allows us to express the energy contents in more convenient ways, namely in terms of dimensionless density parameters Ω_i, here at current time t_0:

$$\Omega_{i,0} \equiv \frac{\rho_{i,0}}{\rho_{\mathrm{crit},0}} = \frac{8\pi G\, \rho_{i,0}}{3H_0^2} \,. \tag{2.15}$$

The subscript '0' is often dropped out of convenience, which we will adopt as well. Therefore, any Ω_i that appears in the following equations is always the density at present time t_0 in terms of the current critical density $\rho_{\mathrm{crit},0}$. Using these dimensionless density parameters, the Friedmann equation (2.8) can be rewritten for the previously introduced matter and energy components as:

$$\frac{H^2(a)}{H_0^2} = \Omega_\mathrm{r}\, a^{-4} + \Omega_\mathrm{m}\, a^{-3} + \Omega_\mathrm{K}\, a^{-2} + \Omega_\Lambda \,, \tag{2.16}$$

where the density parameter for Λ and the newly introduced curvature parameter Ω_K are given by:

$$\Omega_\Lambda = \frac{\Lambda}{3H_0^2} \;\;,\;\; \Omega_\mathrm{K} = -\frac{\mathrm{K}}{H_0^2} \,. \tag{2.17}$$

Next, we want to introduce the cosmological *redshift* z. Let us consider a distant source that emits light at a given wavelength λ_em at time t_em and we observe this source at time t_0 with a wavelength λ_0. This defines the redshift z as:

$$z_{\mathrm{em}} \equiv \frac{\lambda_0 - \lambda_{em}}{\lambda_{em}} \,. \tag{2.18}$$

During the time this light was emitted and observed, the Universe expanded. This expansion affects wavelengths as well, and they scale as $\lambda \propto a$. Rearranging equation (2.18) and using $a(t_0) = 1$ for observations at present time yields:

$$1 + z_{\mathrm{em}} = \frac{1}{a(t_{\mathrm{em}})} \iff a(t_{\mathrm{em}}) = \frac{1}{1 + z_{\mathrm{em}}} \,. \tag{2.19}$$

Combining these results and assuming a flat universe, we can find the following expression for the Hubble parameter $H(z)$:

$$H(z) = H_0 \sqrt{\Omega_r \,(1+z)^4 + \Omega_m \,(1+z)^3 + \Omega_\Lambda} \,, \tag{2.20}$$

where we want to emphasize once more that Ω_i are present day values. In a flat universe we can use $\Omega_\Lambda = 1 - \Omega_{\mathrm{m}} - \Omega_{\mathrm{r}}$. Moreover, at small redshift z we can neglect the contribution of radiation to the energy budget, i.e. $\Omega_{\mathrm{r}} = 0$. This allows us to further simplify equation (2.20) to:

$$H(z) = H_0 \sqrt{\Omega_{\mathrm{m}} \,(1+z)^3 + 1 - \Omega_{\mathrm{m}}} \,. \tag{2.21}$$

2.2 Evolution of inhomogeneities

In the previous section we assumed a completely homogeneous and isotropic universe. While CMB observations show a very homogeneous and isotropic Universe, small inhomogeneities in density are present at early times, which eventually evolve into the cosmic structures we observe today. Although averaged over large enough scales, homogeneity and isotropy still holds. The temperature fluctuations of the CMB were only on the order of $\Delta T/T \simeq 10^{-5}$, which directly translates to fluctuations in the density of baryonic matter of the same magnitude. Before the recombination of charged electrons and protons into neutral atoms, which led to free photons that make up the CMB, radiation and baryonic matter were tightly coupled. Frequent interactions and radiation pressure prevented baryons from clustering before recombination. However, due to the non-interacting nature of CDM with photons, any inhomogeneities in CDM were able to gravitationally cluster even before this time. As baryons and radiation decoupled after the CMB, baryons were now able to collapse as well, and the already present gravitational potential wells from CDM boosted the structure formation of baryons.

In order to understand how inhomogeneities in the density field evolve into the observed (nonlinear) structures, we need to investigate how these idealized fluids are influenced by their own gravity. Since the initial variations in density were quite small, for now we can explore their evolution at linear order in perturbation theory. At some point structures become nonlinear and a more sophisticated treatment than linear theory becomes necessary. Furthermore, in the case of non-relativistic matter and on scales smaller than the Hubble

radius H^{-1}, we can use Newtonian gravity to describe these inhomogeneities, although some cosmological effects like an expanding background and an evolving average density must be included in this description. For the sake of simplicity and since the evolution of CDM and baryons is coupled by gravity, we will treat them as one single ideal fluid. This idealized non-relativistic fluid is characterized by its density $\rho_\mathrm{m} = \rho_\mathrm{m}(\boldsymbol{x}, t)$, a small pressure $p_\mathrm{m} \ll \rho_\mathrm{m}$, and its velocity $\boldsymbol{v}$, with $|\boldsymbol{v}| \ll c$. However, we will refer to its density and pressure simply as ρ and p, respectively, as we ignore other components in this section.

For now we will briefly ignore the expansion of our Universe and solely focus on the evolution through gravity. From conservation of mass, we once more get the continuity equation, albeit now in different form than equation (2.10), given by:

$$\partial_t \rho + \nabla \cdot (\rho\, \boldsymbol{v}) = 0\,, \tag{2.22}$$

where $\partial_t \equiv \frac{\partial}{\partial t}$, with identical definitions for other derivatives. Equation (2.22) states that any change of density in a fixed volume can only occur due to an influx or outflow of matter in this volume. Requiring the conservation of momentum results in the Euler equation [89]:

$$\rho \frac{\mathrm{d}\boldsymbol{v}}{\mathrm{d}t} = \rho\,(\partial_t + \boldsymbol{v} \cdot \nabla)\,\boldsymbol{v} = -\nabla p - \rho\,\nabla\Phi\,, \tag{2.23}$$

where Φ is the gravitational potential, which is determined by the Poisson equation:

$$\nabla^2 \Phi = 4\pi G \rho\,. \tag{2.24}$$

The continuity, Euler and Poisson equation form the basis for determining our unknown functions ρ, p, $\boldsymbol{v}$ and Φ. If we assume a static fluid, i.e. $\boldsymbol{u} = 0$, equations (2.22) and (2.23) are solved by constant values of density and pressure, $\rho = \bar{\rho}$ and $p = \bar{p}$, although this would also imply $\nabla\Phi = 0$, which is inconsistent with equation (2.24), unless $\bar{\rho} = 0$. This simply tells that there cannot be infinite, static and self-gravitating perfect fluids [89], unless some 'antigravitational' force exactly balances gravity [86], a reason Einstein first introduced the cosmological constant to general relativity. Nevertheless, we will continue our study even without a consistent solution of the background and finally introduce small perturbations to our assumed solutions in a static fluid:

$$\begin{gathered} \rho(\boldsymbol{x}, t) = \bar{\rho}(t) + \delta\rho(\boldsymbol{x}, t) \quad , \quad p(\boldsymbol{x}, t) = \bar{p}(t) + \delta p(\boldsymbol{x}, t) \quad , \\ \boldsymbol{v}(\boldsymbol{x}, t) = \delta\boldsymbol{v}(\boldsymbol{x}, t) \quad , \quad \Phi(\boldsymbol{x}, t) = \bar{\Phi}(t) + \delta\Phi(\boldsymbol{x}, t)\,. \end{gathered} \tag{2.25}$$

Any quantities with a bar, e.g. $\bar{\rho}$, are part of the background. Hence, they have to be homogeneous and isotropic. Furthermore, we already indirectly assumed a barotropic fluid, which is a fluid whose pressure solely depends on its energy density, $p = p(\rho)$, like for the equation of state (2.11). This allows us to express perturbations in pressure as $\delta p = \frac{\partial p}{\partial \rho}\delta\rho \equiv c_s^2 \delta\rho$, where c_s is the speed of sound. If we were to solve equations (2.22) and (2.23) at linear order while ignoring gravity completely, this would result in a wave equation for $\delta\rho$ and its solutions are given by sound waves, namely a sum or integral over plane wave solutions [89]. However, we will not go into more detail on solutions without

including gravity. Using these perturbations in equations (2.22) to (2.24) and keeping only terms of linear order in perturbations, we arrive at the following set of linearized equations:

$$\partial_t \delta\rho = -\nabla \cdot (\bar{\rho}\, \delta\boldsymbol{v}) \,, \tag{2.26}$$

$$\bar{\rho}\, \partial_t \delta\boldsymbol{v} = -\nabla \delta p - \bar{\rho}\, \nabla \delta\Phi \,, \tag{2.27}$$

$$\nabla^2 \delta\Phi = 4\pi G \delta\rho \,. \tag{2.28}$$

These equations can be combined and rearranged, which ultimately yields a single equation for density perturbations:

$$\left(\frac{\partial^2}{\partial t^2} - c_s^2\, \nabla^2 - 4\pi G \bar{\rho} \right) \delta\rho(\boldsymbol{x}, t) = 0 \,. \tag{2.29}$$

If we express $\delta\rho(\boldsymbol{x}, t)$ as a Fourier expansion, the Fourier modes $\delta\rho(\boldsymbol{k}, , t)$ must now obey [86]:

$$\frac{\partial^2 \delta\rho(\boldsymbol{k}, t)}{\partial t^2} + \left(c_s^2 k^2 - 4\pi G \bar{\rho} \right) \delta\rho(\boldsymbol{k}, t) = 0 \,, \tag{2.30}$$

which has the following two independent solutions:

$$\delta\rho(\boldsymbol{k}, t) \propto \exp\left(\pm i w(k) t\right) \,, \text{ where } \; w(k) = \sqrt{c_s^2 k^2 - 4\pi G \bar{\rho}} \,. \tag{2.31}$$

This defines a wave number, or equivalently a length scale known as the Jeans length λ_{J}, at which oscillations have a frequency $w = 0$:

$$\lambda_{\mathrm{J}} = c_s \sqrt{\frac{\pi}{G\bar{\rho}}} \,. \tag{2.32}$$

Solutions of equation (2.31) behave differently depending on their length scale or wavenumber. Namely on small scales ($\lambda \ll \lambda_{\mathrm{J}}$) pressure dominates and leads to oscillating sound waves, while on large scales ($\lambda > \lambda_{\mathrm{J}}$), gravity dominates and pressure becomes negligible. Ignoring pressure on these large scales leads to solutions of the form:

$$\delta\rho(\boldsymbol{k}, t) \propto \exp\left(\pm |w| t\right) \,, \tag{2.33}$$

where inhomogeneities in density either decay quickly or grow exponentially fast, leading to a gravitational collapse. However, a proper treatment of nonlinear effects from baryons, such as their pressure and shocks across small and large scales, as well as during gravitational collapse, necessitates complex hydrodynamical simulations (see chapter 4).

So far we ignored the expansion of the Universe, which we will now include. For this, we use the previous equations in physical coordinates $\boldsymbol{x}$, but now move to comoving coordinates $\boldsymbol{q}$, with $\boldsymbol{x} = a\boldsymbol{q}$, where a is the scale factor. The velocity field then becomes:

$$\boldsymbol{v}(t) = \dot{\boldsymbol{x}} = H\boldsymbol{x} + a\dot{\boldsymbol{q}} = H\boldsymbol{x} + \boldsymbol{v}_{\mathrm{pec}}\,, \tag{2.34}$$

which consists of the physical peculiar velocity $\boldsymbol{v}_{\mathrm{pec}}$ and the Hubble flow $H\boldsymbol{x}$. With the inclusion of expansion, we now have to adapt our derivatives. In the previous static space both ∂_t and ∇ were independent, but are not in an expanding space. While $\nabla_{\boldsymbol{x}}$ in physical coordinates simply transforms as $\nabla_{\boldsymbol{x}} = a^{-1}\nabla_{\boldsymbol{q}}$ for comoving coordinates, the partial derivative of a function $f(\boldsymbol{x}, t)$ with respect to time t at constant physical location $\boldsymbol{x}$ becomes:

$$\left(\frac{\partial f}{\partial t}\right)_{\mathbf{x}} = \left[\left(\frac{\partial}{\partial t}\right)_{\mathbf{q}} - H\boldsymbol{q}\cdot\nabla_{\boldsymbol{q}}\right] f \tag{2.35}$$

Using these transformations of derivatives and the velocity $\boldsymbol{v}$ from equation (2.34), equations (2.22) to (2.24) become:

$$\partial_t\rho + 3H\rho + \frac{1}{a}\nabla\cdot(\rho\,\boldsymbol{v}_{\mathrm{pec}}) = 0\,, \tag{2.36}$$

$$\left(\partial_t + \frac{\boldsymbol{v}_{\mathrm{pec}}}{a}\cdot\nabla\right)\boldsymbol{v} = -\frac{1}{a}\frac{\nabla p}{\rho} - \frac{1}{a}\nabla\Phi\,, \tag{2.37}$$

$$\nabla^2\Phi = 4\pi G a^2\rho\,. \tag{2.38}$$

where we dropped any subscripts $\boldsymbol{q}$ and used $\nabla\cdot\boldsymbol{q} = 3$. Of course all time derivatives are at fixed comoving $\boldsymbol{q}$ and all ∇ are with respect to comoving coordinate $\boldsymbol{q}$. This set of equations consists of the continuity, Euler and Poisson equation, all for an expanding background, for which we set $\boldsymbol{v}_{\mathrm{pec}} = 0$. With this, equation (2.36) is simply $\partial_t\rho + 3H\rho = 0$ and the solutions for our background parameters become $\bar{\rho}\propto a^{-3}$, $\bar{\boldsymbol{v}} = Ha\,\boldsymbol{q}$, $\bar{p} = \text{const.}$ and $\nabla\bar{\Phi} = -\ddot{a}a\,\boldsymbol{q}$.

We once more introduce the perturbations like in equation (2.25) and use our solution of the background velocity $\boldsymbol{v} = Ha\,\boldsymbol{q} + \boldsymbol{v}_{\mathrm{pec}}$. Furthermore, we define the density contrast δ as:

$$\delta \equiv \frac{\delta\rho}{\bar{\rho}} = \frac{\rho}{\bar{\rho}} - 1\,, \tag{2.39}$$

where positive values of δ correspond to overdensities with respect to the background value and negative ones to underdensities. As long as $|\delta| \ll 1$ holds, keeping only terms of linear order is a valid approach. Once more we keep only terms of at most linear order in perturbations in equations (2.36) to (2.38). Using the evolution of the background density ($\bar{\rho}\propto a^{-3}$) in the continuity equation (2.36), we find for the density contrast:

$$\dot{\delta} = -\frac{1}{a}\nabla\cdot\boldsymbol{v}_{\mathrm{pec}}\,, \tag{2.40}$$

where the dot on $\dot{\delta}$ denotes a derivative with respect to time at fixed $\boldsymbol{q}$. Similarly, keeping only terms of linear order in the Euler equation (2.37) results in:

$$\dot{\boldsymbol{v}}_{\rm pec} + H\boldsymbol{v}_{\rm pec} = -\frac{1}{a\,\bar{\rho}}\nabla\delta p - \frac{1}{a}\nabla\delta\Phi\,, \tag{2.41}$$

where $(\boldsymbol{v}_{\rm pec}\cdot\nabla)\boldsymbol{x} = \boldsymbol{v}_{\rm pec}$ was used. From equation (2.41) we clearly see that in the absence of gravity and pressure, the peculiar velocity scales as $\boldsymbol{v}_{\rm pec} \propto a^{-1}$. After combining equations (2.40) and (2.41), and using $\delta p = c_s^2\,\bar{\rho}\,\delta$, as well as the linearized Poisson equation in an expanding universe, we ultimately find an equation that describes the evolution of small density fluctuations in an expanding universe [89]:

$$\ddot{\delta} + 2H\,\dot{\delta} - \left(\frac{c_s^2}{a^2}\nabla^2 + 4\pi G\,\bar{\rho}(t)\right)\delta = 0\,. \tag{2.42}$$

The Jeans length for these perturbations has identical form to equation (2.32), although it now depends on time due to c_s and $\bar{\rho}$ depending on the expansion of the background.

In a universe that is filled solely with non-relativistic matter and on scales larger than the Jeans length, we can once more neglect the influence of pressure and set $c_s = 0$. This simplifies equation (2.42), since spatial derivatives vanish and it only contains derivatives with respect to time. Hence, any solution to this equation can be separated as follows:

$$\delta(\boldsymbol{k},t) = \tilde{D}_+(t)\delta_+(\boldsymbol{k}) + \tilde{D}_-(t)\delta_-(\boldsymbol{k})\,, \tag{2.43}$$

where the functions $\tilde{D}_\pm$ describe the linear evolution of densities in time and $\delta_\pm(\boldsymbol{k})$ are the Fourier modes of the density field at some initial point in time. $\tilde{D}_-(t)$ and $\tilde{D}_+(t)$ are the decaying and growing modes. They are normalized such that $\tilde{D}_+(t_0) = 1$ and $\tilde{D}_+$ is referred to as the linear growth function. For a flat matter-dominated universe, solutions are given by:

$$\tilde{D}_+(t) \propto a \propto t^{2/3} \;\text{ and }\; \tilde{D}_-(t) \propto a^{-3/2} \propto t^{-1}\,, \tag{2.44}$$

where we used $a \propto t^{2/3}$ for a matter-dominated universe. The actual fluctuation in density, $\delta\rho$, then evolve as $\delta\rho = \bar{\rho}\,\delta \propto a^{-2}$, since the background density evolves as $\bar{\rho} \propto a^{-3}$ for such a universe. In real space, we can similarly split the evolution of $\delta(\boldsymbol{q},t)$ in a temporal and spatial component:

$$\delta(\boldsymbol{q},t) = D_+(t)\delta(\boldsymbol{q})\,. \tag{2.45}$$

We will revisit this growth function in section 9.4, where we test its prediction around voids in a more realistic model of our Universe.

2.3 Spherical evolution of underdensities

As we introduced the evolution of inhomogeneities at linear order in section 2.2, we now want to focus specifically on the evolution of underdensities, i.e. voids. This section is

based on the considerations in reference [87]. For the sake of convenience we will drop the explicit time dependence of variables in most cases, e.g. $\delta(r,t) = \delta(r)$. For a spherically symmetric fluctuation in density, $\delta(r)$, its average density contrast $\Delta(r)$ is:

$$\Delta(r) = \frac{3}{r^3} \int_0^r \delta(q) q^2 \, \mathrm{d}q \,. \tag{2.46}$$

This average density contrast can be related to the radial velocity field via [92]:

$$v(r,t) = -\frac{1}{3} f(t)\, a(t)\, H(t)\, r\, \Delta(r,t) \,, \tag{2.47}$$

which contains the linear growth rate f given by $f(t) \simeq \Omega_\mathrm{m}^{0.55}(t)$. This equation can be derived from equations (2.43) and (2.41), assuming spherical fluctuations in density. We will reintroduce this relation in more detail in section 3.2 and test its validity for voids in chapter 7. The total mass inside a sphere of radius r is then given in terms of its average density contrast as:

$$M(r) = \frac{4\pi}{3} r^3 \, \bar{\rho} \, (1 + \Delta(r)) \,. \tag{2.48}$$

Birkhoff's Theorem states that any spherically symmetric body gravitationally affects external objects as if all its mass would be located at its center. Hence, in our Newtonian approach the equation of motion for any outside test particle is given by $\ddot{r} = -GM(r)/r^2$. Integrating this equation of motion and using the total mass $M(r)$ from equation (2.48) leads to:

$$\dot{r}^2 - \frac{8\pi G}{3} \bar{\rho}\, r^2 \, (1 + \Delta(r)) = 2K \,, \tag{2.49}$$

where K is a constant of integration and connected to the curvature in equation (2.8). For the special case of $K = \Delta = 0$, we find the same critical density as in equation (2.14), where $\dot{r}/r = H = \dot{a}/a$. Introducing the dimensionless density parameter Ω_m once more, we find:

$$\dot{r}^2 - \Omega_\mathrm{m}\, H^2\, r^2 \, (1 + \Delta(r)) = 2K \,. \tag{2.50}$$

For simplicity, we will consider an Einstein-de Sitter universe (EdS) with $\Omega_\mathrm{m} = 1$ for the rest of this section. In such a case, the initial total velocity $\dot{r}_i$ is composed of the Hubble flow and the peculiar velocity from equation (2.47), with $f = 1$:

$$\dot{r}_i \simeq r_i\, H_i - \frac{1}{3} H_i\, r_i\, \Delta_i(r_i) \,, \tag{2.51}$$

which can be used in equation (2.50), which then yields at initial time:

$$2K = (r_i H_i)^2 \cdot \left[\left(1 - \frac{\Delta_i}{3}\right)^2 - 1 - \Delta_i \right] \simeq -\frac{5}{3} (r_i H_i)^2 \, \Delta_i \,, \tag{2.52}$$

where in the latter part, only terms of at most linear order in $|\Delta_i| \ll 1$ were kept. As mass must be conserved, we can relate the initial and final density contrasts via equation (2.48):

$$1 + \Delta(r) = (1 + \Delta_i) \, \frac{r_i^3}{r^3} \, \frac{\bar{\rho}_i}{\bar{\rho}} \, . \tag{2.53}$$

With $\Omega_\mathrm{m} = 1$ in an EdS universe, where $\bar{\rho} = \rho_\mathrm{crit}$, we find $\bar{\rho}_i/\bar{\rho} = (H_i/H)^2$, which can be used to rearrange equation (2.50):

$$\left(\frac{\dot{r}}{r}\right)^2 = H_i^2 \cdot \left[(1 + \Delta_i) \cdot \left(\frac{r}{r_i}\right)^{-3} - \frac{5}{3} \, \Delta_i \left(\frac{r}{r_i}\right)^2 \right] . \tag{2.54}$$

This equation closely resembles the first Friedmann equation (2.8) in a curved matter-dominated universe, with small perturbations to the densities of matter $\Omega_{\mathrm{m},i} = 1 + \Delta_i$ at initial time t_i and curvature $\Omega_\mathrm{K} = -\frac{5}{3}\Delta_i$. In case no initial perturbations exist, $\Delta_i = 0$ and we recover the Friedmann equation in an EdS universe, which is solved by $r/r_i = (H/H_i)^{-2/3}$, with $H = 2/3t$. However, in the case of initial perturbations $\Delta_i \neq 0$ we can only find solutions in parametric form, which are given by:

$$\frac{r}{r_i} = \frac{1}{2} \left(\frac{5}{3} \, \Delta_i\right)^{-1} (1 - \cos\eta) \, , \tag{2.55}$$

$$H_i \, t = \frac{1}{2} \left(\frac{5}{3} \, \Delta_i\right)^{-\frac{3}{2}} (\eta - \sin\eta) \, , \tag{2.56}$$

where we introduced the parameter η, defined as:

$$\mathrm{d}\eta = \frac{r_i}{r} \sqrt{\frac{5}{3} \, \Delta_i} \; H_i \, \mathrm{d}t \, . \tag{2.57}$$

For initial underdensities we have $\Delta_i < 0$ and η becomes imaginary. Using the substitutions $\Delta_i \leftrightarrow -|\Delta_i|$ and $\eta \leftrightarrow i\eta$, we can express equations (2.55) and (2.56) as [87]:

$$\frac{r}{r_i} = \frac{1}{2} \left(\frac{5}{3} \, |\Delta_i|\right)^{-1} (\cosh\eta - 1) \, , \tag{2.58}$$

$$H_i \, t = \frac{1}{2} \left(\frac{5}{3} \, |\Delta_i|\right)^{-\frac{3}{2}} (\sinh\eta - \eta) \, . \tag{2.59}$$

Underdensities with Δ_i never reach a point where $\dot{r} = 0$, hence they continue to expand forever. Only if an overdensity exists on a larger scale, referred to as the 'void-in-cloud' scenario, can the expansion stop and $\dot{r}$ become 0.

Let us now consider shells of different initial radius r_i. The moment these different shells cross each other is interpreted as the time a void is formed and additionally marks the stage where nonlinearities become relevant. In the instant of time at which these shells

cross, the distance between shells vanishes, i.e. $\mathrm{d}t = \mathrm{d}r = 0$. Calculating both $\mathrm{d}r$ and $\mathrm{d}t$ from equations (2.58) and (2.59), and using the fact that both become zero at the moment of shell-crossing, we can ultimately find:

$$\frac{\mathrm{d}\ln\Delta_i}{\mathrm{d}\ln r_i}\left[1-\frac{3}{2}\frac{\sinh\eta\cdot(\sinh\eta-\eta)}{(\cosh\eta-1)^2}\right]=1\,. \tag{2.60}$$

Furthermore, we can use the definition of the integrated density contrast Δ in equation (2.46) to find:

$$\frac{\mathrm{d}\ln\Delta}{\mathrm{d}\ln r}=3\left(\frac{\delta(r)}{\Delta(r)}-1\right)\,, \tag{2.61}$$

The condition of shell-crossing in equation (2.60) depends on the slope of the initial underdensity. If we assume an initial density contrast δ_i in the form of an inverted top-hat distribution with size $r_0 > 0$ and underdensity $\delta_0 < 0$, we have:

$$\begin{aligned}\delta_i(r_i) &= \begin{cases}\delta_0 & \text{for } r_i < r_0\\ 0 & \text{for } r_i \geq r_0\end{cases}\\ \Delta_i(r_i) &= \begin{cases}\delta_0 & \text{for } r_i < r_0\\ \delta_0\left(\frac{r_0}{r_i}\right)^3 & \text{for } r_i \geq r_0\,,\end{cases}\end{aligned} \tag{2.62}$$

Using this inverted top-hat density contrast, the first part of equation (2.60) becomes:

$$\frac{\mathrm{d}\ln\Delta_i}{\mathrm{d}\ln r_i}=\begin{cases}0 & \text{for } r_i < r_0\\ -3 & \text{for } r_i \geq r_0\end{cases}\,. \tag{2.63}$$

For $r_i < r_0$ we only find the trivial solution $\eta = 0$ for equation (2.60), but for $r_i \geq r_0$, we find instead:

$$\frac{\sinh\eta\cdot(\sinh\eta-\eta)}{(\cosh\eta-1)^2}=\frac{8}{9}\,, \tag{2.64}$$

which is solved by η at shell-crossing for $\eta_{\mathrm{sc}} \simeq 3.488$, which is first satisfied at the boundary shell of the top hat at $r_i = r_0$, but shells of larger size will cross afterwards. Taking a derivative with respect to time of the solution in equation (2.58) computes the shell velocity v and using equation (2.59) ultimately yields with $H = 2/3t$ for an EdS universe:

$$v = r\,H\,\frac{3}{2}\cdot\frac{\sinh\eta\cdot(\sinh\eta-\eta)}{(\cosh\eta-1)^2}\,, \tag{2.65}$$

which becomes $v_{\mathrm{sc}} = \frac{4}{3}\,rH$ at the moment of shell-crossing η_{sc}. Hence, shells move at a peculiar velocity of $v_{\mathrm{pec}} = v_H/3$ in addition to them following the Hubble flow $v_H = rH$

of the expansion of the EdS universe. Moreover, we can find that average density contrast inside this underdensity is given by [87]:

$$1 + \Delta = (1 + \Delta_i) \, \frac{9 \, (\sinh \eta - \eta)^2}{2 \, (\cosh \eta - 1)} \, . \tag{2.66}$$

For our top-hat at the moment of shell-crossing $\eta_{\mathrm{sc}} \simeq 3.488$ we find $1 + \Delta_{\mathrm{sc}} \simeq 0.2047$ and therefore $\delta_{0,\mathrm{sc}} \simeq -0.8$ for the density contrast.

Of course the inverted top-hat density contrast is not a realistic model for an initial underdensity. However, it has been shown numerically that the density around the minima of a Gaussian random field evolves similarly to a top-hat configuration [93, 94]. In observation we only identify voids in biased tracers such as galaxies, so the density contrast has to be modified and include the bias of such tracers. Reference [44] showed that in the linear regime around voids, a multiplicative constant b is sufficient to approximate the density contrast of tracers as $\delta_{\mathrm{t}} = b \, \delta_{\mathrm{m}}$.

These results are based on the assumption of an EdS universe in order to get insights on the evolution of underdensities. Although this assumption is far from reality, calculations in more realistic models of our Universe result in similar values [95], so the dependence on cosmology is rather weak.

Of course in reality voids are neither perfectly spherical, nor are they completely isolated objects. Throughout their evolution in time, they can contain sub-voids, neighboring voids may merge and some voids might even collapse. Such effects lead to far more complicated structures than we investigated in this section and suggests the need for complex N-body simulations of our Universe.

Chapter 3

Methodology

3.1 VIDE void finding

To identify voids in both the halo, as well as the underlying matter distributions, we use the Void IDentification and Examination toolkit VIDE[1] [96]. VIDE works by implementing an enhanced version of the ZOnes Bordering On Voidness algorithm ZOBOV [97], which is a watershed algorithm [98], identifying local basins in the three-dimensional density field estimated from the positions of (any) chosen tracer particles. This density field is constructed via Voronoi tessellation, in which each tracer particle j is assigned a unique Voronoi cell of volume V_j. These Voronoi cells are defined as the volume of space that is closer to its associated tracer particle than to any other particle in the entire simulation. Therefore, combining the volumes of all Voronoi cells fills the whole simulation box. The tracer density anywhere inside the Voronoi cell of particle j is simply given by its inverse volume, $n_j = 1/V_j$. Starting from local minima in the density field, the watershed algorithm searches for neighboring cells with monotonically increasing density, in order to find extended basins of density depressions, which are our cosmic voids.

In addition, VIDE implements a density-based merging threshold within ZOBOV, which is a free parameter in newer versions. Adjoining basins will be added to a void only if the minimal density along their shared ridge line is below this merging threshold in units of the mean tracer density $\bar{n}$. A small threshold prevents voids from extending deeply into overdense structures, which limits the depth of the void hierarchy [96, 97]. If two adjacent basins are merged, this will result in two voids, with one encompassing the other, creating a 'parent' and a 'child' void. Hence, the original number of voids is preserved even after merging. The only difference is that the child-level void is now considered as a sub-void of the larger parent-level void, which encompasses the volume of both original voids. With this definition, every void can only have one parent, but in turn multiple children, or sub-voids. The default value of the merging parameter is set to a very small number, in order to prevent any merging between adjacent basis. This results in a sample of only parent voids, with no sub-voids present. Approaching higher values of the merging threshold on

[1] https://bitbucket.org/cosmicvoids/vide_public/wiki

the order of one and above creates a hierarchy of voids with potentially many levels of sub-voids, though the total number of voids remains independent of the chosen merging threshold. Unless stated otherwise, we will always use the default merging threshold of $10^{-9}\bar{n}$, small enough to prevent merging.

In the literature it is also common to use a merging threshold value of $0.2\bar{n}$, which has a special physical significance. It is derived from the spherical expansion model of an inverted top-hat perturbation in an Einstein-de Sitter universe (see section 2.3). The derived value of $0.2\bar{n}$ marks the characteristic density inside the top hat perturbation when shell crossing occurs at its boundaries [94, 97, 99]. However, this value only applies when the threshold is defined in the complete matter density field and assuming spherical symmetry. For voids identified in the number density field of biased tracers, one has to additionally account for the tracer bias [44, 100–102]. Additionally, the sparsity of tracer particles accounts for an effective smoothing of the density field on scales below the mean tracer separation, which in turn can affect the density ridges between voids [103].

When we investigate effects of merging, we restrict ourselves to two extreme thresholds for merging, namely a value close to zero for no merging of voids (our default $10^{-9}\bar{n}$) and a value of infinity to create a fully merged void hierarchy. We will refer to the former case as an *isolated* and the latter one as a *merged* void catalog, respectively. These resulting catalogs encompass all cases of finite merging thresholds in between. The *merged* catalog with infinite threshold consists of one single parent void with a deep hierarchy of children, whereas *isolated* void catalogs only contain separate and non-overlapping voids.

Performing the void finding with VIDE results in catalogs of non-spherical voids, including a variety of their properties. The center of a void is defined as the volume-weighted barycenter of all of its member particles' Voronoi cells, at comoving tracer locations $\boldsymbol{x}_j$:

$$\mathbf{X}_\mathrm{v} = \frac{\sum_j \boldsymbol{x}_j \, V_j}{\sum_j \, V_j}. \tag{3.1}$$

The barycenter can be thought of as the geometric center of a void, since its position is constrained by its boundary, where most of the tracer particles are located. This definition makes the barycenter of a void robust against Poisson fluctuations and preserves information about the topology of a void. However, it does not necessarily coincide with the position of the Voronoi cell of lowest density due to the lack of spherical symmetry in voids. For this very reason, we can also only define an *effective void radius* r_v, which is the radius of a sphere of identical volume as the void. This volume is calculated simply using the sum over all the associated Voronoi cell volumes of a void:

$$r_\mathrm{v} = \left(\frac{3}{4\pi} \sum_j \, V_j \right)^{1/3}. \tag{3.2}$$

In order to quantify the shapes of voids, VIDE calculates their inertia tensor, defined as:

$$M_{xx} = \sum_j \left(y_j^2 + z_j^2\right) \,, \\ M_{xy} = -\sum_j x_j \, y_j \,, \tag{3.3}$$

where the summation goes over all member particles with comoving coordinates x_j, y_j, and z_j relative to the barycenter. Other components of the inertia tensor are defined accordingly. The ellipticity of a void is then given in terms of the smallest (J_1) and largest (J_3) eigenvalues of its inertia tensor [96]:

$$\varepsilon = 1 - \left(\frac{J_1}{J_3}\right)^{1/4} \,. \tag{3.4}$$

Additional void properties of interest in this work include the core density $\hat{n}_{\rm min}$ and the compensation $\Delta_{\rm t}$ [69]. For the latter, the index 't' for tracers is either 'h' in case of finding voids in the halo distribution or 'm' for matter (CDM or baryons), respectively. The core density is the density of the largest Voronoi cell of a void and thus the cell of minimal density, expressed in units of the mean density of tracers:

$$\hat{n}_{\rm min} = \frac{n_{\rm min}}{\bar{n}} \,. \tag{3.5}$$

The compensation of a void is a measure of whether it contains more or less member particles $N_{\rm t}$ than an average patch of same volume V in the Universe. It therefore conveys information about the environment a particular void is located in, whether it is one of lower or higher local average density $\hat{n}_{\rm avg}$, in units of the mean $\bar{n}$. Voids with $\Delta_{\rm t} < 0$ are referred to as being undercompensated and voids with $\Delta_{\rm t} > 0$ as being overcompensated [32, 38]. The compensation is simply defined as:

$$\Delta_{\rm t} \equiv \frac{N_{\rm t}/V}{\bar{n}} - 1 = \hat{n}_{\rm avg} - 1 \,. \tag{3.6}$$

3.2 Void profiles

The density profile $n_{\rm v}^{(i)}(r)/\bar{n} - 1$ of each individual void i is defined as the spherically averaged density contrast around the void center from its mean value $\bar{n}$ in the Universe. For discrete tracer particles, the density in radial shells of thickness $2\delta r$ at comoving distance r from the center at the origin can be estimated as:

$$n_{\rm v}^{(i)}(r) = \frac{3}{4\pi\,\bar{w}} \sum_j \frac{w_j \; \Theta(r_j)}{(r+\delta r)^3 - (r-\delta r)^3} \,, \tag{3.7}$$

where $\Theta(r_j) \equiv \vartheta\left[r_j - (r-\delta r)\right] \, \vartheta\left[-r_j + (r+\delta r)\right]$ makes use of two Heaviside step functions ϑ to define the radial bins of each profile, with r_j being the distance of tracer j from

the void center. The summation goes over all tracers j in the vicinity of the void and not just its associated tracers, up to the desired maximal distance. The w_j in equation (3.7) represent a placeholder for optional weights for each tracer and $\bar{w} = \frac{1}{N_\mathrm{t}} \sum_k w_k$ is the average of weights over all N_t tracers. When investigating the usual (unweighted) density profile, we simply set $w_j = 1$ for each tracer. An alternative option is the inclusion of halo masses as weights, which we will explore in section 6.2.

Most of the time we are not interested in the individual density profiles of voids, but in the stacked density profiles. These stacks are simply an average over individual void profiles in ranges of various void properties, although typically their radius r_v is used. To maintain characteristic features of voids, such as their compensation walls, at a constant location from the center in a given stack, and in order to have better comparisons between different stacks, we calculate the profile of all individual voids using a constant radial bin size when expressed in units of their radius, i.e. $\delta r / r_\mathrm{v} = \text{const}$. This ensures that every void's compensation wall is centered closely around $r = r_\mathrm{v}$, and is not scattered across different distances when using constant units in physical scale. In this manner, the stacked density profile of voids is simply given by an average over equation (3.7):

$$n_\mathrm{v}(r) = \frac{1}{N_\mathrm{v}} \sum_i n_\mathrm{v}^{(i)}(r) \,. \tag{3.8}$$

When calculating density profiles of voids using baryon and CDM tracers, we will denote these profiles by $\rho_\mathrm{v}(r)/\bar{\rho} - 1$ instead of $n_\mathrm{v}(r)/\bar{n} - 1$ for (biased) halo tracers, and $n_\mathrm{v}^{(\mathrm{w})}(r)/\bar{n}^{(\mathrm{w})} - 1$ for the mass-weighted density profiles based on halo tracers.

To investigate the radial movement of tracers around voids, we calculate their velocity profile around the barycenter. In our definition, positive velocities correspond to an outflow of tracers from the perspective of the center, whereas negative velocities correspond to an inward movement towards the void center. The velocity profile of every individual void i can be estimated by calculating:

$$u_\mathrm{v}^{(i)}(r) = \frac{\sum_j \boldsymbol{u}_j \cdot \hat{\boldsymbol{r}}_j \; V_j \; \Theta(r_j)}{\sum_j V_j \; \Theta(r_j)} \,. \tag{3.9}$$

In equation (3.9), $\boldsymbol{u}_j$ is the peculiar velocity vector of a given tracer j, $\hat{\boldsymbol{r}}_j = \boldsymbol{r}_j / r_j$ the unit vector which connects the tracer particle j with the void center and V_j its Voronoi cell volume. By weighting the velocities of individual particles with their Voronoi volumes V_j, we ensure that our calculated velocity profile is a volumetric representation of the true underlying velocity field [38, 104]. This volume weighting takes into account that a uniform sampling of velocity fields from an uneven tracer distribution is biased high in more dense and biased low in emptier regions [83].

Moving to stacked velocity profiles, there are two different ways for their calculation. The first option is equivalent to the previous way of stacking density profiles, namely by simply averaging over the individual velocity profiles of each void in the desired stack:

$$u_\mathrm{v}(r) = \frac{1}{N_\mathrm{v}} \sum_i u_\mathrm{v}^{(i)}(r) \,. \tag{3.10}$$

We will refer to the stacks using this method as *individual stacks*. Alternatively, we can average both denominator and numerator of equation (3.9) separately for all voids included in the stack, before finally taking their ratio:

$$u_{\mathrm{v}}(r) = \frac{\sum_i \left[\sum_j \boldsymbol{u}_j \cdot \hat{\boldsymbol{r}}_j \; V_j \; \Theta(r_j)\right]^{(i)}}{\sum_i \left[\sum_j V_j \; \Theta(r_j)\right]^{(i)}} \,. \tag{3.11}$$

This method of stacking velocity profiles will be referred to as *global stacks*. Typically there are many voids, especially small ones, which contain no or only very few tracer particles close to their centers. Hence, an estimation of the velocity field is not possible there and it is simply set to zero by default. Stacking many such individual profiles with zero velocity in the center via equation (3.10) will not result in a much better velocity estimate. However, using the method of global stacking one first gathers all tracers within the entire void sample of the stack and then divides by the normalization of equation (3.11). This guarantees better statistics for the tracer counts in shells, although it comes with the disadvantage of statistically favoring larger voids, whose shells are of larger volume in physical scale and usually contain more particles per shell. Both *individual* and *global stacks* come with advantages, as well as disadvantages and depending on the application, one method may be preferred over the other. We will discuss the issues with each method in more detail in the following chapters.

At last, imposing local mass conservation allows us to relate the density profiles of voids with their velocity profiles via the linearized continuity equation [92, 105], which was previously introduced in section 2.3:

$$u_{\mathrm{v}}(r, z) = -\frac{1}{3} \frac{f(z)}{b_{\mathrm{t}}} \frac{H(z)}{1+z} \, r \, \Delta(r) \,, \tag{3.12}$$

where $f(z) = \Omega_{\mathrm{m}}^{\gamma}(z)$ is the linear growth rate of density perturbations, with $\gamma \simeq 0.55$ being the growth index of matter perturbations in GR. Furthermore, $H(z)$ is the Hubble parameter, $\Omega_{\mathrm{m}}(z)$ the matter density parameter and b_{t} the bias of tracer particles, with $b_{\mathrm{t}} = 1$ for baryons and CDM. Lastly, the integrated density contrast $\Delta(r)$, introduced in equation (2.46), is given in terms of void density profiles as:

$$\Delta(r) = \frac{3}{r^3} \int_0^r \left(\frac{n_{\mathrm{v}}(q)}{\bar{n}} - 1 \right) q^2 \, \mathrm{d}q \,. \tag{3.13}$$

Combining equations (3.12) and (3.13) ultimately yields:

$$u_{\mathrm{v}}(r, z) = -\frac{\Omega_{\mathrm{m}}^{\gamma}(z)}{b_{\mathrm{t}}} \frac{H(z)}{1+z} \frac{1}{r^2} \int_0^r \left(\frac{n_{\mathrm{v}}(q)}{\bar{n}} - 1 \right) q^2 \, \mathrm{d}q \,. \tag{3.14}$$

This allows us to see the direct relation between density and velocity profiles. In chapter 7 we will investigate the validity of equation (3.14) in the environment around cosmic voids and across vast scales.

Chapter 4

The Magneticum simulations

This work is based on simulations from the Magneticum[1] suite, multiple state-of-the-art hydrodynamical simulations covering a variety of cosmological volumes at different mass resolutions, ranging from 48 Mpc/h to 2688 Mpc/h in box length and 7.3×10^6 to $1.3 \times 10^{10} M_\odot/h$ in particle mass in this work. In addition to the hydrodynamical simulations, which we will refer to as hydro, each box has a corresponding dark matter only simulation with identical initial seed, referred to as DMo. We will briefly describe the Magneticum suite below and refer to previous work using these simulations for more details [e.g., 24, 106–114]. The Magneticum runs used in this work adopt a flat ΛCDM cosmology, for which the best fitting values of WMAP7 [115] are chosen, with $h = 0.704$, $\Omega_\Lambda = 0.728$, $\Omega_\mathrm{m} = 0.272$, $\Omega_\mathrm{b} = 0.0456$, $n_s = 0.963$ and $\sigma_8 = 0.809$, except for different cosmology runs in box 1a.

The simulations have been conducted using an advanced version of the tree particle mesh-smoothed particle hydrodynamics (TreePM-SPH) code P-Gadget3 [116], which includes an improved SPH solver [117]. The code implements a large variety of processes that describe the physics and evolution of baryons, such as the distribution of various metal species [118], prescriptions describing the growth of black holes and the feedback from active galactic nuclei (AGN), based on the work in references [119–121].

Prior studies with the Magneticum simulations include the reproduction of many observables over multiple scales, such as the observed SZ-power spectrum [24] and the observed thermal history of the Universe [122] on large scales. On smaller scales such as the ones of clusters, the simulations were used to successfully reproduce the pressure profile and chemical composition of the intra-cluster medium [118, 123, 124], the observable luminosity-relation in X-ray [125], as well as the high concentration of halos in fossil groups [126] and gas properties in between galaxy clusters [127]. On even smaller scales, the aforementioned implementation of baryonic physics led to the successful reproduction of various galaxy properties, including realistic stellar masses [128, 129], cluster environment impact on galaxies [130], the population of AGNs [106, 124, 131] and post-starbust galaxy evolution [132].

In this work we mainly focus on the Magneticum boxes 0 and 2b, as these two comprise

[1] http://www.magneticum.org

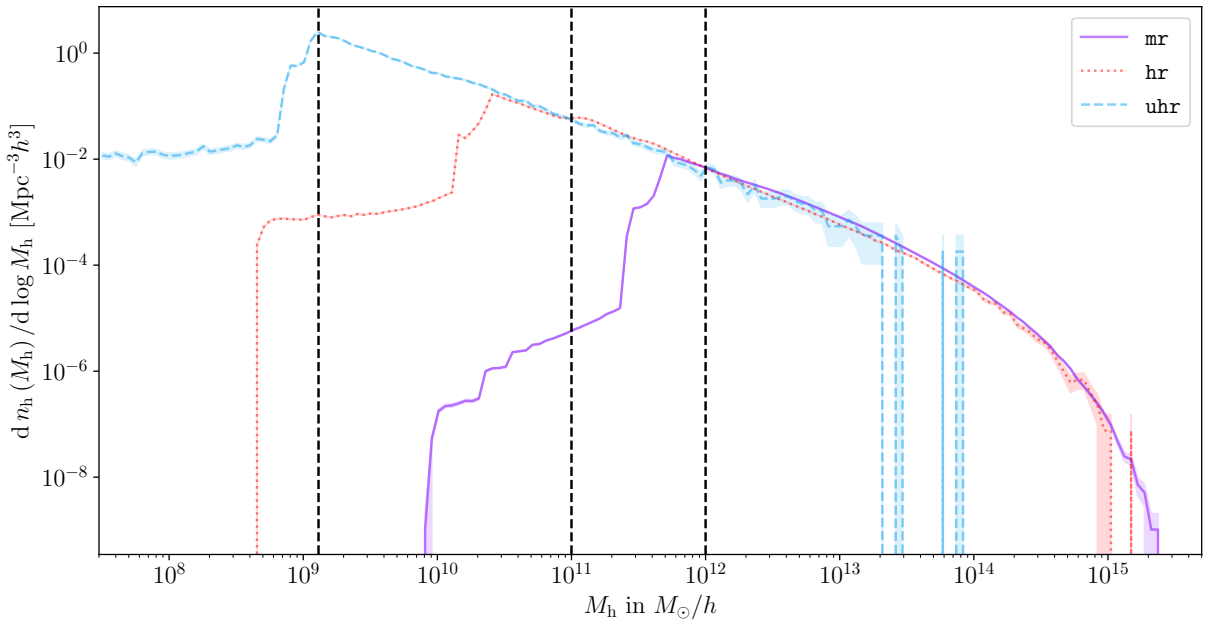

Figure 4.1: Halo mass function in the `midres`, `highres` and `ultra-hr` `hydro` simulations at redshift $z = 0.29$. Vertical lines indicate the chosen halo mass cuts for void finding at $1.0 \times 10^{12}\, M_\odot/h$ (`mr`), $1.0 \times 10^{11}\, M_\odot/h$ (`hr`) and $1.3 \times 10^{9}\, M_\odot/h$ (`uhr`) at this redshift.

the largest volumes of medium (box 0) and high (box 2b) mass resolution. Their volumes are of large enough size to contain sufficient void numbers (see table 5.1), whose typical sizes are in the range of $5 - 80$ Mpc$/h$ (see figure 5.1). Hence, from now on box 0 will be referred to as `midres` (`mr`) and box 2b as `highres` (`hr`). Analysis of the tracer bias around voids already made use of the `midres` simulation in previous work [44]. For additional tests on smaller scales, we make use of box 4 with an even higher resolution, although with the caveat of fewer voids, and refer to it as `ultra-hr` (`uhr`). Moreover, box 1a is a smaller box of identical mass resolution as box 0 and includes a variety of runs with different cosmologies. In further tests using this box, we will refer to it as `midres-1a` (`mr1a`) and give details on the different cosmological parameters used for tests in the relevant sections. Furthermore, we will investigate voids across a wide range of redshifts, which will be stated at the beginning of each chapter or in the relevant figures. For a summary of details on the number of simulated particles, box sizes L_Box, and mass resolution of CDM and baryons in the `hydro` `Magneticum` simulations, we refer the reader to table 4.1. In the `DMo` simulations the box size is unchanged, but the mass of their CDM particles is simply given by $m_\mathrm{part} = m_\mathrm{CDM} + m_\mathrm{baryon}$ from table 4.1, namely the combined mass of CDM and baryon particles of the corresponding `hydro` simulation.

To find voids in the biased tracers, we identify subhalos, as well as their properties via the SubFind algorithm [133], which was modified to take baryonic components into account [134]. From now on, we will refer to subhalos simply as 'halos'. Their centers are defined as the location of the member particle with minimal gravitational potential and

Name	Box	$L_{\mathrm{Box}}[\mathrm{Mpc}/h]$	$N_{\mathrm{particles}}$	$m_{\mathrm{CDM}}[M_\odot/h]$	$m_{\mathrm{baryon}}[M_\odot/h]$
`midres` (`mr`)	0	2688	2×4536^3	1.3×10^{10}	2.6×10^9
`midres-1a` (`mr1a`)	1a	896	2×1512^3	1.3×10^{10}	2.6×10^9
`highres` (`hr`)	2b	640	2×2880^3	6.9×10^8	1.4×10^8
`ultra-hr` (`uhr`)	4	48	2×576^3	3.6×10^7	7.3×10^6

Table 4.1: Properties of the `Magneticum` simulation boxes used in this work. Particle masses (m_{CDM} & m_{baryon}) are given for the `hydro` simulations.

the halo masses are defined by their total mass of baryonic and CDM particles, according to the definition of subhalo mass in SubFind. Since the simulations use different mass resolutions, we can select halos at different minimal masses for the void finding process. In `midres` and `midres-1a` we typically use $1.0 \times 10^{12}\, M_\odot/h$, in `highres` $1.0 \times 10^{11}\, M_\odot/h$ and in `ultra-hr` $1.3 \times 10^9\, M_\odot/h$, as well as $1.6 \times 10^9 M_\odot/h$, depending on the redshift. These mass cuts were chosen such that each one is above the resolution limit of the simulations at a given redshift, which is presented for $z = 0.29$ (with $1.3 \times 10^9\, M_\odot/h$ in `ultra-hr`) in figure 4.1. We will not consider halos with masses below these mass cuts in any further analysis in this work. In these aforementioned boxed we analyze voids found in halos from both `hydro` and `DMo` simulations, as well as in subsamplings of the underlying baryons and CDM that formed these halos.

Chapter 5

Magneticum catalogs

5.1 Tracers

As the void finding with VIDE solely requires the positions of any kind of tracer particles we will use the distributions of CDM, baryons, as well as halos from both `hydro` and `DMo` simulations to identify voids in this work. We will not identify voids in the total distribution of matter, i.e. baryons and CDM combined. From here on, we will refer to voids identified in the CDM and baryon distributions of the `hydro` simulations simply as *CDM voids* and *baryon voids* respectively, while voids identified in the CDM of the `DMo` simulations will be referred to as *CDMo voids*. When using halos, voids identified in the halos of the `hydro` simulations are simply referred to as *halo voids*, while in the case of halos from the `DMo` simulations, they are referred to as *`DMo` halo voids*. However, voids identified in the `DMo` simulations, as well as the baryon particles will only be of relevance for baryonic effects around voids in chapter 8.

Before investigating the impact of baryonic physics on void statistics, we want to explore more general properties of tracers and voids from the `midres` and `highres hydro` simulations in this and the following sections, as well as more general characteristics of void profiles in chapter 6, all at redshift $z = 0.29$. The corresponding numbers and number densities of halos which have masses above the mass cuts $M_{\rm cut}$ of $1.0 \times 10^{12}\,M_\odot/h$ in `midres` and $1.0 \times 10^{11}\,M_\odot/h$ in `highres` are given in table 5.1. The `midres` simulation is the closest match to the expected tracer densities attainable with state-of-the-art galaxy surveys, such as the Euclid mission [135].

Besides the investigation of halo voids, we additionally perform subsamplings of the CDM particles which closely match the number of halos used for the void identification. This is done in order to have identical mean tracer separations $\bar{r}_{\rm t}$, which results in halo- and CDM-defined voids of similar ranges in void radii. Moreover, the matched subsamplings of CDM and halo tracers eliminate any differences in the statistics of CDM and halo voids that are merely caused by the different tracer number densities. Furthermore, running VIDE on the whole simulation is neither feasible in most cases due to computational limitations, nor is it practical, because it would result in extremely small voids, foiling any reasonable

Name	$M_{\mathrm{cut}}\,[M_\odot/h]$	$N_{\mathrm{h}}\,[\times 10^6]$	$\bar{n}_{\mathrm{h}}\,[(\mathrm{Mpc}/h)^{-3}]$	$\bar{r}_{\mathrm{t}}\,[\mathrm{Mpc}/h]$	N_{v} in halos	N_{v} in CDM
`midres`	1.0×10^{12}	62.1	$3.2 \cdot 10^{-3}$	6.8	356 597	600 273
`highres`	1.0×10^{11}	8.21	$3.1 \cdot 10^{-2}$	3.2	33 324	52 951

Table 5.1: Number of halos N_{h} with $M_{\mathrm{h}} \geq M_{\mathrm{cut}}$, mean halo density $\bar{n}_{\mathrm{h}}$ and tracer separation $\bar{r}_{\mathrm{t}}$, number of halo voids and number of CDM voids in the different `hydro` runs, all at redshift $z = 0.29$. For CDM voids, subsamples of the CDM tracers that closely match N_{h} are used for void finding.

comparison between CDM and halo voids. Matching number densities at redshift $z = 0.29$ equates to subsampling to around 0.066% of the total CDM particles in `midres` and around 0.034% of all CDM particles in `highres`, and these subsamplings will be used throughout this work, unless mentioned otherwise. Even though voids found in the three-dimensional distribution of matter are not directly accessible to observations, we nevertheless study these voids in order to compare them to the ones identified through the use of halos, which can be used as proxies for galaxies.

5.2 Voids

Here we present *isolated*, as well as *merged* void catalogs extracted from the distribution of CDM and halos in both `midres` and `highres` simulations at redshift $z = 0.29$. For more details on the number of tracers used for the void identification, we refer to table 5.1 and section 5.1. Table 5.1 additionally contains the numbers of voids that were found using the stated mass cuts and subsamplings, with no change in void numbers between *isolated* and *merged* catalogs.

Figure 5.1 presents the abundance of *isolated* and *merged* voids as a function of their radius (up to around $80\,\mathrm{Mpc}/h$), ellipticity, and core density (up to a value of 1.5). The former is commonly known as the void size function [e.g., 33, 37, 95, 101, 136, 137]. First we note that whether or not voids are *merged* or *isolated* only affects their distribution in radius significantly, but their distributions in ellipticities and core densities are almost indistinguishable. Voids from the `highres` simulation are of smaller size than in `midres`, as the increased resolution provides more low-mass halos and an overall higher tracer density.

Note that even though the total number of halos and CDM particles are matched in each simulation box, we observe almost twice the number of voids in CDM (see table 5.1), which implies smaller CDM voids for a fixed volume. This difference is due to the halos being biased tracers, which are preferentially located in regions where the matter density is higher. CDM particles sample the density field more evenly without this bias, which is the reason we are able to detect voids in less dense regions as well. Hence, establishing a one-to-one correspondence between CDM voids and halo voids in any one simulation is not straightforward [103].

However, the void size functions of *merged* CDM and halo voids in both `midres` and

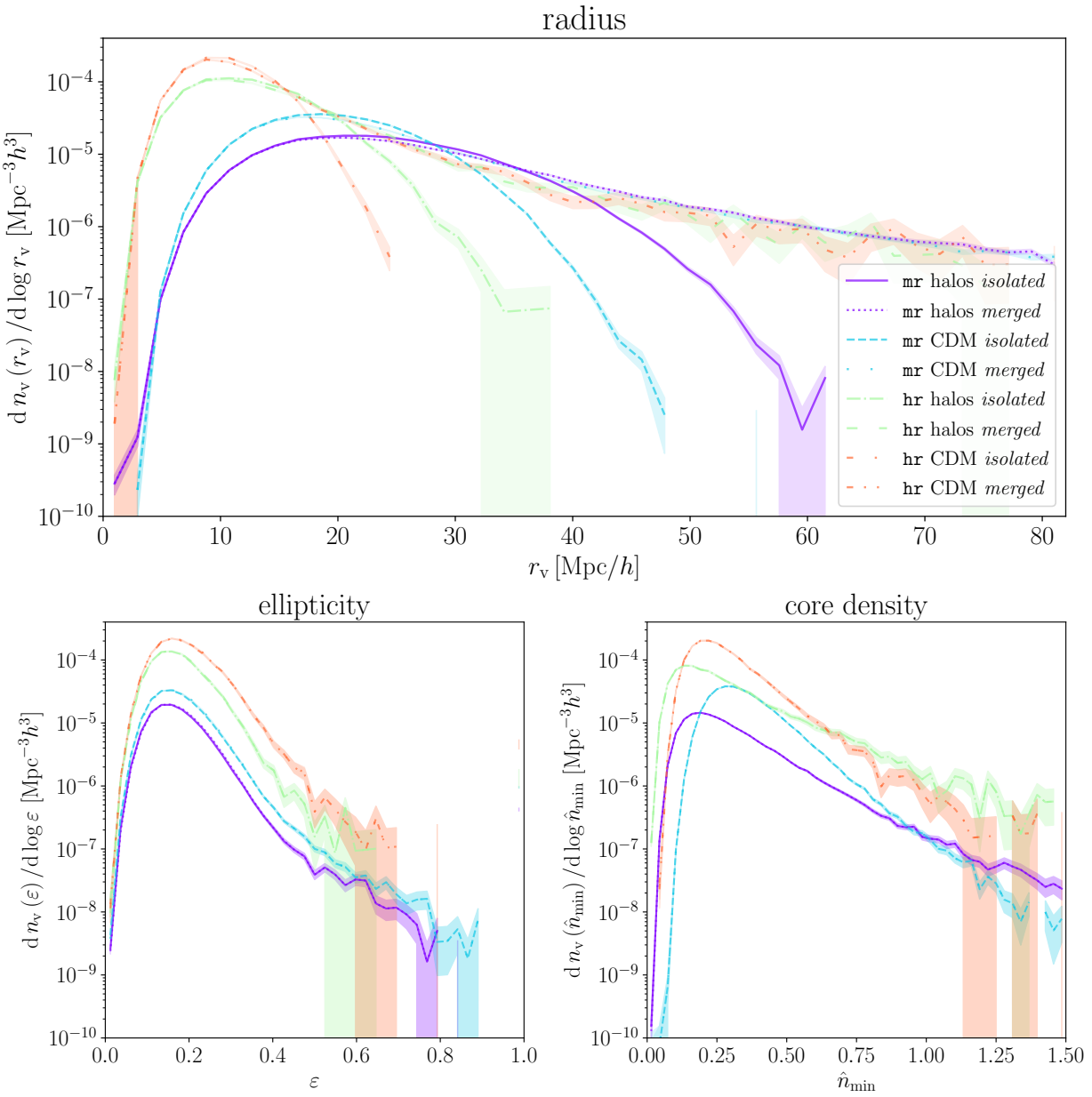

Figure 5.1: Abundance of *isolated* and *merged* voids defined in the distribution of halos and CDM particles in the `midres` and `highres` simulations at redshift $z = 0.29$. Presented as a function of void radius (top), ellipticity (bottom left) and core density (bottom right).

`highres` on the top of figure 5.1 all agree within their error bars for voids larger than around $r_\mathrm{v} \simeq 45\,\mathrm{Mpc}/h$. This suggests that above a certain size the abundance of *merged* voids is much less dependent on the tracer bias, mass cuts, subsamplings and resolution. In an additional test we ran VIDE on a subsample of around 200 million CDM particles in `midres`, which confirms this result for *merged* voids. In contrast, no such convergence can

be found for the void size functions of *isolated* voids. These *isolated* voids continuously fragment into smaller voids as the tracer density increases. However, at the smallest radii the void size function is unaffected by the merging and agrees between both merging parameters. These are small voids in the *isolated* catalog, which get relabeled to 'child' or sub-voids in the *merged* catalog. As already noted, the total number of voids in *isolated* and *merged* catalogs is identical, since no new voids are 'created' and only some voids are *merged*, which results in the hierarchical structure of parent and child voids.

From the ellipticity distribution in the lower left plot of figure 5.1 it is evident that the distribution of void shapes is more or less identical for all cases, be it CDM or halo voids. The curves in `highres` simply experience a vertical shift towards higher values due to the larger number density of voids that can be identified when resolving CDM particles at higher density, or halos of lower mass. All ellipticity distributions consistently peak around a value of $\varepsilon \simeq 0.15$. However, we observe a mild indication for *merged* voids to be slightly more elliptical, most likely due to the increased amounts of substructure within, which results in the possibility of more complex void shapes.

In contrast, the distributions in core density on the lower right panel exhibit clear differences between the resolutions and the tracer types used. Halo voids typically exhibit deeper underdensities in their cores than their CDM counterparts due to the halo bias, which amplifies the fluctuations in the density field [44, 103]. Moreover, core densities show clear deviations between `midres` and `highres` beyond a simple vertical shift of the distributions due to different number densities. Their maxima move towards lower core densities with increasing resolution. This is because at higher resolution, more nonlinear fluctuations in the density can be resolved on smaller scales. On the other hand, the merging of voids does not have an effect on the core densities, because the local minima in the density field remain identical by construction, as merging does not affect the initial Voronoi tessellation.

The joint two-dimensional distributions of various void properties are presented in figure 5.2 for *isolated* halo voids of the `midres` simulation. Voids identified in other merging thresholds, tracer types, and resolutions have qualitatively similar distributions, except for a significantly larger range in r_v when merging is applied. We observe that the ellipticity of voids only slightly depends on their radius, although the distributions becomes more narrow towards larger voids. Amongst the smallest voids we find a few highly elliptical voids with $\varepsilon \approx 1$. These voids are most likely spurious due to the effects of tracer sparsity (see section 7.1). Contrary to this, the core density of voids exhibits a stronger correlation with their radius, clearly evident from the upper right plot of figure 5.2. Larger voids tend to exhibit lower densities in their center with a more narrow distribution [138]. Towards smaller voids this distribution widens considerably, featuring some voids that have minimum densities even above the value of the mean background density. This is a natural and expected consequence of a parameter-free void definition based on the watershed technique, since no density threshold on the interior of voids is imposed. Because the void definition is purely topological, the watershed method is able to identify local basins at any density level, therefore above the mean as well. The distribution between void compensations and their radii is depicted on the bottom left of figure 5.2. Its shape lies between the cases

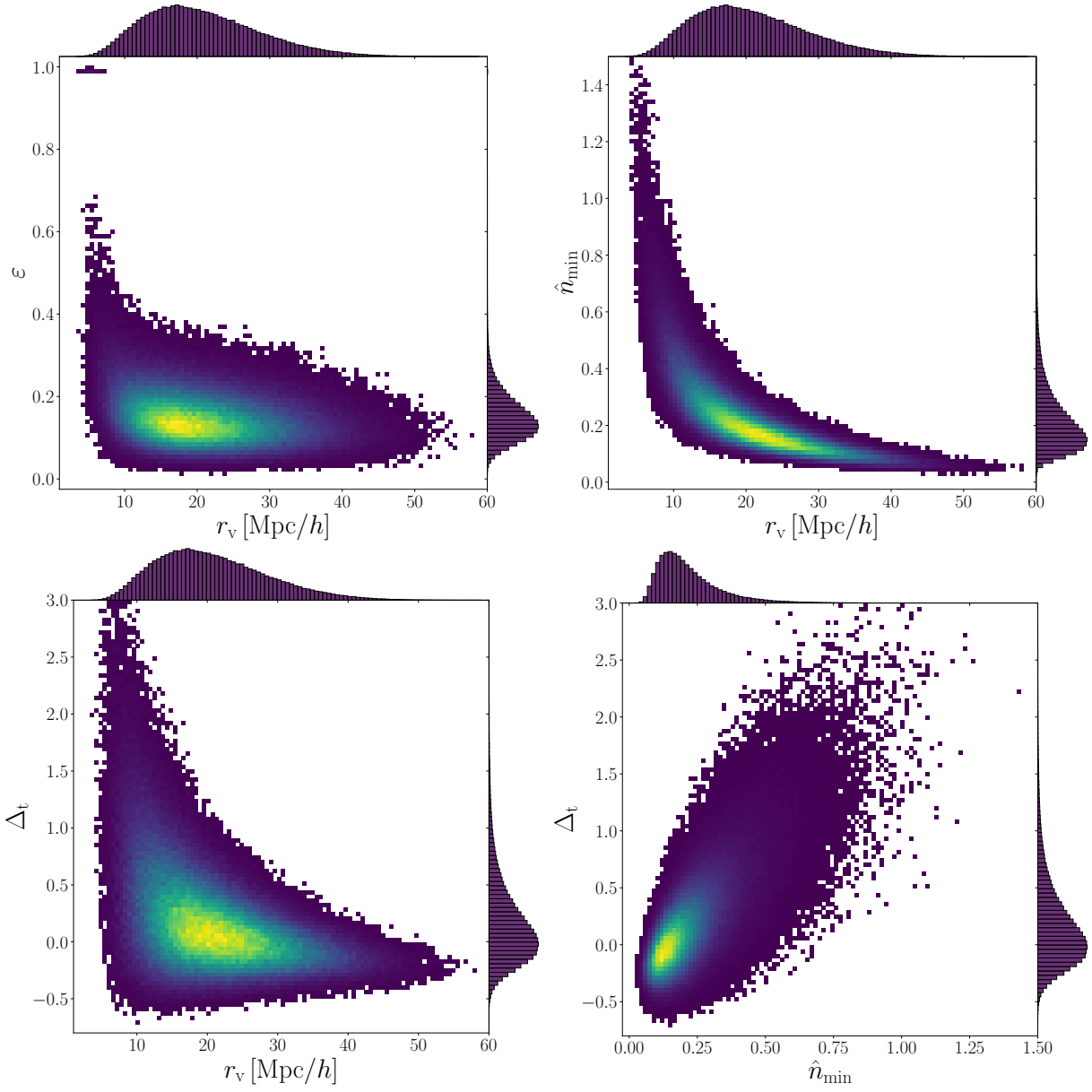

Figure 5.2: Two-dimensional distributions of radius with ellipticity (top left), core density (top right) and compensation (bottom left), as well as distribution of core density with compensation (bottom right) from *isolated* halo voids in the `midres` simulation. Brighter colors correspond to higher numbers of voids per bin.

for core density and ellipticity, as it exhibits an anti-correlation between compensation and void radius. Small voids have a wide distribution, where they can be either overcompensated when found in environments of high local density, or undercompensated when found inside larger underdensities. However, as their distributions are skewed towards positive values of compensations, small voids are on average slightly overcompensated. On

the contrary, large voids have a strong preference towards being undercompensated [32], simply because within they exhibit small densities while their compensation walls typically are on the order of the mean density.

Finally, the distribution between the core density of voids and their compensation is depicted on the bottom right of figure 5.2. Both these void properties correlate, namely voids with higher core densities are typically also overcompensated, while most voids with nearly empty centers are also undercompensated. However, there is a considerable number of voids with low core densities that are still overcompensated over their total volume, and some voids with $\hat{n}_{\mathrm{min}} \simeq 0.5$ are undercompensated despite their high inner densities. In all depicted panels we refrain from including voids of very high $\hat{n}_{\mathrm{min}}$ and Δ_{t}, as there are only few of them.

Chapter 6

Void profiles

In this chapter we focus on the general characteristics of the stacked (averaged) density and velocity profiles of voids from the `hydro` simulations, all presented at redshift $z = 0.29$, although our main findings should be valid across all redshifts. As we will compare void statistics between the `hydro` and `DMo` simulations, as well as between CDM and baryon tracers solely in chapter 8, we will refrain from mentioning that the `hydro` simulations are used for the rest of this chapter. The profiles are calculated for each individual void out to five times its effective radius in bins of width $0.1 \times r_\mathrm{v}$ according to equations (3.7) and (3.9). However, we will only focus on the stacked profiles in bins of different properties, instead of individual void profiles. These stacks are calculated for the density profiles according to equation (3.8) and in case of velocity profiles for both *individual* (Eq. (3.10)) and *global stacks* (Eq. (3.11)). As our default we use *isolated* halo voids, but we also investigate the impact of merging, as well as CDM voids. In addition, we calculate the density profiles of halo voids using the underlying distribution of the (subsampled) CDM particles. Depending on the tracers used for the profiles, we distinguish between the number density profiles and matter density profiles of voids, when either halos or CDM tracers are used for the calculation, respectively. The latter case of CDM around halo voids is relevant in weak lensing studies, where voids can be identified via luminous tracers (such as galaxies) and the matter density around them is probed via the gravitational shear of background objects [43, 46].

6.1 Density profiles

Figure 6.1 presents the matter density profiles of CDM voids on the left and the number density profiles of halo voids on the right, both for *isolated* voids on the top, as well as *merged* voids on the bottom, all from the `midres` simulation. These profiles are stacked in contiguous bins in void radius of $5\,\mathrm{Mpc}/h$ width. The legends indicate the number of voids, as well as the mean void radius of each stacked bin. For *isolated* voids the smallest chosen bin starts at $5\,\mathrm{Mpc}/h$, while for *merged* voids only at $20\,\mathrm{Mpc}/h$, since for stacked profiles of *merged* voids smaller than $20\,\mathrm{Mpc}/h$ the profiles are nearly indistinguishable to

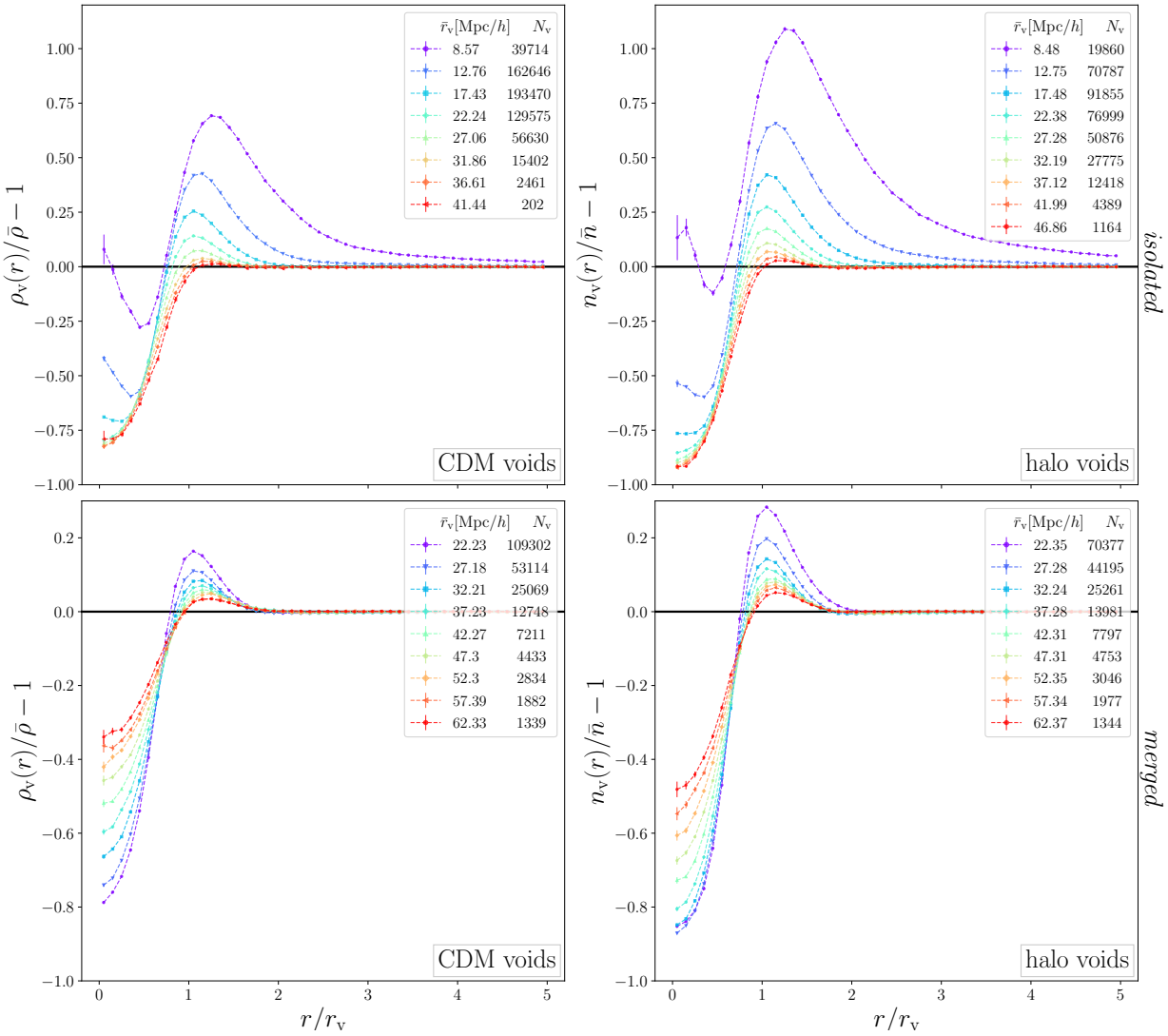

Figure 6.1: Density profiles from the `midres hydro` simulation for *isolated* (top) and *merged* (bottom) voids identified in CDM (left) and halos (right). Profiles are stacked in consecutive void radius bins of width 5 Mpc/h, starting at 5 Mpc/h for *isolated* voids and at 20 Mpc/h for *merged* voids. The mean void radii and void numbers of each bin are indicated in the legend. Error bars depict standard deviations on the mean profiles.

the ones of *isolated* voids.

For *isolated* voids the density around them gradually increases with smaller void size and even reaches values above the mean background density in the centers of the smallest depicted voids. As their size is close to the mean tracer separation of the simulation, one might classify this smallest subset of voids as spurious. However, as they are mostly embedded in environments of high local density [32], the local mean tracer separation decreases as well. These voids exhibit clearly defined compensation walls near $r = r_v$,

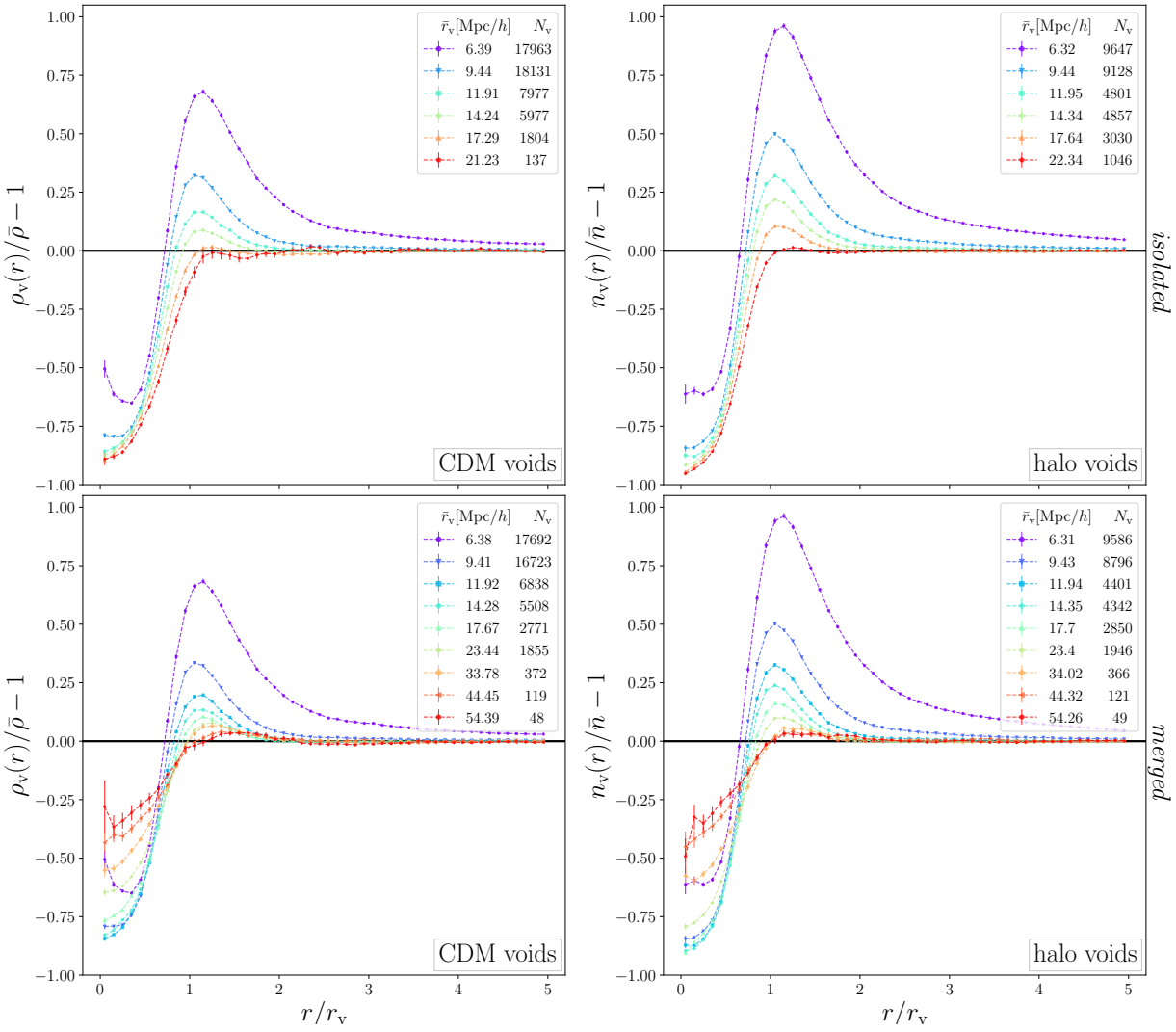

Figure 6.2: Same as figure 6.1, but in the `highres` simulation. Void radius bins have been adapted to better cover their ranges, for *isolated* voids between 4 Mpc/h and 30 Mpc/h (top) and for *merged* voids between 4 Mpc/h and 60 Mpc/h (bottom).

which topologically defines them as local underdensities, i.e. voids. In the inner part of the smallest voids a slight increase in density towards the center can be observed, which is caused by the sparse sampling statistics on scales smaller than the mean tracer separation. As these small voids are only defined by few particles, the density estimation from equation (3.7) returns biased results. In particular, our density estimate is biased high when the shell volume in the denominator of equation (3.7) is very small near the center, but happens to contain one or more tracer particles.

When comparing halo voids with CDM voids, we observe that the former have higher compensation walls and slightly lower densities near their centers. This is consistent with the distributions in core density in figure 5.1, and the impact of halo bias, which amplifies

the CDM density fluctuations [44, 103]. However, we must emphasize that comparing halo voids with CDM voids of the same size is not necessarily meaningful, as they have significant differences between their void size functions. For *merged* voids we find a different behavior, presented in the lower panels of figure 6.1. The density profiles of the smallest voids remain virtually unchanged and are therefore not presented for *merged* voids, but merging gives rise to much larger voids, which have slightly higher compensation walls and shallower cores than *isolated* voids, an effect already noted in reference [38]. This effects happens because *merged* voids can contain sub-voids and hence their internal sub-structures. When these *merged* void profiles are stacked, the sub-structures effectively get smoothed, which leads to more shallow cores and higher compensation walls in the density profiles.

Density profiles of voids at higher resolution from the `highres` simulation are depicted in figure 6.2, where halos with masses above $10^{11}\,M_\odot/h$ are used for the void identification instead of $10^{12}\,M_\odot/h$ in `midres`. In order to obtain a sufficient number of voids in each stacked bin, we now adapt their width in radius, covering a range from $4\,\mathrm{Mpc}/h$ to $30\,\mathrm{Mpc}/h$ for *isolated* voids in the top panels, and from $4\,\mathrm{Mpc}/h$ to $60\,\mathrm{Mpc}/h$ for *merged* voids on the bottom. The results we find are consistent with the ones from the `midres` simulation shown in figure 6.1, but now we resolve even smaller voids, as evident from figure 5.1. Since the small *merged* voids are now depicted as well, we see that their profiles are nearly indistinguishable to the *isolated* ones, which is clear from the minor changes in void numbers in these bins between merging. Once more, we caution against directly comparing voids of any given size between simulations of different resolution, similarly as for voids defined through different tracer types. Only near the regime where the void size functions converge, which happens typically for larger *merged* voids, may this be meaningful.

Figure 6.3 depicts the matter density profiles, $\rho_\mathrm{v}(r)/\bar{\rho} - 1$, of *isolated* halo voids in both simulations, i.e. instead of using the halos as tracers for the profile calculation (as presented in figures 6.1 and 6.2), we now use subsamplings of the CDM particles for this. Differences compared to the number density profiles of halo voids calculated with halo tracers, $n_\mathrm{v}(r)/\bar{n} - 1$, are presented on the bottom panel of each plot. We observe similar trends as for the profiles of CDM voids, although now less pronounced. The matter density profiles generally experience slightly higher densities in the void centers, while at the same time the height of their compensation walls are decreased [44]. This is due to the more even distribution of CDM particles in space compared to halos (i.e., halo bias), which in turn makes their matter density profiles of halo voids more similar to the profiles of CDM voids.

Until now we exclusively focused on density profiles in stacked bins of void radius r_v. Figure 6.4 additionally depicts the number density profiles of *isolated* halo voids from the `midres` simulation in other void properties, namely in bins of ellipticities ε (top right), core densities $\hat{n}_\mathrm{min}$ (bottom left), and compensations Δ_h (bottom right). As in the bins in r_v, we limit ourselves to only using voids with radii between $5\,\mathrm{Mpc}/h$ and $50\,\mathrm{Mpc}/h$ in the other void property bins for the sake of comparability, as otherwise we would have an additional impact of smaller and larger voids. As already seen in figure 5.2 and evident from the bins in ellipticity on the top right, the ellipticity of voids only weakly correlates with their radius, especially in the range of ε between 0.0 and 0.26 that is presented in the figure.

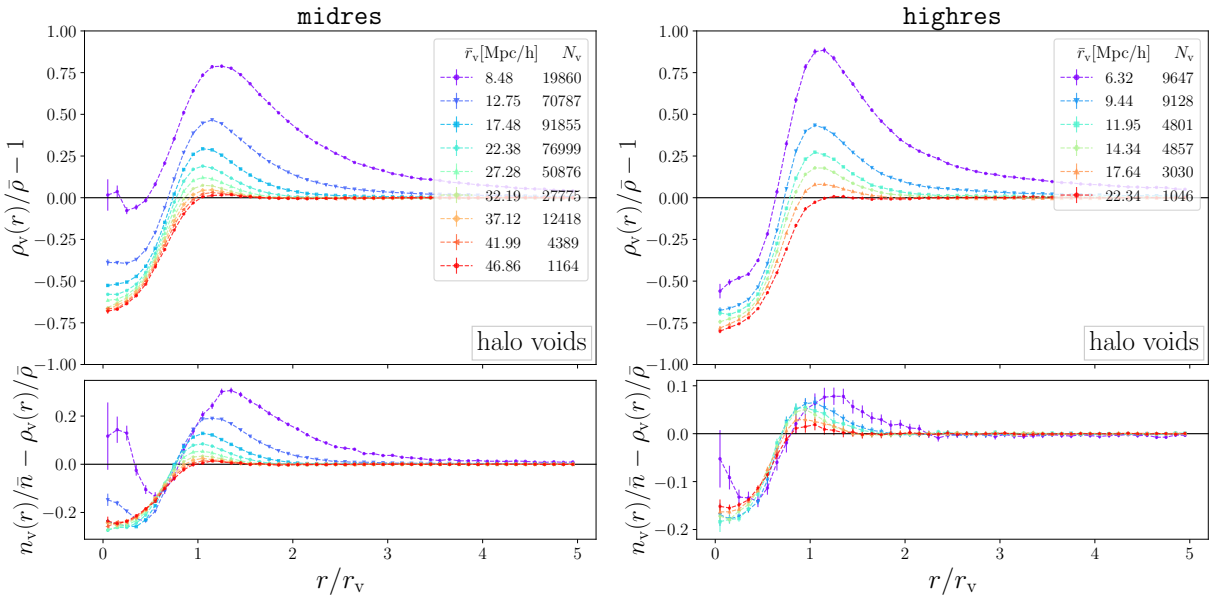

Figure 6.3: Same as figures 6.1 and 6.2, but depicting the matter density profiles based on CDM particles around *isolated* halo voids in the `midres` (left) and `highres` simulations (right). Differences between halo number density and matter density profiles are presented on the bottom.

Because the void size function peaks at small radii, these small voids dominate in every bin of ε, which leads to the relatively high compensation walls in the stacked profiles. The least elliptical voids exhibit the sharpest walls, as well as the deepest cores in the stacked profiles, and vice versa. This is simply a consequence of the spherical averaging in shells around the void center: if regions of roughly similar density are non-spherical, they will overlap with shells at different distances, which effectively smooths out the density profiles and explains the 'stretched' density profile of more elliptical voids compared to more spherical ones. To account for these effects, an alternative stacking method has been proposed by the authors of reference [42], which follows the geometry of void boundaries when constructing their density profiles. This leads to even deeper cores and sharper compensation walls, in agreement with our findings above.

In the lower left panel of figure 6.4 we depict the density profile stacks in bins of core density $\hat{n}_{\mathrm{min}}$ within a range from 0.0 to 0.8. As expected, voids of small core density exhibit deeper density profiles and vice versa. Moreover, the height of the compensation wall is anti-correlated with the core density, which results in the close resemblance to the stacks in bins of r_v, where a similar pattern is observed for *isolated* voids. This is consistent with the findings from the joint two-dimensional distribution of radius and core density in figure 5.2, where smaller voids feature higher core densities, as well as compensations.

Lastly, bins in compensation are shown on the bottom right of figure 6.4, where values from -1 (undercompensated) to 2 (overcompensated) are covered. Undercompensated voids tend to have the deepest cores and exhibit no clear compensation wall. In fact, the

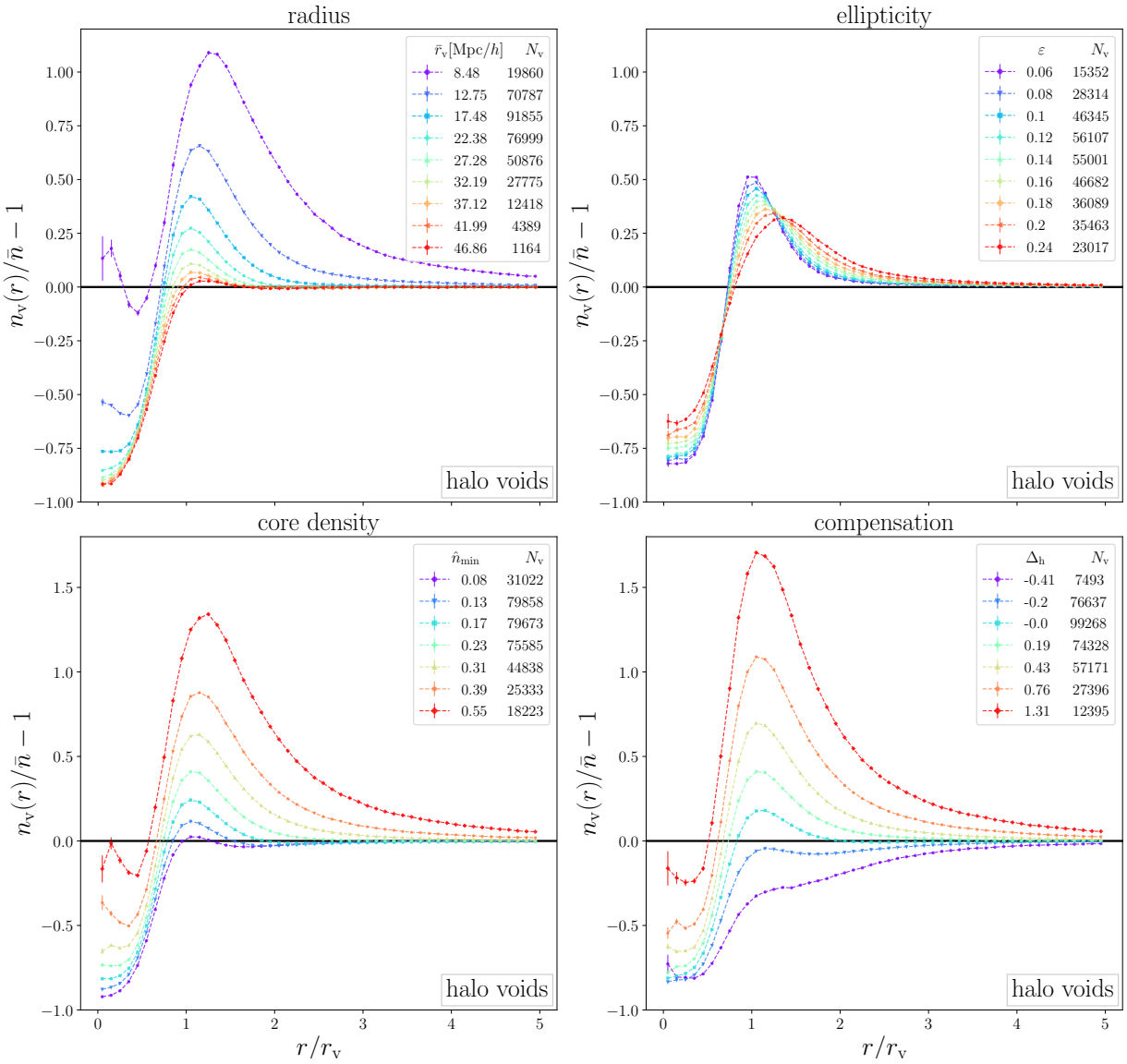

Figure 6.4: Stacked number density profiles of *isolated* halo voids from the `midres` simulation in bins of their radius (top left, as in figure 6.1), ellipticity (top right), core density (bottom left), as well as compensation (bottom right). All voids are selected only within a radius range from 5 Mpc/h to 50 Mpc/h.

density profiles of the most undercompensated voids have the smallest densities up to a significant distance from their centers amongst all bins in Δ_h, gradually increase outwards and only approach the mean background density at much larger distance from the void center, typically larger than the void itself. Nevertheless, there is a hint of the void boundary at $r = r_\mathrm{v}$, where the slope of the density profile becomes flatter. With increasing compensation, the height of the compensation wall increases as well and becomes more pronounced. The bin of the most overcompensated voids barely reaches below the mean

density near the void centers, which resembles the behavior of small voids. Figure 5.2 supports this, as these small voids on average exhibit higher values of compensation, while larger voids have a tendency to be more undercompensated. As the compensation depends on the void size and its total number of member particles, it is a measure of the environment a particular void is located in. Overcompensated voids reside in regions of higher local density, whereas undercompensated voids happen to be within more underdense environments, which is reflected in the stacked profiles. These two phenomena are typically known as the "void-in-cloud" and "void-in-void' scenarios, respectively [94]. For exactly compensated voids with $\Delta_\mathrm{h} = 0$ this defines an interesting transition point [32]. Their density profile converges to the mean background density at the shortest distance from the void center in units of r_v among all stacks in compensation bins, at around $r \simeq 2r_\mathrm{v}$. We will revisit these profiles in compensation bins in section 9.5 and investigate them in more detail.

6.2 Mass weighting

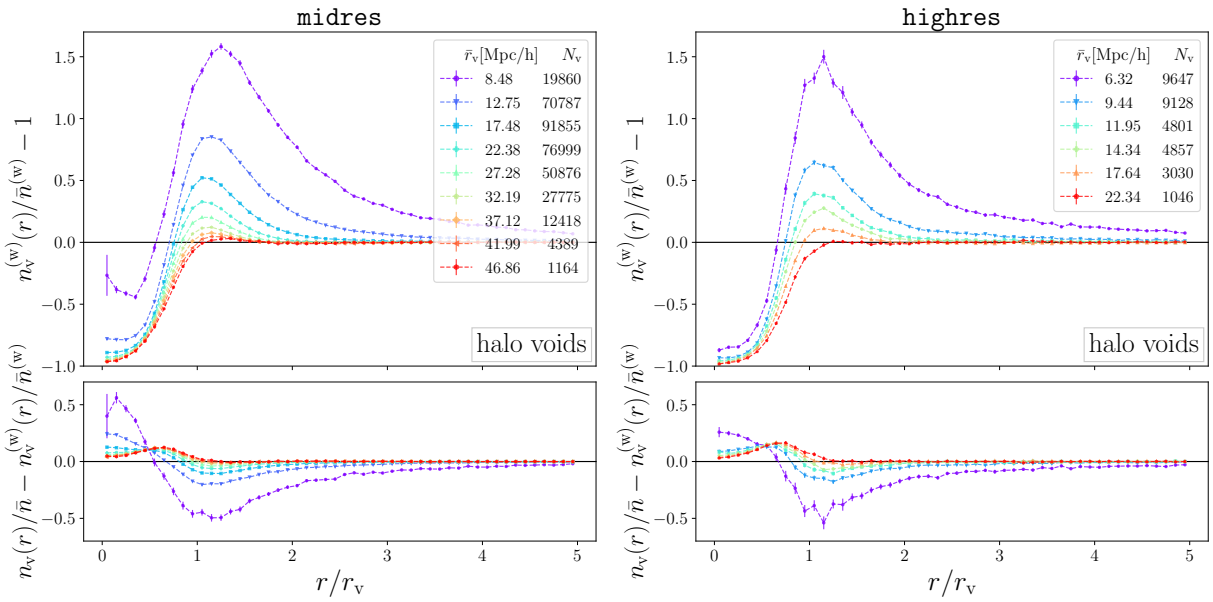

Figure 6.5: Stacked mass-weighted density profiles of *isolated* halo voids from the `midres` (left) and `highres` simulations (right). Lower panels compare them with the unweighted number density profiles of halo voids from figures 6.1 and 6.2 in identical bins of void radius.

So far we have neglected the masses of halos for the calculations of the density profiles of voids, apart from the imposed mass cuts on our halo catalogs for the void identification. However, using the halo masses as weights $w_j = M_j$ for every halo j in equation (3.7), we can use them to estimate the mass-weighted density profiles around voids from all

matter that is contained in halos. This is different from previous profiles of CDM particles around halo voids, as not all of the CDM is clustered inside halos. Nevertheless, this mass-weighted estimation yields a special type of the matter density profile around voids, which additionally probes the spatial distribution of halos of different mass. While the individual masses of halos are difficult to obtain through observations in large-scale cluster surveys, the magnitudes of their hosted galaxies could provide an observational proxy weight for them [139, 140].

In figure 6.5 we depict stacks of the mass-weighted density profiles of halo voids in both the `midres` and `highres` boxes, with differences to the regular unweighted number density profiles on the bottom. Once more, the profiles are stacked in bins of r_v identical to the ones used in previous figures 6.1 and 6.2. With respect to the number density profiles, mass-weighted profiles are amplified and feature higher compensation walls, as well as deeper cores, most notably for smaller voids. This implies that the most massive halos are rather located in more densely clustered regions at and near the void boundary, whereas the least massive halos tend to reside closer to the centers of voids, as expected from previous studies [e.g., 70, 102]. With increasing void size, however, this effect decreases. Alternatively, this effect of mass weighting can be interpreted as a boost of the halo bias [140].

6.3 Velocity profiles

After investigating the spatial distribution of both CDM and halos inside, as well as around voids, we now focus on their movements. Typically the dynamics of voids are characterized by a coherent and radially directed flow of matter around their centers, which can be explored via the stacked velocity profiles. As previously described in section 3.2, we distinguish between two different ways of calculating these stacks, using global stacks via equation (3.11) and individual stacks via equation (3.10). Figures 6.6 and 6.7 present both methods for *isolated*, as well as *merged* halo voids from the `midres` simulation, while figure 6.8 presents it for *isolated* voids from the `highres` simulation. All are depicted with identical void radius bins as those used in previous figures 6.1 and 6.2 for number density profiles. We depict both the velocities of halos (solid), as well as CDM (dotted), with differences highlighted in the lower panels.

First of all, we note an exquisite agreement of the velocities between CDM particles and halos around halo voids in both stacking methods. This is as expected, since the equivalence principle states that test particles in a common gravitational potential fall with identical speeds, irrespective of their mass and composition. Differences between CDM and halo velocities become more visible when approaching the centers of voids, where tracer statistics are sparser. However, the CDM particles might be a better tracer of the velocity field in simulations, as they are more uniformly distributed than halos, which leads to better sampling in sparse regions. When investigating the general movement of tracers, we note that large voids are characterized by outflows, with steadily increasing velocities from almost zero in their centers to a maximum velocity near the compensation

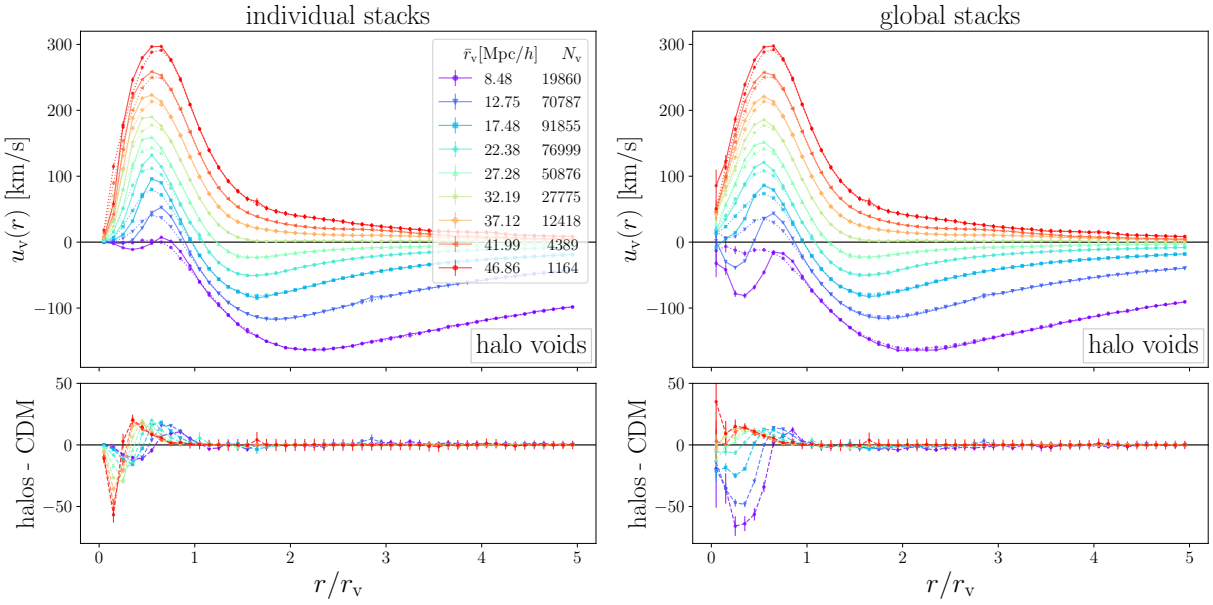

Figure 6.6: Velocity profiles from individual stacks (left), as well as global stacks (right) around *isolated* halo voids from the `midres` simulation with identical void radius bins as in figure 6.1. Solid lines indicate the velocity of halos, dotted lines of CDM, while their differences are shown in the lower panels.

wall, which then drops again and approaches zero in the large distance limit. This is consistent with deep and extended matter underdensities in the vicinity of these voids, as seen in figure 6.3. Since the compensation wall of smaller voids becomes much more pronounced, their average direction of motion features a turning point and tracers flow radially inward towards the compensation wall [38]. This influx of matter is most extreme around the smallest set of voids, which may eventually overcome their interior expansion, leading to a collapse that eliminates them [94]. One may argue that this is already the case for the smallest voids of `midres` in figure 6.6, but our results in figure 6.8 from the `highres` simulation show that voids of even smaller size can experience outflows from their centers.

While the most prominent features of velocity profiles are similar for both stacking methods, some important differences can be noticed in the proximity to the void centers. In individual stacks the velocities closely converge towards zero in the center, while in global stacks finite values are reached in the center. As the inner shells of small voids often contain no tracers, the velocity is set to zero in these shells, and averaging many profiles in the bin of small radii with zero velocity results in individual stacks giving a velocity estimate close to zero as well, while global stacks can average out the tracer sparsity more reasonably. In global stacks the differences between CDM and halo velocities decrease with increasing void size, while the opposite trend happens in individual stacks, where the best agreement happens in the smallest voids, which should be affected most due different levels

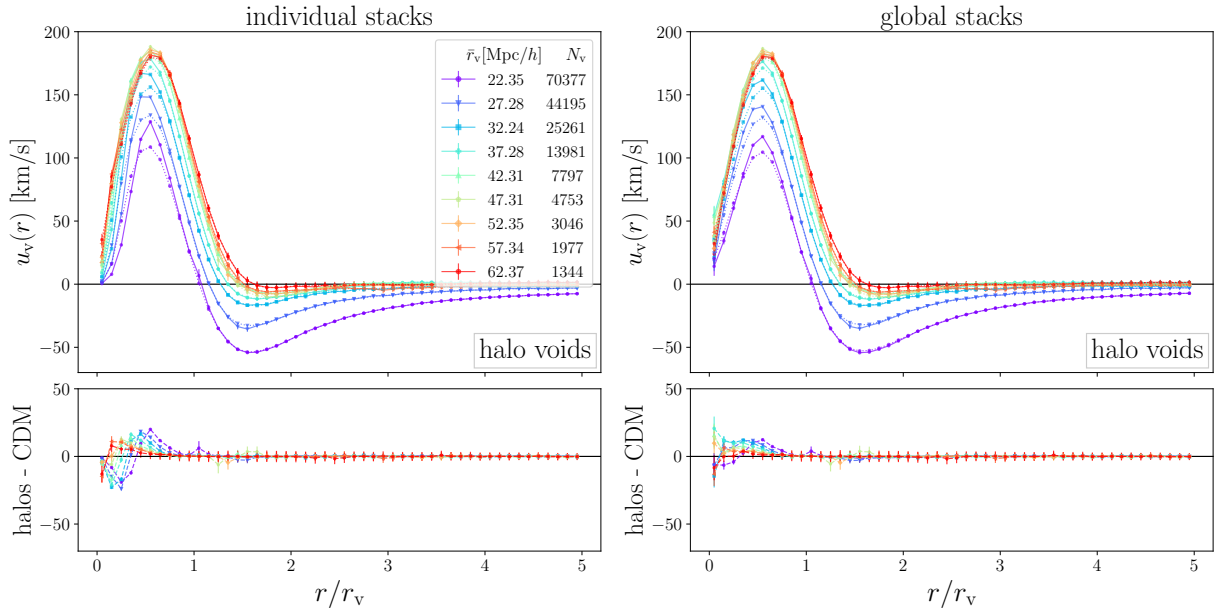

Figure 6.7: Same as figure 6.6, but for *merged* voids. Identical void radius bins as in figure 6.1.

of tracers sparsity from CDM and halos. At closer look we see that mainly the velocities of halos are affected by the choice of the stacking method, while CDM velocities are more consistent with each other in both methods. Since the same halos are used for the profile calculation as for the void identification, this suggests that the residuals in velocity between halo and CDM we observe are caused by the same sparse sampling effects that were already found near void centers in the density profiles of the smallest voids in figures 6.1 and 6.2, as previously discussed in section 6.1.

In fact, the velocity profiles of CDM voids, which are presented in figures 7.4 and 7.5 of chapter 7, experience similar artifacts from sampling, because once more the same tracers are used for the void identification and the profile calculation. This effect becomes most severe for voids defined by the fewest tracers. Of course we should bear in mind that any direct comparison between halo voids and CDM voids is of limited scope, as their size functions significantly differ. One could alternatively argue for other potential causes leading to a discrepancy between CDM and halo velocities, like a velocity bias from halos, or some kind of relevant nonlinear dynamics [141, 142]. However, when increasing the resolution of the simulation in figure 6.8, the discrepancies between velocities diminish and move towards smaller scales. We therefore cannot find any evidence which may be in favor of such effects beyond a simple resolution limit in simulations, which leads to sparse sampling, especially for biased tracers.

When comparing the velocity profiles of *isolated* and *merged* voids through figures 6.6 and 6.7, we note that our general conclusions remain valid even for *merged* voids, although the magnitude of their velocity changes significantly compared to *isolated* voids of similar

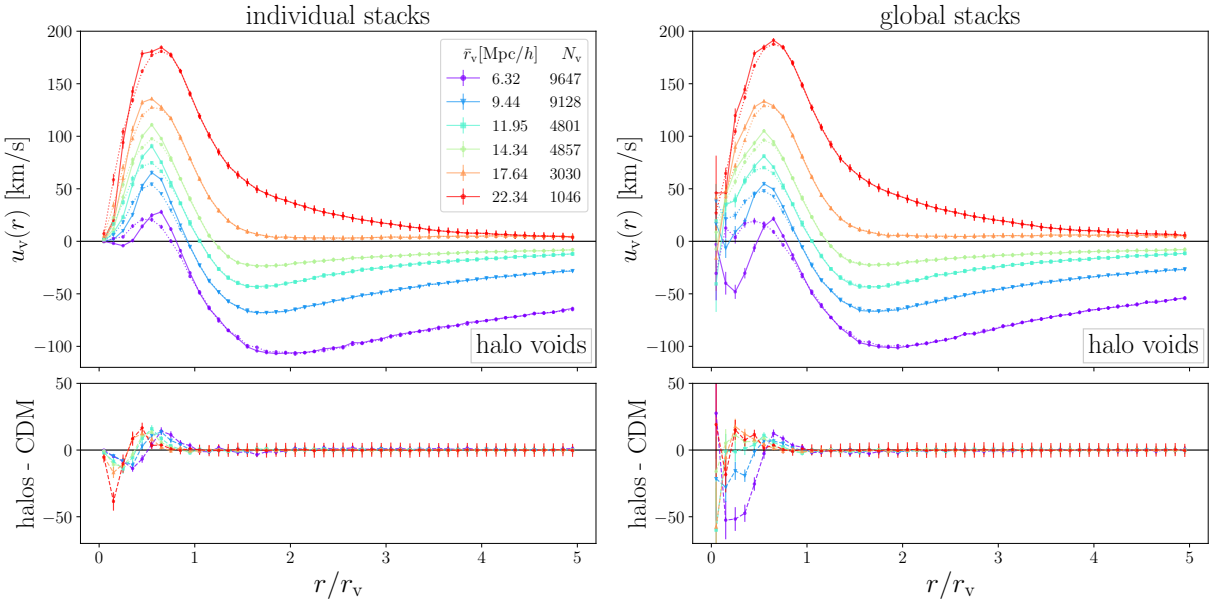

Figure 6.8: Same as figure 6.6, but in the `highres` simulation. Identical void radius bins as in figure 6.2.

sizes. While the maximal velocity around *isolated* voids increases steadily with increasing size, *merged* voids of same size have significantly smaller velocities and they also feature a turning point in the height of their maxima for large voids, at around the bin of $\bar{r}_v = 47.31\,\mathrm{Mpc}/h$, and decrease slightly for even larger voids. These lower values in velocities in and around *merged* voids are caused by the structures around their sub-voids. As these sub-voids feature compensation walls as well, these walls can lead to a decrease in outflow velocities of *merged* voids due to their gravitational potential. This potential leads to an acceleration of matter towards the sub-voids' compensation walls, which do not necessarily align with the locations and orientations of the boundaries of *merged* voids, decreasing their overall velocities.

Analogous to the density profiles in figure 6.4, we can use other void properties than radius to stack their velocity profiles. Figure 6.9 presents this for the global stacking method of profiles for *isolated* halo voids from the `midres` simulation in bins of void ellipticity ε, core density $\hat{n}_{\mathrm{min}}$, and compensation Δ_{h}, in addition to the bins in void radius r_v presented earlier, although solely for halo velocities. As done before, we only select voids with radii between $5\,\mathrm{Mpc}/h$ and $50\,\mathrm{Mpc}/h$ in the stacks for the sake of comparability, but we now also compare both methods of stacking velocity profiles through differences in the lower panels.

When we consider the stacked bins in ellipticity in the upper right plot of figure 6.9, we notice that all bins in ε experience the same characteristic outflow of halos from the center, with their maximum velocity steadily decreasing with increasing ellipticity, which is in correspondence with the shape of their density profiles in figure 6.4. This is true in both

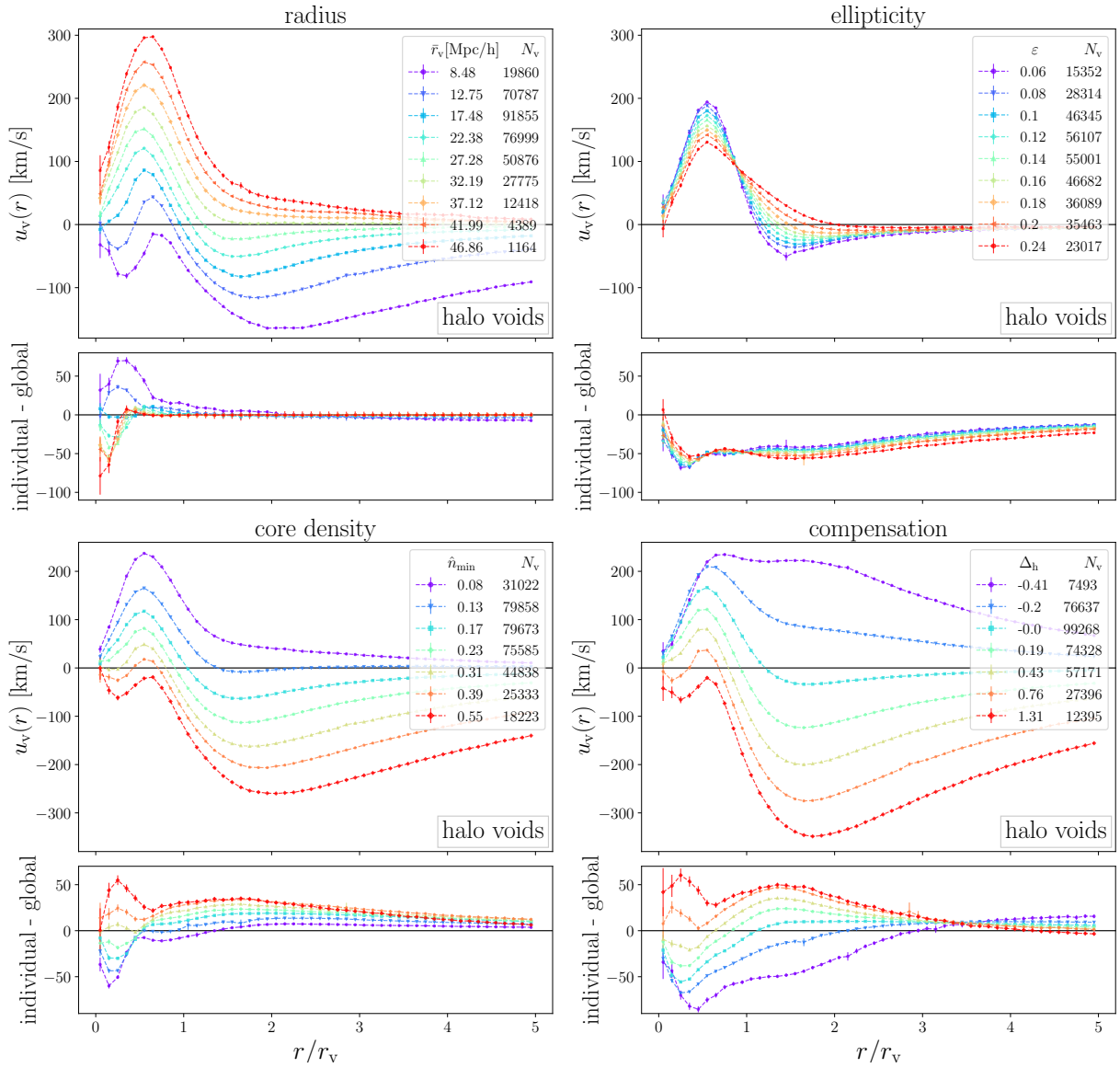

Figure 6.9: Velocity profiles using global stacks, for halos around *isolated* halo voids in the `midres` simulation for bins in void radius (top left), ellipticity (top right), core density (bottom left) and compensation (bottom right). Lower panels depict the differences between individual and global stacks. The bins, as well as the void selection are identical to figure 6.4.

stacking methods, although the profiles using individual stacks result in generally lower velocities than in global stacks, even at distances far out from the void center. In global stacks the most elliptical set of voids is dominated by outflows of halos across all scales, while only the more spherical voids exhibit the inflow of halos toward their compensation walls. This is contrary to effects in individually stacked profiles, which feature inflows

in all bins of ellipticity. This significant difference in behavior of halo velocities can be understood when considering the definition of both stacking methods in equations (3.10) and (3.11), combined with figure 5.2, which shows that radii and ellipticities of voids are largely independent from each other. This results in bins of ellipticity covering a significant range of void sizes within them. Therefore, averages over the individual velocity profiles from equation (3.9) are biased towards the more numerous small voids. On the other hand, equation (3.11) sums up the volume-weighted velocities of tracers around the full void sample of the stack before normalizing by the total volume of Voronoi cells of all tracers per shell, which in contrast is biased towards shells that contain a higher number of tracers, hence it is biased towards typically large voids. The dependence of velocity profiles on the radius of voids, as depicted on the top left of figure 6.9, then ultimately translates into the noted differences between the two stacking methods that appear in the upper right panel.

In the lower left panel of figure 6.9 we show the velocity stacks in bins of core density $\hat{n}_{\mathrm{min}}$. The correspondence with their associated number density profiles from figure 6.4 is once more evident: voids that feature the most underdense cores experience the strongest outflow velocities of halos, while voids with the densest cores experience enormous inflows. Differences between the two stacking methods are apparent, although they do not affect the general trends in profiles already manifest in figures 6.4 and 6.6. This is due to the stronger correlation between void radii and their core densities, compared to their ellipticities, which in turn leads to the averaging effects discussed above being of lower importance in these stacks.

For velocity profiles in stacked bins of their compensation, as presented in the lower right panel of figure 6.9, general trends in the profiles are similar to previous cases, although we note that the compensation of a void has a stronger impact on its environment than its core density, as expected from their density profiles in figure 6.4. Undercompensated voids expand out to enormous distances from their centers, while overcompensated voids are dominated by the influx of tracers. In between those two regimes, the peculiar motions around exactly compensated voids with $\Delta_{\mathrm{h}} = 0$ vanish at the shortest distance from the void center, as test particles near a region of average background density do not experience any net force and simply move with the Hubble flow [38].

To summarize, an important conclusion from bins in different void properties in figure 6.9 is the fact that the different estimators for stacked velocity profiles around voids can be biased in different ways, which depends on both the diversity of the considered void sample and the property that is selected for the stacked bins. Velocity profiles using individual stacks are biased towards the profiles of more numerous small voids, whereas the profiles using global stacks are biased towards the ones of voids that are sampled with more tracer particles, i.e. larger voids. This issue can be partially alleviated by placing limits on the range of void radii in any given stack, but a comparison between both stacking methods is nevertheless helpful in revealing residual biases that the velocity profile estimators may encounter.

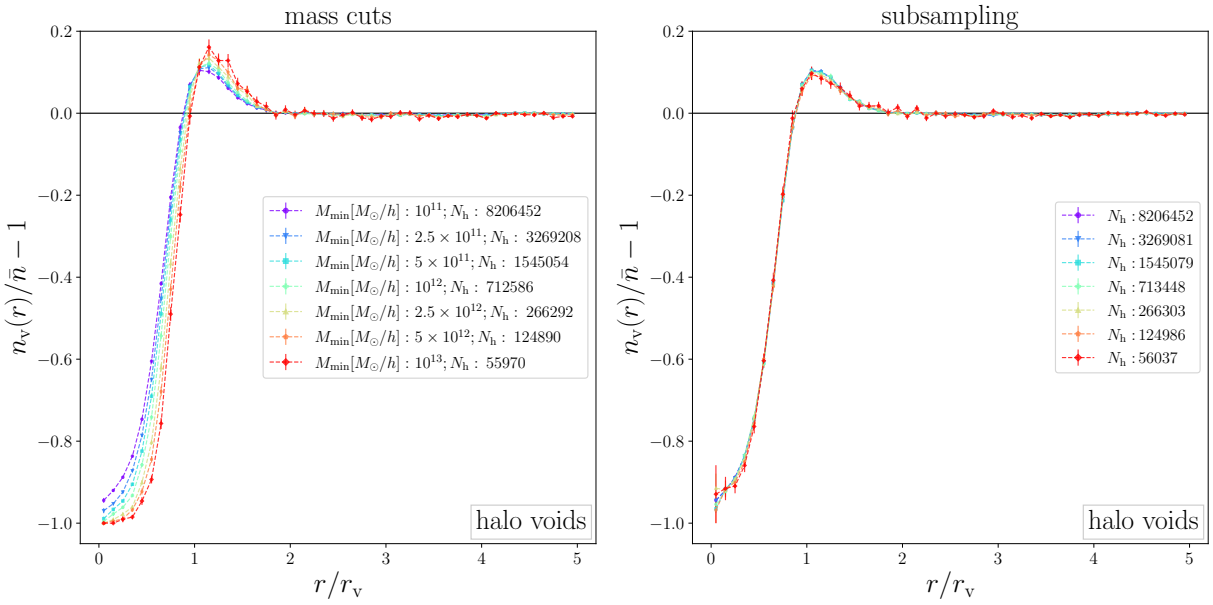

Figure 6.10: Stacked number density profiles of *isolated* halo voids in the `highres` simulation after applying mass cuts (left) and subsamplings (right) to the halo tracers. Voids are always identified in the full (unsampled) halo distribution and selected in a radius range from $16\,\mathrm{Mpc}/h$ to $20\,\mathrm{Mpc}/h$. Legends indicate the chosen minimum halo masses M_min (left) and the number of halos N_h after subsampling (right).

6.4 Sampling effects

Our comparison of different profile estimators in the previous sections revealed some of their limitations and biases in certain regimes. We expect that these limitations mostly arise from sparse statistics of both voids and tracers, which are unavoidable when approaching scales close to the mean tracer separation at any resolution. However, we can artificially amplify this impact of sparse statistics by randomly subsampling the tracers used in the profile calculations, or by removing the halos of lowest mass. Nevertheless, we do not repeat the void finding process on these modified tracer samples, as this would render any direct comparison between different void samples impossible due to the altered void size function. This can be seen for example when we compare number density profiles of *isolated* halo voids in both `midres` and `highres` simulations from figures 6.1 and 6.2. Their distributions in void sizes are significantly different between both cases, and voids of same radii do not necessarily share the same properties at different resolutions.

Without loss of generality we restrict ourselves to *isolated* halo voids from the `highres` simulation in a void radius range from $16\,\mathrm{Mpc}/h$ to $20\,\mathrm{Mpc}/h$, and subsequently apply mass cuts in the halos and subsamplings to the halo sample for estimating void profiles. Figure 6.10 shows the stacked number density profiles after selecting halos above different mass thresholds M_min, given in the legend, and after random subsamplings that match these previously selected number of halos after mass cuts. Applying mass cuts to the halo

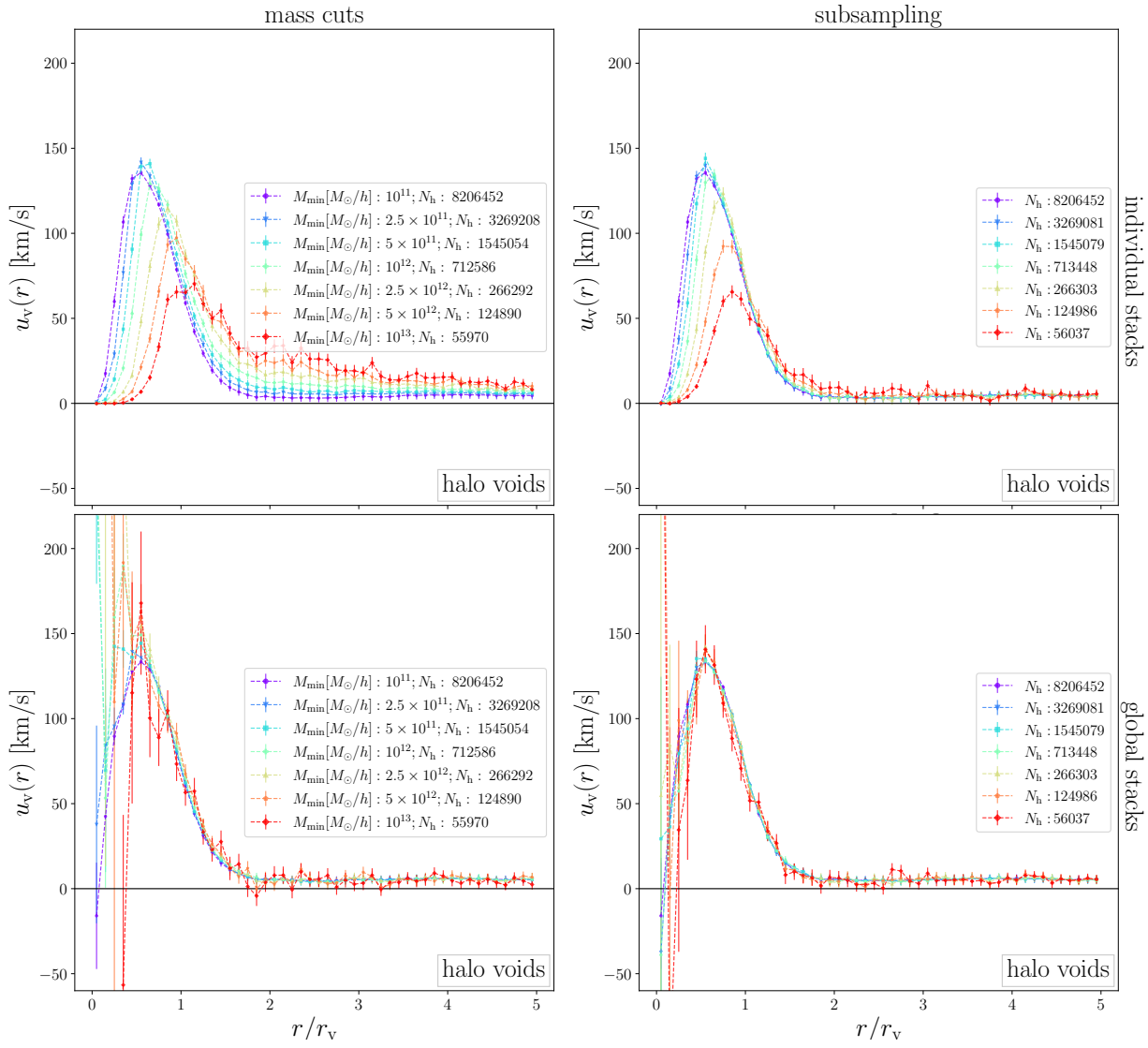

Figure 6.11: Same as figure 6.10, but for the velocity profiles using halo velocities in individual stacks (top) based on equation (3.10) and in global stacks (bottom) based on equation (3.11).

tracers affects the density profiles in a similar way as previous mass weights (cf. figure 6.5) and reveals once more that more massive halos have a tendency to be more likely located within the compensation walls of voids, while being scarcer near the void centers. On the contrary, randomly subsampling the halos has no significant effect on the number density profiles of voids, except for a noticeable increase of the error bars, as expected. This certifies that the density estimator from equation (3.7) is not biased in sparse tracer samples, except for the bias of few particles in extremely small shells inside small voids, previously discussed in section 6.1, and of course the small bias of averaging non-spherical

objects in spherical shells.

The corresponding velocity profiles of this bin in void size are depicted in figure 6.11. Evidently, applying mass cuts and subsamplings to the halos affects individual stacks and global stacks in significantly different ways. While the velocity profiles from individual stacks continuously decrease when the number of tracers is reduced through either mass cuts or subsampling, the profiles from global stacks remain stable within their error bars. Regarding sampling effects, the global stacking method is clearly preferred, as it does not generate a bias from the increased sparsity of tracers, nor does the velocity depend on the tracer mass. A dependence of a tracers velocity on its mass would violate the equivalence principle adopted in the gravity solver of the simulation, it therefore must be spurious. Issues arise whenever tracers become too scarce to give a faithful sampling of the velocity field, yielding too low estimates for the velocity. This is particularly severe near the void centers in individual stacks, where massive halos, as well as any other tracer particles are scarcest.

6.5 Velocity-split profiles

So far we were only interested in the average velocity profiles of tracers around voids and in the density profiles of all selected tracer particles. Instead, we now want to investigate differences in void profiles between outward flowing particles and tracers experiencing radial infall. The velocity of every tracer relative to the void center is determined and then depending on whether it is positive or negative, we use this tracer particle for the calculation of the velocity, as well as density profiles of either outflowing or infalling tracers, respectively. The density profiles are simply denoted by $n_{\mathrm{v}}^{+}(r)/\bar{n} - 1$ or $n_{\mathrm{v}}^{-}(r)/\bar{n} - 1$, as well as $u_{\mathrm{v}}^{+}(r)$ or $u_{\mathrm{v}}^{+}(r)$, for positive and negative tracer velocities, respectively. However, each density profile is still divided by the mean density of all tracers, irrespective of their velocity.

Figure 6.12 presents these velocity-split profiles for *isolated* halo voids from the `midres` simulation and halo tracers in the profiles, while figure 6.13 presents the same for *merged* voids of `midres` and figure 6.14 for *isolated* voids from the `highres` simulation. These figures depict the split velocity profiles using individual stacks (left), as well as global stacks (right) in the upper plots, and on the bottom the density profiles of outflowing halos (left) and infalling halos (right).

When first looking at the split velocity profiles, we note that in individual stacks, both positive and negative velocity profiles start at zero velocity in the void center and the magnitude of their velocities steadily increases towards the compensation wall and then drops with increasing void size for positive velocities, or remains almost constant for negative velocities. On the contrary, the split profiles in global stacks never exhibit velocities close to zero. Focusing on the centers of voids first, interpreting the profiles using individual stacks would lead to the conclusion that all halos are almost stationary close to the void centers. Global stacks instead hint at a more 'chaotic' behavior of tracer particles. Here the tracers move at high velocities near the void center, both inward and

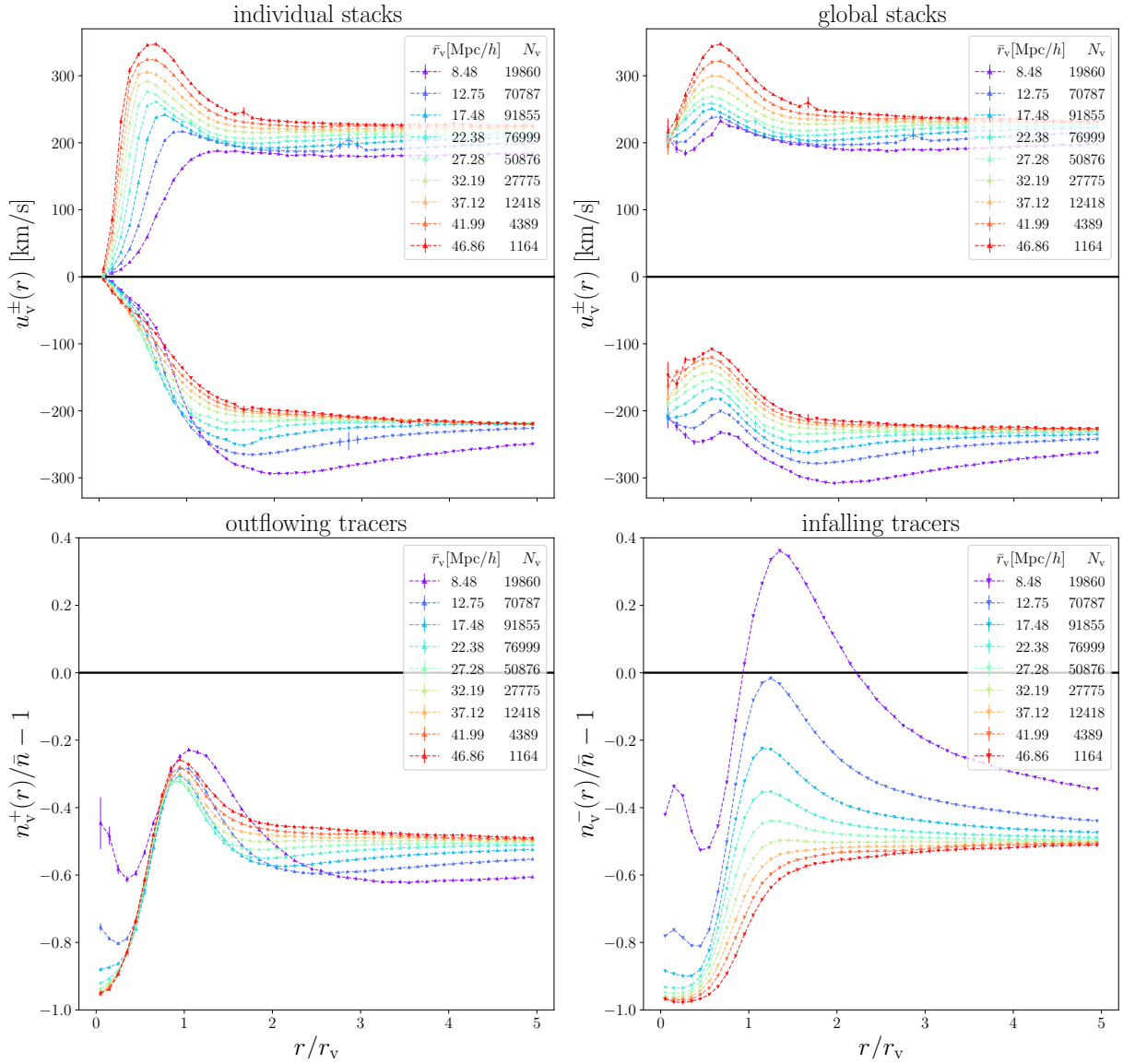

Figure 6.12: Velocity profiles (top) and density profiles (bottom) for *isolated* halo voids from the `midres` simulation, split for halo tracers with positive (outflowing, bottom left) and negative (infalling, bottom right) velocities. Velocity profiles are presented in both individual stacks (left) and global stacks(right), with identical void radius bins as in figure 6.1.

outward. Some of these particles that move towards the center will surely cross it and would switch from positive to negative velocity with respect to the center at some later time and vice versa. This interpretation from global stacks seems more likely than almost stationary particles near the centers and further showcases the internal biases between different velocity estimators. Past the compensation wall at $r = r_v$, both stacking methods agree to a much higher degree, as effects from sparse sampling are eliminated at these

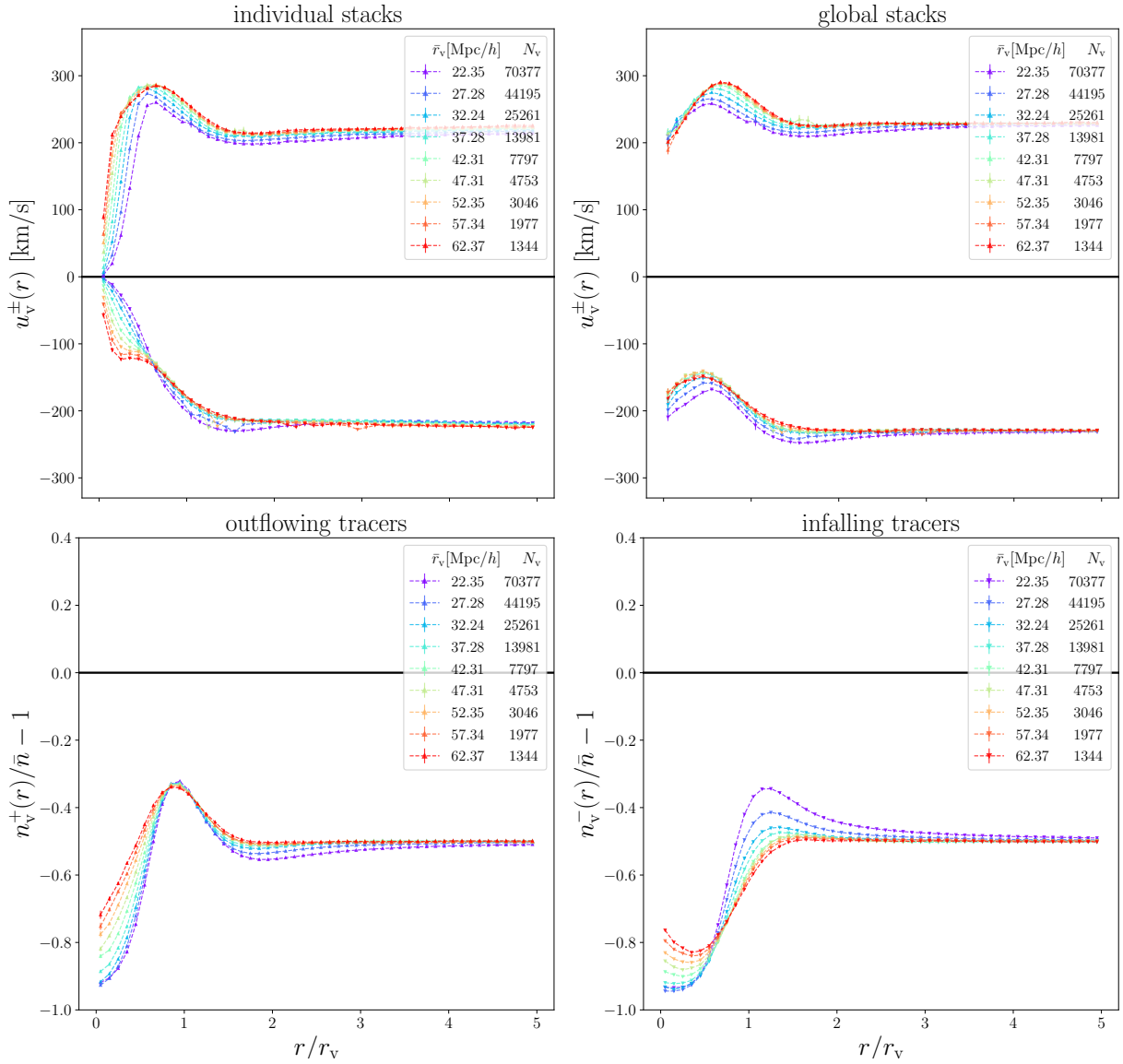

Figure 6.13: Same as figure 6.12, but for *merged* voids. Identical void radius bins as in figure 6.1.

scales.

Regarding the general properties of split velocity profiles, we note that smaller voids almost always have lower velocities than large voids, except in the innermost regions of individual stacks due to effects from tracer sparsity. They have either smaller velocities for positive profiles, or more extreme values for negative velocities. Comparing positive and negative velocities, we note that while their absolute values differ significantly, their shapes are surprisingly similar, especially for global stacks. All of this is equally true for the velocity-split profiles of *merged* voids, as well as for the profiles of *isolated* halo voids from the `highres` simulation and for CDM voids (not depicted). While the velocity profiles

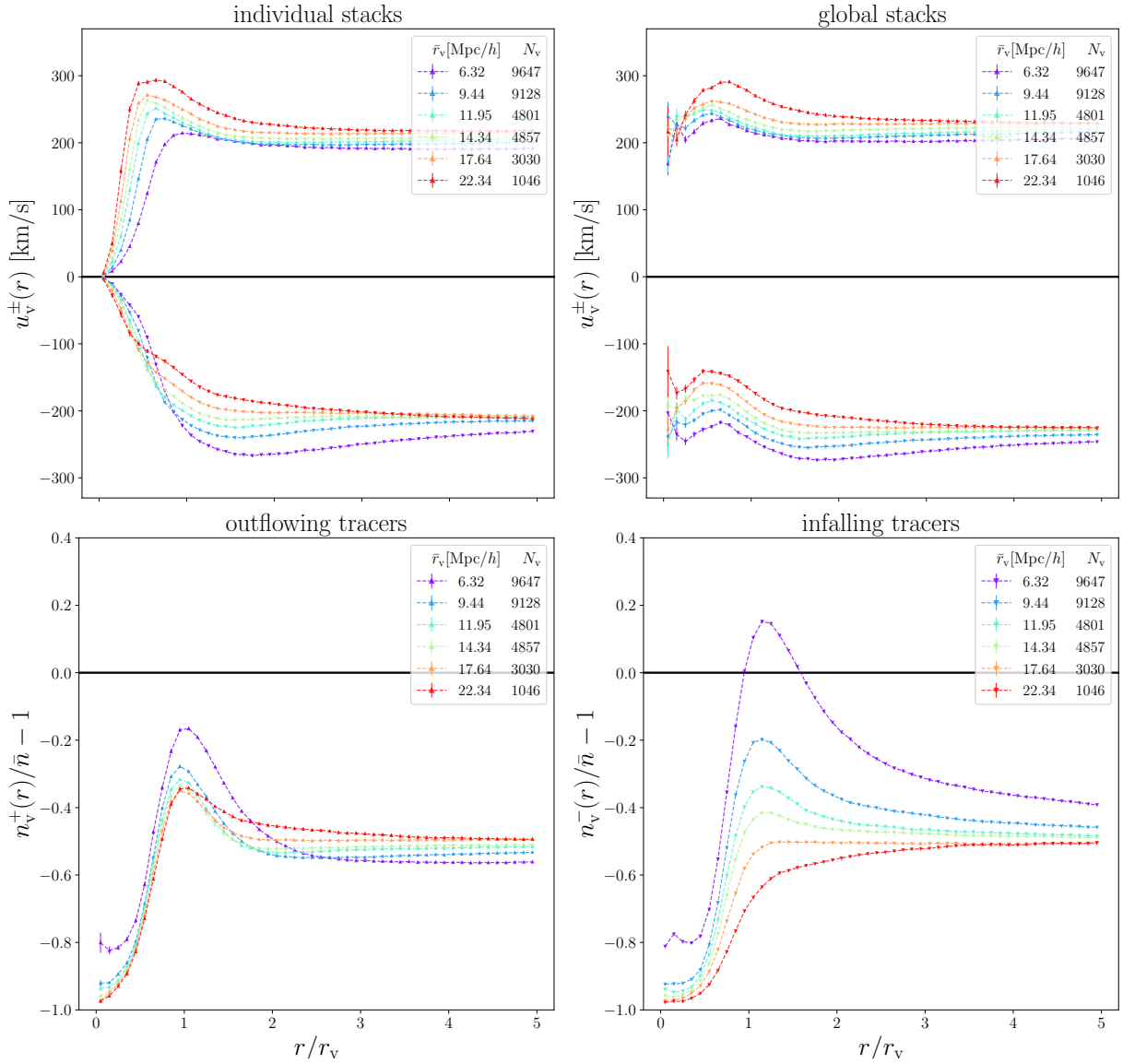

Figure 6.14: Same as figure 6.12, but for the `highres` simulation. Identical void radius bins as in figure 6.2.

of both in- and outflowing tracers combined have significantly different values in `highres` (cf. figure 6.8) compared to the ones in `midres` (cf. figure 6.6), their split profiles have much more similar values. Furthermore, the split velocity profiles of *merged* voids are more similar to the ones of *isolated* voids than their regular velocity profiles.

Of course the 'true' velocity profiles of particles with both negative and positive velocities have more complicated shapes and are not simply given by the difference between positive and negative velocities, as both profiles have significant differences in their number densities. These split number density profiles are presented on the bottom of figure 6.12 around *isolated* halo voids of `midres` for halos with positive velocities on the left and ones

with negative velocities on the right, as well as in figure 6.13 for *merged* voids and in figure 6.14 for *isolated* halo voids in `highres`. We note that in split density profiles of *isolated* voids in `midres`, outflowing particles have almost identical profiles within voids, except for smallest voids and in the innermost shells. The larger voids become, the more their outflowing density profiles align within, and only outside voids we see environmental differences in the profiles. We observe a similar behaviour in `highres`, however the alignment is slightly worse, as these voids are potentially still too small for this effect. In contrast, the density profiles of outflowing particles around *merged* voids do not align, evident from figure 6.13, as their internal structures around their sub-voids add to the density of outward moving particles inside large voids. Moreover, we found this alignment only in the *isolated* halo void profiles, while the profiles of CDM around both *isolated* CDM and halo voids do not align, but are still rather similar, far more than for *merged* voids.

On the contrary, the inward moving tracers experience significant differences between the bins in r_v over all distances. Their shapes highly resemble the shapes of the usual stacked density profiles in all cases, just at smaller values. Especially for large *merged* voids the densities become quite small, while the outflowing densities increase with r_v, as these large voids expand across their whole interior and loose more tracers than they gain. In contrast, the compensation wall of the smallest *isolated* voids is quite large in split profiles as well and further supports the dominated inflow velocities seen previously in figure 6.6. In the smallest depicted bin of r_v, the majority of tracers even moves towards void centers, instead of the usual domination of outflowing tracers inside voids. This inflow of halos around small voids supports conclusions that voids can accrete significant amounts of matter over time [143], here in the form of halos, but split profiles of CDM around halo voids suggest a similar accretion of matter inside small voids. On the other hand, large voids are dominated by the outflow of tracers.

Comparing the density profiles of tracers with both positive and negative velocities, we see that the larger voids become, the closer their density profiles moves towards -0.5 on large scales, either from below or above, respectively. This ultimately results in densities near the mean background seen in the usual density profiles in figure 6.1 and a net velocity close to zero for large voids, as split velocity profiles are rather similar.

Chapter 7

Linear mass conservation

After examining properties of stacked density, as well as velocity profiles of various voids separately in the previous chapter, we now want to investigate their close interrelation via the linear continuity equation (3.14), discussed in more detail in section 3.2. For any given density profiles, we refer to their velocity profiles calculated via that equation as *linear theory profiles*. Equation (3.14) still contains a free parameter that is to be determined when using halos as tracers: their bias b_t. We achieve determining this parameter by fitting our linear theory profiles to the velocity profiles that were estimated via equation (3.9) for individual voids, and via equations (3.10) and (3.11) for stacked voids, treating this bias as a free (inverse) amplitude. Except for tests at different redshifts in section 7.3, all void catalogs are at redshift $z = 0.29$.

7.1 Individual voids

We begin testing the validity of equation (3.14) on the density and velocity profiles of individual voids, estimated via equations (3.7) and (3.9), respectively. The left panel of figure 7.1 presents the individual matter density profiles of five *isolated* CDM voids from the `midres` simulation, while their velocity and linear theory profiles (with $b_\mathrm{t} = 1$) are depicted on the right. These five CDM voids are more or less a random draw from our void catalog, with the only condition to sample a range of significantly different void radii. Although these individual density profiles are subject to a high sample variance and scatter, one can still perceive the characteristic underdensity near the center of voids, an overdensity in the compensation wall around $r = r_\mathrm{v}$, and the trend of profiles going towards the mean background density at large scales. A particular void with $r_\mathrm{v} = 32.06\,\mathrm{Mpc}/h$ (depicted in yellow) exhibits a peak in the density in its very center, which serves as a good example for the effects of tracers sparsity that can occur in the density estimator from equation (3.7) at the smallest inner shells.

Their velocity profiles measured from tracer velocities mirror these fluctuations, where some voids are dominated by outward motion of tracers across all scales and other voids experiencing an infall towards their compensation wall from large distances. Nevertheless,

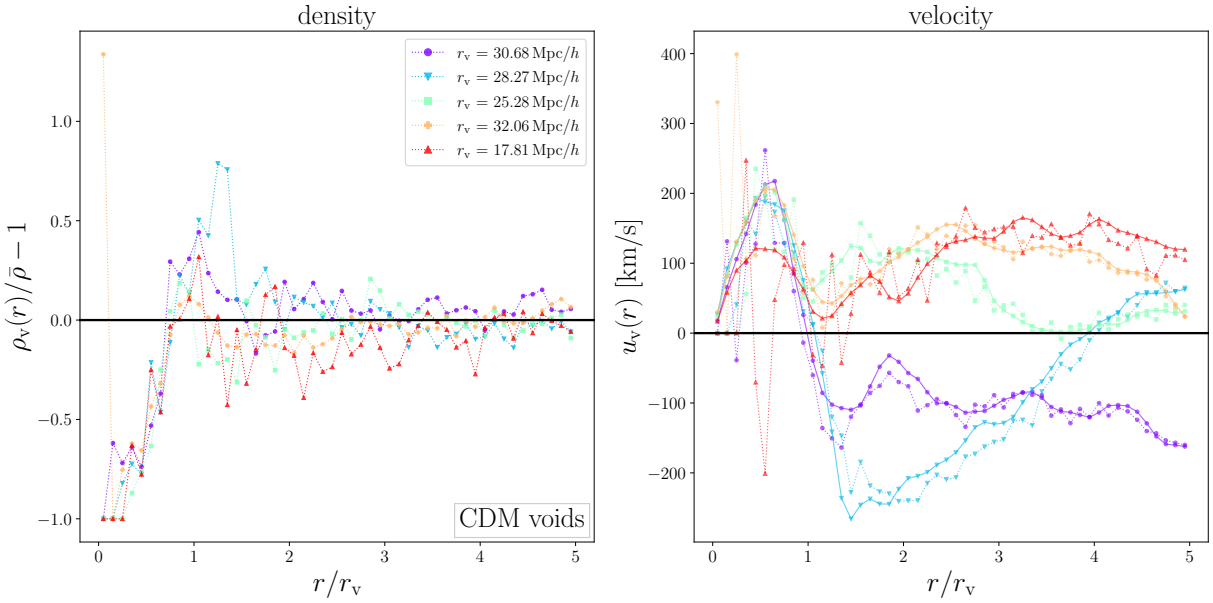

Figure 7.1: Matter density (left) and velocity (right) profiles of *isolated* individual CDM voids from the `midres` simulation. Dotted lines show the measured density and velocity profiles based on equations (3.7) and (3.9), respectively. Solid lines in the right panel depict the linear theory predictions based on equation (3.14), with $b_t = 1$ for CDM. The legend provides the effective radii of the individual voids.

the linear theory profiles match the measured velocities with a remarkable accuracy for every single case. However, due to the integral over the density profile appearing in equation (3.14), the linear theory profiles become much smoother than the measured velocity profiles, as the scatter is averaged out. Near the centers of voids differences are more significant due to the sparsity of tracers inside voids, but they are still consistent with the scatter of the measured velocity. We emphasize that in this procedure, no free parameters have been adjusted and the tracer bias of CDM is simply fixed to its value $b_t = 1$.

When we use halos as tracers for the profiles, we can no longer assume a unity bias $b_t = 1$, but have to determine this bias separately. The individual number density profiles of five *isolated* halo voids selected at random of the `midres` simulation are depicted in figure 7.2. Moreover, we revisit the mass-weighted density profiles on the bottom panel for the same five voids, as introduced in section 6.2. These two types of density profiles follow similar shapes, although the mass-weighted ones have a tendency for deeper troughs and higher peaks, since more massive halos are more likely to reside in regions of higher density, as discussed before. One particular void with with $r_v = 23.7\,\mathrm{Mpc}/h$ (in red) is embedded within a much larger underdensity, located between $r = 3r_v$ and $r = 4r_v$, and it serves as a nice example for the void-in-void scenario.

The individual velocity profiles once more reflect the density structure of all five depicted voids. We now treat the bias b_t in equation (3.14) as a free parameter, in order to

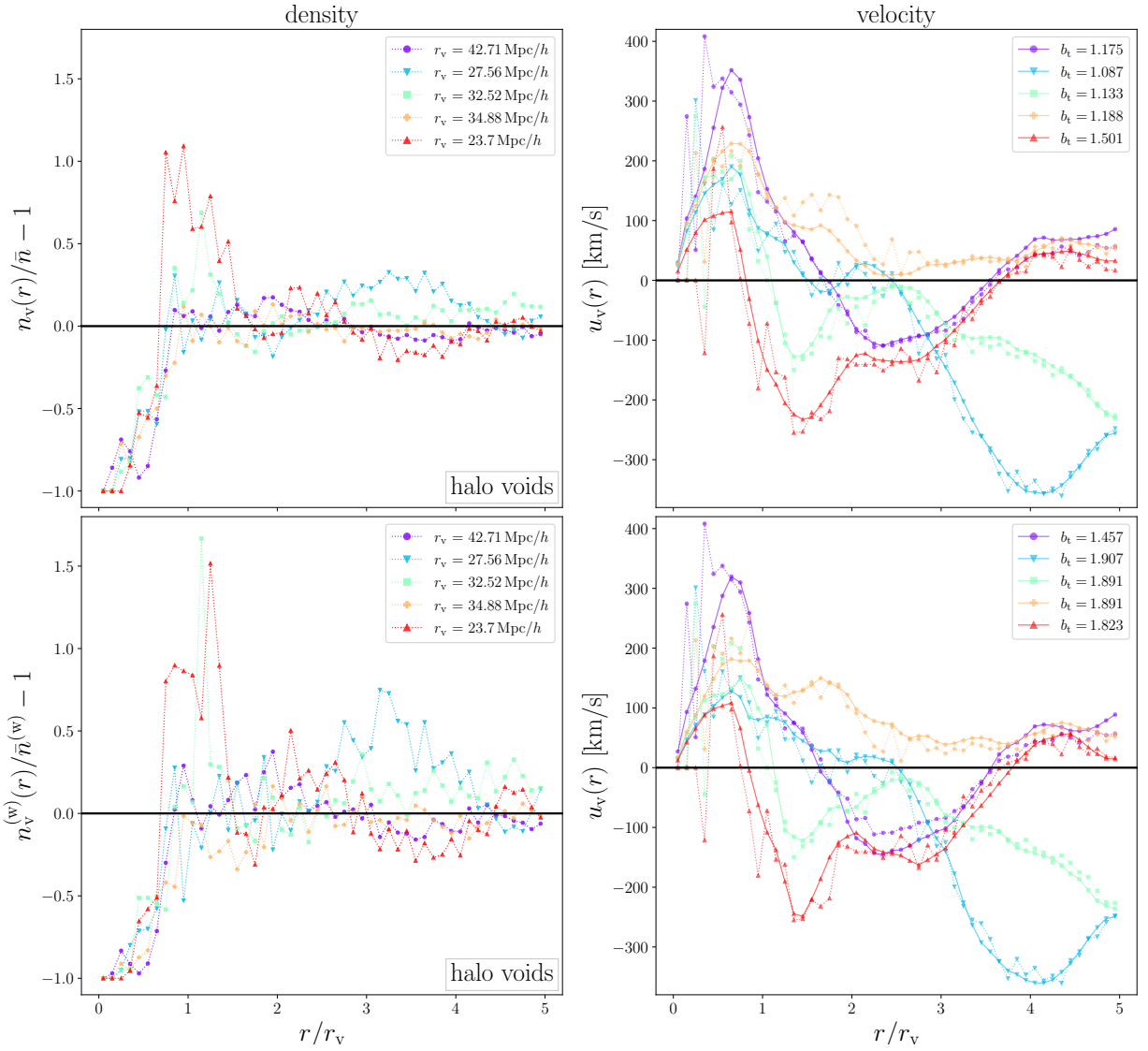

Figure 7.2: Same as figure 7.1, but for *isolated* halo voids with both unweighted (top), as well as mass-weighted (bottom) number density profiles of halos. The bias b_t is now a free parameter and fitted to the measured velocity profiles from velocities of halos, with best-fit values given in the legend.

fit the linear theory profiles to the measured velocity profiles. Again, both profiles share a striking similarity, even for the case of using mass-weighted density profiles. The only difference from the latter are enhanced values of the best-fit bias parameters, which further corroborates our conclusions from section 6.2.

For completeness we additionally present five profiles of *isolated* halo voids from the `highres` simulation in figure 7.3. This time we have intentionally selected four voids of around similar size in order to point out the diversity in their profiles. The void with

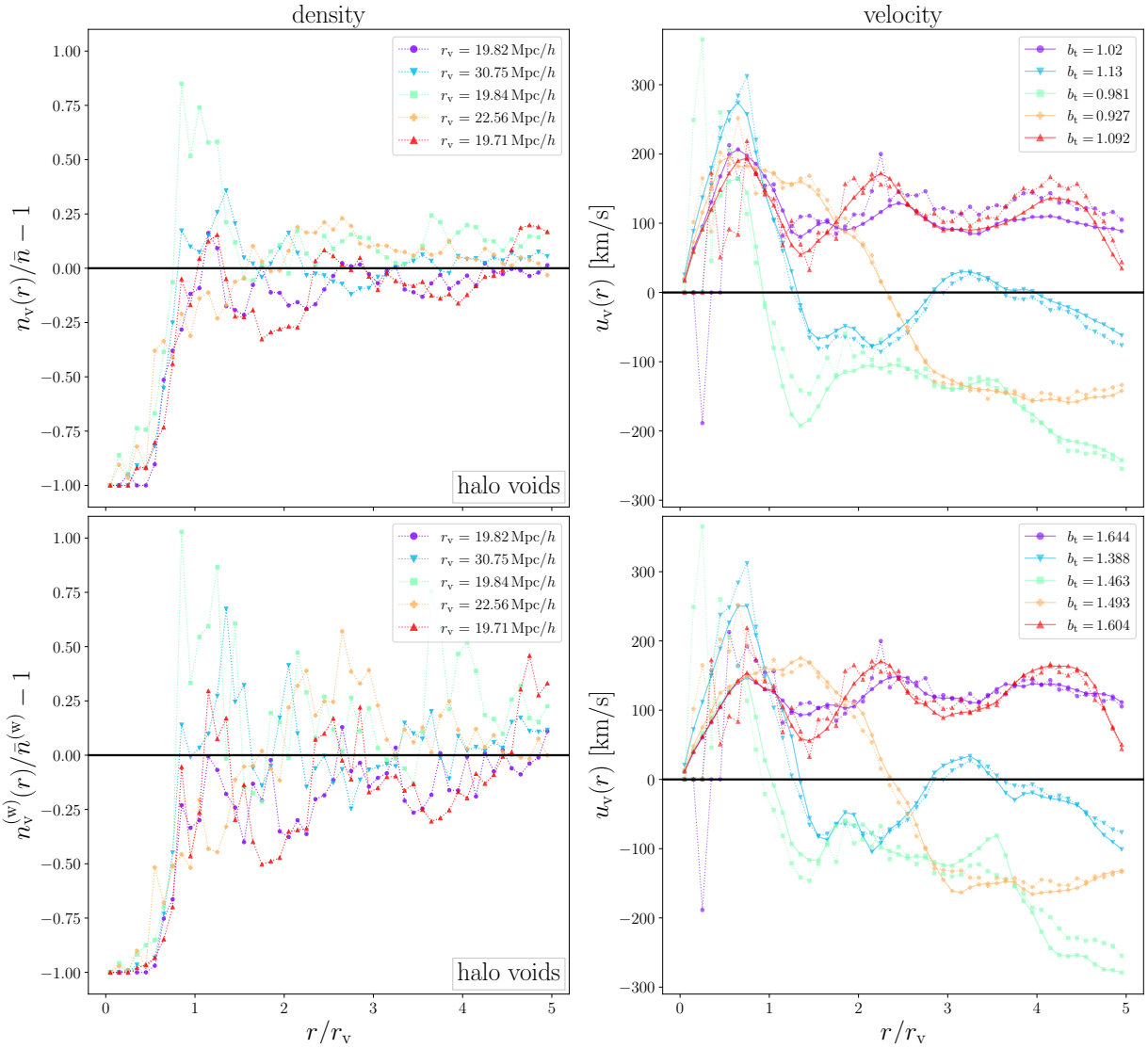

Figure 7.3: Same as figure 7.2, but in the `highres` simulation.

$r_\mathrm{v} = 19.71\,\mathrm{Mpc}/h$ (in red) could be associated with a rare "void-in-void-in-void" scenario, which exemplifies how deep hierarchies with multiple levels of sub-voids can occur. This fact is substantiated by its velocity profile, which exhibits three distinct peaks of enhanced outflow of tracers around the boundaries of each sub-void in the density profile. No matter the complexity of a void's structure, linear theory manages to successfully reproduce the dynamics even within individual voids. The only major difference in `highres` are lower values of the bias obtained from our fitting, due to the lower mass cuts in halos at $10^{11}\,M_\odot/h$.

To summarize, mass conservation based on the linear continuity equation (3.14) can provide an extremely accurate description of the dynamics around individual voids that are well resolved, independent of whether CDM or halos are used as tracers for the void

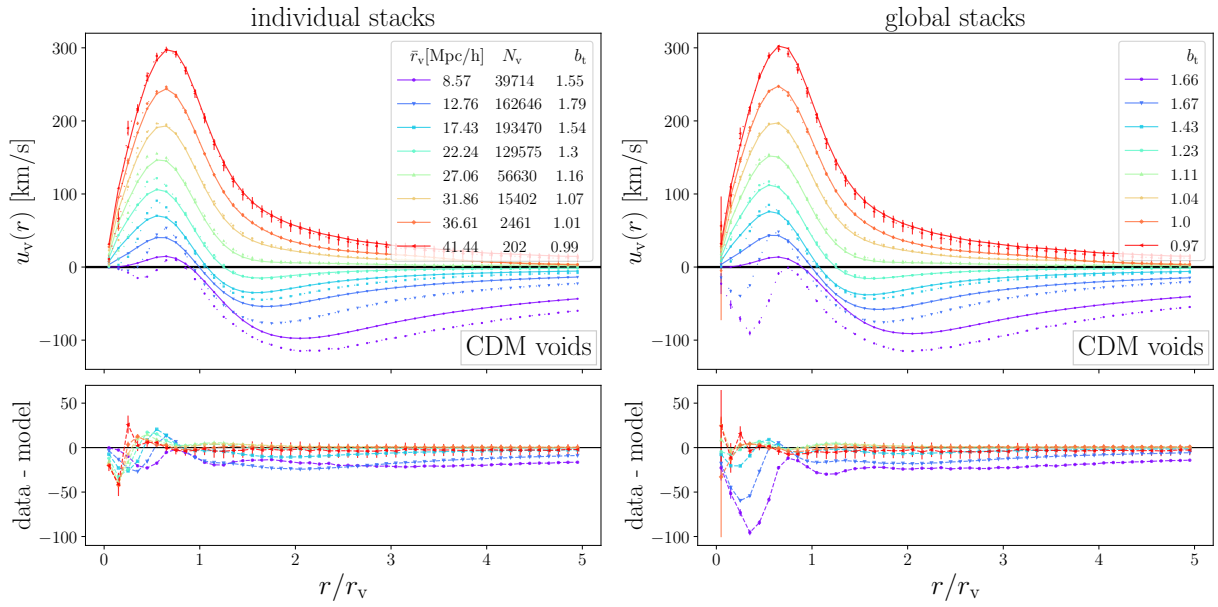

Figure 7.4: Application of equation (3.14) on the stacked matter density profiles of *isolated* CDM voids in the `midres` simulation (from the top left of figure 6.1). Solid lines depict the linear theory predictions and dotted lines the measured velocity profiles for individual (left) and global stacks (right). The bottom panels highlight differences between measured velocity profiles (data) and linear theory profiles (model).

identification. To the best of our knowledge, this unique behavior of simple dynamics has not been found in any of the environments of large-scale structure so far.

7.2 Stacked voids

In the same manner as done for individual voids, we may apply the linear continuity equation (3.14) to the profiles of stacked voids. Here we can make use of the previously examined matter density profiles of CDM voids, the number density profiles of halo voids (with and without mass weighting), as well as their corresponding velocity profiles in individual and global stacks. With all these different variants there are multiple options to test linear dynamics with stacked profiles. Reference [38] already depicted such a test based on individually stacked velocity profiles of *merged* CDM voids, which we repeat here with *isolated* CDM voids in both stacking methods in figure 7.4. We use the identical bins in void radius as already used in the upper left panel of figure 6.1. Furthermore, even though the bias of CDM tracers is $b_t = 1$, we treat b_t as a single free parameter, through which deviations from $b_t = 1$ can indicate any additional biases of estimators.

We confirm the very good agreement between the prediction from the linear continuity equation for both individual and global stacks, especially for the largest voids. The profiles from global stacks exhibit a more linear rise in velocity near the void center, which is

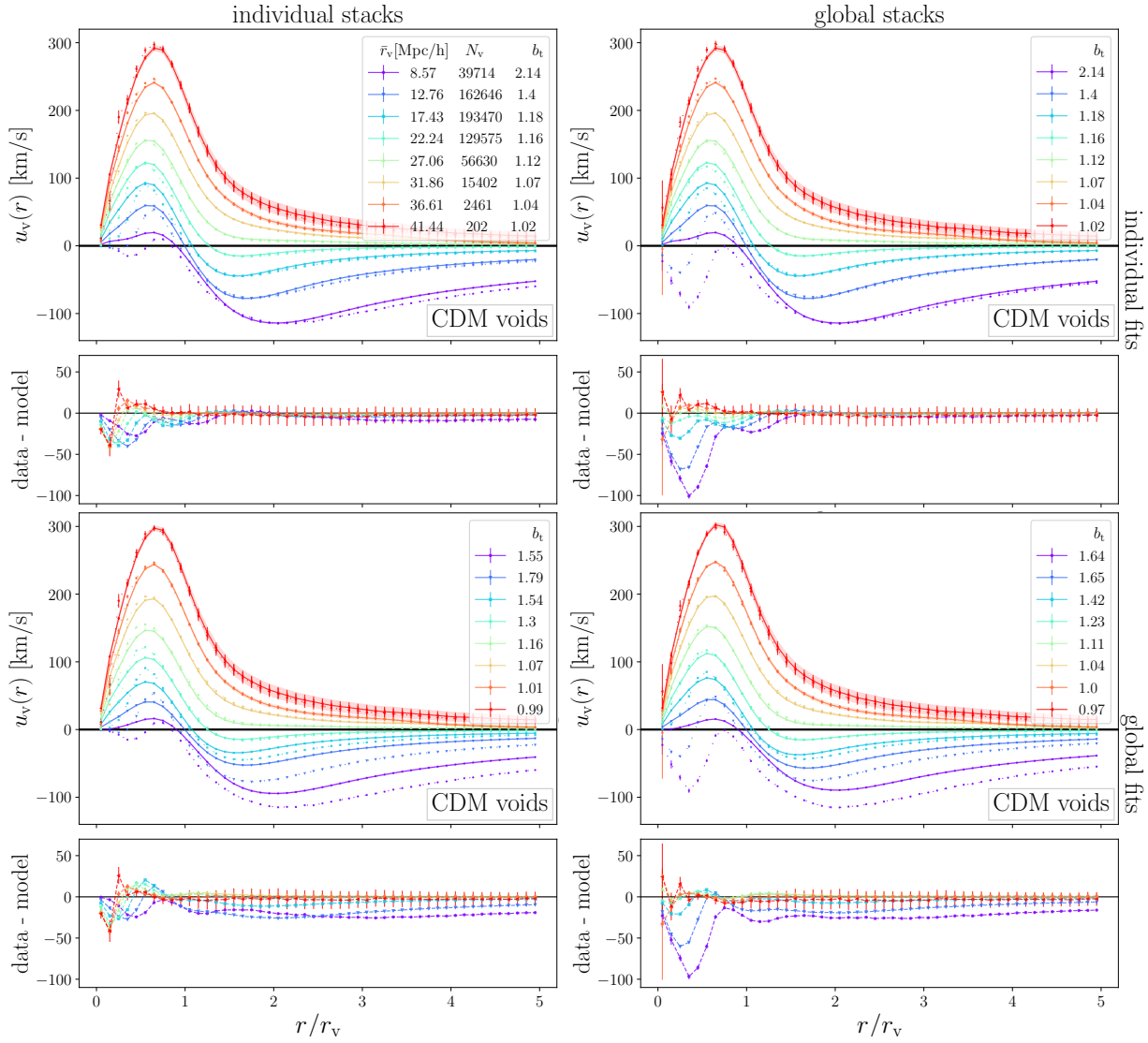

Figure 7.5: Same as figure 7.4, but for individual fits (top), as well as global fits (bottom) of the tracer bias. In individual fits the tracer bias is determined via the linearized continuity equation (3.14) for each individual void before averaging. For global fits a single tracer bias parameter is determined after averaging all individual linear theory profiles with $b_t = 1$ and applying equation (3.14). Shaded regions indicate standard deviations around the mean linear theory profiles.

slightly better in line with the linear theory prediction than in the case of individually stacked velocity profiles. Deviations become stronger in small voids, especially close to their centers due to the sparsity of tracers within, as discussed in section 6.3. However, even at larger distances from the void centers a significant constant offset remains for small voids. The best-fit values of the tracer bias converge towards $b_t = 1$ for large voids, which is as expected for CDM tracers. Smaller voids exhibit bias values significantly higher than

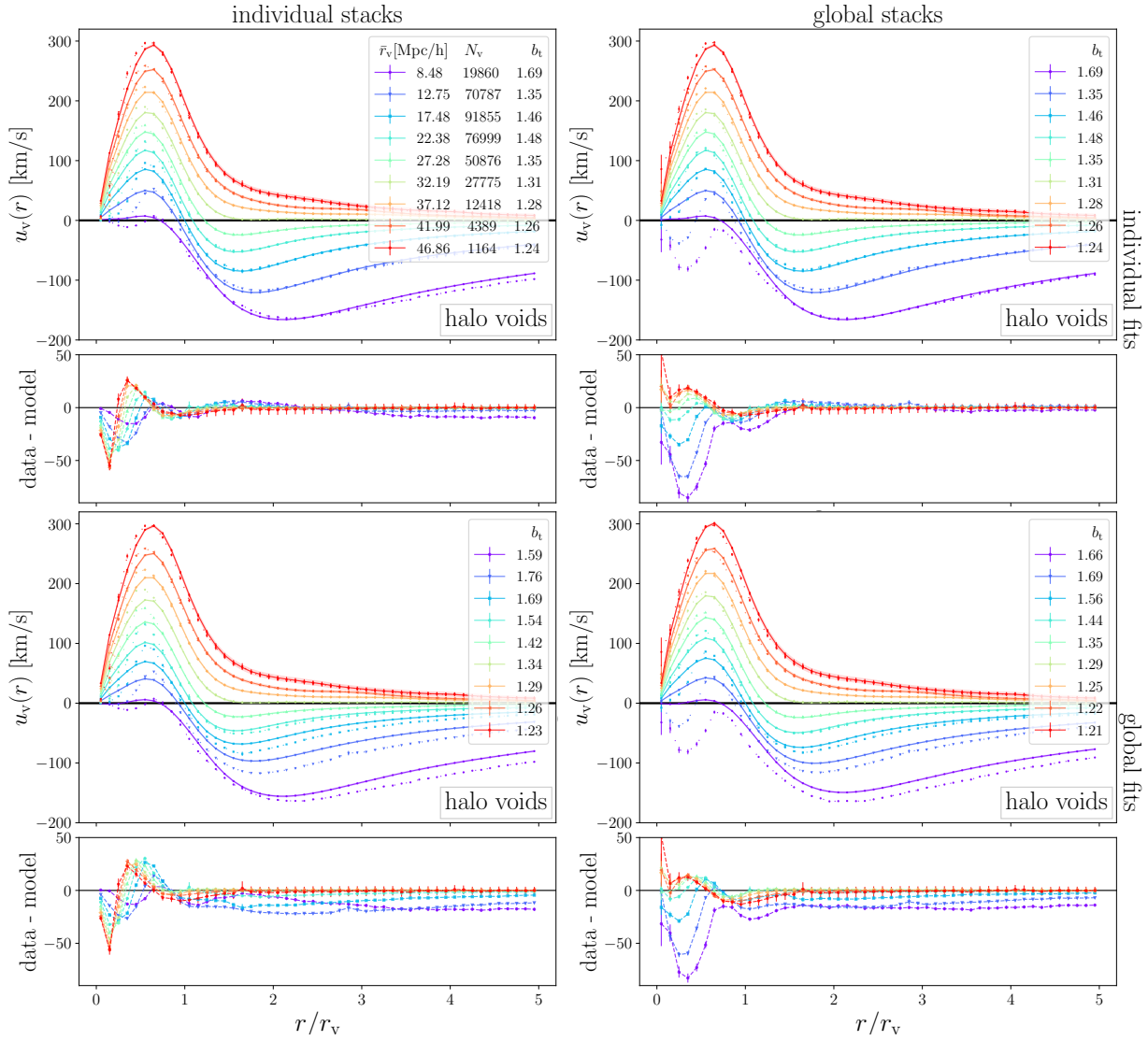

Figure 7.6: Same as figure 7.5, but for *isolated* halo voids in the `midres` simulation.

unity, in accordance with the results of reference [44]. The choice of a different merging threshold than for *isolated* voids does not affect these conclusions and they remain valid for halo voids and their number density, as well as velocity profiles, which yield higher values for b_t, as expected for halos.

With the methodology we developed for the profiles of individual voids in section 7.1, we can now introduce two additional tests for the linear dynamics around stacked voids. In the first option we apply equation (3.14) to each individual density profile of a given void sample of the stack, fit b_t for every individual void profile separately, and average the linear theory profiles, as well as best-fit bias parameters in the end. This method will be referred to as *individual fits*. For the second option, we once more apply equation (3.14) to the individual density profiles of voids, but fix the bias b_t to 1. We then average the

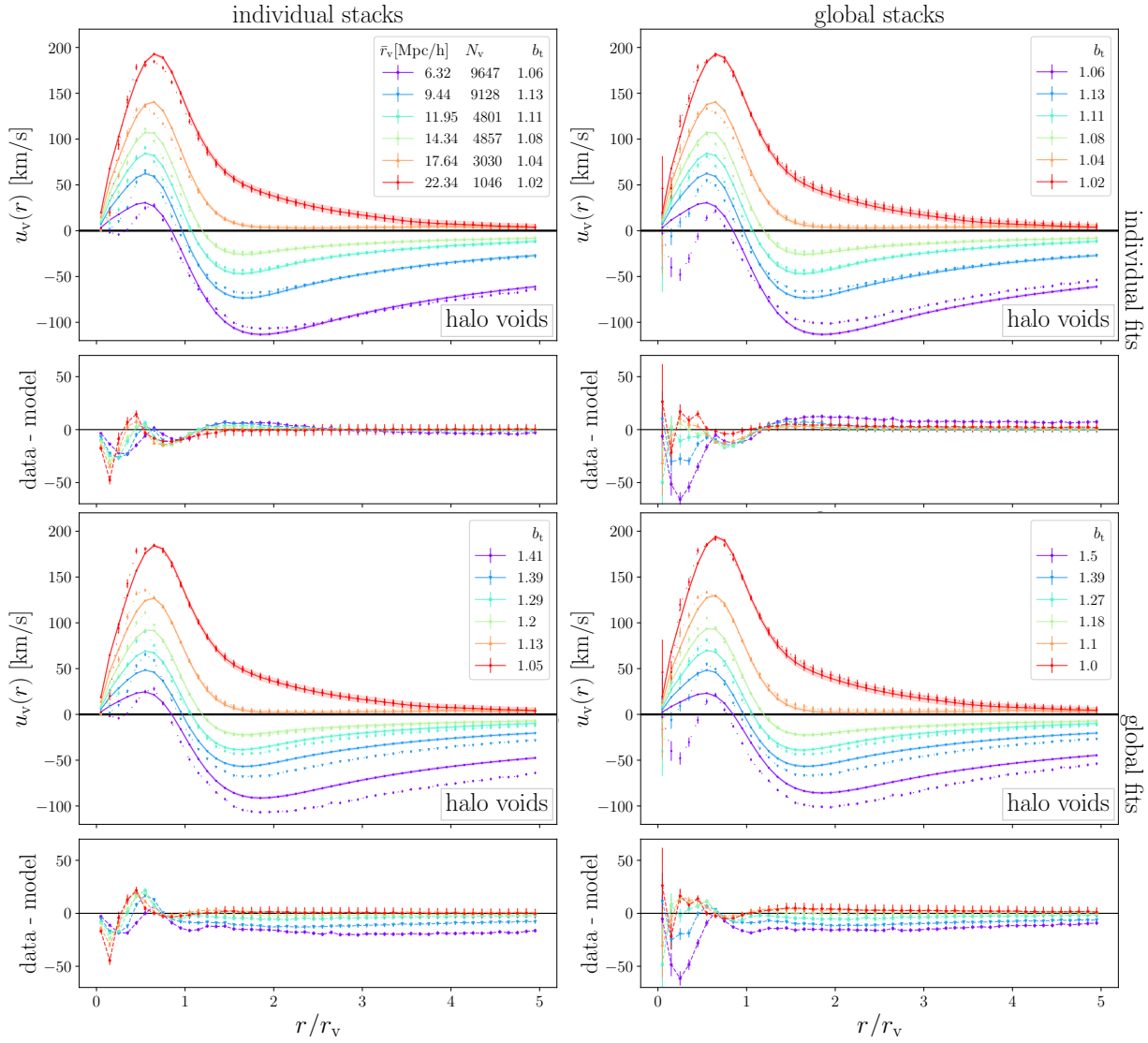

Figure 7.7: Same as figure 7.6, but for the `highres` simulation.

resulting linear theory profiles and fit for a single 'global' tracer bias parameter for each stacked bin in the end. We will refer to this method as *global fits*. Both methods come with the advantage that they naturally provide an entire posterior distribution of predictions for linear theory profiles, which can be used to quantify any uncertainties (error bars).

Figure 7.5 depicts the results from the two linear theory methods (individual and global fits) for *isolated* CDM voids. In all cases the linear theory predictions and measured velocity profiles match closely, while stronger differences once more occur around small voids. Furthermore, the differences between data and model gradually reduce towards larger voids in global stacks, whereas in individual stacks differences are of the same magnitude for all void radius bins. Generally, results from global fits are quite similar to the previous case from figure 7.4. In contrast, profiles from individual fits feature a slightly better agreement

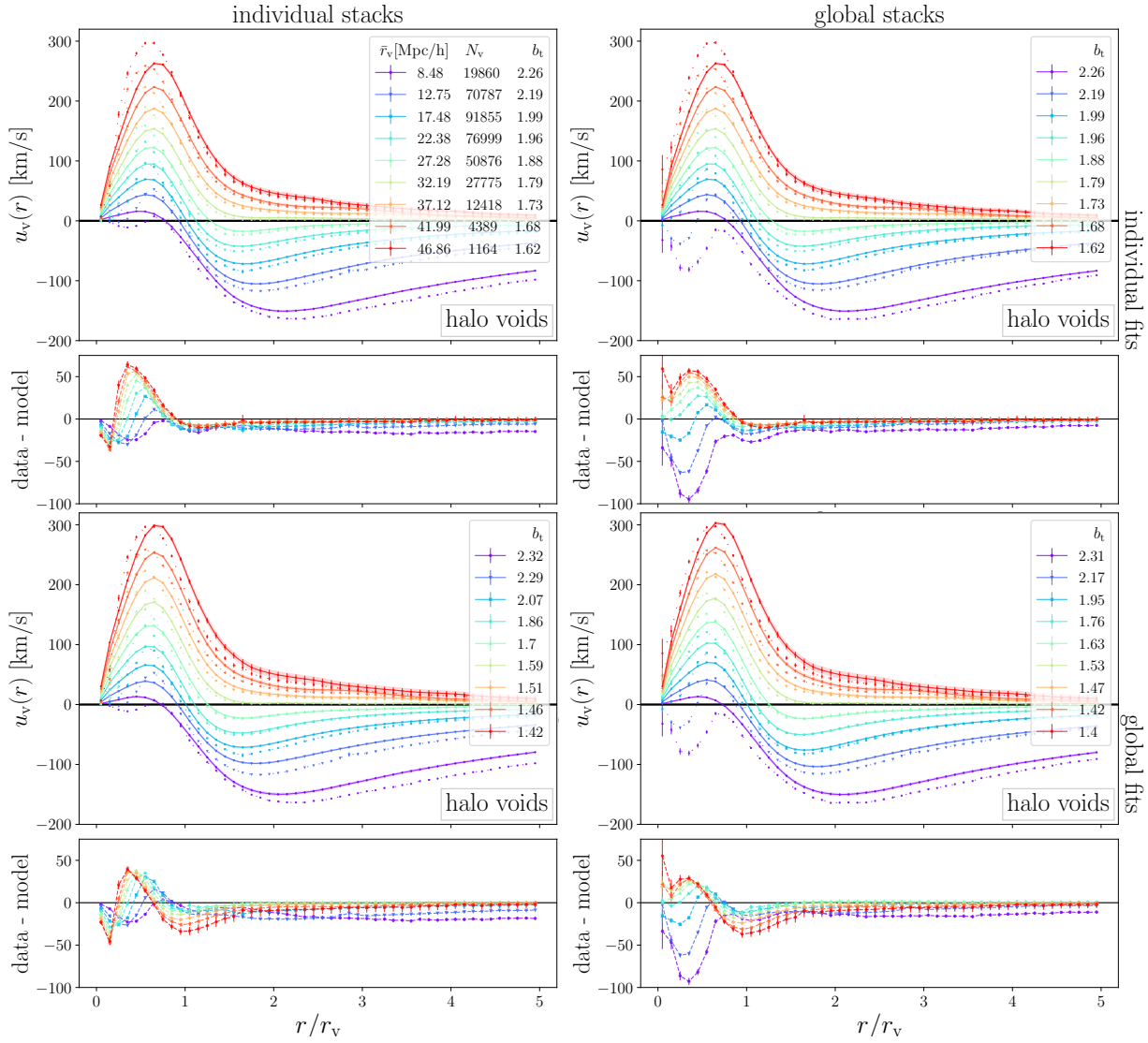

Figure 7.8: Same as figure 7.6, but using mass-weighted density profiles in equation (3.14).

between data and model, especially at larger distance from the void center. On the other hand, in the case of global fits the best-fit values of the tracer bias are somewhat closer to unity. It must be noted that for individual fits the obtained bias values are identical in both stacking methods of velocity profiles, since the fitting is performed before stacking. For global fits there are slight variations in the bias values between the two stacking methods.

Subsequent figures 7.6 and 7.7 present the individual and global fits to profiles of *isolated* halo voids in both the `midres`, as well as the `highres` simulation. Essentially all conclusions from CDM voids remain valid even for halo voids. Only the values of the tracer bias parameters are higher, as expected, but they also decrease towards larger void radii. A comparison across the different resolutions of the simulations allows us to explore a wider range in void sizes and enables us to potentially identify a limit of the validity

of linear theory for voids below some characteristic scale. For the `highres` simulation, the following bin edges in void radius are used: 4 Mpc/h, 8 Mpc/h, 11 Mpc/h, 13 Mpc/h, 16 Mpc/h, 20 Mpc/h, and 30 Mpc/h. In contrast, in the `midres` simulation bins in void radius are arranged from 5 Mpc/h to 50 Mpc/h, always in steps of 5 Mpc/h width. Now we can compare voids within a given range in radii at different resolutions. For example, the voids in `highres` with radii around 12 Mpc/h exhibit significantly smaller residuals between model and data than voids in `midres`. In order to reach a similar level of agreement in `midres`, one has to look at the profiles of much larger larger voids, of around 22 Mpc/h in radius. Voids of this size are amongst the largest voids in `highres` and exclusively feature outflows of tracers, similar to the largest voids above radii of 40 Mpc/h in `midres`. This strongly indicates that residual mismatches between data and model are due to tracer sparsity in the `midres` simulation, rather than an existing limit of linear theory below some fundamental scale.

For a final test we exchange the number density profiles with their mass-weighted versions for halo voids. This is depicted in figure 7.8 for the `midres` simulation. Our theoretical model still produces correct shapes of stacked velocity profiles, although the residuals somewhat increase in comparison to using the unweighted number density profiles. For individual stacks, the differences now increase with the size of voids, however the mass-weighted density profiles of the largest voids are most similar to their number density profiles (see figure 6.5). In each stacking method we observe that individual fits experience the largest discrepancies in the inner regions of voids, where the maximal velocity predicted by linear theory falls considerably short of the measured velocity. At larges scales the profiles align once more, except for the smallest subset of voids. In contrast, global fits reproduce the maxima in the velocity profiles more accurately, although they disagree more in regions near the compensation walls. In all cases, the fitted values of the tracer bias increase, which is expected from mass weighting, but the agreement between data and model is generally worse than for the unweighted profiles. This decrease in accuracy can be explained by the fact that mass weighting further amplifies the impact of high-mass halos, which are much scarcer than the majority of the halo population. This in turn leads to a stronger sensitivity to the impact of tracer sparsity in void profiles, most notably close to the centers of voids.

We repeated the same analysis on the matter density profiles of halo voids, as well as for *merged* voids. Furthermore, we tested additional mass cuts at higher values when selecting halos for the void identification and profile calculation. We find identical conclusions in all scenarios, so we refrain from presenting these in additional figures. Another option is to stack voids based on other properties than their radius, as already presented in figures 6.4 and 6.9. Here linear theory profiles often yield less accurate predictions due to the extended ranges in void size in each stack. This can be slightly remedied by using the methods of individual fits combined with individual stacks, as then voids are modeled completely independent from each other.

7.3 Alternative cosmologies and redshifts

So far we have only tested the validity of linear mass conservation via equation (3.14) at the 'default' cosmology of the `Magneticum` simulations, namely the best fitting values of WMAP7 [115], with values $\Omega_\mathrm{m} = 0.272$, $\Omega_\mathrm{b} = 0.0456$, $\sigma_8 = 0.809$ and $h = 0.704$. For more details, we refer to chapter 4. However, the `Magneticum` simulation suite additionally offers simulations (boxes 1a) at identical mass resolution as the `midres` simulations at smaller box length, which we will refer to as `midres-1a` and `mr1a`. These `midres-1a` simulations are performed in a box of $L_\mathrm{Box} = 896\,\mathrm{Mpc}/h$, with further details provided in table 4.1. They consist of a range of simulations with varying values of the cosmological parameters. Most importantly, their matter content starts at a smallest value of $\Omega_\mathrm{m} = 0.153$ in box C1, and increases with its numbering to the maximum value of $\Omega_\mathrm{m} = 0.428$ in box C15. In order to test linear mass conservation in more extreme cosmological scenarios, we will makes use of boxes C1 and C15, whose other varying cosmological parameters are $\Omega_\mathrm{b} = 0.0408/0.0492$, $\sigma_8 = 0.614/0.830$ and $h = 0.666/0.732$ for boxes C1 / C15, respectively, while Ω_Λ is given by $\Omega_\Lambda = 1 - \Omega_\mathrm{m}$.

For the void identification process we apply the identical halo mass cut as in `midres`, namely $M_\mathrm{cut} = 10^{12}\,M_\odot/h$, as then halos are still resolved. The number of halos above this mass cut and subsequently the number of identified voids therein strongly correlates with the amount of matter in the Universe, i.e. Ω_m. We ultimately end up with 0.967×10^6 halos and 4 807 voids in the C1 run, while C15 contains 4.35×10^6 halos, as well as 27 693 identified voids, all at redshift $z = 0.29$.

We tested our analysis on the linear mass conservation in the same manner as for `midres` in these two cosmologies and a summary is presented in figure 7.9 for the C1 box on the left and the $C15$ box on the right, where the normal number density profiles are used. It is presented for both linear theory and velocity profiles of individual *isolated* halo voids in the upper panels, as well as for their global stacks of velocity profiles on the bottom, including linear theory profiles with individual fits. While the radii of voids between C1 and C15 differ significantly due to the shift in the void size functions caused by enormous differences in the number of voids identified, and the height of maximal velocities in identical bins of r_v almost triple in C15, we observe that the general results at different cosmologies look more or less identical to the ones of the `midres` and `highres` simulations, although with significantly different values of the tracer bias b_t. At small Ω_m we find high values b_t, while at large Ω_m, b_t is much closer to unity. With these results we argue that the application of linear theory via equation (3.14) should successfully reproduce the dynamics of both individual and stacked voids in all observationally relevant ΛCDM cosmologies to a high degree.

In addition, we perform tests of our analysis at multiple redshifts. As our previous results on linear mass conservation were all obtained at redshift $z = 0.29$, which is already close to $z = 0$, we instead present a summary of our analysis at much higher redshifts and equivalently in a much less evolved Universe. As we will investigate the time evolution of voids and their profiles, as well as redshift effects in chapter 9, we will not go into more details here, except when relevant for our analysis, presented in figure 7.10. Once more, we

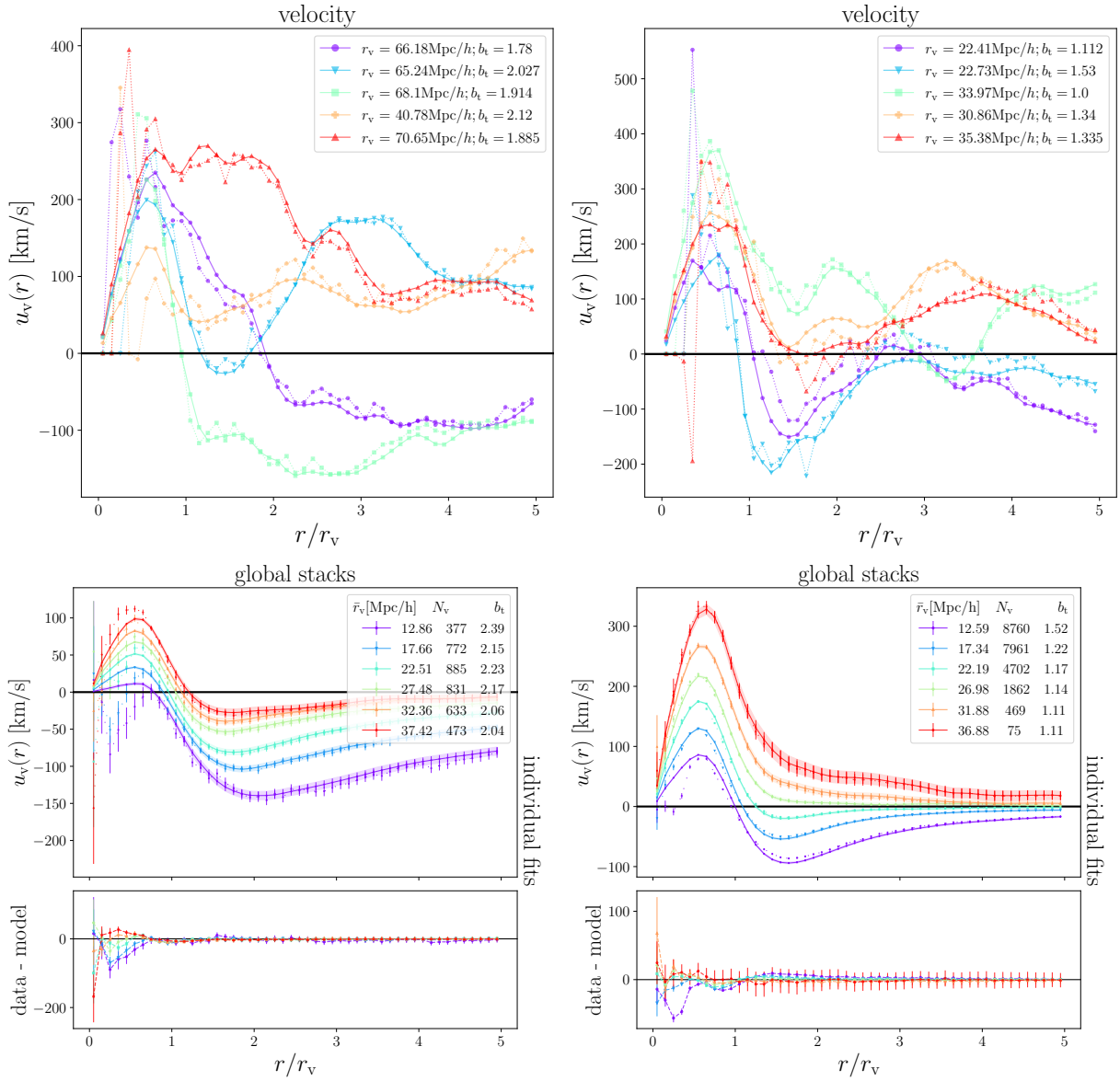

Figure 7.9: Linear mass conservation applied on individual (top) and stacked (bottom) *isolated* halo voids (using halo tracers) in the C1 (left) and C15 (right) cosmologies of the `midres-1a` simulations, at $z = 0.29$, presented for global stacks of velocity profiles. Solid lines show the linear theory predictions and dotted lines the measured velocity profiles.

depict the linear theory profiles, as well as velocity profiles of individual voids on the top and global stacks of velocity profiles in addition to the linear theory profiles using individual fits on the bottom. Here it is depicted for *isolated* halo voids in the `midres` simulation at redshift $z = 2.79$ on the left and in the `highres` simulation at redshift $z = 4.23$ on the right. At the usual $10^{12}\,M_\odot/h$ mass cut in `midres` we use 9.90×10^6 halos to identify 77 029 voids at $z = 2.79$, while `highres` at mass cut $10^{11}\,M_\odot/h$ contains 6 866 voids within the

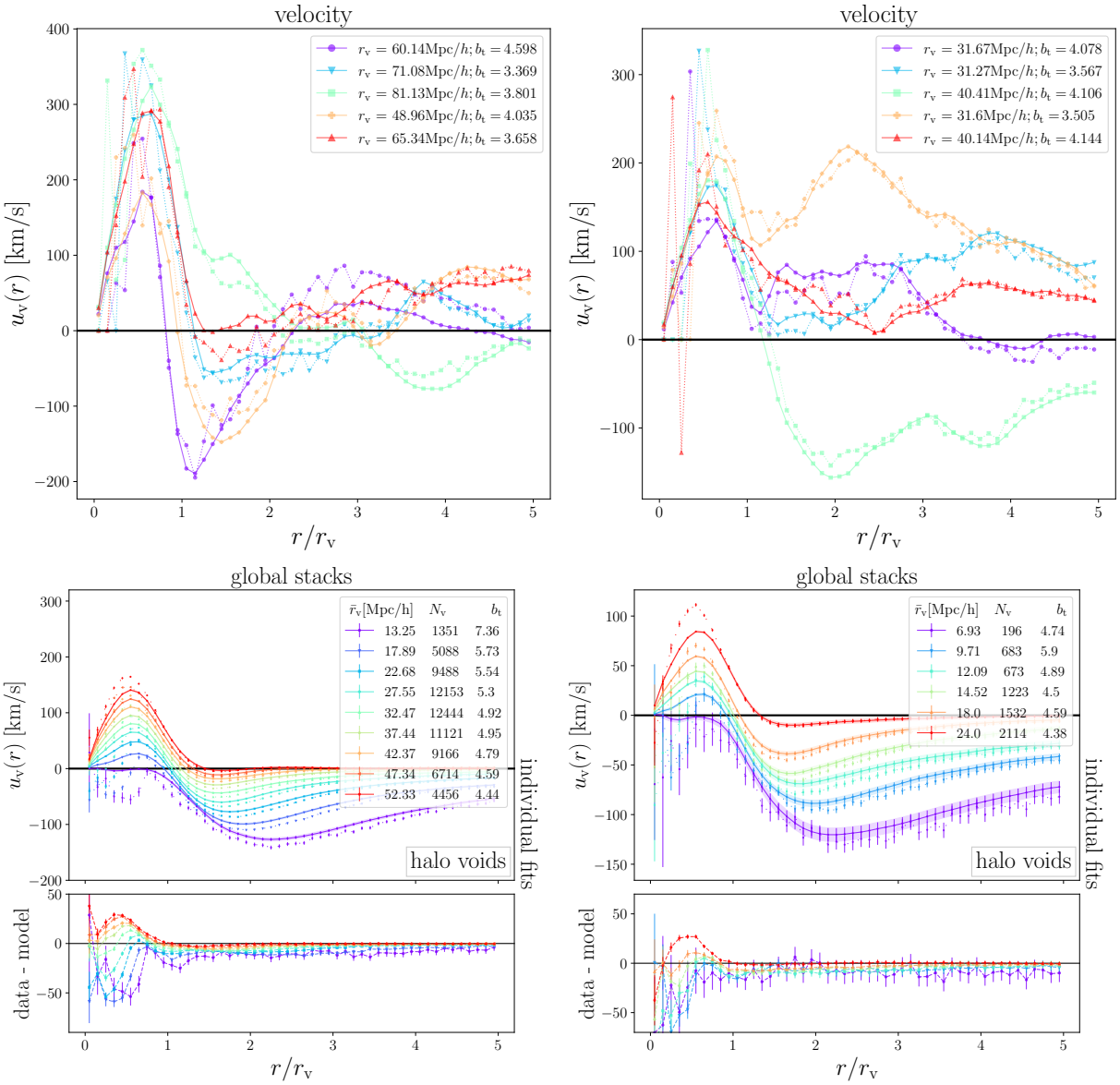

Figure 7.10: Linear mass conservation applied on individual (top) and stacked (bottom) *isolated* halo voids (using halo tracers) in `midres` at $z = 2.79$ (left) and `highres` at $z = 4.23$ (right), presented for global stacks of velocity profiles. Solid lines show the linear theory predictions and dotted lines the measured velocity profiles.

distribution of 1.23×10^6 halos at $z = 4.23$.

At these rather early times in our Universe, we find only few halos, which represent the strongest peaks in the early density field. Due to this, we find significantly higher values of the tracer bias than previously, on the order of $b_t \gtrsim 4$. Furthermore, voids are now of larger size due to their limited numbers. However, even at these high redshifts we find that linear mass conservation successfully reproduces both individual, as well as

stacked velocity profiles, as evident from figure 7.10. Once again, the results are almost indistinguishable from those of the previous sections at redshift $z = 0.29$ and further tests at $z = 0$ show equally similar results. We therefore argue that besides being applicable at different cosmologies, linear mass conservation still holds over the majority of the age of our Universe.

7.4 Resolution study

Our tests on the linear continuity equation in the previous sections show a remarkable agreement between the measured velocity profiles and profiles obtained from equation (3.14), in stacked, as well as even individual profiles of both CDM and halo voids. Comparing the `midres` and `highres` simulations has not revealed any limitations for the validity of the linear continuity equation around voids, apart from effects due to tracer sparsity. In this section we extend this through a resolution study by one more layer, where we make use of the `ultra-hr` simulation. This simulation covers a small box volume of merely $48\,\mathrm{Mpc}/h$ a side, but features a much higher resolution than used in the `highres` simulation. For the void identification in halos we used a mass cut of $1.3 \times 10^9\,M_\odot/h$, as at this value, halos are still resolved. This mass cut led to around 0.136 million halos with a mean particle separation of $\bar{r}_\mathrm{t} = 0.93\,\mathrm{Mpc}/h$, which ultimately resulted in a total of 346 *isolated* halo voids in this simulation at redshift $z = 0.29$. This void sample is too small to consider for any realistic cosmological applications, although it is still very useful for testing linear dynamics at very small scales.

Figure 7.11 presents both individual and stacked density profiles of halo voids on the left. The latter clearly exhibit enormous error bars compared to previously analyzed profiles, owed to the much smaller number of voids in the sample. Nevertheless, characteristic features of density profiles are still consistent with our previous findings, except that now we are investigating voids of only a few Mpc in size, with a maximum radius of $4.5\,\mathrm{Mpc}/h$ depicted. The right side of figure 7.11 shows the corresponding velocity profiles, with individual stacks used for the velocity profiles on the bottom. Almost all of these small voids experience infall of tracers from their environment, albeit there is one example of a clearly undercompensated void with $r_\mathrm{v} = 4.15\,\mathrm{Mpc}/h$ (in green) experiencing outflows.

Based on the density profiles on the left of figure 7.11, we once more repeat the application of equation (3.14) in order to get predictions of the velocity profiles on the right. In the individual void profiles on the top we find that even the smallest void depicted, with a radius of $1.38\,\mathrm{Mpc}/h$ (in red), has a velocity profile consistent with linear dynamics within the scatter. This is still in line with the individual profiles in both `midres` and `highres` simulations from section 7.1. Despite the enormous variety in shape, the individual profiles are all described strikingly well by the linear continuity equation. Additionally, the stacked velocity profiles on the bottom confirm this: even in the smallest bin of void radii between $1.0\,\mathrm{Mpc}/h$ and $2.5\,\mathrm{Mpc}/h$, the linear theory profiles based on individual fits still align with the individually stacked velocity profiles within their errors on all scales around the void center.

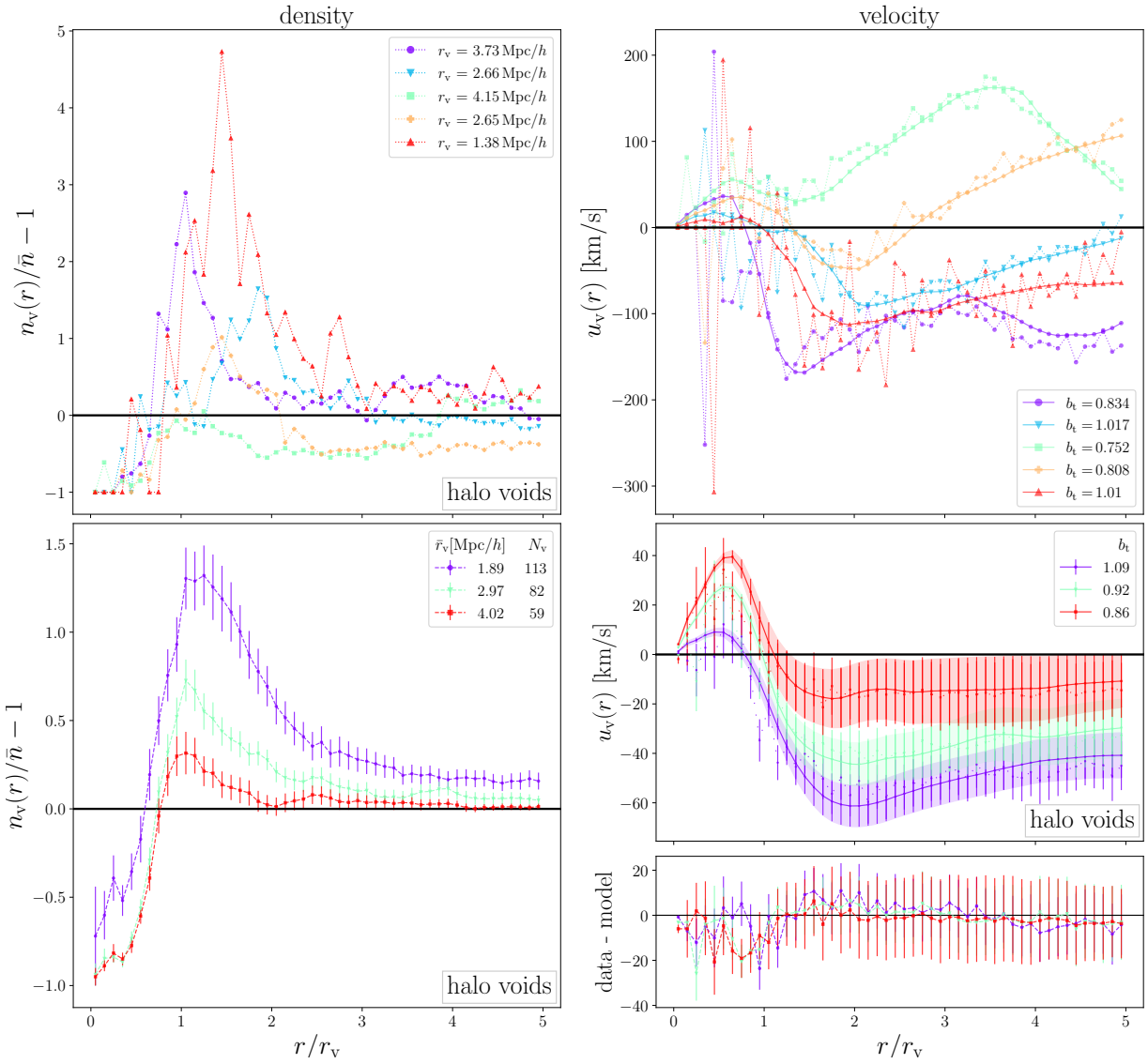

Figure 7.11: Individual (top), as well as stacked (bottom) number density profiles of *isolated* halo voids from the `ultra-hr` simulation on the left. Corresponding velocity profiles (dotted lines) and predictions of linear mass conservation (solid lines) via equation (3.14) on the right.

Such small scales, reaching $1\,\mathrm{Mpc}/h$ and below, are typically considered to be highly nonlinear in the field of large-scale structure. Nevertheless, we find no evidence for any onset of nonlinear dynamics around underdense environments in voids of this size. A similar conclusion on the linearity of voids has been reached in reference [47], where it was shown that voids of size $r_v > 5\mathrm{Mpc}/h$ are well-described by the Zel'dovich approximation. It might be possible that these linear dynamics are a general characteristic of voids and might hold irrespective of length scale. At the same time, voids clearly dominate the

volume fraction in the Universe, which indicates that linear dynamics should prevail within the large-scale structure. It is conceivable that due to practical reasons the study of the brightest galaxies and most massive objects, typically located in the densest environments of the cosmos, may have concealed this new insight from cosmologists until now.

Chapter 8

Baryonic effects in voids

In previous chapters we focused solely on voids identified in the `hydro` simulations of the `Magneticum` suite, in order to investigate general properties of voids and their profiles in chapters 5 and 6, as well as test the validity of linear mass conservation around voids across a wide range of scales in chapter 7. However, most cosmological simulations do not include the more complicated baryonic physics and are purely dark matter only simulations, in order to save significant computational resources. Neglecting the effects from baryonic physics in these dark matter only simulations naturally leads to substantial changes in the properties and internal structures of biased tracers, such as halos.

So far the impact of baryonic physics in and around voids has been explored in only few studies, such as the ones by Paillas et al. [144] and Rodríguez-Medrano et al. [145]. As these papers only studied spherical voids in either much smaller cosmological volumes or lower resolutions, we aim to investigate impacts of baryonic physics on watershed voids in greater detail. Comparing common void statistics from both `hydro` and `DMo` simulations can help determining the validity of void statistics derived from dark matter only simulations when comparing these statistics with observations. Furthermore, in order to learn more about the differences between baryons and CDM around voids and where they are of great importance, we will investigate their different distributions and dynamics around halo defined voids in the `hydro` simulations in a variety of resolutions and scale. All this is explored at fixed redshift $z = 0.25$ in the `highres` and `ultra-hr` simulations.

In section 8.1 we will briefly discuss the relevant changes in tracer catalogs between the `hydro` and `DMo` simulations, as well as baryonic impacts on common void statistics. Afterwards in section 8.2 we will investigate the density and velocity profiles for a variety of different cases of voids and tracers used in these profiles.

Name	hydro/ DMo	M_{cut} $[M_\odot/h]$	N_{h} $[\times 10^6]$	$\bar{n}_{\mathrm{h}}$ $[(\mathrm{Mpc}/h)^{-3}]$	$\bar{r}_{\mathrm{t}}$ [Mpc/h]	N_{v} in halos	N_{v} in matched halos
midres	hydro	1.0×10^{12}	65.5	$3.37 \cdot 10^{-3}$	6.67	366 709	–
midres	DMo	1.0×10^{12}	66.4	$3.42 \cdot 10^{-3}$	6.64	371 943	367 791
highres	hydro	1.0×10^{11}	8.20	$3.13 \cdot 10^{-2}$	3.17	33 254	31 139
highres	DMo	1.0×10^{11}	7.53	$2.87 \cdot 10^{-2}$	3.27	32 050	–
ultra-hr	hydro	1.6×10^{9}	0.113	$1.02 \cdot 10^{0}$	0.992	281	–
ultra-hr	DMo	1.6×10^{9}	0.143	$1.30 \cdot 10^{0}$	0.917	348	278

Table 8.1: Summary of halo and void numbers in hydro and DMo runs, including the number of halos N_{h} with $M_{\mathrm{h}} \geq M_{\mathrm{cut}}$, mean halo density $\bar{n}_{\mathrm{h}}$ and tracer separation $\bar{r}_{\mathrm{t}}$ after mass cuts, number of halo voids identified in the halo catalogs after applying the mass cut and matched halo densities (for simulation with larger N_{h}) in the different Magneticum runs, at redshifts $z = 0$ for midres and $z = 0.25$ otherwise.

Name	subsampling fraction	N_{t} after subsampling $[\times 10^6]$	N_{v} in CDM	N_{v} in baryons	N_{v} in CDMo
midres	0.0665 %	62.1	538 255	539 284	537 951
highres	0.0344 %	8.21	51 741	52 712	51 772

Table 8.2: Subsampling fraction from total number of particles of each kind and resulting number of subsampled matter tracers used for the void identification, number of voids found in the CDM and baryons of the hydro runs, as well as the CDM of the DMo runs (CDMo).

8.1 Catalogs

8.1.1 Tracers

As previously discussed, the void finding with VIDE solely requires the position of any kind of tracer particles. Hence, we will find voids in both the distributions of halos, as well as the different matter tracers. In case of the hydro simulations, we identify voids in both CDM and baryon particles, while we only identify CDMo voids in the DMo simulations. In contrast, voids can be identified in the halos of both hydro and DMo simulations and will be referred to as halo- and DMo halo voids, respectively.

The halos utilized for void identification are once more selected after applying different mass cuts (see table 8.1), which are above the resolution limit of each box, explained in more detail in chapter 4. This is valid for halo voids in both the hydro and DMo runs. However, as the number of halos above a given mass cut differs between hydro and DMo runs, this results in significant differences in void numbers, which in turn affects common void statistics, such as their void size functions and void profiles. This could already be attributed to baryonic effects, though in real observations we only observe a given number

of galaxies and halos. Therefore, we choose to additionally match the halo number densities in both `hydro` and `DMo` runs to identify voids in these matched catalogs as well. This is done in order to pinpoint where baryonic physics has an effect on void statistics and to see if void statistics from other dark matter only simulations at a given tracer density would have to take into account these effects when comparing the statistics with observations. For the matching, we select the most massive halos of those simulations, which have the most halos above a given mass cut. Therefore, when investigating baryonic effects around halo defined voids, we will present void statistics in both catalogs obtained from mass cuts and from matched halo densities.

In the `midres` as well as the `highres` simulations we additionally identify voids in subsamplings of the underlying matter particles. These subsamples were chosen to approximately match the total number of halos used for the void finding, in order to obtain matter and halo defined voids of similar ranges in r_v. This is done for both baryons and CDM from the `hydro` simulations, as well as for the CDM from the `DMo` simulations (CDMo). The subsampling fractions compared to the total number of tracer particles of each kind and the resulting tracer numbers are given in table 8.2.

8.1.2 Voids

As we have found no significant baryonic effects between the `hydro` and `DMo` runs of the `midres` simulations in all matter and halo defined voids, we refrain from presenting plots from these simulations and instead focus on voids identified in the `highres` simulations. However, the numbers of `midres` voids are still presented in tables 8.1 and 8.2. The absence of relevant baryonic effects in the `midres` simulations is also the reason why we do not investigate alternative cosmologies in this chapter, as they are only available at identical resolution to `midres`, but at substantially smaller void numbers. Furthermore, we analyzed both *isolated* and *merged* voids, but merging does not impact our conclusions so we refrain from presenting the *merged* void catalogs and solely focus on *isolated* voids. Void profiles from the `ultra-hr` simulation will be presented only in a resolution study in section 8.2.5 to further corroborate our results and common void statistics will not be presented in other sections due to the extremely low number of voids identified in `ultra-hr`.

Table 8.1 contains the number of halo and `DMo` halo voids identified in the tracer selection after mass cuts. In addition, it contains the void numbers for the matched halo density catalogs. These matched density catalogs are constructed for the simulations that have a higher halo density after the mass cuts. We see that in the case of `midres` there are more halos and therefore more voids in the `DMo` run for the mass cuts. This behavior changes for `highres` with a higher halo number density in the `hydro` simulation and reverses again in `ultra-hr`. As expected, after matching halo densities, the number of identified voids are more alike.

The void numbers found in CDM and baryons are presented in table 8.2. We see that at a fixed tracer density after subsamplings (slight variations in N_t exist), there are generally slightly more voids found in the baryons than in the CDM of the `hydro` simulations due to the more uniformly distributed baryons, while the number of voids in the CDM of both

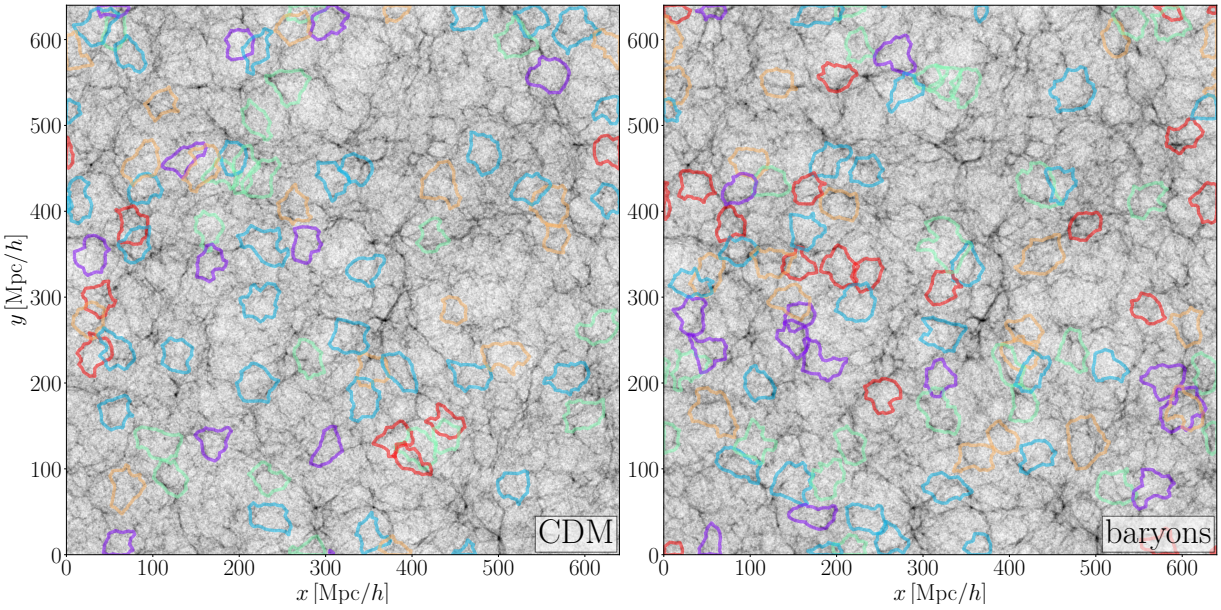

Figure 8.1: Projected density field in a 50 Mpc/h deep slice of the `highres` simulations, including projected void boundaries of voids with $r_\mathrm{v} \geq 15\,\mathrm{Mpc}/h$, whose spherical equivalent lies completely within the slice. Presented for the density field and therein identified voids in CDM (left) and baryons (right) of the `hydro` simulation. For the projected density field of matter, subsamplings with more particles than used for the void finding are depicted. Colors of void boundaries indicate the depth of the void centers within the slice.

`hydro` and `DMo` simulations is almost identical. This result contrasts previous findings [144], where significantly more matter voids were identified in dark matter only simulations. However, as we use a different void finder and do not impose any density or size cuts, we argue that both results hold, especially when considering the distributions of different matter voids later on in figure 8.3.

To showcase similarities in both matter and halo voids, figures 8.1 and 8.2 present the projected density fields across the whole `highres` simulation box in a 50 Mpc/h deep slice, including projected void shapes. Regions of higher density are depicted in darker colors while regions of lower projected density correspond to lighter tones in color. This is done for CDM (left) and baryons (right) from the `hydro` simulation in figure 8.1, as well as for halos (left) and `DMo` halos (right) in figure 8.2, where only the last case is from the `DMo` simulation. For better visibility, we restrict ourselves to depict only voids with $r_\mathrm{v} \geq 15\,\mathrm{Mpc}/h$, whose spherical equivalent lies completely within the projected slice. While in the case of all halo voids (figure 8.2), the projected tracers are identical to the ones used for the void finding after mass cuts, the matter voids are identified in subsamples of around 8.21 million tracers, whereas the projected density fields use subsamples of around 50 million tracers to resolve cosmic structures more accurately. Colors of void boundaries indicate the depth of the void center within the slice. This is done to illustrate which voids are next to each other and which ones simply overlap in projection. Purple/blue voids are

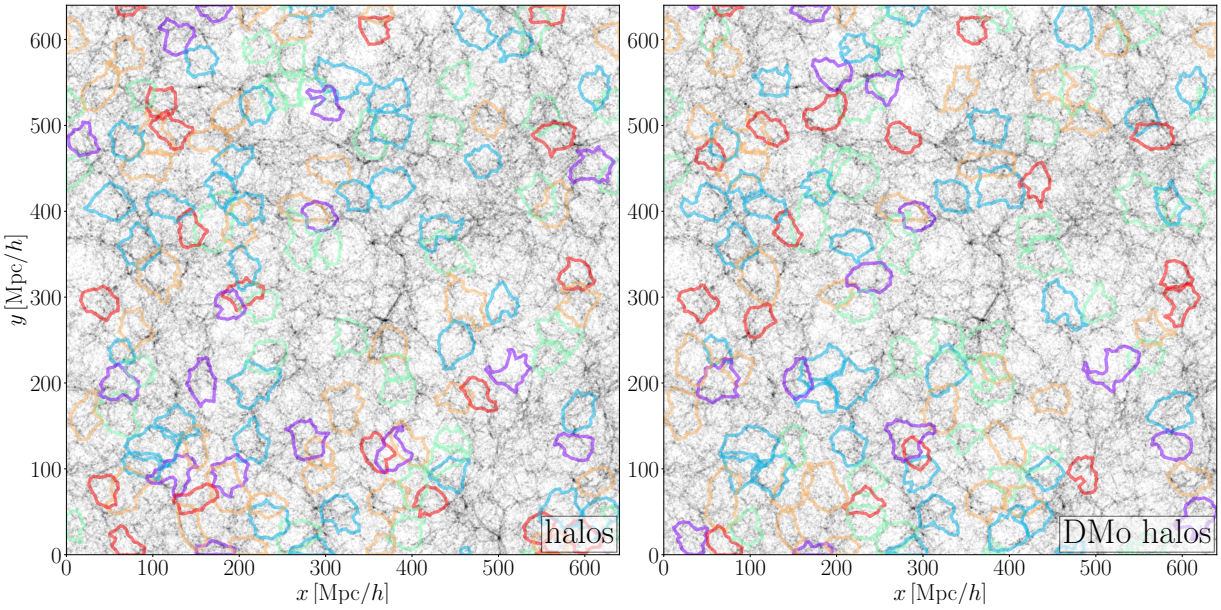

Figure 8.2: Same as figure 8.1, but for the halos at fixed mass cut in the `hydro` (left) and `DMo` (right) simulations. No additional tracers compared to the ones used in the void finding are depicted in the projected density field.

closest to the beginning of the slice, while orange/red are deepest. It is important to note that since all voids are *isolated* ones, there is no direct overlap of voids in real space and every void occupies a unique volume. Some voids even cross from one end of the simulation box to the other due to periodic boundary conditions.

Even in projection, the typical structures of the cosmic web are clearly visible, namely the nodes of clustered tracers in dark, the extended filaments and more empty regions in lighter colors. While filaments and nodes are clearly visible, most of the visibility of sheets gets lost in the projection. Between figures 8.1 and 8.2 the nodes and filaments align, as expected, since any type of matter is attracted to the potential wells of the gravitational field and halos simply arise from clustered matter particles. Void boundaries align with these visible structures quite often. However, a one-to-one congruence between the plots is not quite as clear for the projected void shapes, since only a certain selection of voids is depicted. Some matter voids get 'merged' when looking instead at the biased tracer field of halos, and the exact shapes of voids are highly sensitive to variations in tracer positions between the different cases depicted. Additionally, slight variations in the radii and barycenters might lead to some more or less 'identical' voids being left out of the projection or depicted in different colors. However, there is still an overlap of voids in all cases, with only slight variations in their projected shapes. Examples include the blue void present in both CDM and baryons, located at around $x \simeq 250\,\mathrm{Mpc}/h$ and $y \simeq 50\,\mathrm{Mpc}/h$, which is also present in the halos though with larger projected size, as well as a void located at around $x \simeq 80\,\mathrm{Mpc}/h$ and $y \simeq 20\,\mathrm{Mpc}/h$ in both halos and `DMo` halos. Nevertheless, finding and comparing 'identical' voids between the different tracer types is neither possible

for most of them, nor is it very useful. We are only interested in how void statistics are affected by baryonic physics, and not the effects on individual voids identified in different tracers, as variations between tracer positions are expected to be stronger than any effects caused solely by the implemented baryonic physics.

Furthermore, even in projection we already find that the distribution of baryons looks more diffuse than for CDM, as previously found in reference [144], which also indicates a higher baryon fraction inside voids [145]. A prominent difference between the projected matter and halo voids in figures 8.1 and 8.2 is that there are significantly fewer projected matter voids seen in the first figure, compared to halo voids in the latter. This can be explained by looking at N_v found in each tracer type and at the void size function in the upper plots of figure 8.3. As we find considerably more matter than halo voids at similar tracer densities, the matter voids necessarily become smaller than their halo counterparts, as all voids combined have to fill the box volume. This results in a shift of the void size function of matter voids towards smaller voids and less projected voids are present in figure 8.1 due to the imposed size cut for projected voids. As already discussed in section 5.2, this higher number of matter voids happens because in case of halos, only the peaks in the density field are observed, while in matter subsamplings, both matter tracers that are part of halos are present, as well as matter tracers that have not clustered in halos, but instead reside in regions where no halos formed. Due to this, a more detailed structure of the cosmic web can be found inside halo voids, which results in matter-made structures 'splitting up' some of the identified halo voids, leading to the higher number of matter voids.

Besides these universal differences in the void size functions of matter and halo voids, figure 8.3 presents the void abundance of *isolated* voids for all different matter tracers (top left), as well as for halo voids obtained from mass cuts and matched densities (top right). For all cases of matter voids, their void size functions are almost indistinguishable, which can be seen in the lower panels, where the abundances of either baryon or CDM voids are divided by the abundance of CDMo voids. There is a slight scatter in the divisions, though within the error bars, the void size functions align almost perfectly, which could already be expected from the similar void numbers. Just a tiny increase in small baryon voids can be seen compared to the CDM voids, while CDM and CDMo voids show no substantial differences.

On the other hand the halo void size functions experience slight changes, caused by the more significantly different void numbers. The `DMo` halo voids are used as the baseline and halo voids from the `hydro` run after mass cut experience a slight shift towards smaller voids, while after matching halo number densities, this effect reverses and the matched halo voids are typically larger than the voids identified in the `DMo` run at identical halo density. Due to these fixed halo number densities, we attribute this effect to the implemented baryonic physics, though it is important to note that when fixing densities, we cut the least massive halos, which have a larger probability to reside within voids than the more massive ones (see section 6.2). Therefore, some of the structures at low densities that connect halo voids obtained from mass cuts at their boundaries might 'vanish', resulting in larger, but also fewer voids in the matched density catalogs.

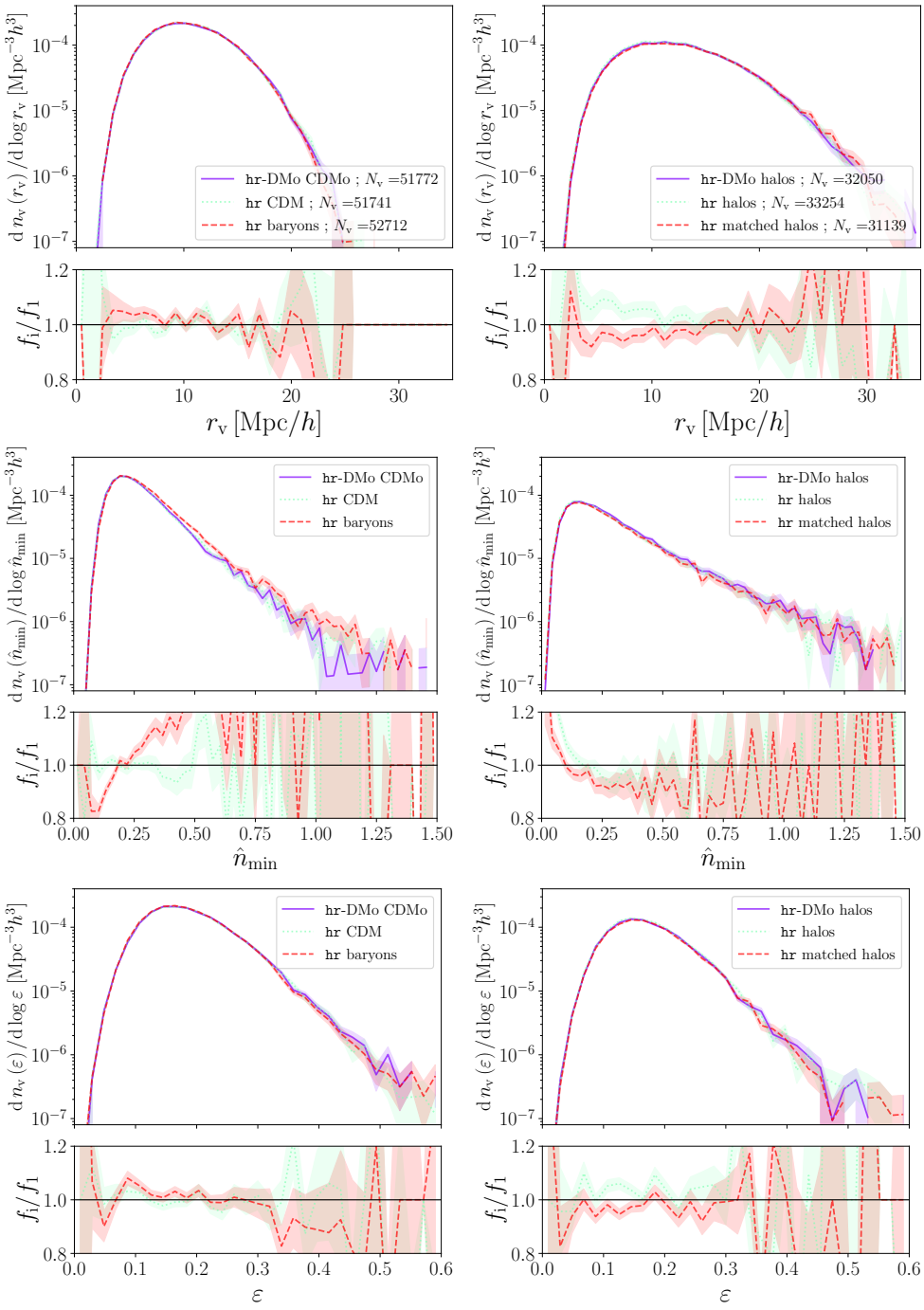

Figure 8.3: Distributions in radius (top), core density (middle) and ellipticity (bottom) of *isolated* voids identified in matter (left) and halos (right) in the `highres` simulations. Upper panels show the functions, whilst lower panels present the division of the ith element ($i > 1$) in the legend by the first one. For halos, catalogs obtained from a fixed mass cut and the one with matched density are presented.

In contrast, the abundances of voids as function of their core densities (up to $\hat{n}_{\rm min} = 1.5$) in the middle of figure 8.3 exhibit much clearer differences. While CDM voids in both `hydro` and `DMo` have the same core density distributions within their error bars, voids found in the baryons experience a clear shift towards higher values in their core densities, i.e. baryon voids are typically slightly less underdense than CDM voids, most likely due to their more diffuse distribution. As for halo voids, when comparing those obtained from mass cuts in the halos, the ones from the `hydro` simulation have a slight overabundance of voids with lower core densities compared to the `DMo` halo voids, while voids with higher core densities show no discernible differences between `hydro` and `DMo` runs within the scatter (see panels with divisions). When matching halo densities, this effect shifts towards even smaller core densities, which generally very few voids have. There is a slight indication that after matching tracer densities, fewer voids have higher core density values, although this most likely stems from the reduced void numbers in the matched catalogs of the `hydro` run, as this shift seems to be mostly constant over a wide range in $\hat{n}_{\rm min}$.

Lastly, the distribution in void ellipticities in the plots on the bottom of figure 8.3 suggests that the increase in baryon void numbers happens mostly at the peak of the ellipticity distribution between $\varepsilon \simeq 0.1$ and $\varepsilon \simeq 0.2$, while there are slightly fewer voids with high ellipticities. Contrary to this, voids in CDM and CDMo have no significant differences in their shapes. Voids with ellipticities larger than $\varepsilon = 0.6$ were cut from these panels, as these voids are mostly spurious and very few in numbers. When comparing the different halo void catalogs, we notice that dividing the abundances leads to almost constant values in each case, representing the simple shift of the distributions due to different void numbers, while the shapes of their distributions remain the same.

To summarize, most distributions of void properties remain unchanged between `hydro` and `DMo` runs except for changes due to different void numbers, while exclusively baryon voids experience a clear shift towards higher core densities than CDM voids. For a discussion on the general differences in void distributions between matter and halo voids, we refer the reader to section 5.2.

8.2 Void profiles

This section focuses on the effects of baryonic physics on the density and velocity profiles of voids. Once more, profiles are calculated for each individual void out to five times its effective radius in spherical shells of width $0.1 \times r_{\rm v}$, unless mentioned otherwise. Afterwards we stack them in bins of their void radius, as well as other void properties. We analyze both the profiles of matter voids, as well as the ones of halo voids, where in the latter case we distinguish between using halos and different matter tracers for the profile calculation. We examine both halo voids obtained from halos after performing mass cuts and matching halo number densities in `hydro` and `DMo` simulation. Additionally, we compare the distribution of baryons and CDM around halo voids and reinforce our results with a resolution study in the `ultra-hr` simulation. While calculating the profiles of matter around either matter or halo defined voids, we always use subsamplings of much higher tracer numbers (around

50 million) than were used in the void identification (8.21 million), in order to reduce effects from sparse sampling in regions of low density and to more accurately constrain baryonic effects. When investigating stacked velocity profiles of voids in this section, we will always use individual stacks via equation (3.10), as the choice of velocity estimator does not impact our conclusions.

Figures 8.4 to 8.9 depict the void profiles in stacked bins of their void radii in the upper plots and in bins of core density on the bottom, with mean values and void numbers of each bin given in the legends. Even though there is some correlation between the radius of a void and its core density (see figure 5.2), core density bins cover a wider range of different void radii and we find that in this case, stronger effects due to the implemented baryonic physics are present. Stacks in other void properties, namely ellipticity ε and compensation Δ_t, will be depicted exclusively in figures 8.10 to 8.13, as effects between `hydro` and `DMo` simulations, as well as between baryons and CDM of the `hydro` simulation are most severe in radius and core density bins. This is due to ellipticity and compensation bins covering a much wider range in void radii, which we will argue further in section 8.2.4.

8.2.1 Matter voids

Figure 8.4 depicts the matter density profiles of CDM voids on the left, with differences compared to the CDMo voids from the `DMo` simulation in the lower panels of each plot, while the right side depicts profiles of baryon voids, with differences compared to the CDM voids in lower panels, all from the `highres hydro` simulation. In each case, the density increases outward from the void center, with clear compensation walls around $r = r_\mathrm{v}$. The largest voids, as well as the voids with the lowest core densities, have much shallower compensation walls, though a sharp decline in the increase of density clearly marks the void boundaries, with densities close to the mean density $\bar{\rho}$. The correlation between core density and void radius can be seen as well, since the profiles of small voids closely resemble the profiles of voids with high core density, and vice versa.

When comparing CDM voids in both `hydro` and `DMo` simulations on the left of figure 8.4, we see that profiles and void numbers of each bin resemble each other closely. Most dissimilarities are still within the error bars, namely in the bins of largest and smallest voids, where in the former, only a very sparse sample is present. Further differences in voids of medium size, like the bin with $\bar{r}_\mathrm{v} = 11.93$, are only on the order of $|\Delta\rho| \simeq 0.02$ between the simulations. When looking at core density bins, we notice the most substantial differences in bins of highest core density, which are of order $|\Delta\rho| \simeq 0.1$, although with large errors and effects only exist past the compensation wall, outside of voids. Further deviations are present in the subset of voids with smallest $\hat{n}_\mathrm{min}$, though still minor.

More substantial effects are found in the comparison of baryon and CDM voids on the right side of figure 8.4. We observe substantially distinct profiles near the compensation walls of the smallest voids, where CDM voids have higher compensation walls, and near the centers of these small voids, where baryon voids have higher inner densities. The results from figure 8.3 support these conclusions, as we found that baryon voids typically have higher core densities and therefore on average higher densities inside. These findings

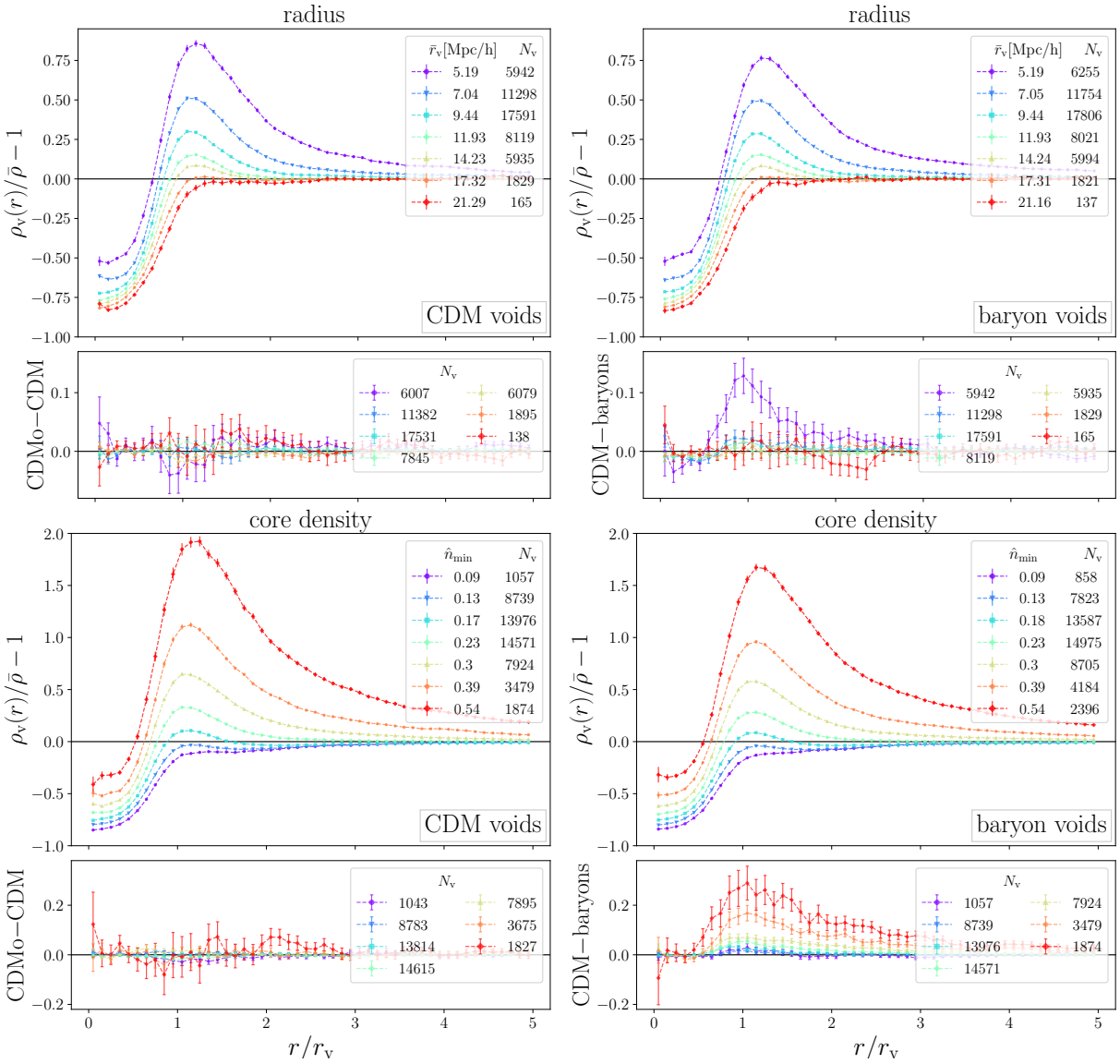

Figure 8.4: Stacked density profiles of matter voids in the `highres` simulations in bins of void radius (top) and core density (bottom). Plots on the left show the profiles of CDM voids with differences compared to CDMo voids in the `DMo` simulations in the lower panels, whilst plots on the right show profiles of baryon voids, with differences between CDM voids and baryon voids in the lower panels, both from the `hydro` run.

from small voids indicate that baryons are distributed more evenly than CDM, supporting previous results [144, 145]. We will investigate this further in sections 8.2.4 and 8.2.5. These deviations quickly decrease for increasing void size and vanish almost completely in the largest voids. When selecting voids by their core densities instead, differences become more obvious, starting at around $r \geq 0.5\, r_v$. Of course, close to void centers no significant variations are expected, as bins in core density automatically limit the range of the

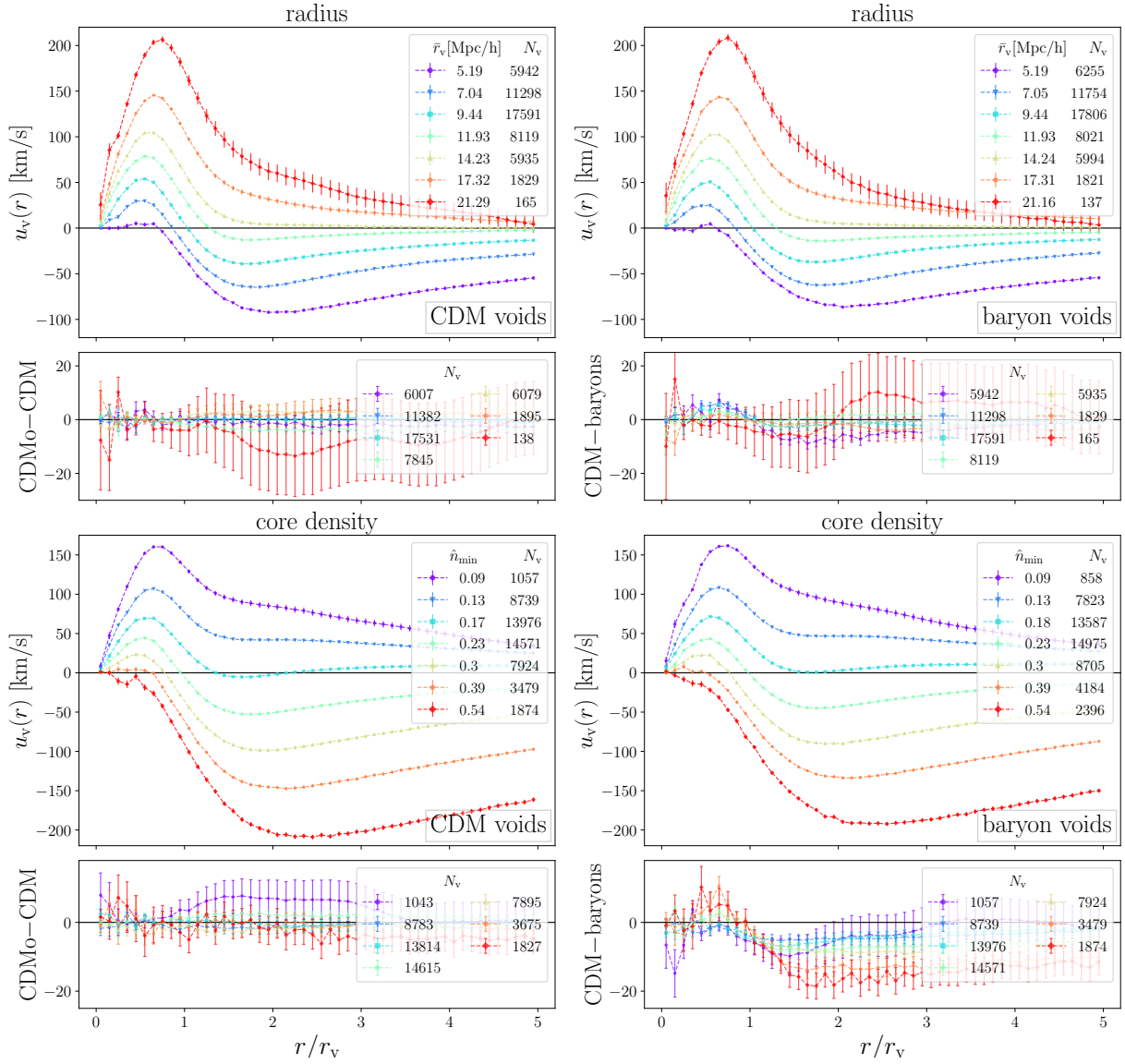

Figure 8.5: Same as figure 8.4, but for the stacked velocity profiles.

innermost densities. Voids of lowest core density have almost identical profiles between baryon and CDM voids, but with increasing core density, the profile variations increase as well, reaching values of up to $|\Delta\rho| \simeq 0.25$ near the compensation wall of the voids with highest $\hat{n}_{\mathrm{min}}$, where again, baryon voids have smaller compensation walls. These smaller compensation walls stretch out over vast distances from the void centers and differences only vanish once the profiles themselves are close to the mean density $\bar{\rho}$.

The velocity profiles, depicted in figure 8.5, showcase that CDM and CDMo voids have almost identical velocity profiles, except for deviations in velocities of order $|\Delta u_v| \simeq 4\,\mathrm{km/s}$ in medium sized voids. Only the bin of largest voids hints at strong deviations in velocities, though even with the increased tracer numbers for profile calculation, error bars are still

large due to the small number of voids present, and the large variation in velocity profiles of individual voids (e.g., figure 7.1). These identical profiles can be expected, since their density profiles are almost identical as well, and in both CDM and CDMo voids, linear mass conservation holds, which ultimately leads to insignificant differences. In stacked bins of core density we observe similar results, only the voids with smallest $\hat{n}_{\mathrm{min}}$, which are typically the ones with largest r_{v}, hint at significant deviations, still with error bars reaching almost $|\Delta u_{\mathrm{v}}| \simeq 0$, though now with more voids present than in the largest r_{v} bin.

In the baryon void profiles of figure 8.5 we notice stronger effects in the core density bins, while the void radius bins behave similarly to the ones of CDM and CDMo voids, except for the smallest voids with $|\Delta u_{\mathrm{v}}|$ on the order of 10 km/s, and for largest voids due to their small number. The former result is as expected, since the smallest voids experience small variations between the density profiles of baryons and CDM. As all types of matter should still obey linear mass conservation (see chapter 7), differences in density profiles would in turn predict small deviations in their velocity profiles, as both have a tracer bias $b_{\mathrm{t}} = 1$. Contrary to the bins in void radius, the core density bins experience more substantial shifts between CDM and baryons at a given value of $\hat{n}_{\mathrm{min}}$. Within these voids, the velocities behave similarly, but once past $r = r_{\mathrm{v}}$, deviations appear in all presented bins. As seen for the density profiles, variation is strongest for voids of highest core density and decrease with decreasing $\hat{n}_{\mathrm{min}}$. These might be physical effects, however it is also likely that they are spurious. Because we are stacking the velocity profiles of voids within a larger void radius distribution when selecting core density bins, and baryon voids have higher core densities, this can lead to differences due to the strong dependence of velocity profiles on the void radius, as there is some correlation between both void properties (see figure 5.2).

In conclusion, both density and velocity profiles of CDM and CDMo voids are quite similar, while mayor differences arise when comparing baryon and CDM voids, where it is evident that the core density determines the deviations in profiles more strongly than their radius though there is a strong correlation between both void properties.

8.2.2 Halo voids

Moving on to results more relevant for observations, we present the number density and velocity profiles of halo voids in figures 8.6 and 8.7, for voids obtained from halo mass cuts (left) and matched halo densities (right) between the `hydro`/`DMo` simulations, once more presented in bins of their radius (top) and core density (bottom). We depict the profiles of halo voids from the `hydro` simulation in the upper panels, while showcasing differences between `DMo` and `hydro` simulations on the lower panels. The binning of void radii is identical to the one used for matter voids of section 8.2.1 in larger bins, but the two bins of smallest matter voids are combined into one bin for halo voids, due to larger halo voids compared to CDM voids and to reduce effects from sparse sampling. Core density bins are entirely identical.

The density profiles in void radius bins in figure 8.6 indicate small deviations near the compensation wall, where small voids from the `hydro` run have higher walls, while the

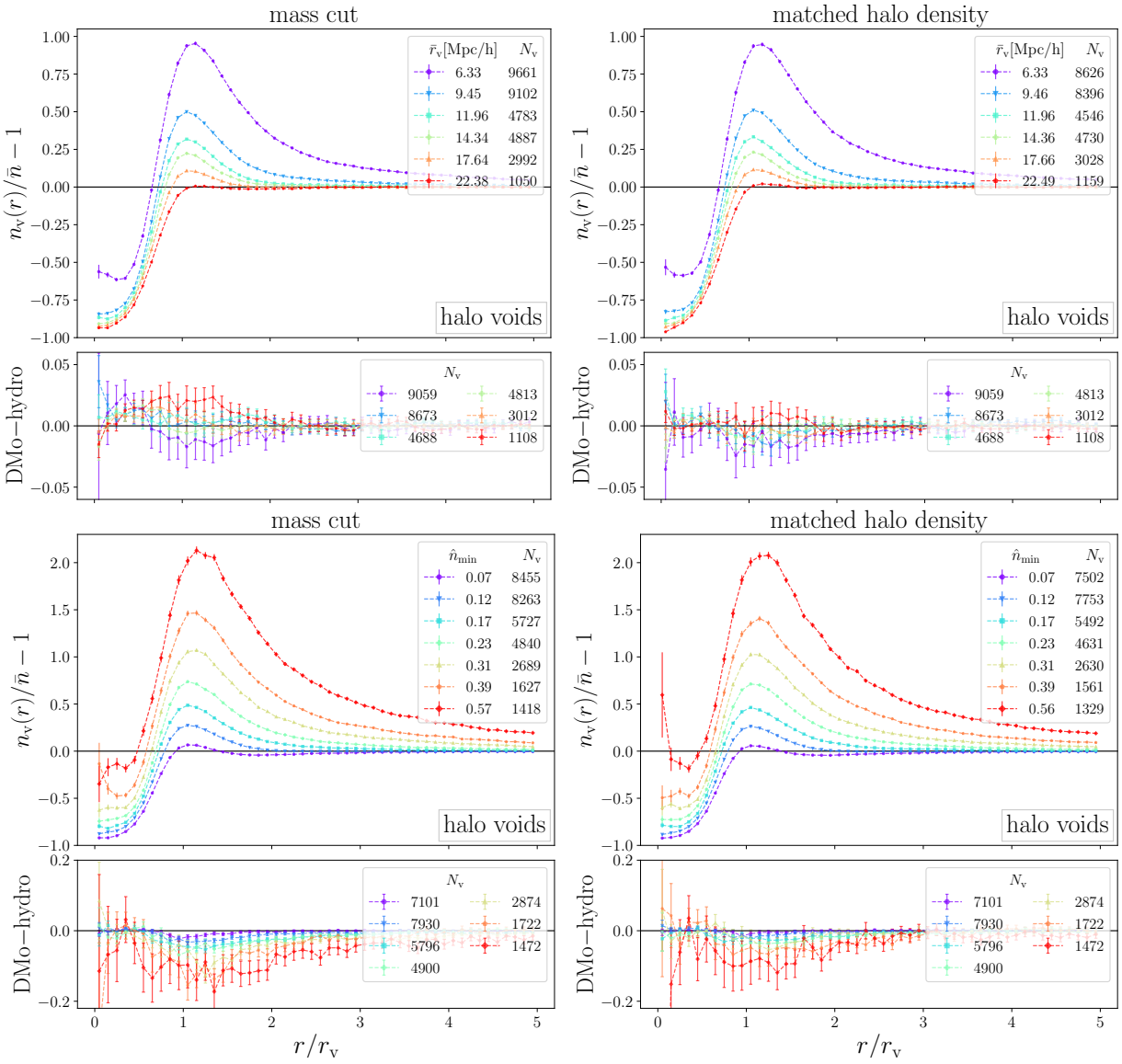

Figure 8.6: Stacked density profiles of halo voids in the `highres` simulations for voids found in tracers with mass cuts (left) and matched halo densities (right) in bins of void radius (top) and core density (bottom). Upper panels depict the profiles in the `hydro` simulation and lower panels the differences between `DMo` and `hydro` simulations.

opposite is true for large voids. However, the most substantial differences are only on the order of $|\Delta n_v| \lesssim 0.025$, and when investigating matched density voids, they decrease even further. We also note that in the largest bin of r_v, the strongest difference between mass cuts and matched density profiles are smaller densities near the void center for matched density voids. This is expected, since matched densities cut the halos of lowest mass, which have a higher probability of residing inside voids than more massive halos (see section 6.2).

Similar to the matter void profiles in section 8.2.1, we see that when stacking halo voids

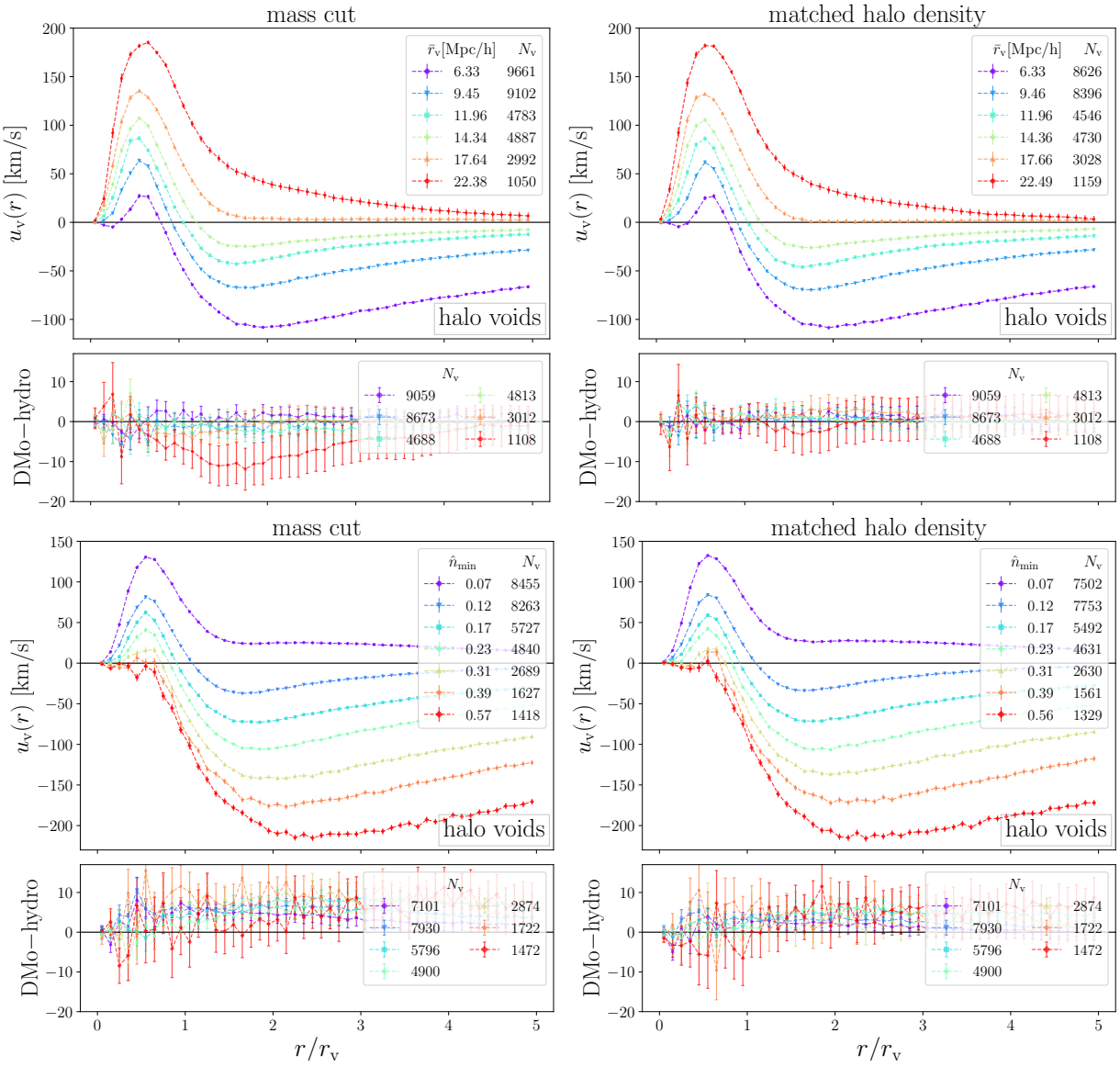

Figure 8.7: Same as figure 8.6, but for velocity profiles.

by their core densities, differences between `hydro` and `DMo` simulations become more significant. Once again, after matching halo densities deviations decrease, though less severe than for stacks in r_v, and halo voids in the `hydro` run have up to $|\Delta n_v| \simeq 0.1$ higher densities near their compensation wall, but their central densities are almost indistinguishable, except for the innermost bin with huge errors due to sparse sampling below the mean tracer separation. Baryonic effects in the halo void density profiles increase with increasing core density, reaffirming our earlier result that a voids' core density is the strongest indication on how relevant baryonic effects are in the profiles, while the void radius is less important, even though both properties are strongly correlated. Of course, binning voids by their

radii is more common in cosmological applications of voids. Therefore, effects in bins of r_v would have to be accounted for when comparing simulations with observations, though in practice, the deviations of $|\Delta n_\mathrm{v}| \lesssim 0.025$ are negligible in radius bins and halo void profiles from `DMo` simulations are still useful for comparisons with observations.

For the velocity profiles in figure 8.7, we note that when binning in void sizes, the largest halo voids of mass cut catalogs seem to have the largest deviations. A similar result was found for the velocity profiles of CDM voids in figure 8.5, where it was ascribed to the small number of voids present in the bin and the variations of individual velocity profiles. In the case of halo voids, a much larger number of voids is present in this bin, so we expect that our results are more solid here, though smaller voids experience changes in velocity only of order $|\Delta u_\mathrm{v}| \lesssim 4\,\mathrm{km/s}$. Matching halo densities reduces these differences again and most error bars are closely centered around zero deviations between the simulations. In contrast, when comparing the profiles from mass cuts and matched densities in core density bins, almost all bins experience slight changes on the order of 10 km/s, though error bars are comparable to the deviations. This leads us to the conclusion that small deviations in velocity profiles might be present, though not very significant, especially when investigating halo voids at fixed density and using velocity profiles in bins of their radii.

At even higher mass cuts for void identification, namely $M_\mathrm{h} \geq 10^{12}\,M_\odot/h$ as in `midres`, we do not find significant effects in the profiles of halo voids, though statistics are more sparse in the `highres` simulation. Especially for state-of-the-art galaxy surveys, such as the Euclid mission [135], we do not see a need in accounting for baryonic effects of halo voids, as the `midres` simulations are the closest match in expected tracer densities, and we find no significant effects at this resolution, or even the identical mass cut in `highres`.

8.2.3 CDM profiles around halo voids

In order to estimate the impact of baryons on weak lensing studies around halo defined voids in both `hydro` and `DMo`, we investigate the density and velocity profiles of CDM around halo voids in figures 8.8 and 8.9. As for CDM voids, we use subsamplings of higher CDM densities to calculate profiles, in order to reduce sampling effects. Comparing these profiles with the ones of halos around halo voids in figures 8.6 and 8.7, we find higher CDM densities within halo voids and slightly smaller compensation walls compared to the halo number density profiles. This is most noticeable in the bin of smallest r_v and due to the halo bias [44, 103].

However, the deviations between `hydro` and `DMo` runs are strikingly similar to the ones on the top of figure 8.6 and once more, vanish almost completely in matched halo densities. In core density bins, we find conforming results. The density profiles themselves experience reduced compensation walls, as well as higher inner densities, while differences between both simulations match the ones of halo profiles and remain significant in matched densities on the bottom right.

When investigating velocity profiles of CDM around halo voids in figure 8.9, we notice almost identical velocities to the ones of halos in figure 8.7, except for higher velocities in the innermost regions of voids. This is most likely not a genuine deviation between halo

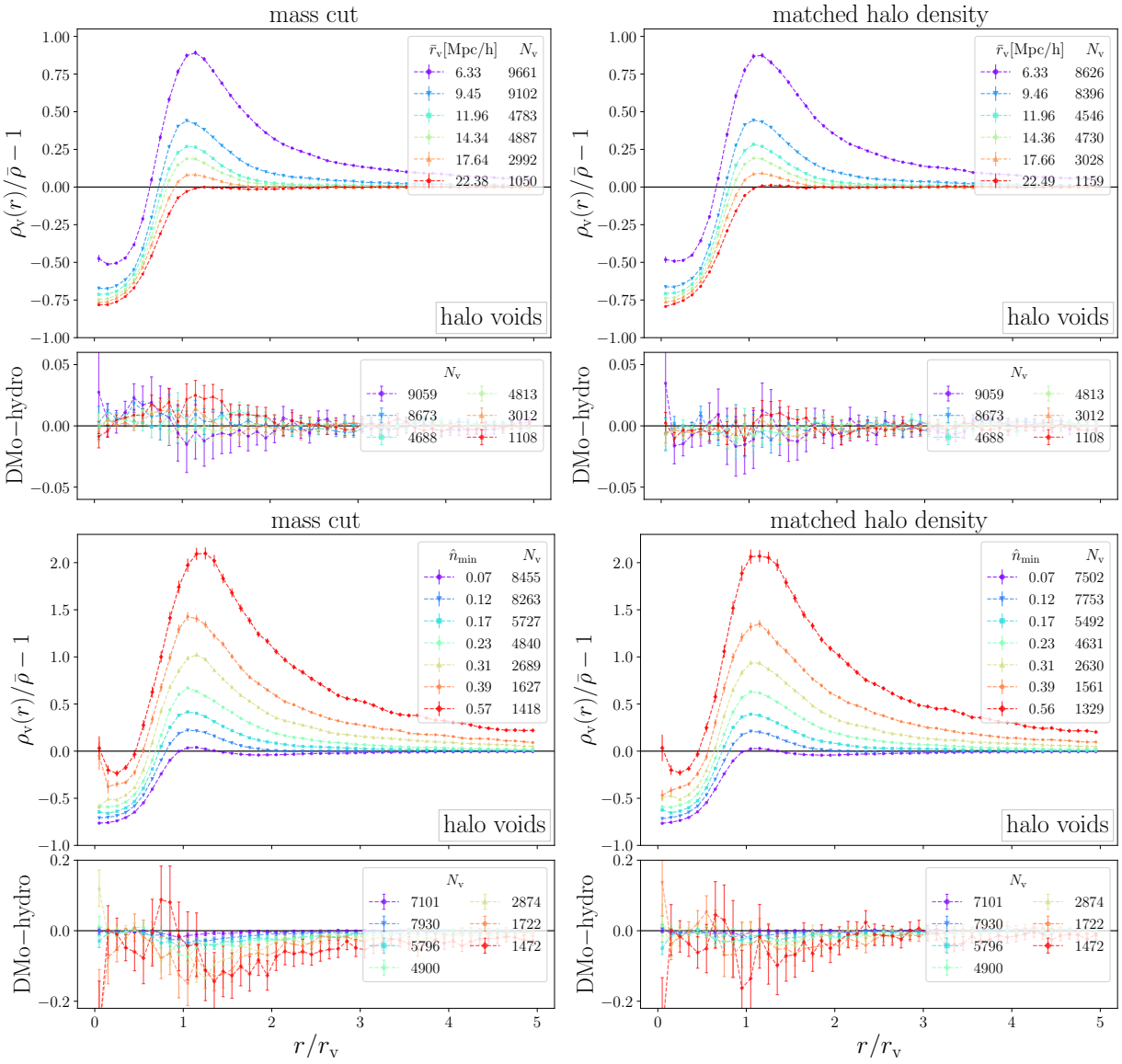

Figure 8.8: Stacked CDM density profiles around halo voids in the `highres` simulations for voids found in tracers with mass cuts (left) and matched halo densities (right) in bins of void radius (top) and core density (bottom). Upper panels depict the distribution of CDM around halo voids in the `hydro` simulation and lower panels the differences for voids between `DMo` and `hydro` simulations.

and CDM velocities, but a result from the higher sampling rate for CDM. As discussed in length in section 6.3, individually stacked velocity profiles are biased towards small voids, of which most have very small velocities due to sparse sampling in their centers, which is true for the halo velocities of figure 8.7. Now due to the higher sampling, less profiles have velocities close to zero inside voids and we get a glimpse at the 'true' velocities in these regions. These velocities behave much more linear, as expected from linear mass

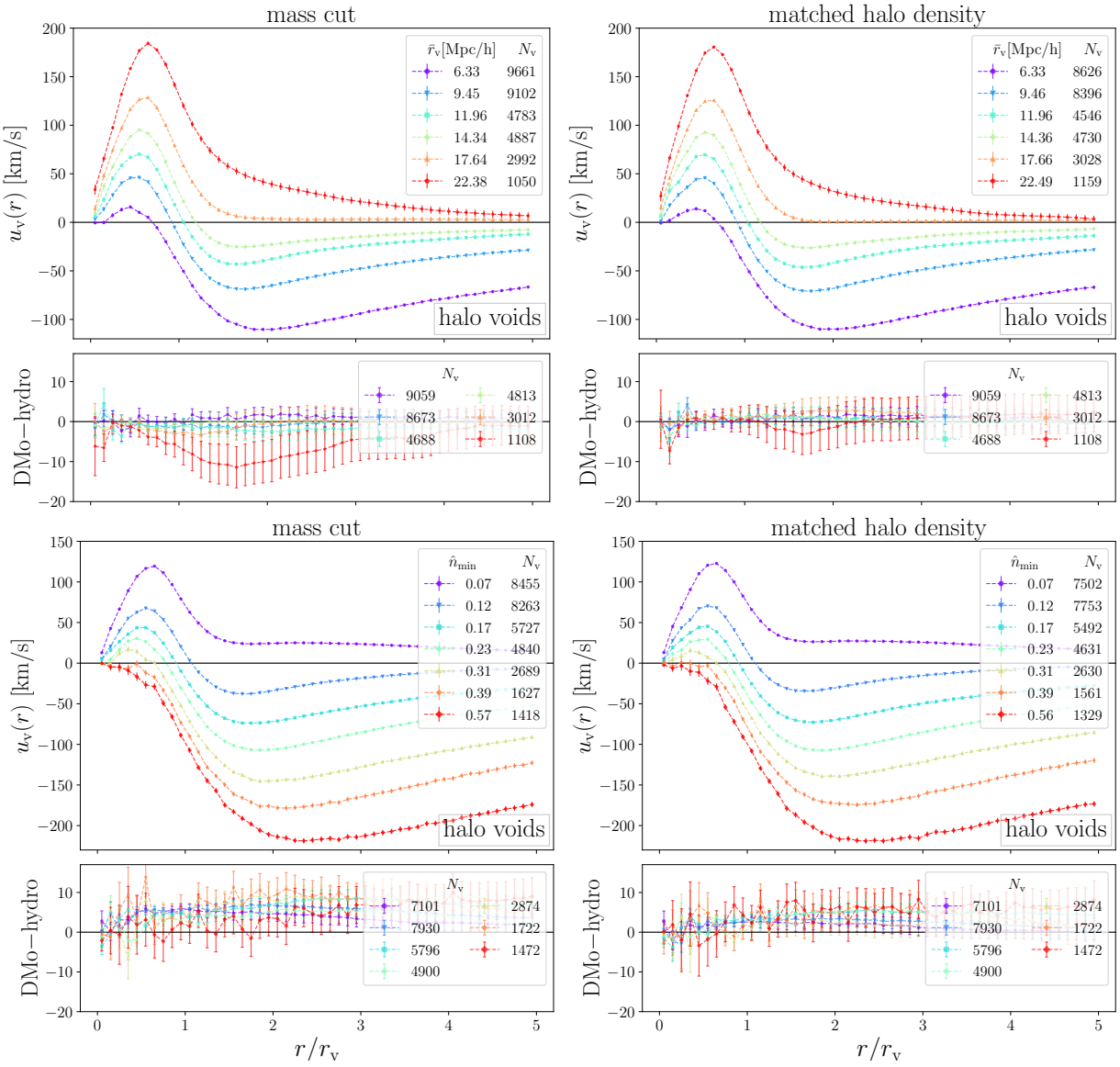

Figure 8.9: Same as figure 8.8, but for velocity profiles.

conservation. As for the density profiles in figure 8.8, differences between the `hydro` and `DMo` simulations are strikingly similar to the halo velocity differences, both in stacks of r_v and the core densities. Therefore, baryonic effects seem to impact the velocities of the largest voids after mass cuts, but no substantial effects are present at matched halo density voids, except of order $|\Delta u_v| \lesssim 6\,\mathrm{km/s}$ in core density bins.

8.2.4 Baryons and CDM around halo voids

For the last test of baryonic effects in `highres` we want to investigate how CDM (dashed), as well as baryons (dotted) are distributed and move around halo defined voids in fig-

ures 8.10 to 8.13. For this we use halo voids obtained from mass cuts in the `hydro` run. Matched halo densities are not relevant here, since there is no one-to-one correspondence between individual voids from the `hydro` and `DMo` simulations, as discussed with figure 8.2. Furthermore, as we found no relevant baryonic effects in the `midres` simulations, where halos with mass $M_\mathrm{h} \geq 10^{12} M_\odot/h$ have been selected for the void finding, we test this particular mass cut in the `highres` simulation, along with the previously used $10^{11} M_\odot/h$ mass cut. This allows us to test whether baryonic effects are only relevant in voids identified in lower mass halos, or if the absence of baryonic effects in voids of `midres` is due to the lower resolution.

In addition to the previous stacks in void radius (always top left) and core density (bottom right), we present stacked bins in ellipticity ε (top right), and compensation Δ_t (bottom left). Using these two new void properties for the stacks, we will argue why the core density is the strongest discriminator of baryonic effects. In all cases, we use subsamplings of higher N_t in CDM and baryons to reduce sampling effects in the calculation of profiles. Contrary to prior analysis, we now compute baryon and CDM differences around individual voids and stack these 'individual differences', presented in the lower panels. They are of equal magnitude as when simply subtracting the stacked profiles, however, if baryonic effects are relevant even for (most) individual voids, error bars in the differences can be reduced.

The matter densities of both CDM and baryons are presented in figures 8.10 and 8.11 for voids identified in halos of mass $M_\mathrm{h} \geq 10^{11} M_\odot/h$ and $10^{12} M_\odot/h$, respectively. Contrary to previous results of this work and from analyzing `midres` simulations, we find deviations from zero outside of the error bars in the CDM and baryon densities for voids of all size, as well as identified in both mass cuts, although the magnitude of differences is highly scale-dependent. Baryons are typically distributed more evenly, with higher densities compared to CDM inside voids and smaller heights of the compensation wall [144, 145]. This can be expected, as voids identified in the distributions of baryons tend to have higher core densities than their CDM counterparts, as discussed in figure 8.3. For larger voids, these effects decrease to the order of an almost constant offset $|\Delta\rho| \simeq 0.01$ in both mass cuts in regions inside voids, starting in the bin of $\bar{r}_\mathrm{v} = 14.34\,\mathrm{Mpc}/h$. While small, these findings show that in order to identify baryonic effects in voids through simulations, a high enough resolution is necessary and the particle masses in `midres` (table 4.1) are simply not small enough for baryonic effects to be of any relevance. In section 8.2.5 we investigate this in more detail at even higher resolution. At first glance, it may seem like the amplitude of profiles in void radius bins is simply modulated for baryons. However, tests showed that a multiplicative amplitude on the depicted profiles of baryons, including an optional offset, does not reproduce the profiles of CDM accurately.

We find that in bins of ellipticity, the offset between CDM and baryon densities is almost identical in all ε bins, both inside and outside of voids. This is due to ellipticity depending only slightly on the size of voids (see figure 5.2), and thus, effects from small and more numerous voids dominate the stacks. This is true in both halo mass cuts. Nevertheless, for the lower mass cut, effects are more significant compared to the higher one. Due to this minimal scale dependence of void ellipticity, these bins only hint at the average deviation

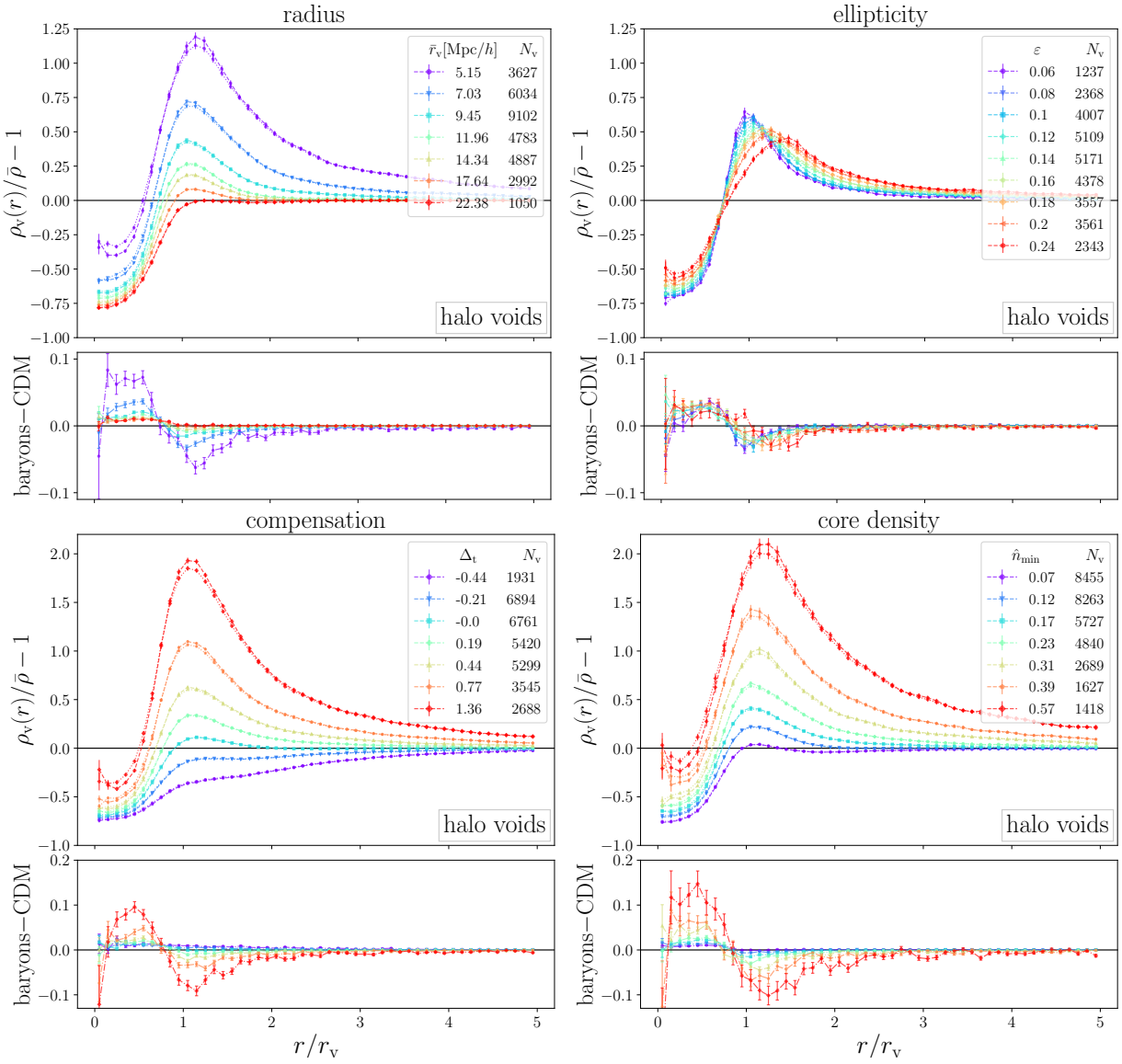

Figure 8.10: Stacked matter density profiles around halo voids identified at 'standard' mass cut ($M_h \geq 10^{11} M_\odot/h$) in the `highres hydro` simulation in bins of radius (top left), ellipticity (top right), core density (bottom left), and compensation (bottom right). Upper panels depict stacked CDM (dashed) and baryon (dotted) density profiles, while lower panels depict stacks of differences between baryons and CDM around individual voids.

at a given resolution in halo mass and are not well suited to describe scale dependent effects.

In contrast, binning voids by their compensation (bottom left) results in strikingly similar deviations to the core density bins. Undercompensated voids tend to experience the smallest differences in baryon and CDM densities, which continuously increase with increasing compensation. This is expected, as the compensation is a measure of the envir-

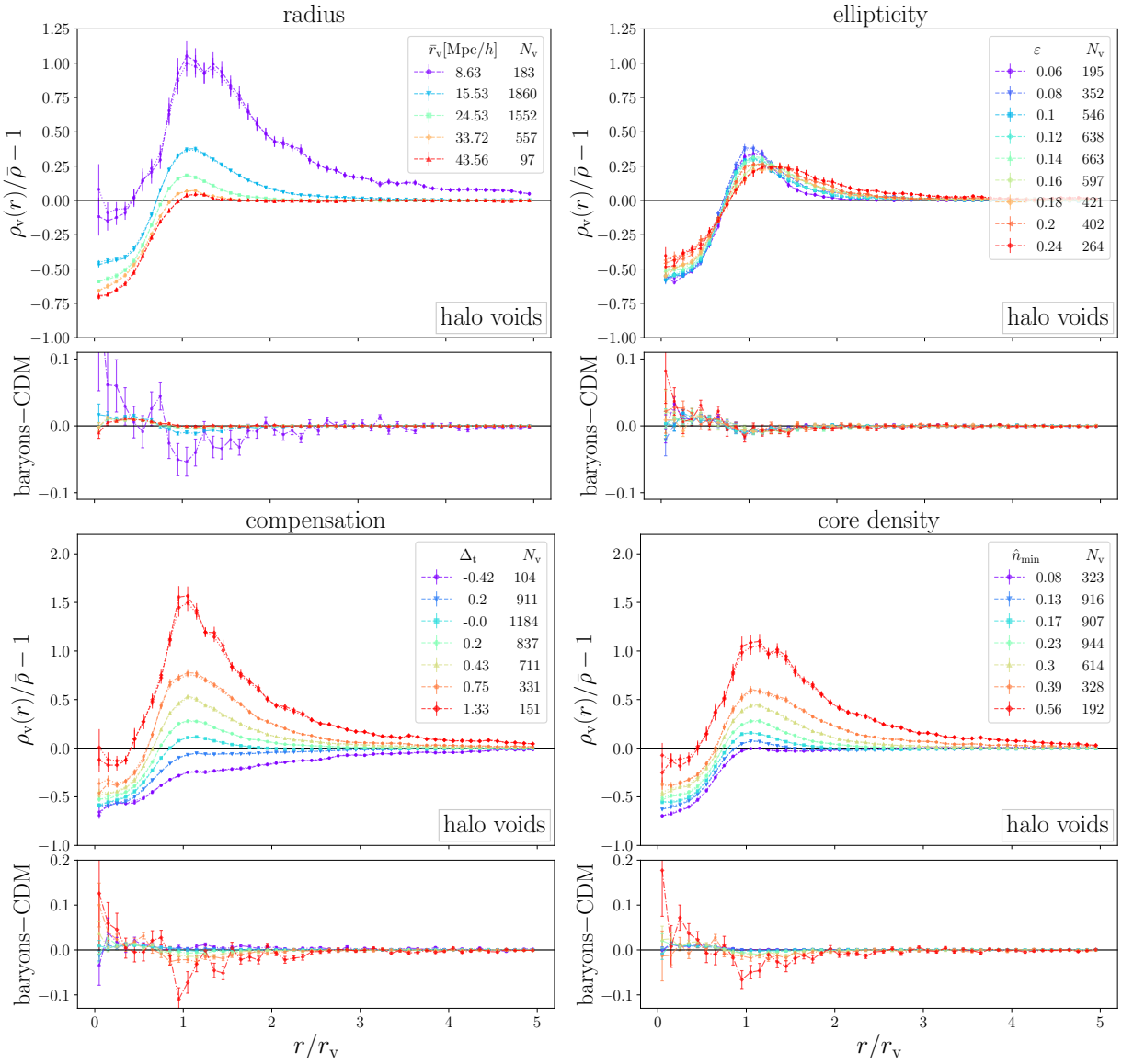

Figure 8.11: Same as figure 8.10, but for halo voids identified at mass cut $M_h \geq 10^{12} M_\odot/h$.

onment a void is located in, of which the inner void regions are part as well. This leads to the correlation between overcompensated voids and voids with high core densities, as overcompensated voids are located in environments of high local density, where naturally most depressions in the density field are also at a higher level (equivalent to 'mountain lakes' in watershed terms). The correlation for undercompensated voids is more complicated, as many voids can have a low density centre while experiencing higher densities near their walls and fewer voids have low density centres with only slowly increasing densities towards their wall, while still being below the mean. Due to this correlation, the profiles of voids with $\Delta_t > 0$ look strikingly similar to the ones of $\hat{n}_{min} > 0.25$, while profiles of

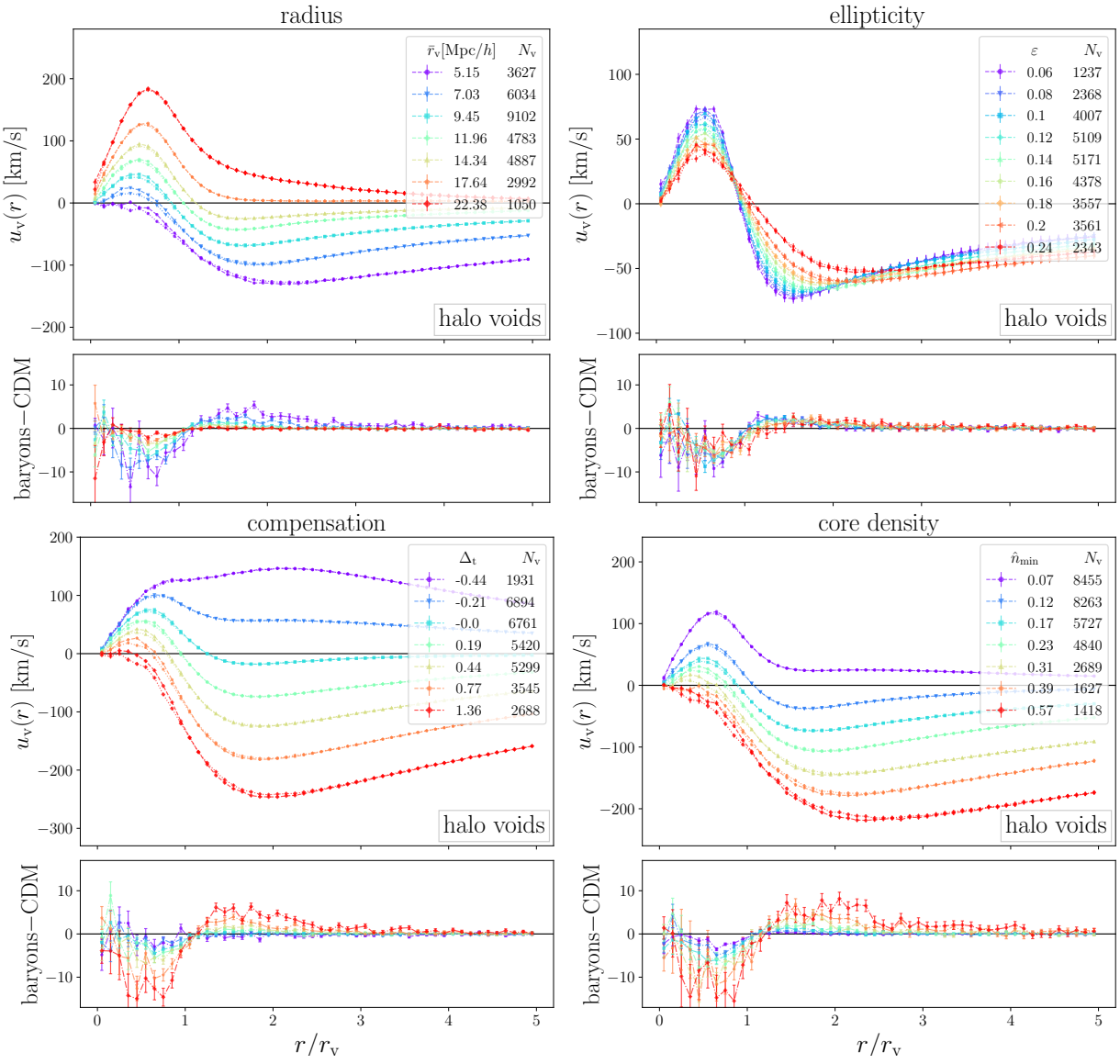

Figure 8.12: Same as figure 8.10, but for velocity profiles ($M_h \geq 10^{11} M_\odot/h$).

undercompensated voids differ significantly outside the void centre, compared to low core density voids, and have profiles unlike any bin in other presented void properties.

As seen before, bins in core density showcase the most substantial effects, now amongst all presented void property bins, instead of just the r_v bins. A bin in even higher $\hat{n}_{min}$ values would have still been possible, yet we refrain from presenting this, as the number of voids with higher $\hat{n}_{min}$ is only on the order of 230 and the presented inner densities are already quite high. Nevertheless, this bin experiences differences inside voids on the order of $|\Delta\rho| \simeq 0.5$, though at densities around $2\bar{\rho}$.

The significant deviations in $\hat{n}_{min}$ bins reinforce our conclusion that baryonic effects

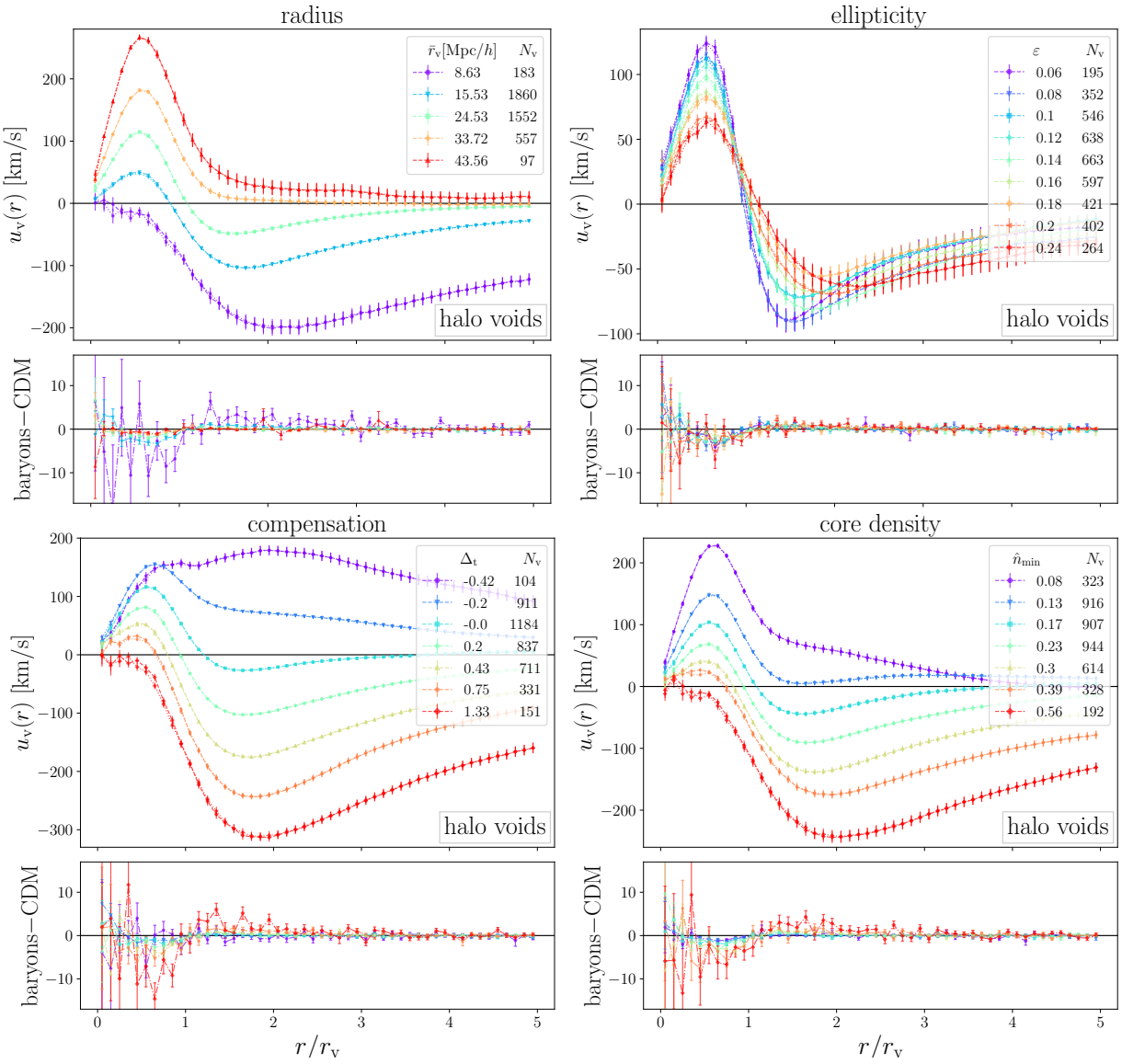

Figure 8.13: Same as figure 8.12, but for halo voids identified at mass cut $M_h \geq 10^{12} M_\odot/h$.

most strongly depend on a voids' core density, while still appearing scale-dependent. One reason is the strong correlation between r_v and $\hat{n}_{min}$. Further tests of binning voids in r_v with a selection on either voids of low core density or high $\hat{n}_{min}$ confirm this. Small voids of low $\hat{n}_{min}$ have almost no effects except for the constant offset, while in small voids of high $\hat{n}_{min}$ the effects increase substantially. However, we observe that in the higher mass cut in figure 8.11, where the void sample is of larger size, differences in identical bins of $\hat{n}_{min}$ are significantly smaller than in figure 8.10, despite that the same matter tracers were used for calculations. In addition, restricting the voids in core density bins at $10^{11}\, M_\odot/h$ mass cut to only voids of sizes used for the r_v bins in figure 8.10 reduces

the effects, yet they are still larger than in the bin of smallest r_v. This suggests a more complex interplay between a voids' size and its inner density that ultimately determines the strength of baryonic effects. Furthermore, as clear differences remain even in the higher mass cut originally used in `midres`, this once more affirms the strong resolution dependence of baryonic effects.

Even though the magnitude of differences is on the order of deviations in other void profiles from previous figures, errors are noticeably smaller, which can be seen in r_v bins as well. As differences were calculated around individual voids and then stacked, this indicates that baryonic physics fundamentally affects the profiles of individual voids and causes effects not merely arising in the statistics averaged over many voids, which will be explored in section 8.2.5 through profiles of individual voids.

The velocity profiles in figures 8.12 (mass cut $10^{11}\,M_\odot/h$) and 8.13 ($10^{12}\,M_\odot/h$) mirror and support these results. At void identification with the $10^{11}\,M_\odot/h$ mass cut, differences are larger than $|\Delta u_\mathrm{v}| > 0\,\mathrm{km/s}$ in the inner regions of voids and outside near the compensation wall in every bin of all presented void property stacks, with a sign-change in differences slightly outside $r = r_\mathrm{v}$. At most, these deviations in velocities are on the order of $|\Delta u_\mathrm{v}| \simeq 12\,\mathrm{km/s}$ for all stacks. This suggests that, while velocity profiles in stacks of different void properties can differ significantly in shape and order of magnitude, baryons and CDM always move with almost matching velocities around individual voids, while small deviations persist.

Furthermore, velocity profiles in bins of r_v intuitively support the differences in corresponding density profiles, clearest for the smallest voids. Baryon velocities are more negative inside these voids than for CDM, i.e. baryons have a stronger trend to stream towards void centers due to being pushed out of the compensation walls in higher density regions due to pressure and shocks, which results in higher densities inside voids. Past the compensation walls, baryons have smaller inflowing velocities than CDM, i.e. CDM is mostly attracted to the compensation wall around small voids, while baryons are either decelerated when moving inwards or are still pushed outwards, which counters the inward velocities of some particles, resulting in smaller net velocities, as well as higher CDM densities in compensation walls.

Stacks in ellipticity once more showcase the averaging of baryonic effects over different void sizes, with a decrease in $|\Delta u_\mathrm{v}|$ in the $10^{12}\,M_\odot/h$ mass cut in figure 8.13, while absolute velocities are higher in this mass cut due to the increase in average void size.

For the compensation and core density stacks, undercompensated voids, as well as voids with lowest density centers experience only slight deviations between CDM and baryon velocities, which increase both with increasing compensation and core density. This follows naturally, as overcompensated voids and ones with high core density are correlated (see figure 5.2), and are both located in environments of higher density, which leads to a more complicated interplay of matter than in regions of lower density. This in turn can lead to stronger baryonic effects due to more frequent interactions compared to CDM.

8.2.5 Resolution study

The previous sections revealed the magnitude of baryonic effects in voids and the complex interplay of a void's size and core density to determine the strength of these effects, most noticeably in differences between CDM and baryon distributions around halo defined voids in the `highres hydro` simulation. These effects are dependent on the resolution of a given simulation, since effects at a halo mass cut of $10^{12}\,M_\odot/h$ were found in `highres`, but not `midres`. We investigate this further in a resolution study, by making use of the `ultra-hr` simulation. Only 281 voids can be identified in halos above a mass of $1.6 \times 10^9\,M_\odot/h$ for the `hydro` simulation, as well as 348 and 278 halo voids in the `DMo` simulation at mass cuts and matched halo densities, respectively. No deviations between the halo void profiles are present between `hydro` and `DMo` simulations in both mass cuts and matched densities due to extremely sparse statistics, hence we refrain from presenting these cases.

Instead, we focus once more on the distribution of CDM and baryons around halo voids and compare results from `ultra-hr` (right, with $M_\mathrm{h} \geq 1.6 \times 10^9\,M_\odot/h$) with the ones from `highres` (left, with $M_\mathrm{h} \geq 10^{11}\,M_\odot/h$) in figure 8.14, now with an additional bin in r_v of even smaller voids than presented in figure 8.10, while voids with $r_\mathrm{v} > 16\,\mathrm{Mpc}/h$ were left out to increase visibility. Due to the limited number of voids in `ultra-hr`, we use subsamples of around 60 million tracers of each matter species ($\sim 31\%$ of all tracers in the simulation) for the calculations, to increase the significance of results with extremely high sampling. Furthermore, to test the scale dependence of these effects, we choose to present the density (top) and velocity (bottom) profiles in comoving scales up to $18\,\mathrm{Mpc}/h$ from the void center instead of in units of r_v. For this, we calculated profiles further outward than $5\,r_\mathrm{v}$, still stacked voids in units of r_v and multiplied the x-axis values with the mean radius $\bar{r}_\mathrm{v}$ of each stack.

The additional smaller voids in `highres` on the left have radii on the order of the mean tracer separation of halos. On average their CDM, as well as baryon densities do not go below the mean. Typically these voids would be considered spurious, but nonetheless a clear underdensity can be seen compared to the higher compensation wall, defining them as local voids in a high density environment, with only slight effects from sparse sampling near the center due to higher CDM and baryon numbers. These small voids feature even stronger differences between the matter distributions, on the order of $|\Delta\rho| \simeq 0.2$. These represent even larger deviations than in core density bins, but as previously mentioned, restricting core density bins to voids of sizes presented in figure 8.10 revealed larger differences than in void radius bins, once more hinting at an interplay of size and core density for baryonic effects. The same is true for the smallest voids presented in `ultra-hr`, which experience the largest changes between CDM and baryon distributions, with $|\Delta\rho|$ around 0.5, almost identical to $\hat{n}_\mathrm{min}$ bins (not presented). Given the CDM density of $0.5\,\bar{\rho}$, this essentially means that within these voids of radii $1-2\,\mathrm{Mpc}/h$ there are around twice as many baryons as CDM particles, although in terms of mass, voids still contain significantly more CDM. In voids of larger size $|\Delta\rho|$ quickly reduces and becomes the same order as in the `highres` simulations. In higher halo mass cuts for void identification in `ultra-hr`, namely $10^{10}\,M_\odot/h$ and $10^{11}\,M_\odot/h$, we identify even fewer and therefore larger voids, in

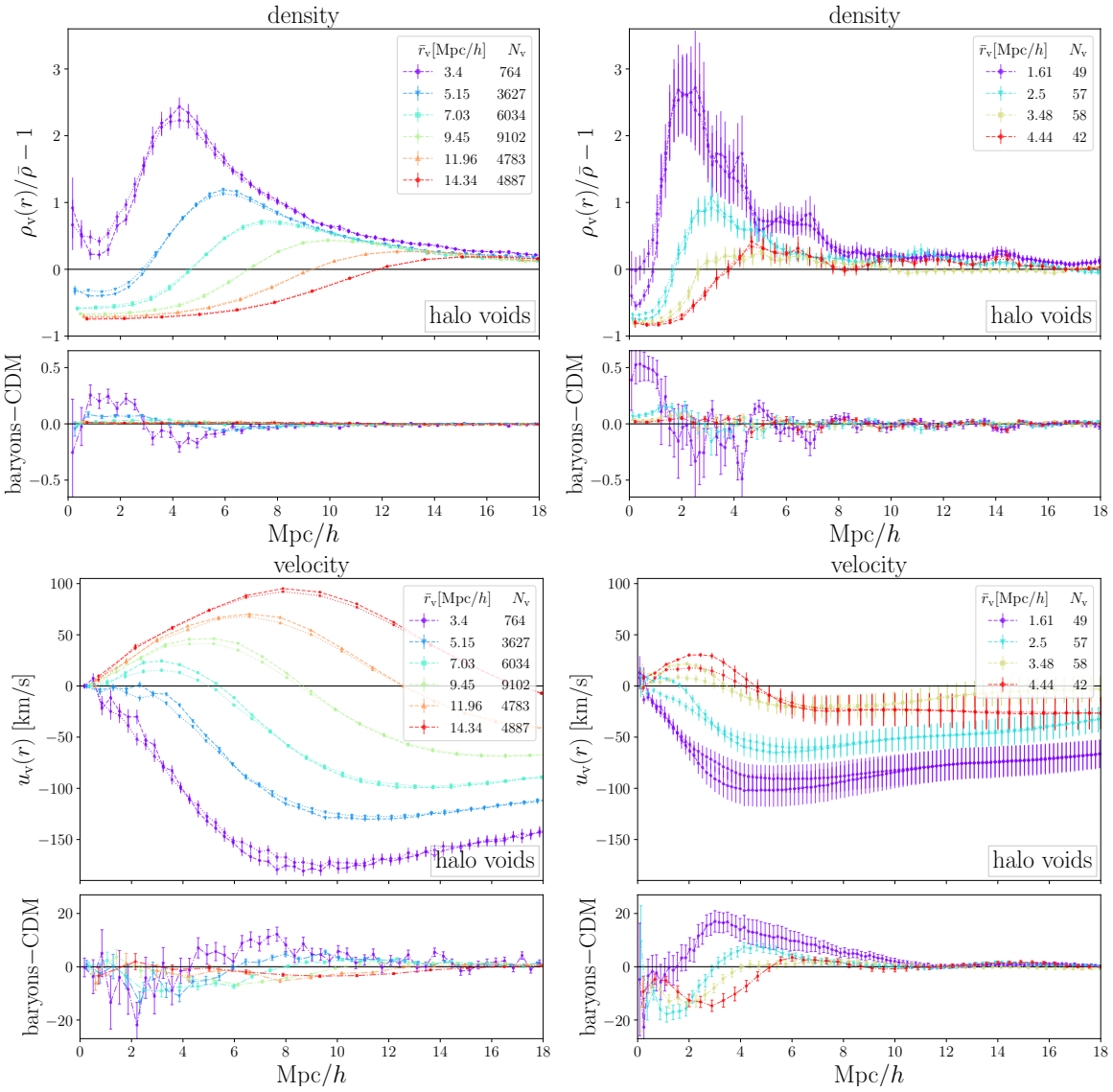

Figure 8.14: Stacked density (top) and velocity (bottom) profiles of baryons (dotted) and CDM (dashed) around halo voids in the `highres` (left) and `ultra-hr` (right) simulation in bins of void radius, with the profiles plotted in comoving scale on the x-axis to showcase scale dependent effects. The `highres` profiles contain an additional smaller bin in r_v compared to figure 8.10 for better comparison with the `ultra-hr` profiles, whilst bins of large r_v have been left out.

which deviations in the baryon and CDM distributions are again at most on the order of results from the `highres` simulation. This indicates an upper limit on the differences in matter distributions, irrespective of resolution.

A prominent feature seen when presenting voids in comoving scales is that the outer tails of their compensation walls align almost perfectly and go towards the mean density

at similar distances from void centers, except for smallest voids, which typically reside in higher density environments. Moreover, in `highres` the differences between CDM and baryons in the compensation walls start aligning at distances of around $7\,\mathrm{Mpc}/h$ from void centers, if voids are of small enough size, and vanish at around $12\,\mathrm{Mpc}/h$. On smaller scales they differ substantially, especially inside voids. For `ultra-hr` this shifts towards even smaller scales. Some small deviations outside errors still appear on larger scales, however due to the small number of voids, we do not place too much importance onto these deviations.

The velocity profiles in the lower panels of figure 8.14 confirm previous results from figures 8.12 and 8.13. Around the smallest voids in `highres` (left), matter tracers experience even more substantial differences in their velocities, mostly on the order of $|\Delta u_\mathrm{v}| \simeq 15\,\mathrm{km/s}$, except for scatter. In comoving scales we see that deviations in velocity vanish almost completely at similar scales as differences in density, albeit slightly farther outside, at around $15\,\mathrm{Mpc}/h$ instead. In `ultra-hr` (right), these scales once more shift towards smaller values and differences increase to at most $|\Delta u_\mathrm{v}| \simeq 18\,\mathrm{km/s}$. While the stacked profiles significantly overlap within their error bars due to sparse statistics, most clearly seen in the smallest voids, differences between CDM and baryon velocities persist. This once more confirms that these discrepancies are relevant even for individual voids. Furthermore, all stacked bins in figure 8.14 experience an infall of matter towards the compensation wall from outside, albeit due to comoving scales, this is only barely noticeable for the largest presented voids of `highres`.

Before concluding, we want to take a last look at the structure, as well as dynamics of CDM (dashed) and baryons (dotted) around four individual halo voids of `ultra-hr` in figure 8.15, once more as functions of r/r_v. Here profiles are calculated in 100 shells per r_v instead of the previous 10, to investigate differences at tiny scales. This corresponds to a physical shell width of $47.9\,\mathrm{kpc}/h$, or correspondingly 2.22×10^5 light years ($h = 0.704$), for the largest void depicted with $r_\mathrm{v} = 4.79\,\mathrm{Mpc}/h$. Hence, shells have a width only around twice the size of our own milky way galaxy. These four voids are an almost random draw from the catalog, only with the condition of significantly different shapes in density and velocity profiles at similar radii.

All four density profiles in the upper plot of figure 8.15 exhibit a clear peak in density near $r = r_\mathrm{v}$ and around most voids, the density fluctuates around the mean further out. In contrast, the smallest depicted void (in red) is clearly undercompensated and only near the void boundary does the density reach values slightly above the mean, whilst being embedded in an underdense environment on larger scales.

Comparing CDM and baryon distributions, we note that peaks in the densities are always higher in CDM and baryons are spread out over the surrounding volume, with smaller peaks in the density field at identical locations to CDM. This is not only true for overdensities above the mean, but instead any local overdensity and local underdensity exhibits these effects. In global overdensities, e.g. in the two voids with the highest compensation walls, we see that in regions outside of these voids there are many local peaks in the CDM densities. In between those peaks, CDM densities almost never go below the mean, whereas baryons exhibit smaller peaks and higher densities compared to

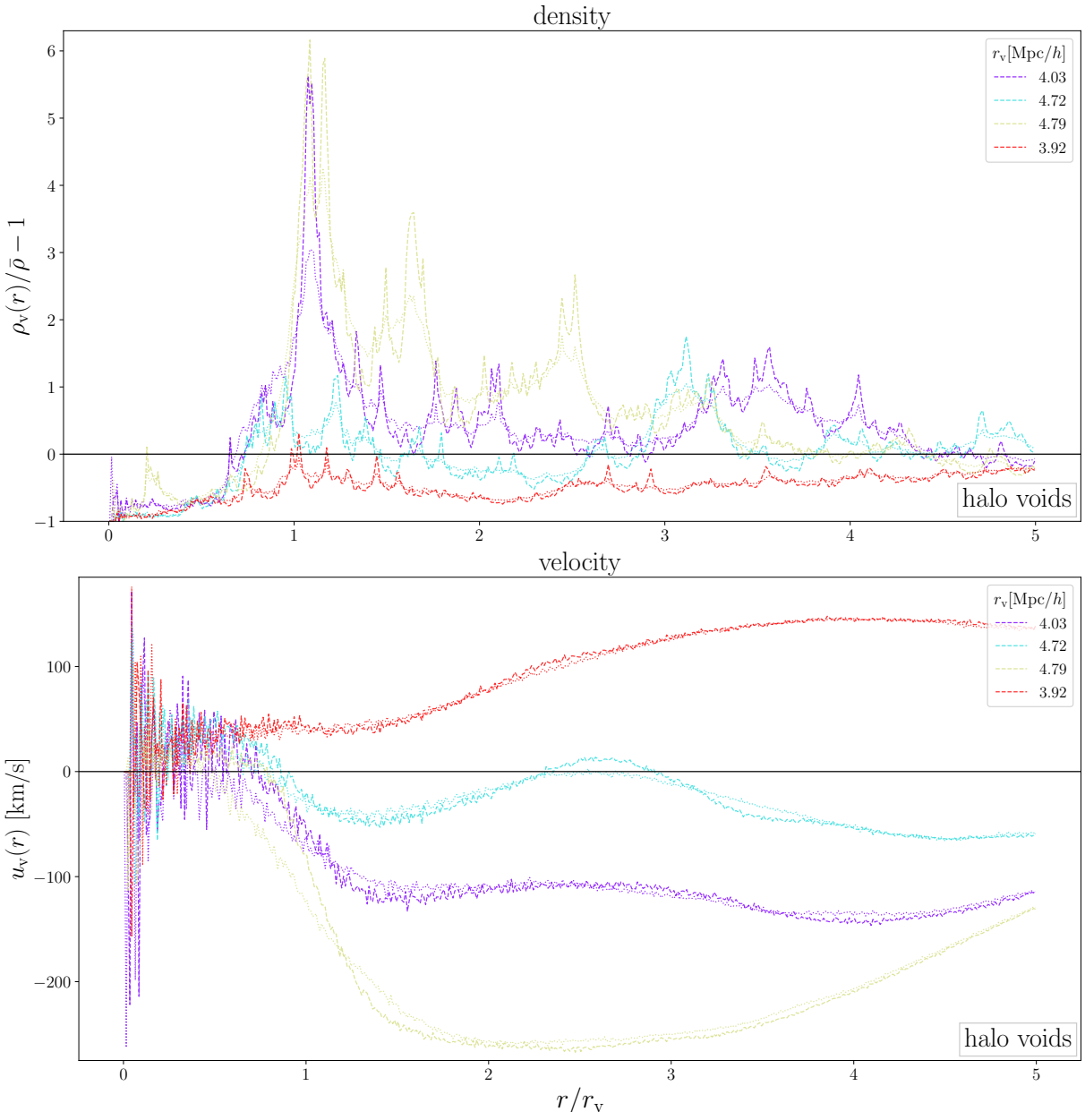

Figure 8.15: Density (top) and velocity (bottom) profiles of baryons (dotted) and CDM (dashed) around individual halo voids identified in halos with a mass cut of $1.6 \times 10^9 M_\odot/h$ in the `ultra-hr` simulation. Profiles are calculated in 100 shells per r_v, corresponding to a physical shell width of $47.9\,\mathrm{kpc}/h$ for the largest void depicted.

CDM in between. Similarly, in global underdensities, e.g. in the profile of the smallest void, we still see peaks in the density field with higher CDM densities, while more baryons are distributed around local minima. This is identical to the effects in stacked profiles, where local underdensities (voids) contained more baryons and CDM clustered more heavily in

local overdensities, i.e. the compensation walls. The undercompensated void exhibits the smallest differences compared to the others depicted, further showcasing the environmental dependence of baryonic effects.

These density profiles clearly show that baryonic physics has a direct impact on individual voids and does not merely cause effects arising in the statistics of many voids, as already indicated by smaller errors in stacks of differences around individual voids. CDM is always more clustered, as it has no self-interaction, while baryons are spread out more evenly, caused by the impact of other forces than gravity. We interpret this as AGN feedback and other implementations of baryonic physics pushing baryonic matter to the outskirts of clustered regions, i.e. baryonic physics leads to some of the matter being ejected from galaxies and halos into the surrounding regions, whereas CDM is only indirectly affected by this through the gravitational force from baryons. This on average leads to the lower compensation walls in baryons and higher densities inside voids. An observational example of baryonic physics affecting the distributions between baryons and CDM can be found in the 'Bullet cluster' (1E 0657-56) [e.g., 146, 147].

The individual velocity profiles of these four voids in the bottom plot of figure 8.15 exhibit a large scatter in velocities up to around $r = 0.5\,r_\mathrm{v}$ and become much smoother further outward. This is solely an effect from the tiny shells. In the previously used $0.1\,r_\mathrm{v}$ wide shells, scatter is significantly reduced and these particular voids have inner velocities of matter on the order of $15 - 40\,\mathrm{km/s}$. The velocity deviations between different matter species happen on much larger scales compared to density fluctuations and are typically higher when closer to the compensation walls, as already seen in the stacks in figure 8.14. In addition, the general shape and magnitude of deviations looks strikingly similar to the ones of stacks.

The void with the most negative velocities exhibits a higher infalling velocity of baryons inside the void and up to around $r = 1.2\,r_\mathrm{v}$, where CDM and baryons move at the same speed in a small region. Further outward, baryons on average move with slightly smaller net velocities towards the compensation wall. This once more depicts the effects where some of the baryonic matter is accelerated to the outside regions of the compensation wall or decelerated in their infall due to interactions, while CDM is only accelerated towards the compensation wall. The most undercompensated void (in red) has a matching velocity profile, as matter tends to stream outwards of underdense environments. Furthermore, it exhibits almost perfectly matching baryon and CDM velocities with only slight deviations, due to the dependence on the environment. Another feature only present in these small shells is that while the shapes of the velocity profiles look smooth on large scales, e.g. in $0.1\,r_\mathrm{v}$ shells, on small scales CDM exhibits a stronger scatter in velocities and moves much more 'chaotic' than baryons, as interactions through other forces smooth the velocity flow much better than only gravity in the CDM.

Chapter 9

Evolution of voids over cosmic time

So far we always investigated voids at constant, albeit sometimes different, redshifts. However, as the Universe evolves with time, so do voids, as they follow the expansion of the Universe, merge together into larger voids and become more devoid of matter. In this chapter we do not follow the evolution of individual voids, which can be done when following the evolution of CDM, like in reference [148], but proves much more difficult for halo voids due to their formation and merging, which does not happen for CDM. Consequently, we follow only the statistical evolution of voids. Hence, we now focus on the evolution of common void properties in section 9.1, as well as the redshift evolution of their density and velocity profiles in stacked bins of r_v in sections 9.2 and 9.3, all in the `hydro` simulation and using CDM as the tracers of matter, since we already explored the impact of baryons in chapter 8. Unless mentioned otherwise, we always discuss the properties and profiles of *isolated* voids. Furthermore, we investigate the growth of structures in section 9.4. While a clear evolution in time can be observed for most void statistics, section 9.5 investigates a more universal void density profile.

9.1 Properties

Before exploring the evolution of common void properties in redshift, we first want to examine how the number of halos above given mass cuts and the corresponding number of voids identified therein grow with decreasing redshift. Figure 9.1 presents the halo mass functions at selected redshifts in the `highres` simulation. The vertical line indicates the mass cut of $1.0 \times 10^{11}\, M_\odot/h$ that is chosen to select halos for the void identification (see chapter 4). As expected, a steady increase in halo masses with decreasing redshift can be seen. Most notably, at around $z = 1.98$ and below, the halo mass function remains almost constant at the position of the mass cut. Only at higher halo masses, the mass function continues to evolve at lower redshifts, as halos attract more matter and their masses grow.

Figure 9.2 depicts the number of halos above the mass cuts and the number of identified halo voids, as well as the number of voids identified in constant subsampling of CDM from both `midres` and `highres` simulations. Tracer numbers are depicted in red to yellow colors

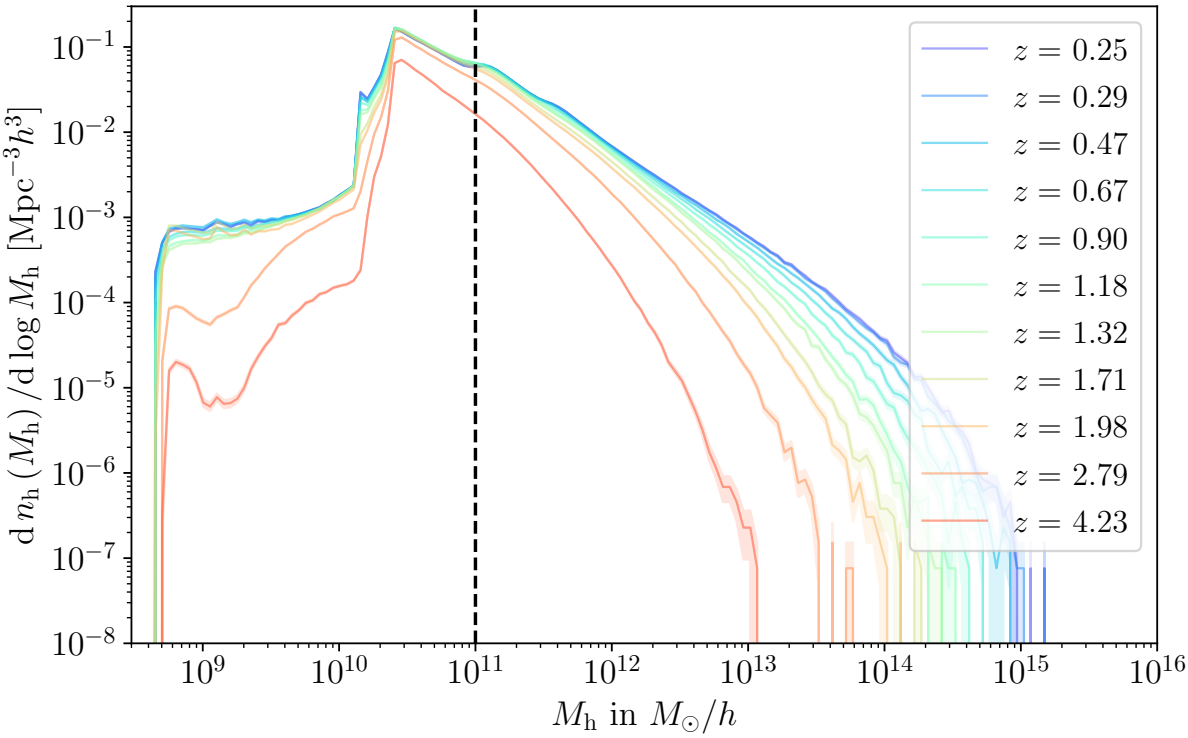

Figure 9.1: Redshift evolution of the halo mass function in `highres` at selected redshifts, given in the legend. The vertical line indicates the chosen halo mass cut for void finding at $1.0 \times 10^{11}\, M_\odot/h$.

with axis values given on the right side, while the left axis depicts the number of voids, given in blue and green colors. Once more, halos are always selected at a mass cut of $M_\mathrm{h} \geq 10^{11}\, M_\odot/h$ in `highres` and $M_\mathrm{h} \geq 10^{12}\, M_\odot/h$ in `midres` for the void identification, except for an analysis at additional halo mass cuts for the void identification in section 9.5.

For the `midres` simulation, the highest presented redshift is $z = 2.79$, as the halo mass function is not well resolved at higher redshifts for the given mass cut, while the lowest redshift is $z = 0$. Higher redshifts would be attainable at higher mass cuts, although the reduced number of halos above these mass cuts severely limits the number of identified voids. For example, in a mass cut of $M_\mathrm{h} \geq 10^{13}\, M_\odot/h$ at redshift $z = 4.23$ only 433 halos remain in the `hydro` simulation, which are too few to obtain reasonable void catalogs. In `highres` we showcase tracer and void numbers from $z = 4.23$ up to $z = 0.25$. At even higher redshifts halos are still fully resolved at the given mass cut, although their numbers are extremely small, resulting in even fewer voids. These will not be of any further relevance in this work, hence we refrain from including them in figure 9.2. Moreover, we analyze halo voids at a larger number of different redshifts than CDM voids. Not all redshifts will be presented in plots of void property distributions and void profiles, but when redshifts are left out, the void statistics at these redshifts naturally follow the evolution we observe

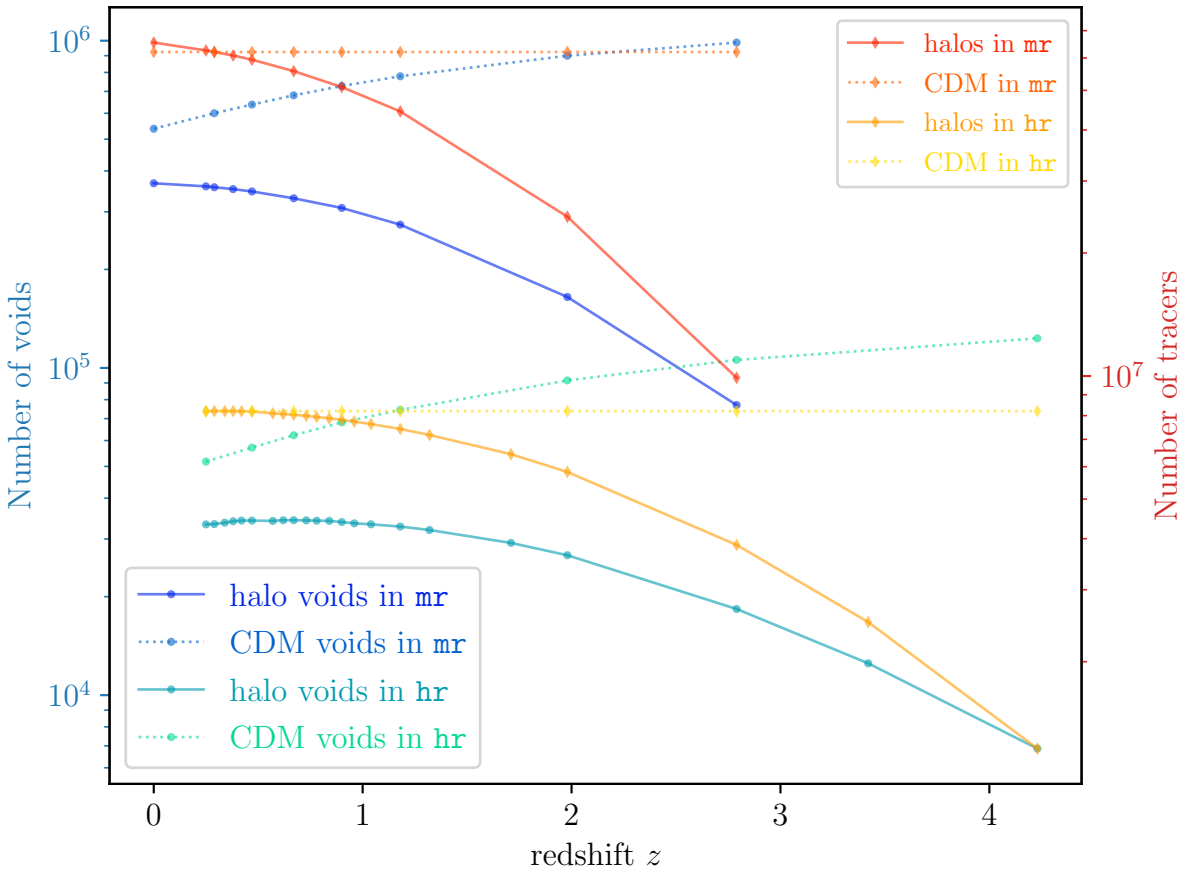

Figure 9.2: Redshift evolution of tracer numbers (right axis in red/yellow colors) and number of *isolated* voids (left axis in blue/green colors) found therein, all in the `hydro` simulations. Halos used in the void identification are selected with $M_\mathrm{h} \geq 10^{12}\,M_\odot/h$ in `midres`, while halos in `highres` use $M_\mathrm{h} \geq 10^{11}\,M_\odot/h$. CDM tracers use a fixed subsampling of around 62×10^6 in `mr` and 8.2×10^6 in `hr` at all redshifts.

between other redshifts.

In addition to identifying voids in halos above the given mass cuts, we further identify voids in constant subsamplings of the underlying CDM particles, namely in subsamplings of 62×10^6 in `midres` and 8.2×10^6 `highres`. These subsamplings are not chosen at random, as we previously used them to match the number densities of halos and CDM at $z = 0.29$ in chapters 5 and 6. Using a constant number of CDM particles at different redshift is more reasonable than matching the halo number densities for each redshift, as the number of CDM tracers in the simulations is constant, while halo numbers evolve in time as they form and grow in mass. A constant CDM number density therefore ensures that our results are not impacted by any influence of the halo formation, as it would be for matched number densities, and we can explore how these fixed number of CDM tracers evolve in time, while fixed halo mass cuts ensure that the impact of halo formation is

included in halo void evolution.

At constant CDM subsamplings in both `midres` and `highres`, the number of voids identified therein decreases with decreasing redshift. At the highest redshifts in figure 9.2, we find around 9.9×10^5 voids in `midres` and 1.2×10^5 voids in `highres`, which decreases to around 5.4×10^5 and 0.52×10^5 at lowest redshifts, respectively. This decrease in CDM void numbers happens because at early times, matter was more uniformly distributed, with a large number of small local underdensities within. As the Universe evolves, matter continues to cluster and forms the structures of the cosmic web. Many small CDM voids merge into larger ones, as former structures between them cluster together and boundaries between voids 'vanish', which is true for every resolution. Reference [148] finds opposite conclusions, namely an increase in void numbers, as more and more voids form in CDM over time. However, this previous work imposed cuts on the minimal void size and additionally used the full CDM distribution for void identification, which decreases the size of voids. In our work we impose no minimal void size and argue that the different evolutions in void numbers are caused by these cuts.

In contrast, at early times there are only few halos that have already formed, which results in a smaller numbers of halo voids. These few halos represent the highest peaks in the cosmic density field and the most strongly clustered regions of the Universe. Many halos that will ultimately reside in clusters, filaments, walls and voids have not yet formed at these early times and therefore, many of the void boundaries at late times are not yet present in the halo density field, which results in fewer voids at early times. With decreasing redshift, the number of halos with masses above the mass cuts increases significantly, and many of the visible structures in our Universe appear, which split up the few voids at high redshift, resulting in the increasing number of halo voids. In `midres` the number of halos and halo voids steadily increases, as halos accrete more mass and cross the mass cut. However, in `highres` the number of halos above the mass cut peaks at $z = 0.34$ and slightly decreases at lower redshifts, as only few new halos form and some merge. Similarly, the number of halo voids in `highres` peaks at slightly higher redshifts and decreases for later times, which is most likely due to the merging of some cosmic structures that trace the boundaries of voids, such as halos in filaments moving towards clusters and merging with halos residing in these clusters. This ultimately leads to the merging of a small number of voids, as some of their shared boundaries 'disappear' over time. Moreover, the evolution of void numbers in figure 9.2 suggests that at some point in the future of our Universe, the number of voids identified in both CDM and halos could match, or at least become even closer than at present times.

As the number of voids evolves in time, so do their properties. Figure 9.3 presents the evolution of void radii (top left), ellipticities (top right), core densities (bottom left), and compensations (bottom right), for both *isolated* CDM, as well as halo voids in the `highres` simulation. At selected redshifts we present schematic histograms of halo void properties facing left and CDM void properties facing right. These histograms showcase the shape of the distributions in void properties, although they do not accurately portray the evolving number of voids. In addition, the medians of each property are depicted for every redshift in dark (halo voids) and light blue (CDM voids) markers. Furthermore,

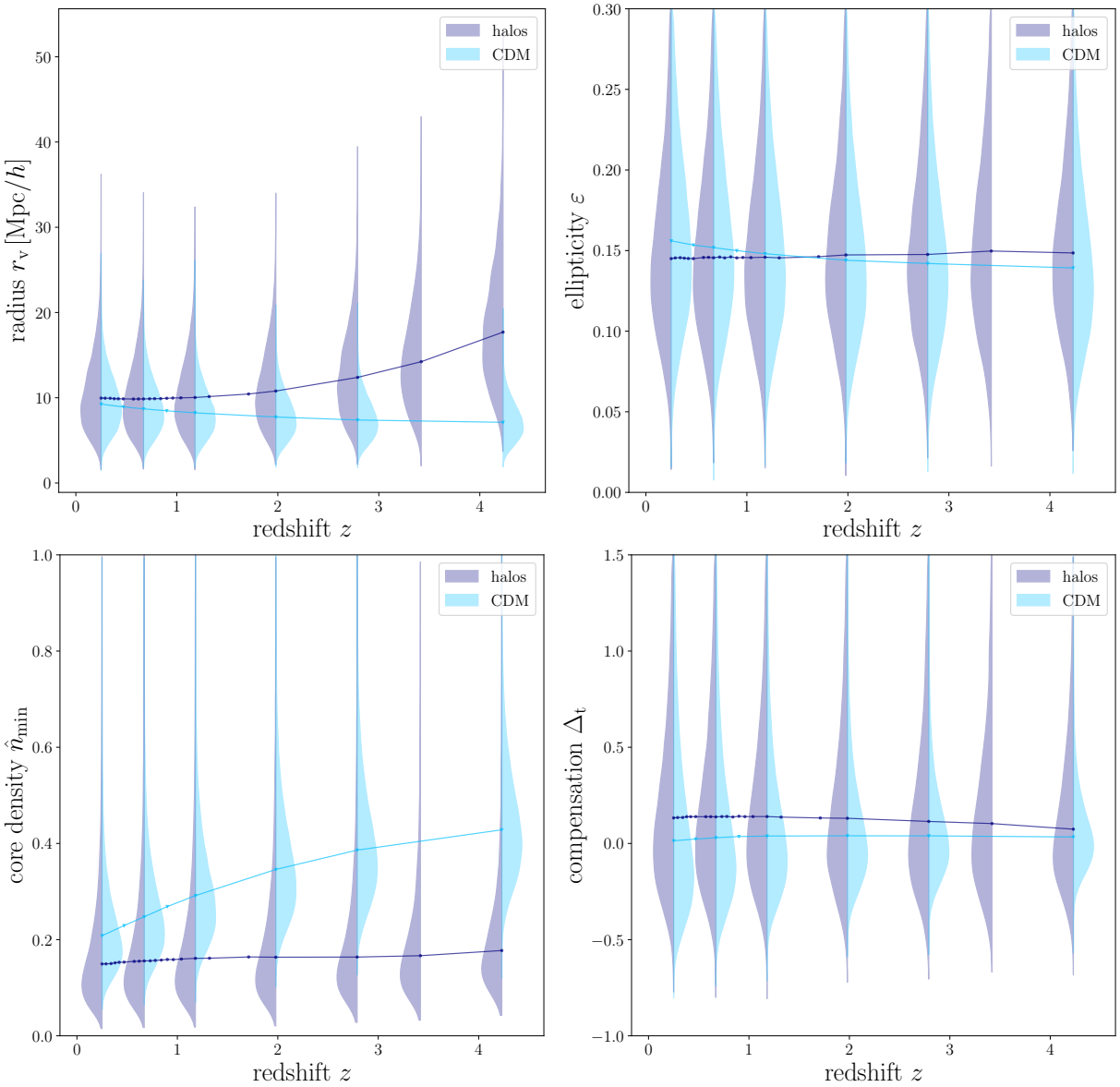

Figure 9.3: Redshift evolution of medians (connected markers) and schematic histograms (normalized, not representing the void numbers) of void radius (top left), ellipticity (top right), core density (bottom left) and compensation (bottom right) for *isolated* halo voids (left facing histograms), as well as CDM voids (right facing histograms) in `highres`, with $M_\mathrm{h} \geq 10^{11}\, M_\odot/h$ and $N_\mathrm{CDM} = 8.2 \times 10^6$ for the void identification.

figure 9.4 depicts the void size functions of *isolated* CDM (top) and halo voids (bottom) in the `midres` simulation at different redshifts, while figure 9.5 depicts their distributions in ellipticity (top), core density (middle), and compensation (bottom) for CDM (left), as well as halo voids (right).

For the distribution in void radii, we observe the largest differences between CDM and

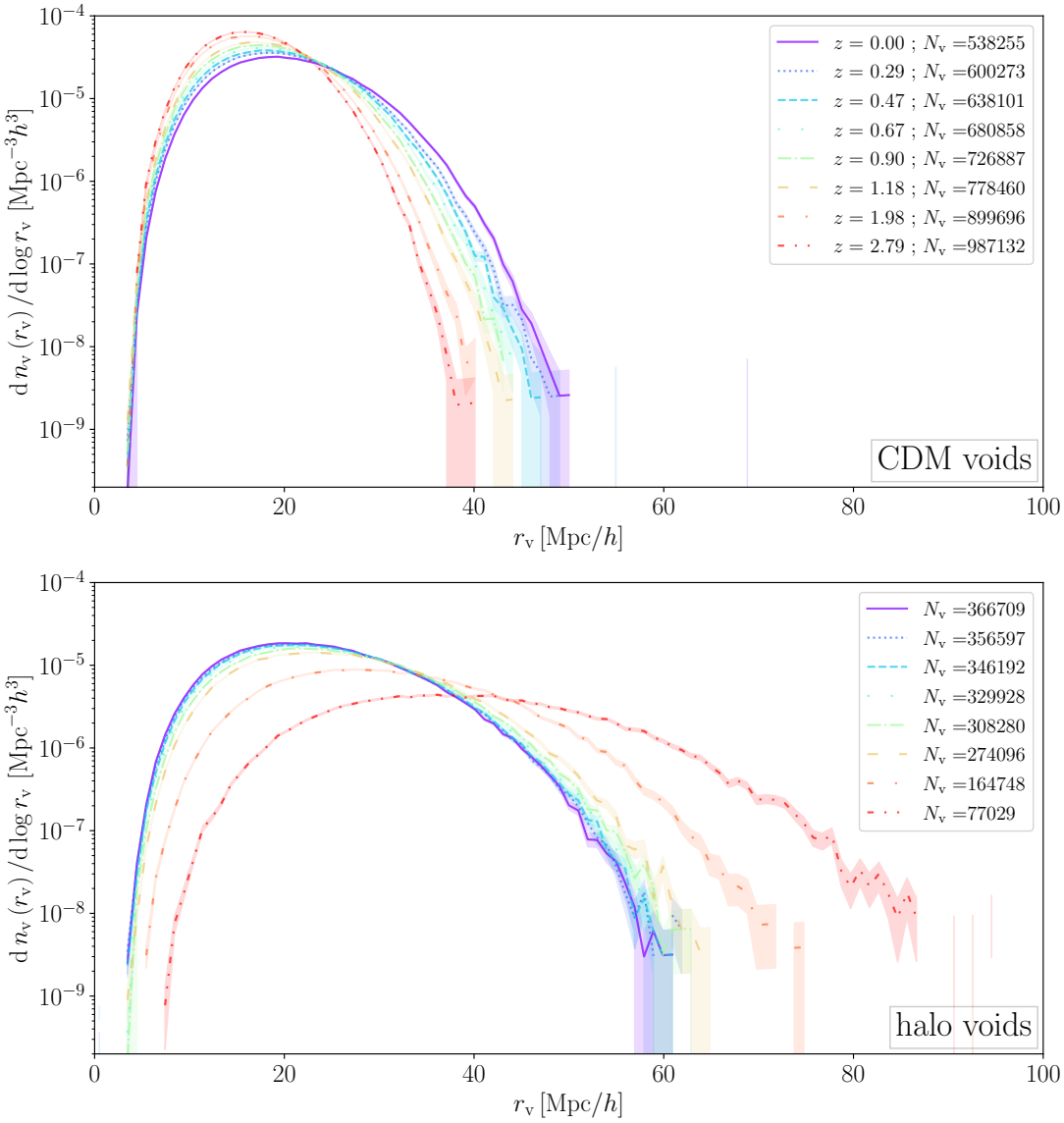

Figure 9.4: Evolution of the void size function of *isolated* CDM voids (top) and halo voids (bottom) in `midres`, redshifts are given in the upper legend and respective void numbers in both legends.

halo voids at highest redshifts, as at these early times their numbers differ most, albeit by construction of the tracer catalogs. There are numerous small CDM voids, while few, but large halo voids exist. With decreasing redshifts, CDM voids increase in size as their numbers decrease, while the opposite is true for halo voids. At the lowest redshifts, their distributions in r_v are almost alike, similar to the void size functions presented on the top of figure 5.1. While not presented in figure 9.4, at the lower end of redshifts the void size functions of *merged* voids in `midres` once more align on large scales, which does not

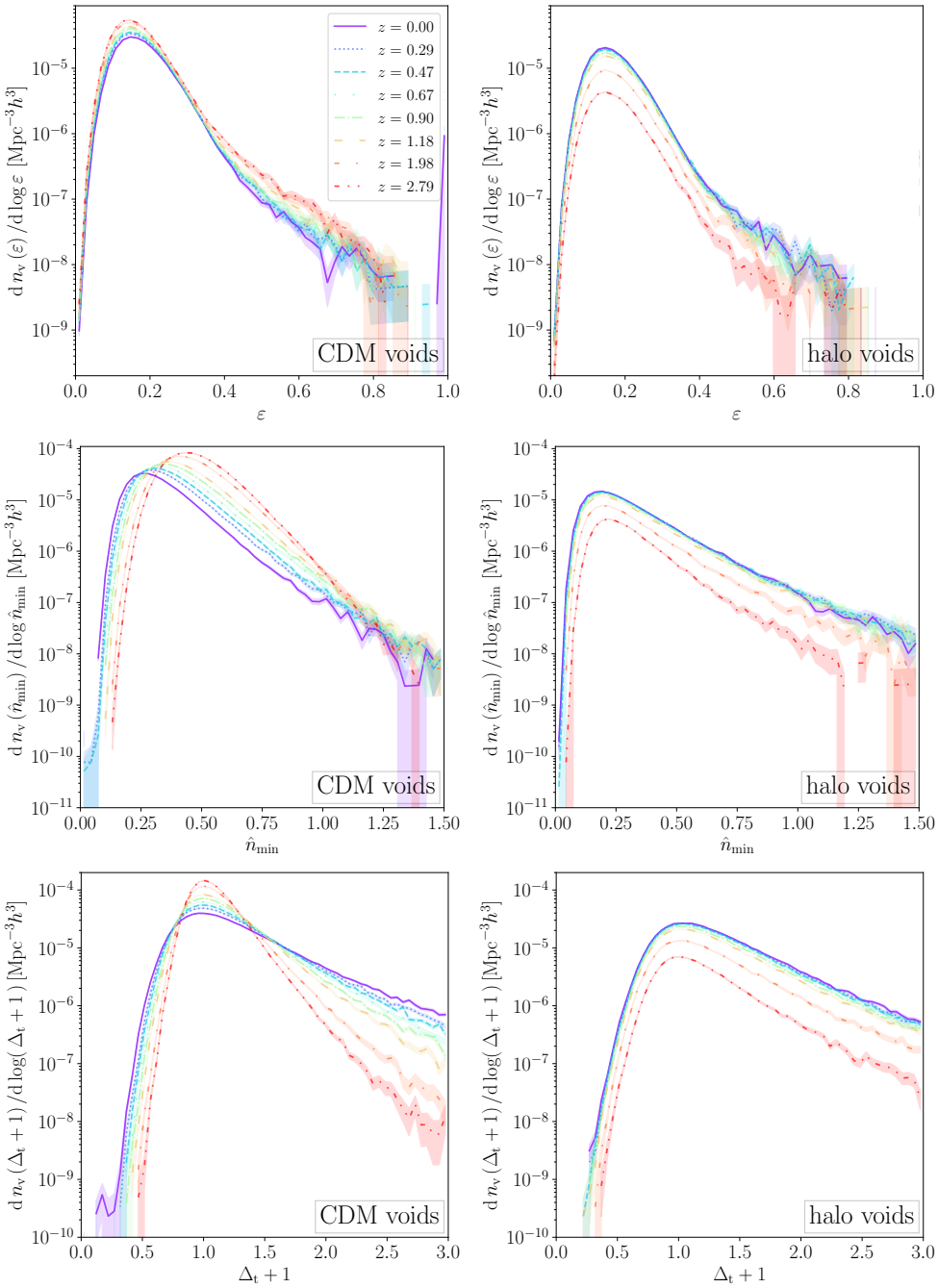

Figure 9.5: Evolution of ellipticity (top), core density (middle) and compensation (bottom) of CDM voids (left) and halo voids (right) in `midres`, redshifts are given in the legend of the upper left panel.

happen at high redshifts, as even *isolated* voids have higher number densities at large size than *merged* voids at low z due to the small halo void numbers at high z. Moreover, in `highres` the void size functions of *isolated* halo voids align almost perfectly at redshifts of

$z = 1.32$ and below, due to minor changes in the void and halo numbers at low redshift. A similar pattern can be observed in `midres`, starting at $z = 0.67$ and below, although with slightly worse alignment than in `highres` due to more substantial shifts in halo and void numbers. Even though these void size functions align, the physical size of halo voids increases with the expansion of the Universe, and the alignment of void size functions in their comoving radii simply implies that at these times, the evolution of void size closely follows the evolution of the Universe.

In contrast to their sizes, the shapes of voids, represented by their ellipticities, do not evolve as significantly in time, supporting previous findings [143, 149]. The medians for CDM voids tend to evolve towards slightly higher ellipticities at low redshifts, while the opposite is true for halo voids. These shifts of the medians occur near $\varepsilon \simeq 0.15$ and are on the order of $\Delta\varepsilon \lesssim 0.02$. Since void numbers change, we cannot follow the redshift evolution of individual voids, so we can only make reasonable assumptions as to why this shift in the medians happens. CDM voids decrease in numbers as the Universe evolves and some of them merge into larges ones, which offers the chance for more complex shapes, resulting in potentially higher ellipticities. On the other hand, halo voids at early times are defined by the highest peaks of the density field, which could lead to more irregular shapes. At low z, this complexity in void shapes might reduce, since many irregularly shaped voids break up into smaller and on average slightly more spherical voids.

The distributions in core densities on the bottom left of figure 9.3 for voids in `highres` and the middle panels of figure 9.5 for `midres` showcase how the most underdense regions of CDM voids become more devoid of matter over time [143, 148, 149]. CDM voids experience high core densities at early times and with their evolution, matter accretes and moves away from their centers towards the boundaries, hence their core densities decrease substantially. Halo voids experience much smaller changes in their distributions, except due to changes in the void numbers, as the medians of core density remain almost constant over a vast amount of time. Only a slight decrease of the median can be observed in `highres`, as well as a slight shift of the peak in the distributions in `midres`. Moreover, at around the same redshift at which the void size functions start aligning, the maxima in the core density distributions align as well, which can be seen in the distributions of halo voids in `midres`. As previously discussed in section 5.2, voids in `midres` typically have slightly higher core densities compared to voids in `highres`, but their evolution follows a similar path.

Even though the evolution of core densities is fundamentally different between halo and CDM voids, both can be expected. As explained above, matter moves out of the centers of CDM voids and since no new matter particles are 'created', their centers become more underdense in time. In contrast, even at early times there are only few halos near the centers of halo voids. These are typically the least massive halos (see section 6.2), so they most likely formed at later times than halos near the void boundaries and continue to grow slower in mass, since just a smaller amount of matter is available to be accreted by them. As halo voids evolve, halos continue moving outwards, but as this happens, new halos form as well and cross the threshold of the mass cut. This leads to minor changes in the core density values, since the newly formed halos can almost balance the amount of halos leaving void centers.

Lastly, we explore the evolution of void compensations in `midres` and `highres`. For CDM, as well as halo voids, we find that medians are almost constant over all redshifts. In the case of CDM voids the median is extremely close to 0, hence the number of under- and overcompensated voids is almost identical. At late times we observe a slight decrease of the median for CDM voids, while the median of halo voids shifts towards slightly higher values. This indicates that the compensation of a void at early times most likely determines its compensation at late times. Furthermore, it indicates that voids typically do not evolve from being undercompensated to overcompensated and vice versa, since the compensation is a measure of the environment around voids, which is already determined by the initial cosmic density field [32, 38]. Of course as halo void numbers evolve, some undercompensated, as well as overcompensated halo voids are most likely split up into smaller ones, with similar values in Δ_t. The opposite happens for CDM voids. As they as merge over time, their compensations combine and it is to be expected that most adjoining voids at early times have at least similar values in compensations, which get combined in the merging. The mean values in compensation (not depicted) of both CDM and halo voids evolve towards slightly higher values, as matter accretes more in regions of overcompensation, which amplifies Δ_t with time. In undercompensated regions matter moves towards regions of high density, which further decreases the compensation of already undercompensated voids. However, as the compensation has a lower bound of $\Delta_t = -1$, the evolution of overcompensated voids has a stronger effect on the evolution of the means. The effects of undercompensated voids becoming more undercompensated with time and similarly overcompensated voids becoming more overcompensated can be clearly seen in the distributions of CDM voids in figure 9.5. They start with a narrow distribution in Δ_t, which becomes much broader as the redshift decreases. On the other hand, halo voids have much more similar shapes in their distributions over all times and their distributions are mostly shifted vertically towards higher values as the number of voids increases, with a slight amplification of extreme values in Δ_t.

9.2 Density profiles

After examining how void properties change with time, we want to analyze the evolution of their density profiles. Previously we analyzed density profiles in stacked bins of other void properties, namely their ellipticities, core densities, as well as compensations. However, as void profiles are almost exclusively investigated in stacked bins of their radii, we will solely focus on those r_v bins except for revisiting compensation bins later in section 9.5.

Figure 9.6 presents the evolution of density profiles for *isolated* CDM voids identified in the `midres` simulation, with redshifts given in the legend and bin edges on the bottom of each panel, identical to the ones previously used for `midres`. The evolution of CDM voids in `highres` is not depicted, as our conclusions from `midres` also apply to voids from `highres`, just at different values in density and size. In all bins of r_v we can observe how matter clusters over time and is attracted to the overdense compensation walls, thus moving away from the centers of voids [38, 148, 149]. This leads to increasing heights of

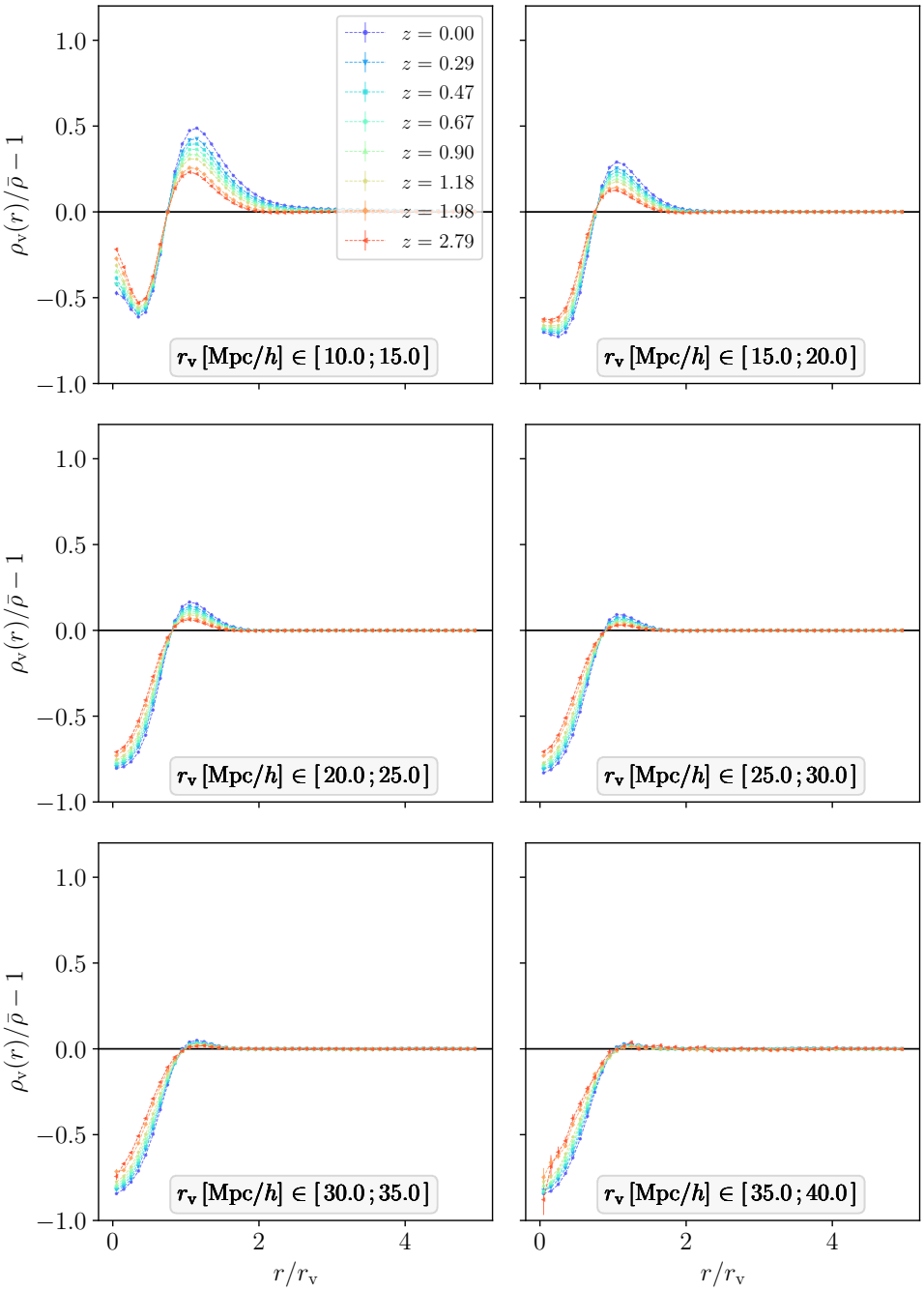

Figure 9.6: Density profiles of *isolated* CDM voids from the `midres` simulations at different redshifts, given in the legend on the top left. Profiles are stacked in void radius bins, with bin edges given on the bottom of each panel.

the compensation walls, except for largest voids with no significant walls, while the void centers become more underdense as redshift decreases. Densities inside voids that are close to the mean density do not evolve significantly and the distance from the void center in

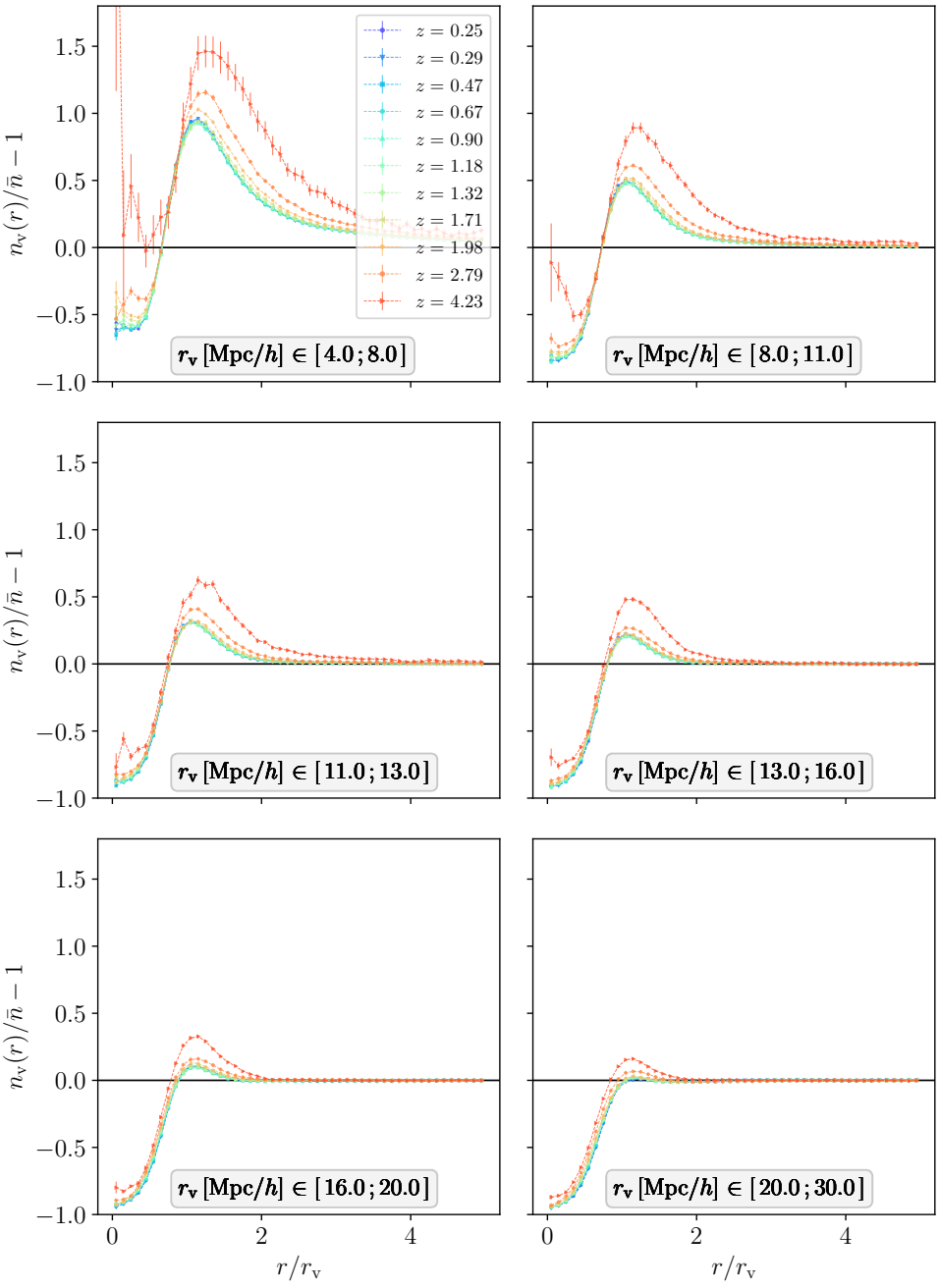

Figure 9.7: Same as figure 9.6, but for *isolated* halo voids in the `highres` simulation.

units of r_v at which $\rho_v \simeq \bar{\rho}$ remains almost constant in time for a given bin size. This distance moves closer to the compensation wall as the range of r_v in the bins increases. Of course it is once more important to mention that these results represent the statistical evolution of voids of similar size, as void numbers and their sizes evolve in time.

Next, we want to focus on the redshift evolution in the density profiles of halo voids,

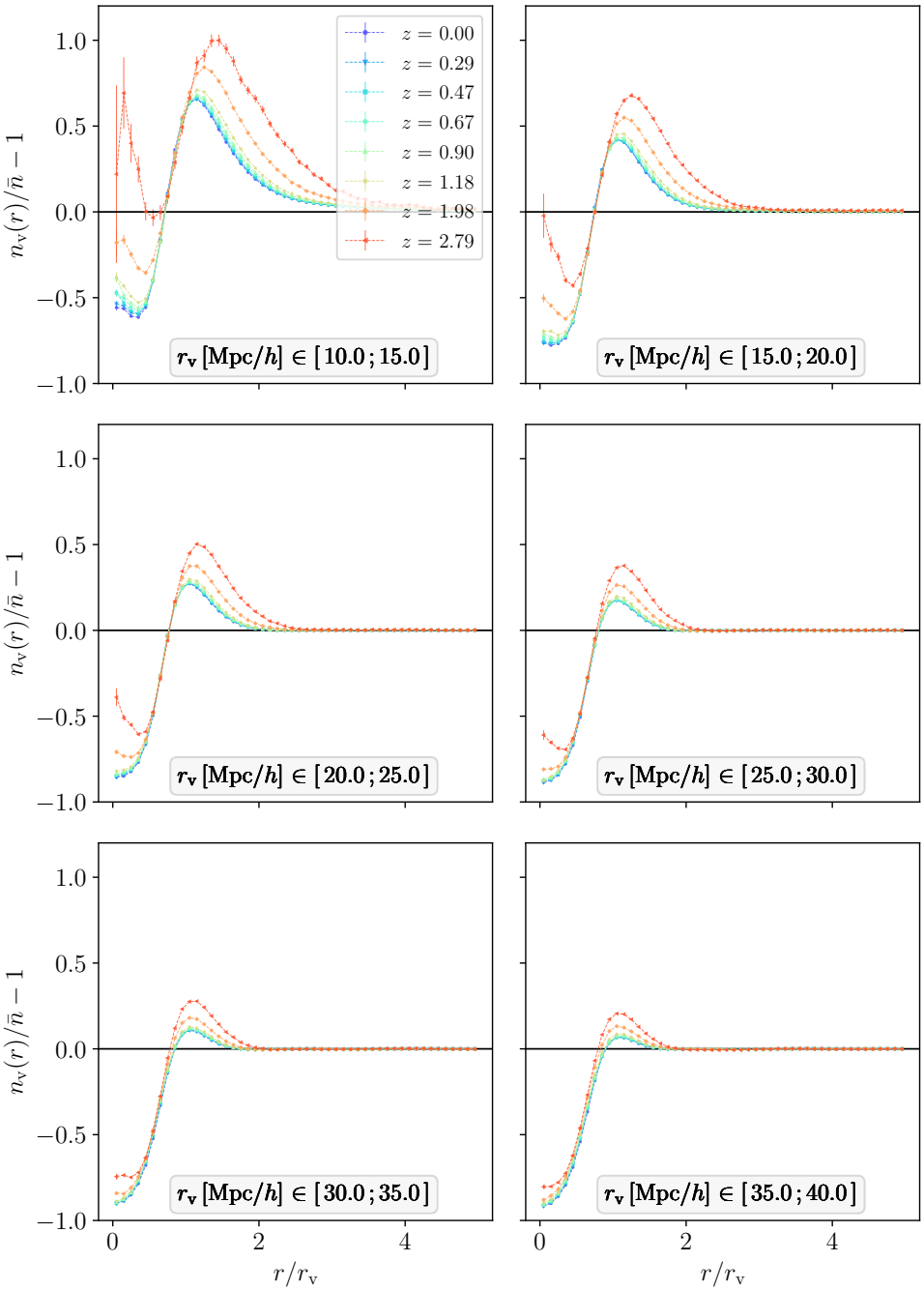

Figure 9.8: Same as figure 9.6, but for *isolated* halo voids in the `midres` simulation.

depicted in figure 9.7 for voids in `highres` and in figure 9.8 for `midres`. Contrary to CDM voids, we now observe the highest densities in the compensation walls at highest redshifts and they decrease with time. However, when we stack all voids of a given redshift, we instead find a similar evolution as for CDM voids. All halo voids combined (not depicted) have the highest compensation walls, as well as the deepest centers at lowest redshift, and

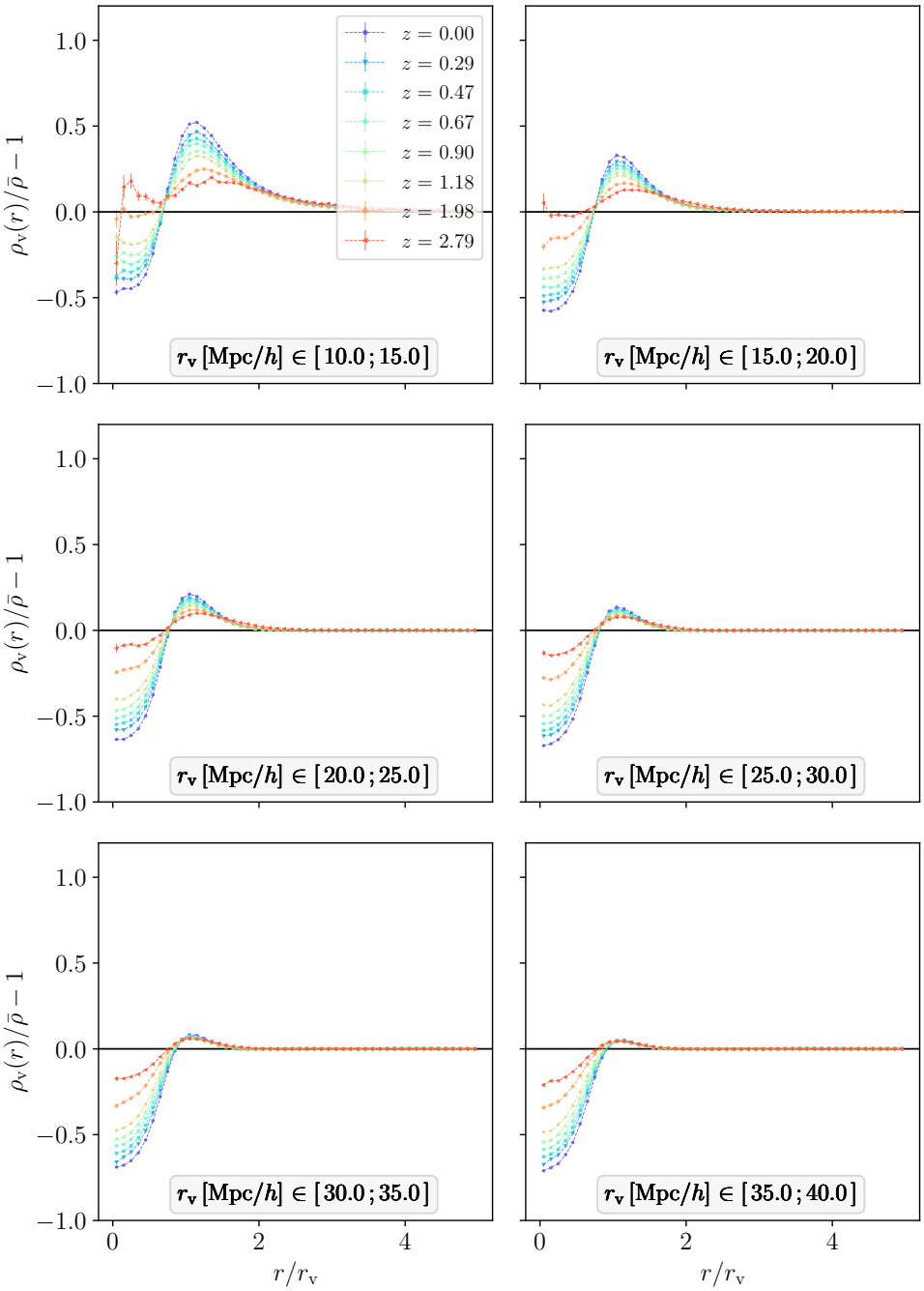

Figure 9.9: Same as figure 9.6, but for the density profiles of CDM around *isolated* halo voids in the `midres` simulation.

lowest density in the compensation walls, as well as highest densities near their centers at highest z. While the observation of highest densities near void boundaries at high redshift might seem unexpected, the stacks of all void profiles suggests that it is merely an effect originating from stacking in bins of fixed r_v. Since the void size functions of halo

voids change substantially with time, we compare highly different voids at fixed radii. For example the bin with $r_\mathrm{v}[\mathrm{Mpc}/h] \in [15.0\,;20.0]$ covers a fraction of comparatively small voids at high redshift, while at low z the same bin covers a fraction of voids of roughly average size for the given redshift. When comparing voids at different resolutions in chapter 6, we found that the smallest subsets of voids always have high compensation walls, irrespective of their actual size. Combined, this results in halo voids having higher compensation walls at high redshift for fixed bins in r_v compared to voids at low z. In addition, effects from the halo bias can potentially amplify the high peaks in the compensation wall, since halos first formed at the highest peaks of the matter density field, which are usually located at the boundary of voids. Hence, we can expect a higher fraction of halos near the compensation walls, as many halos inside voids have yet to form at lower redshifts.

Furthermore, at around the same redshifts at which the void size functions of halo voids start aligning, namely $z = 0.67$ in `midres` and $z = 1.32$ in `highres`, their density profiles align as well. This redshift value is highly dependent on the halo mass cut that is used for the void identification. At later times, the densities in scales of r_v inside and around halo voids do not evolve, except for voids themselves following the expansion of the Universe. This is further supported by the evolving halo numbers in figure 9.2 for `highres`, as well as the halo mass function evolution in redshift, depicted in figure 9.1. Since the number of halos above $M_\mathrm{h} \geq 10^{11}\,M_\odot/h$ does not change significantly at lower redshift than $z = 1.32$, almost all halos have already formed and simply grow in mass as the Universe evolves. In fact, when using mass-weighted density profiles (not depicted), the density profiles do not align at low redshifts due to this growth in mass. Naturally the effect of constant density profiles happens at later time in `midres`, as the mass cut is much higher.

To conclude the evolution of density profiles in stacks of r_v, figure 9.9 presents the profiles of CDM around halo voids in `midres`, which look more similar to the ones of CDM voids from figure 9.6. In contrast to the rather constant evolution of halos around halo voids at low redshifts, CDM continues to evade these void centers, leading to lower densities as redshift decreases. In most bins, the height of compensation walls increases and solely in the largest depicted bin, the compensation wall is near constant in time. This might be an effect due to changes in the void size function of halo voids, similarly to the effect in the evolution of halo void profiles. We will revisit the density profiles of CDM around halo voids once more in section 9.4 to investigate the growth of structures in more detail.

9.3 Velocity profiles

As we have seen how the density evolves around voids, we now turn to the movement of tracers. In this section we only depict velocity profiles using global stacks via equation (3.11), since both stacking methods lead to identical conclusions. Any significant changes in individual stacks will be mentioned in the text.

Unlike the density profiles of CDM voids, their velocity profiles in figure 9.10 have a more complex evolution in redshift. While the velocities outside of small voids experience a linear increase in the absolute magnitude of their velocity, the velocities of larger voids

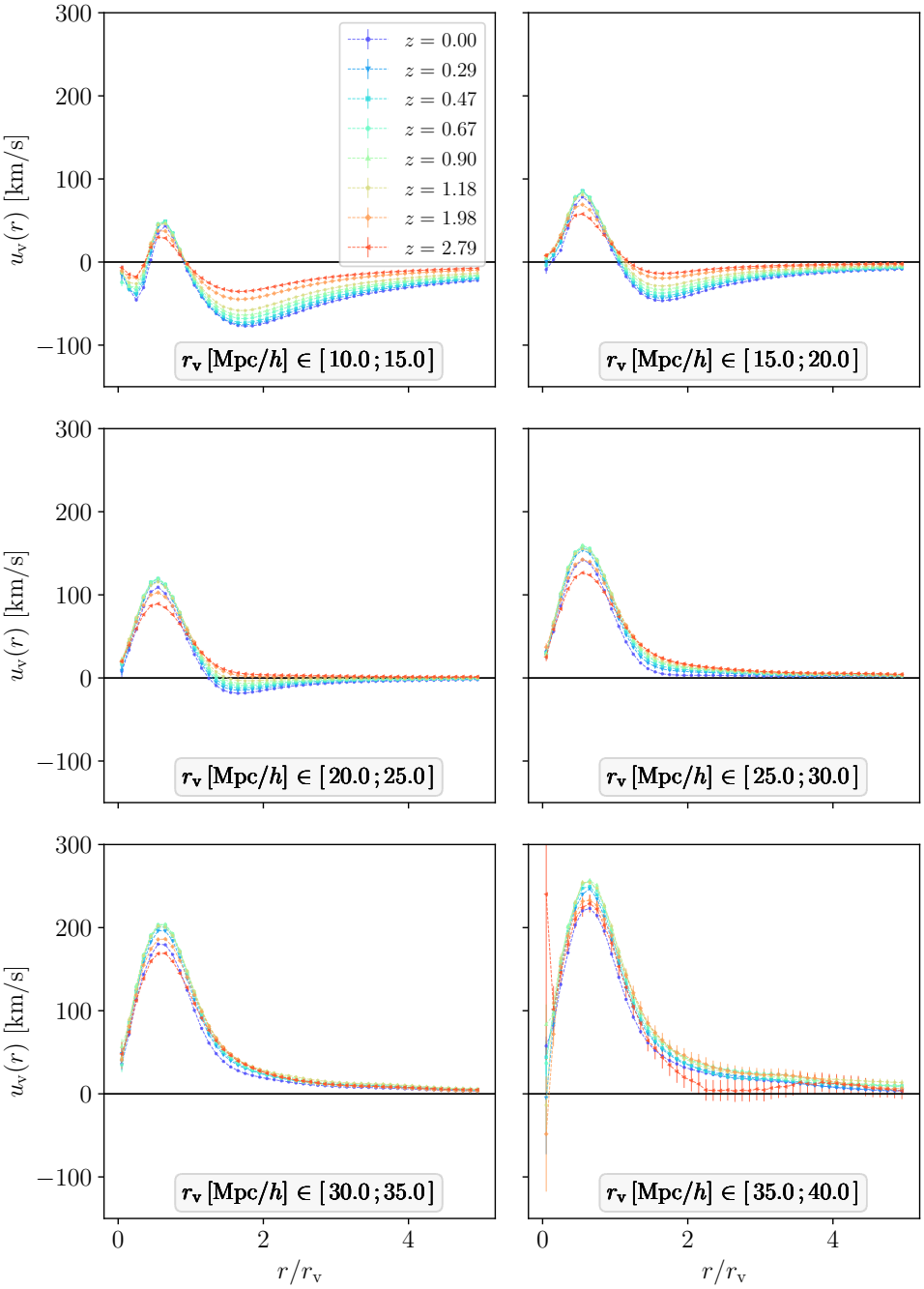

Figure 9.10: Velocity profiles of *isolated* CDM voids from the `midres` simulations at different redshifts, given in the legend on the top left. Profiles are stacked in void radius bins, with bin edges given on the bottom of each panel.

experience both a decrease in velocities (e.g. in the bin with r_v[Mpc/h] ∈ [25.0 ; 30.0]) and velocities outside of voids remain almost constant. Inside CDM voids, the velocities first increase with time, but experience a turning point at $z = 0.67$ in `midres` ($z = 1.18$ in

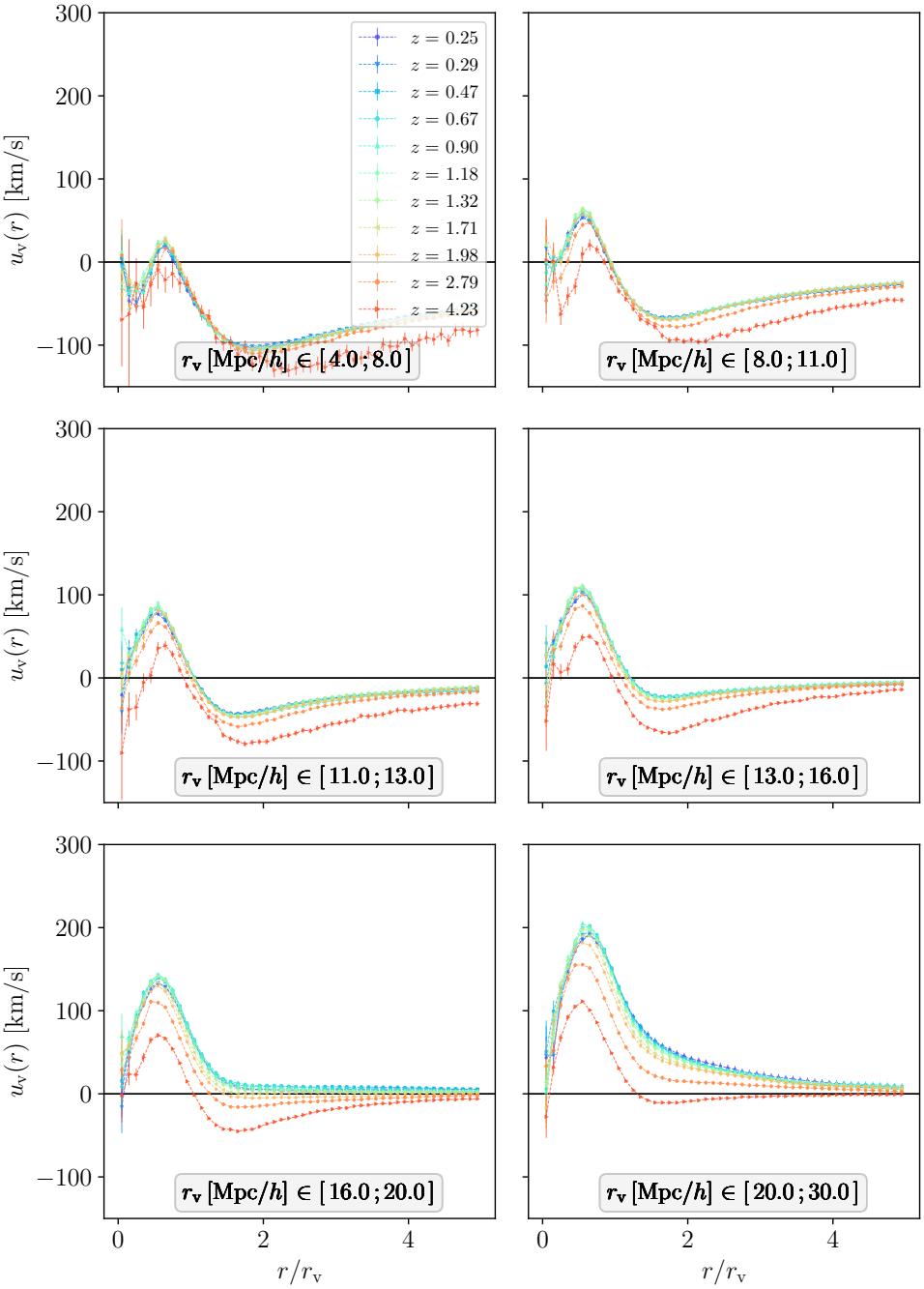

Figure 9.11: Same as figure 9.10, but for *isolated* halo voids in the `highres` simulation.

`highres`) and decrease at later times. Currently we have no clear interpretation as to why this happens, but it might simply be an effect originating from the changes in the void size function, similar to effects in the density profiles of CDM voids. Another potential cause might be effects from the accelerated expansion due to the cosmological constant Λ. The only difference in individual stacks is that velocities in the centers of voids are always

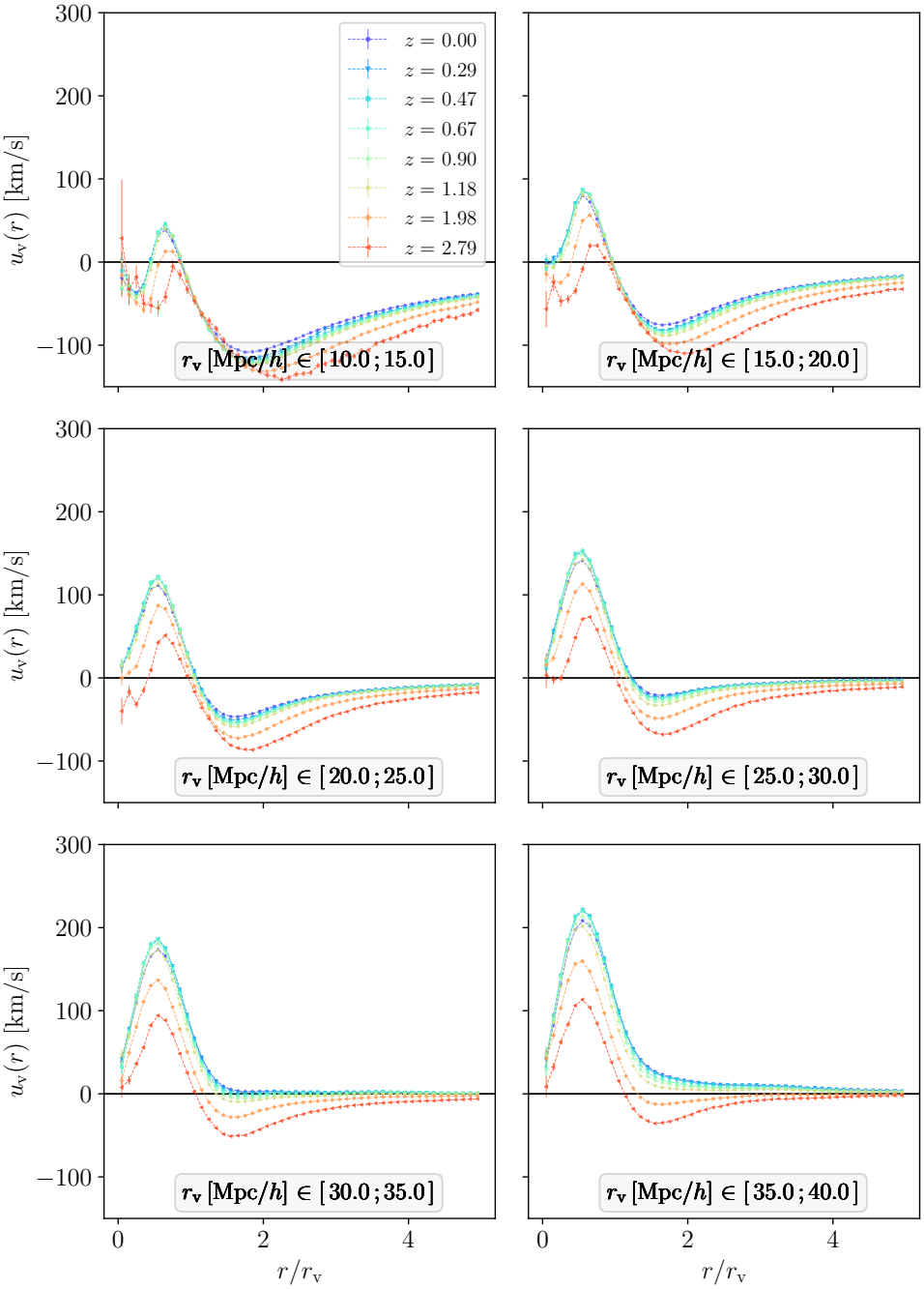

Figure 9.12: Same as figure 9.10, but for *isolated* halo voids in the `midres` simulation.

extremely close to zero due to the inherent bias of this velocity estimator.

The velocity profiles of halo voids, presented in figures 9.11 and 9.12 for voids in `highres` and `midres`, experience a slightly different behavior in redshift than CDM voids. Small voids have the largest inflowing velocities past their compensation walls and the smallest outflowing velocities inside them at high redshift. The velocities increase with time and in

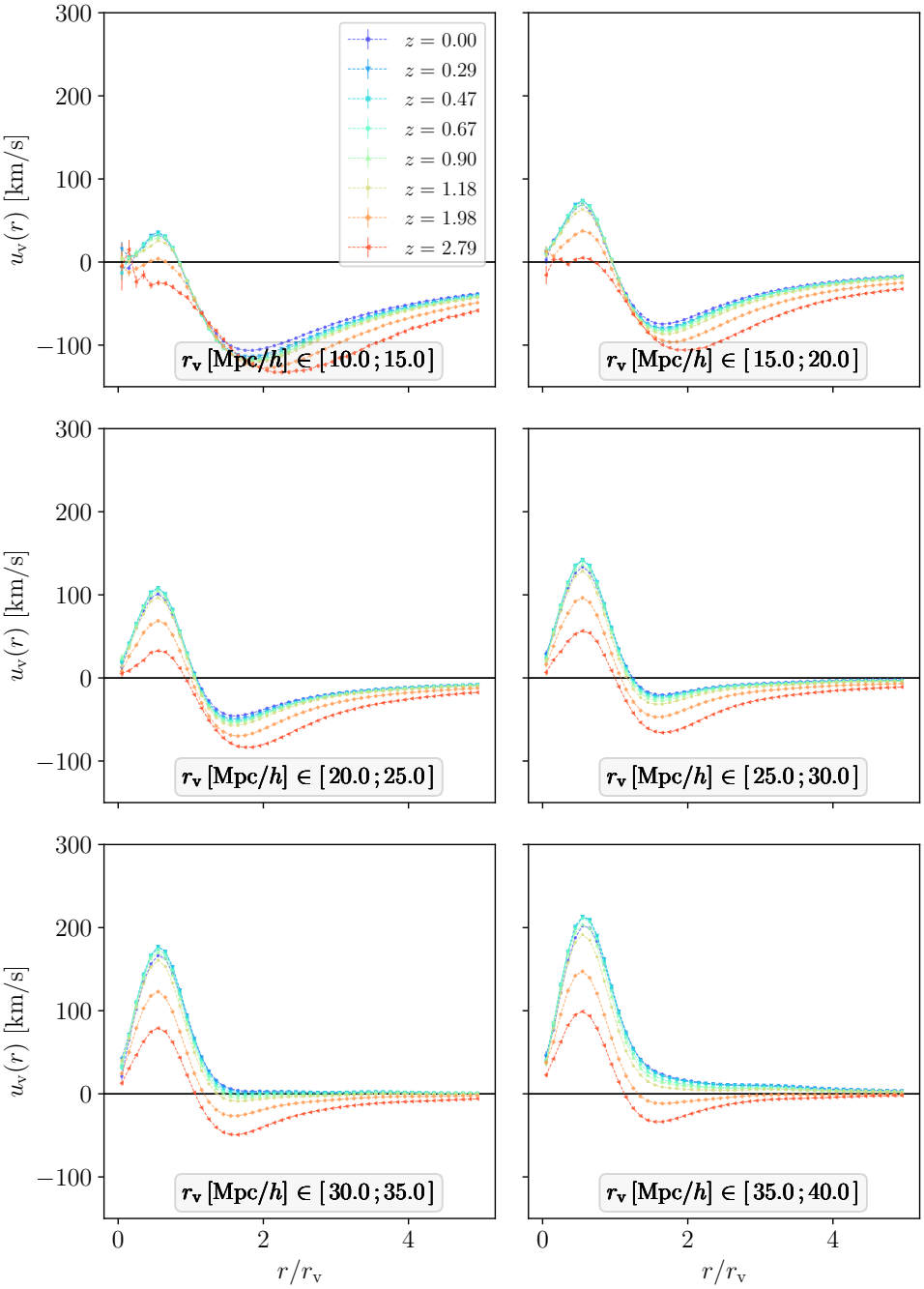

Figure 9.13: Same as figure 9.10, but for the velocity of CDM around *isolated* halo voids in the `midres` simulation.

`highres` they become almost constant at around the same redshift at which their density profiles start aligning, although we still observe a slight decrease in velocities at the peak for low z, similar to CDM voids. In both `midres` and `highres`, the velocities outside of large voids continually increase and do not align at any redshift. In their centers, velocities

increase as well, become almost constant, but we once more observe a turning point, after which they slightly decrease. At identical bins in `midres`, the profiles of halo and CDM voids share few similarities due to their inherently different nature.

Finally, we present the velocity of CDM around halo voids from the `midres` simulation in figure 9.13. As previously seen in section 6.3, CDM and halos move at almost the same speed around halo voids, especially outside of voids. Any differences, which typically arise within voids, are most likely due to effects from tracer sparsity. This is clearest at high redshift, where we note significant deviations between CDM and halo velocities even outside of voids. At $z = 2.79$ we only have around 9.9×10^6 halos above the mass cut and for the calculations of profiles, while the subsample of 62×10^6 is used for CDM, which can lead to deviations due to the large differences in number densities.

9.4 Predicting the growth of structures around voids

Section 9.2 examined the evolution of various density profiles in redshift, some of which experience a continuous increase in the depths of void centers and heights of compensation walls with decreasing redshift. We now want to investigate these evolving profiles in more detail and see how well the theoretical predictions from the linear growth of density perturbations compare against measured profiles in the simulations. If Λ is a cosmological constant and Ω_m, as well as Ω_k are the only relevant background parameters in our Universe, the growth factor D_+ is given by [88]:

$$D_+(a) = \frac{5\,\Omega_\mathrm{m}}{2}\,\frac{H(a)}{H_0}\int_0^a \frac{\mathrm{d}\tilde{a}}{\left(\tilde{a}\,H(\tilde{a})/H_0\right)^3}\,. \tag{9.1}$$

Assuming linear mass conservation once more and using this growth factor, although now in normalized form $D(t, t^\star)$ for any reference time $t^\star$, the density profiles should evolve in time as $\rho\,(\boldsymbol{x}, t)\,/\bar{\rho}\,(t) - 1 = D(t, t^\star)\,[\rho\,(\boldsymbol{x}, t^\star)\,/\bar{\rho}\,(t^\star) - 1]$ (see section 2.2). The normalized growth factor D increases with time and is by convention equal to 1 at current time ($z = 0$).

Figure 9.14 presents a summary for the density profiles of CDM around *isolated* halo voids. Here we first use the density profiles at lowest redshift due to solid statistics with high void numbers, and divide them by the value of the growth factor at the given redshift. This gives us a 'universal growth' profile, namely the prediction of the density profile as it would be at $z = 0$. This profile is then multiplied with the value of the growth factor at other redshifts, resulting in predictions for density profiles at any redshift. These predictions (dotted lines) are then compared with the profiles measured from data (solid lines) at multiple redshifts, with differences between data and prediction presented in the lower panels of each plot. These differences only include the error of the measured profiles, as we purposefully underestimate the errors in order to see how predictions fare against data in the worst case.

In the upper row of figure 9.14 we present CDM density profiles around halo voids

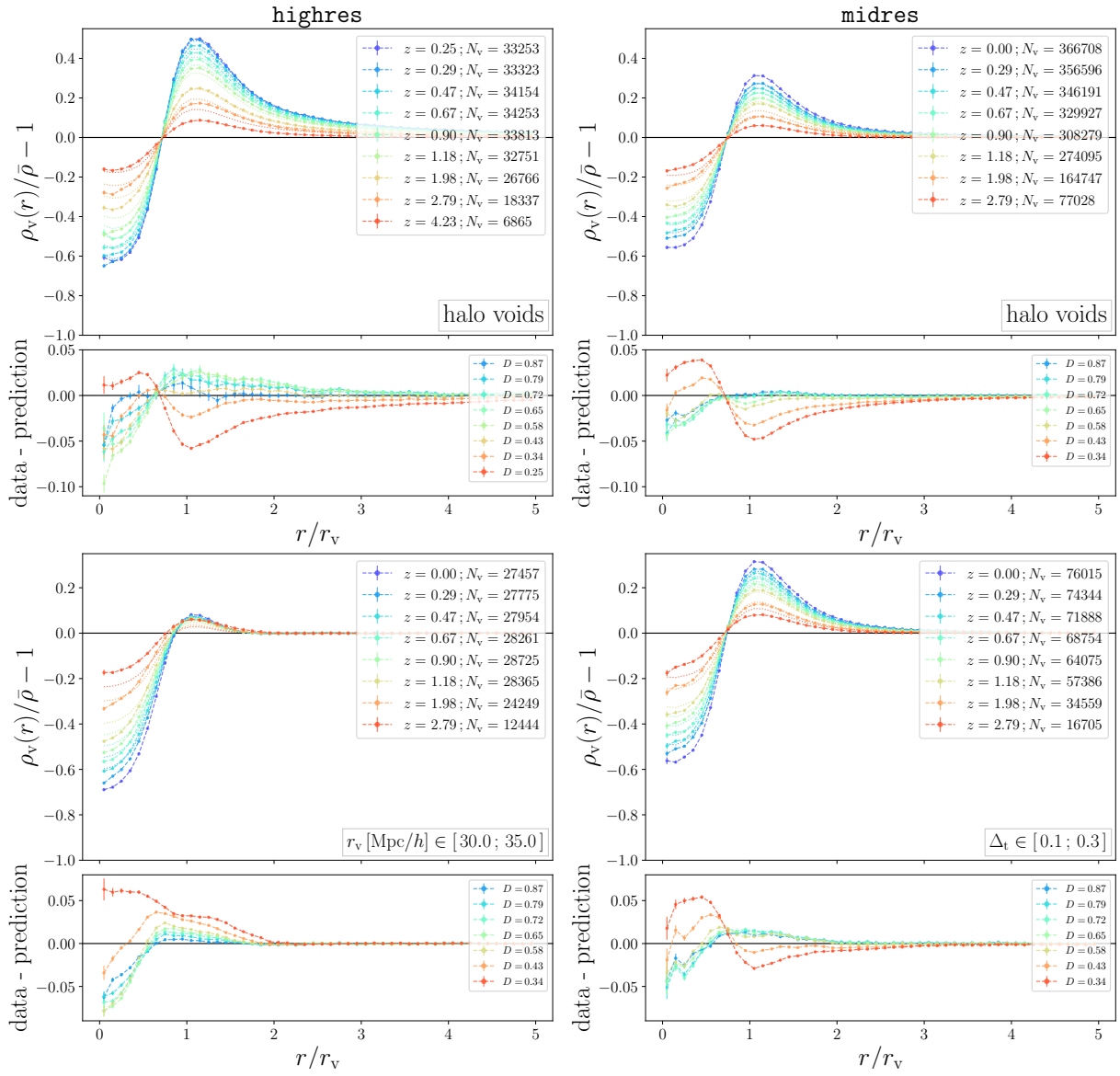

Figure 9.14: Density profiles of CDM around halo voids ('data', dashed) and the growth factor prediction of profiles (dotted), including differences (lower panels), see main text for more details. Presented in stacks of all voids in `highres` (top left) and `midres` (top right), as well as for a selected bin in radius (bottom left) and compensation (bottom right), both in `midres`. Values of the normalized growth factors D are given in the lower legends.

in stacks of all voids in the `highres` (left) and `midres` (right) simulations, as well as the predictions from the growth factor. We find a similar agreement between measured profiles ('data', in dashed lines) and the growth factor prediction (dotted lines) in `midres` and `highres`, where deviations are mostly on the order of $|\Delta\rho| \lesssim 0.05$, except for the innermost regions of voids. The shape of deviations also looks remarkably similar at

identical redshifts, even though profiles between `highres` and `midres` differ.

In contrast, when analyzing the profiles in stacked bins of void radii (bottom left), we selected the bin with $r_\mathrm{v}[\mathrm{Mpc}/h] \in [30.0\,;35.0]$. In this bin the discrepancies between data and prediction have the smallest values out of all bins in r_v depicted in figure 9.9. The predictions fare significantly worse than in stacks of all voids, which is most likely due to shifts in the void size functions at different redshifts, since the predictions assume the growth at unchanging sizes. However, this can be remedied by stacking in bins of void compensation (bottom right), using $\Delta_\mathrm{t} \in [0.1\,;0.3]$ as our example. Here differences are once more on the same order as for all voids combined, and only in bins of extremely under- or overcompensated voids, predictions match the data slightly worse, with $|\Delta\rho| \lesssim 0.15$. While the radii of voids still change in redshift, compensation bins most likely result in better agreement because the compensation is a measure of a voids' environment, which does not change as substantially in time as its size.

We additionally analyzed the profiles of CDM voids, halo voids, as well as of baryons around halo voids. The latter case works as good as the profiles of CDM around halo voids, but the profiles of CDM and halo voids do not yield good predictions when comparing them with measured profiles. For halo voids this can already be expected from figures 9.7 and 9.8, since the growth factor evolves with time, but profiles remain almost constant over a range of redshifts. In the case of CDM voids in `midres`, the predictions at $z = 2.79$ yield substantially higher densities inside voids on the order of $|\Delta\rho| \simeq 0.3$ and smaller compensation walls with $|\Delta\rho| \simeq 0.1$. These deviations are presumably caused by the effects of redshift evolution in CDM voids, as they merge and grow in size.

9.5 Universal characteristics of compensated profiles

After investigating the evolution of density profiles in stacks of void radii, we once more investigate them in bins of their compensation Δ_t. While not depicted here, the density profiles of halo voids in stacked bins of ellipticity experience an increase in density of the compensation walls, as well as a decrease in densities near their centers with increasing age of the Universe, and profiles in core density have a similar increase in the compensation walls, but almost constant densities in their centers, which naturally follows from stacking in bins of their most underdense regions.

The stacks in compensation bins for profiles of CDM voids and CDM around halo voids experience similar effects to bins in void radii, the density of already overdense regions increases and underdensities become more underdense as the Universe ages. However, halo voids showcase a major difference in their evolution in compensation bins, namely they do not experience any substantial changes in their density profiles over time.

Figures 9.15 and 9.16 present the redshift evolution of density profiles for halo voids in stacked bins of compensation, for `highres` at halo mass cut $10^{11}\,M_\odot/h$ and `midres` at $M_\mathrm{h} \geq 10^{12}\,M_\odot/h$, respectively. In both mass cuts, the profiles of undercompensated and

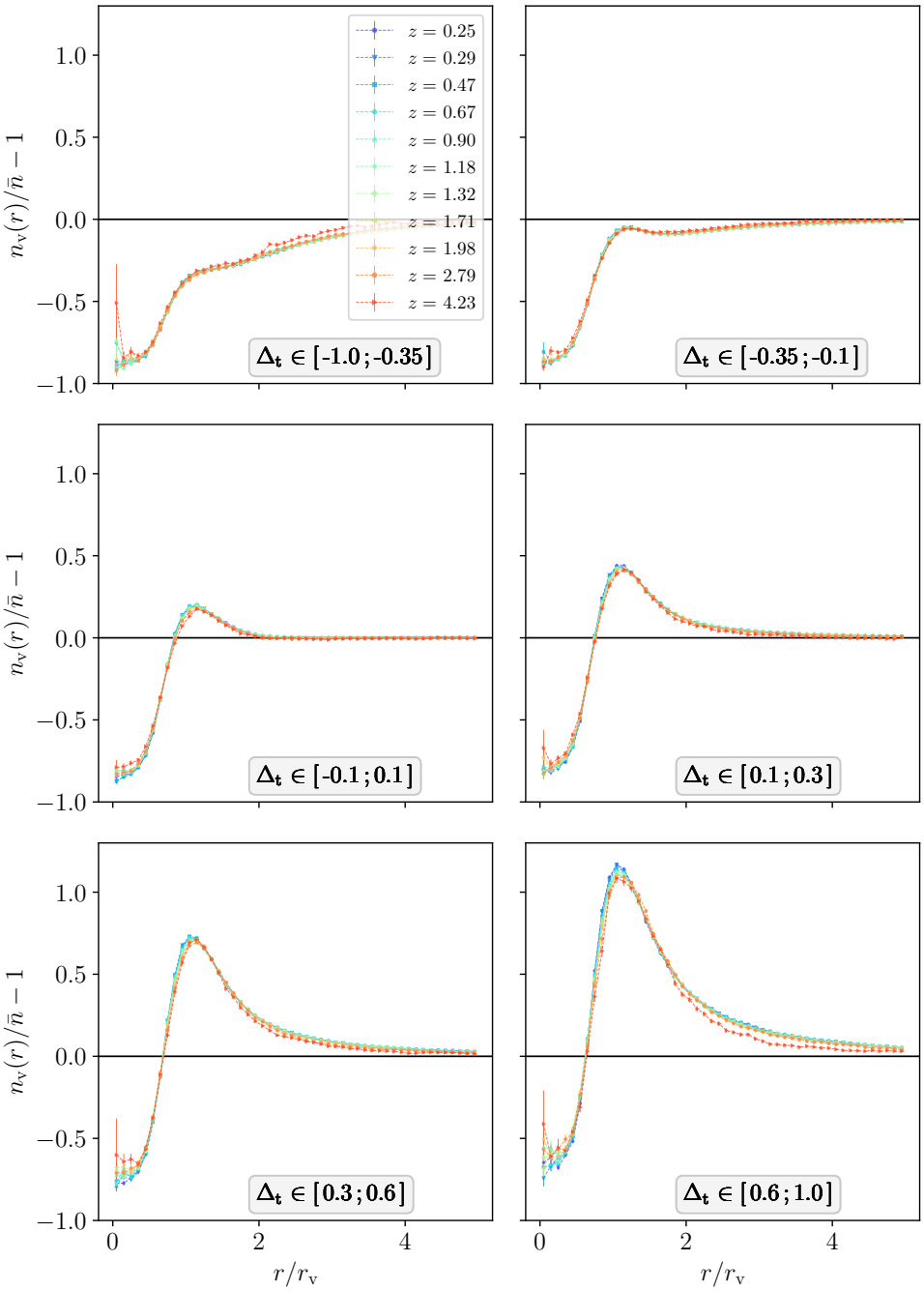

Figure 9.15: Density profiles of *isolated* halo voids from the `highres` simulations at different redshifts, given in the legend on the top left. Profiles are stacked in compensation bins with bin edges given on the bottom of each panel. Selected halos have $M_h \geq 10^{11}\,M_\odot/h$.

compensated voids do not show any substantial evolution in their densities, except for small deviations in void centers and compensation walls at very high redshifts. At these high redshifts there exist only few halos, so effects from tracer sparsity could potentially

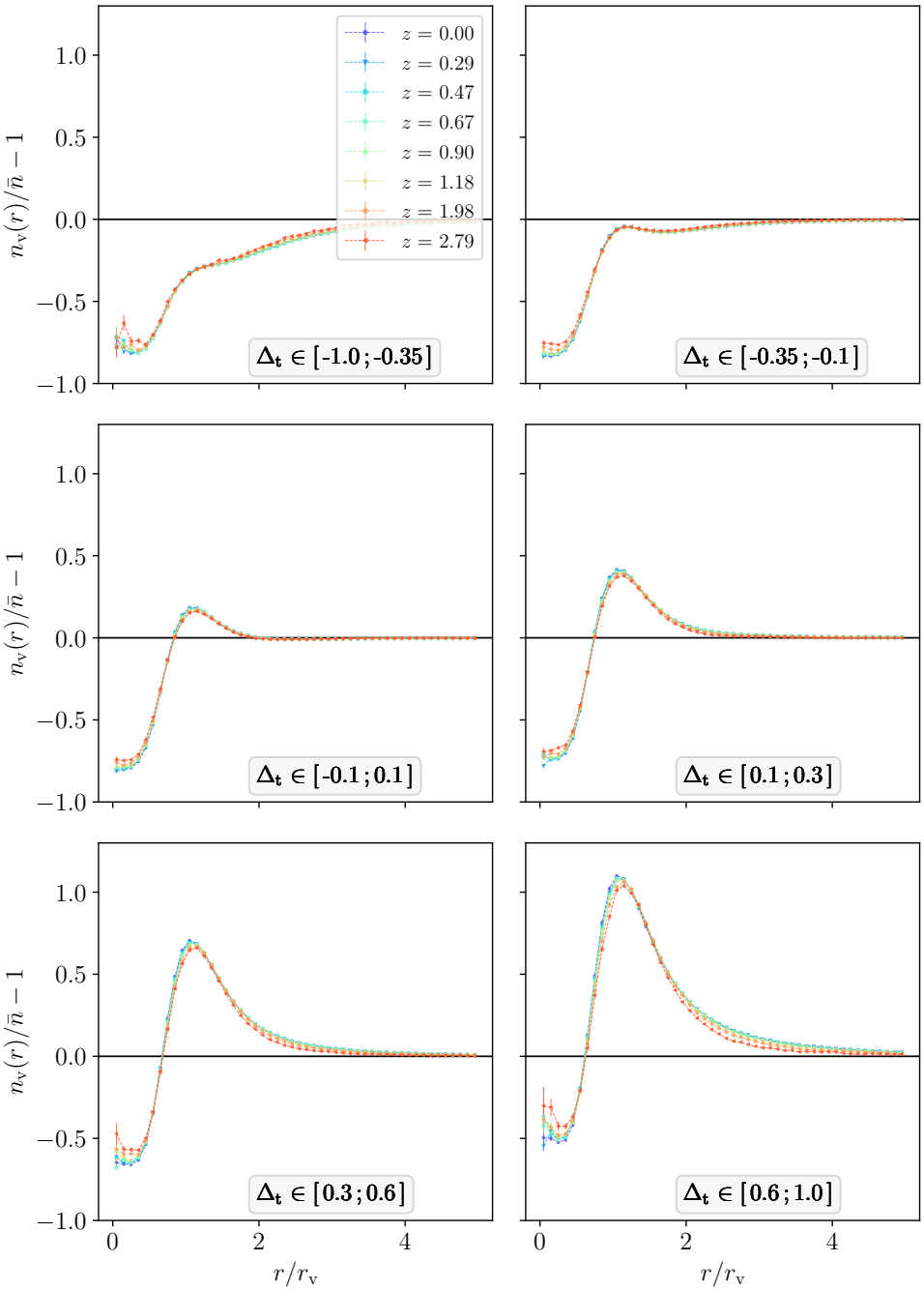

Figure 9.16: Same as figure 9.15, but for voids in the `midres` simulation at halo mass cut $M_h \geq 10^{12}\,M_\odot/h$.

explain these deviations. Only in stacks of overcompensated voids do small differences arise, although they are significantly smaller than differences in the evolution of profiles in other void properties. It is quite remarkable how little these density profiles evolve, despite the fact that we cover the evolution of void profiles over most of the age of the Universe. For

the given cosmology of the `Magneticum` simulations, the age of the Universe is around 13.8 billion years[1] and the redshift range of $z_{\mathrm{max}} = 4.23$ to $z_{\mathrm{min}} = 0.25$ in `highres` corresponds to an evolution of density profiles from the time the Universe was only 1.5 billion years old until 2.9 billion years ago. The results from `midres` suggest that at even smaller redshift than $z = 0.25$, the profiles of voids identified in halos of mass $M_{\mathrm{h}} \geq 10^{11}\, M_{\odot}/h$ would align with the stacks in compensation at higher redshift.

To explore this effect in more detail, we additionally analyzed the profiles of halo voids at even higher halo mass cuts, namely at $M_{\mathrm{h}} \geq 10^{13}\, M_{\odot}/h$ and $M_{\mathrm{h}} \geq 10^{14}\, M_{\odot}/h$ in the `midres` simulation. At all times we only used halos above these mass cuts for both void identification, as well as the calculation of profiles. In the $10^{13}\, M_{\odot}/h$ mass cut we once more investigated profiles between $z = 0$ and $z = 2.79$, but at $10^{14}\, M_{\odot}/h$ we can only identify voids starting at $z = 1.18$ and below, due to an insufficient number of halos at higher redshifts. While we do not depict their redshift evolution, we find similar conclusions to figures 9.15 and 9.16. In these higher mass cuts only a slightly 'stronger' evolution can be found, potentially from the sparsity of few massive halos at high redshift. Furthermore, we tested the evolution of *merged* halo voids in compensation bins in `midres` and find that their density profiles are almost indistinguishable to the ones of *isolated* voids. They still show no significant evolution in redshift and simply experience slightly higher densities in their centers than *isolated* voids, as previously discussed in section 6.1. In addition, we find an identical evolution of density profiles in the `DMo` simulations, as expected from chapter 8. Of course, since we bin solely in compensation, most of the stacked bins contain a large number of small voids, which surely contribute to this effect. Eliminating these voids through a simple cut in radius would not be appropriate, as their sizes evolve significantly, so a more intricate selection cut should be used in further tests in future work.

Next to their almost constant evolution in redshift, the profiles between figures 9.15 and 9.16 look extremely similar, even though the underlying halos differ significantly in mass. We therefore investigate the impact of halo mass in compensation bins further in figure 9.17. We present the profiles at fixed redshift $z = 0.29$ for a larger range of halo mass cuts used in the void identification and profiles compared to previous figures. In `ultra-hr` we depict profiles using halos with $M_{\mathrm{h}} \geq 1.3 \times 10^{9}\, M_{\odot}/h$, while the other mass cuts are as previously described, from both `highres` ($10^{11}\, M_{\odot}/h$) and `midres` for even higher masses. In the profiles at lowest mass cut, some bins feature decreasing densities below the mean far outside of voids. This is however not a physical drop in densities, but simply an effect from the calculations of individual profiles before stacking. As the `ultra-hr` simulation has a box length of only $48\,\mathrm{Mpc}/h$, large voids occupy a significant volume of this box. When calculating individual profiles, the distances from the void centers can reach values larger than the box length for some voids. While we use periodic boundary conditions for the calculation of profiles, we do not count tracers more than once, so naturally the density goes towards zero at large distances for these voids, which gets imprinted in the stacks as well. As already discussed with figure 5.2, large voids tend to be undercompensated, hence the drop in density outside voids is most noticeable in these compensation bins.

[1] https://www.astro.ucla.edu/~wright/CosmoCalc.html

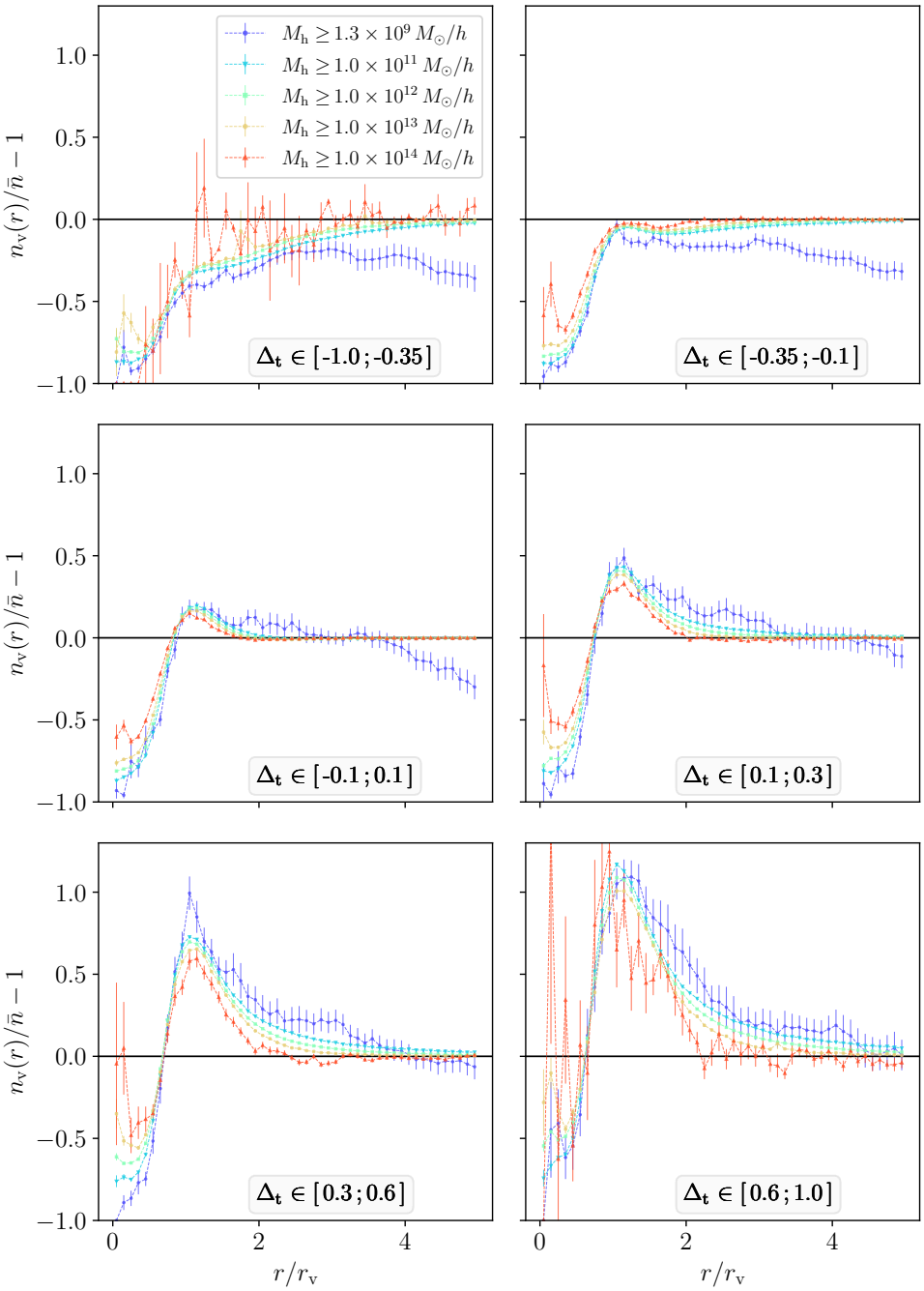

Figure 9.17: Density profiles of *isolated* halo voids at $z = 0.29$ for voids identified in various halo mass cuts, given in the legend.

Nevertheless, density profiles of halo voids in compensation bins look quite similar between different mass cuts, even though they cover a range of almost 5 orders of magnitude in minimal halo mass. Profiles in other void properties, such as ellipticity and core density, look significantly different at various mass cuts, and for bins in void radii, this comparison

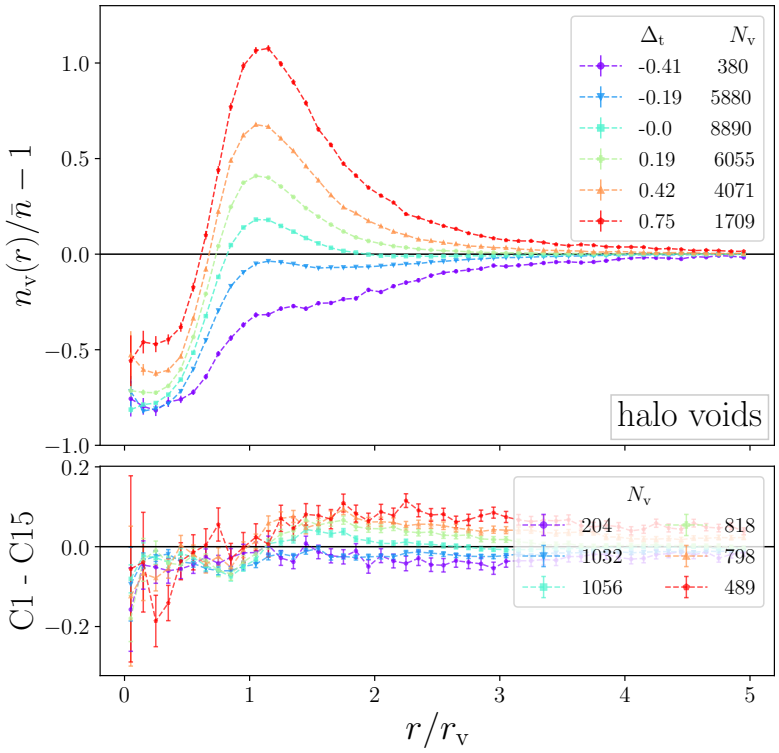

Figure 9.18: Density profiles of *isolated* halo voids in stacked bins of compensation in the `midres-1a` simulations at $z = 0.29$ for the C15 cosmology, with differences compared to the C1 cosmology on the bottom.

is almost pointless to even attempt, since void sizes change substantially between mass cuts (see e.g. figure 5.1).

Moreover, figure 9.18 presents the compensation bins for profiles of *isolated* halo voids at different cosmologies in the `midres-1a` simulation at redshift $z = 0.29$. In order to test the impact from different values of cosmological parameters on these profiles, we present the profiles for the two most extreme cosmologies available, the C1 and C15 boxes. These cosmologies most notably differ in their matter content, namely $\Omega_m = 0.153$ in box C1 and $\Omega_m = 0.428$ in C15. For more details, such as the other values of cosmological parameters, we refer the reader to table 4.1 and section 7.3.

In figure 9.18 we depict the halo void profiles of the C15 cosmology in the upper panel, as well as void numbers of each bin in the legend. Differences between C1 and C15 are presented in the lower panel, where the legend indicates void numbers for C1. As is typical at this resolution, halos are selected with $M_h \geq 10^{12}\, M_\odot/h$. We find a striking resemblance in profiles with only relatively small differences, even though the matter contents of the simulations differ substantially. As expected from this little influence of cosmology on the profiles, they also look remarkably close to the ones of the 'standard' cosmology of the `Magneticum` simulations from previous figures. From this, we expect that even in

different cosmologies, our results from the evolution of compensation bins should still hold. While not depicted in figures, the density profiles in bins of void radius, ellipticity and core density do not share this resemblance between C1 and C15, as they have significantly larger differences between these cosmologies.

So far we have not discussed the evolution of halo void velocity profiles in stacked bins of compensation and we refrain from depicting them in this work. However, they do not share the surprising lack of evolution in time we found in their density profiles, except for the bin of exactly compensated voids with $\Delta_t \in [-0.1\,;0.1]$. Only in this bin do the velocity profiles of halo voids remain almost constant in redshift, the values of which can be seen for voids identified in the `midres` simulation at $z = 0.29$ in figure 6.9. Although velocity profiles of compensated voids remain mostly constant in time, they have substantially larger differences in their magnitudes at different halo mass cuts.

To conclude this section, we have found a remarkable new characteristic of halo voids when investigating their redshift evolution from the perspective of stacking them in bins of their compensation. As the Universe evolves, the profiles do not change significantly over a vast amount of cosmic time, nor between different mass selections of halos and different resolutions. Furthermore, even when analyzing them in cosmological parameters of rather extreme values, these profiles look remarkably similar. As of yet, we do not have a satisfying explanation for this behavior and can only speculate. Namely, as the compensation is a measure of the environment of a void and its average density compared to the Universe, this should somewhat determine the shape of these profiles. In spite of this, the average density of voids can still remain unchanged if some tracers move from the centers towards the void boundaries at the compensation wall, as more underdense centers and slightly higher compensation walls can balance each other and still result in identical average densities. In fact, this exact behavior is seen in the redshift evolution of CDM around halo void and CDM voids themselves (both not depicted), which is similar to the evolution of CDM in stacked bins of void radius. However, we suspect that reasons for the constant density profiles lie on one hand in the insignificant evolution of distributions in compensation, except for changes in number density (see figures 9.3 and 9.5), and on the other hand are caused due to a complex interplay of halo formation and halo bias. As the profiles already align at high redshifts, we additionally rule out Λ as the source for these constant profiles.

Chapter 10

Conclusion and outlook

In this thesis we investigated the interrelation between various general properties of voids, as well as their density and velocity profiles. We explored these relations across a substantial range in both mass and scale by analyzing the hydrodynamical simulation suite `Magneticum`, as well as counterpart simulations containing only dark matter. This enabled us to reveal and further inspect a multitude of void characteristics, some of which are scale and resolution dependent, while others are universal across simulations. Furthermore, we explored the impact of baryonic physics on common void statistics and even individual voids, as well as the evolution of voids and their statistics over cosmic time. The main results of this thesis can be summarized as follows:

- Merging voids creates significantly larger voids, including a hierarchy of sub-voids. On average, these *merged* voids have shallower density profiles, due to internal structures of their sub-voids, and slightly higher densities in their compensation walls (figures 6.1 and 6.2). The smallest voids remain unaffected by merging, as they host no sub-voids, and they are identical to *isolated* voids. In contrast to the void size function of *isolated* voids, the size function of *merged* voids converges on large enough scales, irrespective of the tracer type voids were identified in and the resolution of simulations (figure 5.1).

- Stacked number density profiles of halo voids feature similar characteristics as the matter density profiles of CDM voids, although with an enhancement of their amplitude caused by the halo bias (figures 6.1 and 6.2). Using halo masses as weights in the calculation of density profile further enhances this effects, as the masses of halos correlate with the density of the environment they reside in (figure 6.5). Furthermore, the CDM density profiles of halo voids are quite similar to the density profiles of CDM voids (figure 6.3).

- The ellipticity of voids is strongly reflected in the shape of stacked density, as well as velocity profiles due to spherical shell averaging. More elliptical voids experience smoother density profiles with shallower cores and wider compensation walls (figure 6.4).

- The minimum (core densities) and average densities (compensations) inside voids correlate to an extent and both are anti-correlated with the heights of their compensation walls: the most shallow voids feature the highest walls and vice versa. Overcompensated void, usually residing in overdense environments, are typically significantly smaller than undercompensated ones, some of which can be interpreted as sub-voids inside their larger parent voids. Both these void properties are clearly reflected in the shapes of their density and velocity profiles (figures 6.4 and 6.9).

- The stacked velocity profiles of voids follow expectations from the structure of their density: large and undercompensated voids are dominated by a coherent outflow of matter, while in and around small and overcompensated voids, infall of matter towards the compensation wall dominates. Around the same voids, halos and CDM move at identical speed, as expected from the equivalence principle of general relativity (figures 6.6 and 6.8). The velocities around *merged* voids are typically smaller than for *isolated* ones of equal size due to the movement of tracers around sub-voids. Moreover, the radial velocity profiles of voids accurately obey predictions from linear mass conservation. Residual deviations are most likely caused by artifacts arising from the sampling of sparse tracer statistics. Especially inside small voids, these become increasingly significant due to length scales close to the resolution limit and the mean tracer separation. In addition, they depend on the type of estimator that is used for the calculation of velocity profiles (figures 7.4–7.8).

- Applying mass cuts and subsampling tracers to calculate profiles of voids identified at fixed tracer density affects the estimators in significantly different ways. Density profiles are stable against subsampling except for larger errors, while reducing halos through mass cuts has a similar effect to mass weights in density profiles. For velocity profiles, global stacks are more independent of the tracer mass and subsamplings compared to individual stacks (figures 6.10 and 6.11).

- Splitting both the density and velocity into profiles for inflowing, as well as outflowing tracers reveals more substantial deviations between the different velocity estimators, each with a different interpretation for the movement of tracers close to void centers. The density profiles of inflowing particles closely resemble the shape of their regular density profiles, just at lower densities, while the density profiles of outflowing tracers align almost perfectly inside voids (figures 6.12–6.14).

- All our previous conclusions on stacked profiles remain valid even for the profiles of individual voids, although their profiles are significantly affected by noise and sampling variance. Nevertheless, individual voids still obey linear mass conservation with exquisite accuracy (figures 7.1–7.3), irrespective of tracer type. This can be exploited to explain and further improve the linear interrelation between the corresponding stacked profiles of voids, which plays an essential role in cosmological applications.

- The apparent breakdown of linear dynamics in the inner regions of voids analyzed at moderate resolutions seems to be merely caused by the sparse sampling of tracers

when scales are close to their mean separation. We tested this by comparing voids of identical sizes in simulations of increasing resolution, and we find no sign for an onset of nonlinear dynamics around voids, down to scales of order $1\,\mathrm{Mpc}/h$ (figure 7.11). At a given resolution, sparse sampling affects velocity profiles more severely than the density profiles, so the application of the linearized continuity equation to their densities is better suited for the modeling of both velocities and observable RSD around voids compared to using more biased templates for velocity profiles measured in simulations. In addition, linear dynamics are valid over a wide range in redshift, as well as for significantly different values of cosmological parameters (figures 7.9 and 7.10).

- The magnitude of effects from baryonic physics is highly resolution dependent. Differences between `hydro` and `DMo` simulations in `midres` exist only within statistical errors, but we were able to identify deviations between `hydro` and `DMo`, as well as between CDM and baryons of the `hydro` simulation in the `highres` and `ultra-hr` simulations, even using halo mass cuts typically applied in `midres`. Investigating deviations in individual voids between `hydro` and `DMo` simulations is not feasible, as there is no one-to-one correspondence between individual voids (figures 8.1 and 8.2)

- Within their errors, the statistics of CDM voids are identical between `hydro` and `DMo` simulations. Compared to CDM voids, voids identified in baryons exhibit significantly higher core densities and are slightly smaller due to higher numbers identified in fixed subsamplings of matter (figure 8.3). Only the smallest subset of baryon voids features slightly higher inner densities, as well as smaller compensation walls in the density profiles, while investigating profiles in bins of core density reveals more significant deviations in density and small deviations in the velocity profiles (figures 8.4 and 8.5).

- The number densities of halos at fixed mass cut noticeably differ between `hydro` and `DMo` simulations (table 8.1), which in turn leads to differences in void numbers and slight variations in the distributions of their properties. Voids in the `highres hydro` simulation are slightly smaller and both core density and ellipticity distributions experience a vertical shift due to higher void numbers compared to `DMo`. When fixing halo number densities instead, deviations in the distributions of void properties decrease significantly (figure 8.3).

- Compared to halo voids in the `DMo` simulation at fixed mass cut, the density profiles of the smallest halo voids in the `hydro` simulation feature higher compensation walls and lower inner densities, while large voids exhibit smaller compensation walls and statistics of intermediate sized voids remain unaffected. In fixed halo number densities these differences vanish almost completely. In contrast, binning in core density reveals more significant deviations, which increase with increasing $\hat{n}_{\mathrm{min}}$ and are of same magnitude in mass cuts and fixed halo number densities (figure 8.6). Velocity profiles only feature slight variations for the largest subset of voids and in core density bins, which once more decrease at fixed number densities (figure 8.7).

When using CDM as tracers for the profiles around halo voids, the density profiles differ significantly compared to the ones with halo tracers, but in both density and velocity profiles, deviations between `hydro` and `DMo` simulations are almost identical to deviations of profiles using halo tracers (figures 8.8 and 8.9).

- We find similar effects to the ones between CDM and baryon voids when investigating the structure, as well as dynamics of baryons and CDM around halo voids in the `hydro` simulations. The relative abundance of baryons compared to CDM is higher inside voids and smaller around the compensations walls, but differences decrease with increasing void size and decreasing core density/compensation, where a void's core density is the strongest indicator of baryonic effects (figures 8.10 and 8.11). Even though the equivalence principle states that matter should move at the same speed irrespective of tracer type, we find small deviations between the velocity of baryons and CDM, where the former typically have a smaller absolute velocities. These deviations once more decrease similar to differences in density as voids increase in size (figures 8.12 and 8.13). This does not necessarily imply a violation of the equivalence principle, since the dynamics of baryons are not only affected by gravity, but also by pressure and other baryonic effects. These effects can cause an additional acceleration of baryons and expel them out of overdense halos residing near compensation walls and into underdense regions. This feedback explains both the differences in velocity, as well as the higher baryon content inside voids, which holds even for local underdensities around individual voids in `ultra-hr` at scales on the order of $50\,\mathrm{kpc}/h$ (figure 8.15).

- A comparison of profiles in comoving scales between `highres` and `ultra-hr` not only reveals an alignment of compensation walls at identical scales, but also allows us to place an upper limit on deviations between baryons and CDM around halo voids (figure 8.14).

- The evolution of voids over cosmic time reveals significant differences between CDM and halo voids. Identified in constant subsamplings, the former decrease in numbers due to merging as the Universe evolves in time, while halo voids identified at fixed mass cuts increase in numbers, as more halos form and reveal more details in the structures of the cosmic web, splitting up large voids from earlier times (figure 9.2). However, depending on the selected mass cuts, the number of voids almost stops evolving once most halos have formed and crossed the threshold of the mass cut.

- Due to these changes in void numbers over time, halo voids decrease in size, but remain almost constant once most halos have formed, while the size of CDM voids increases as CDM continues to cluster. In contrast, distributions in ellipticity only experience vertical shifts due to changes in void numbers and the average void shape remain almost constant in time. In halo voids, both core densities and compensations are almost solely affected by changes in N_v, while CDM voids experience a decrease in core densities and their compensations move towards being more under- or over-

compensated (figures 9.3–9.5). This decrease in core densities is also noticeable in the density profiles of CDM voids, where void centers become more underdense and compensation walls grow in height, as matter moves outside of voids and clusters at their compensation walls as redshift decreases (figure 9.6).

- The evolution of density profiles for halo voids of fixed size is highly dependent on the selected mass cut. At high redshift we find the largest compensations walls due to the halo bias. In their evolution we find that the lower the chosen mass cut, the earlier the density profiles start aligning and stop evolving when depicted in units of r_{v}, typically at similar redshift at which their size functions stop evolving significantly (figure 9.7 and 9.8). As halos still move towards compensation walls, this implies a complex interplay of halo formation inside voids and halo dynamics that leads to these constant profiles. Of course in comoving scales both the size functions and density profiles still evolve, but simply follow the expansion of the Universe.

- While large CDM voids exhibit almost constant velocity profiles in time, the dynamics of small CDM voids and all halo voids closely follow the evolution of their density profiles. For CDM voids we observe an increase in absolute velocities over time, while the dynamics of both CDM and halos around halo voids are once more alike. They have the largest negative velocities at early times, which increase towards more positive values and become almost constant at similar times when density profiles align, although velocities inside them slightly decrease afterwards (figures 9.10–9.13). Small deviations between CDM and halo velocities at early times are most likely caused by sampling effects to due the significantly higher CDM number density.

- While the evolution of CDM density around halo voids looks similar to the evolution of CDM void density profiles, differences compared to CDM voids remain due to different evolution of the CDM and halo void size functions. In fact, we find that the growth of matter structures around halo voids closely follows the predictions from linear growth (figure 9.14), especially when averaging all voids or stacking in their average densities.

- Investigating the evolution of halo void density profiles from the perspective of their average density, i.e. in bins of their compensation, we find no significant evolution at all for most of the age of the Universe, between $z = 4.23$ to $z = 0$ (figures 9.15 and 9.16). Moreover, these profiles are remarkably similar across a vast range of different halo mass cuts and are only slightly affected by different cosmological parameters (figures 9.17 and 9.18). This suggests a previously unknown universal characteristic of halo voids.

These findings have various important implications for observational studies on voids, their use as cosmological probes, and for theoretical studies on voids. While the identification of voids in the full three-dimensional matter distribution of the Universe is not yet feasible, a variety of luminous tracers have already been considered for void finding. These luminous tracers include, but are not limited to galaxies [e.g., 150–154], galaxy

clusters [155], the 21cm emission from neutral Hydrogen [156, 157] and the Ly-α forest [158–161]. For most of our conclusions, except effects from baryonic physics and certain aspects of redshift evolution, we cannot foresee compelling reasons as to why they would not apply for voids identified in a variety of different tracers.

Additionally, testing our conclusions with alternative void definitions and void finders, such as the one introduced in reference [162], might be of great interest, either to see if they still hold, or if not, to test the fundamental differences between void definitions. Even though most of our general conclusions do not depend on varying cosmological parameters in a ΛCDM universe, except for variations in numerical values in profiles and shapes in the distributions of void properties, testing some conclusions in alternative models of CDM and dark energy, as well as simulations employing modifications to GR might reveal more insights on these models in underdense environments. Analyzing the impact of other particle species, such as massive neutrinos or axions, on our conclusions might be beneficial as well. Furthermore, continuing the study of voids in simulations of ΛCDM models such as the ones employed in this work may reveal additional universal properties of voids.

Our conclusions open up a vast observational window for conducting cosmological experiments with voids. They allow us to make use of voids ranging in sizes from only few (or potentially less) to hundreds of Mpc in size and from inner densities even above the mean density, which are typically not considered as cosmic voids, but still behave as local underdensities. Comparing the statistics of voids from much simpler dark matter only simulations with observations instead of needing hydrodynamical simulations should be feasible when applying appropriate cuts in size or core density, which eliminates voids from the sample that are typically classified to be of type "void-in-cloud". In current observational studies, cuts in void properties might not even be necessary, as baryonic effects for voids identified in halos (and most likely galaxies) are almost negligible. They are only relevant at quite small tracer masses and scales, which are not yet attainable in large-scale surveys. Furthermore, as linear dynamics holds up in voids irrespective of their size and redshift, void catalogs from observations can be extended by conducting deeper observations that provide dense tracer samples at low redshift and thus smaller sub-voids (e.g., as planned for 4MOST [163] and Roman [164]), as well as by enlarging the volumes of large-scale structure surveys at higher redshifts (as it is planned for a number of next-generation surveys, such as *Euclid* [135, 165–167]). As large-scale observations at increasing redshifts will be attainable with these surveys, the negligible evolution of void profiles for voids binned by their compensation might be beneficial in developing new cosmological tests using voids.

These findings allows us to maximize the number of observable linear modes of the density field of large-scale structure than can be utilized for inference of cosmological parameters far beyond previously imposed limits, for example via the Alcock-Paczynski effect, as well as RSD [76, 82, 135], where the redshift evolution of void shapes plays a major role. Moreover, data sets from upcoming surveys over a vast range in redshift will contain hundreds of thousands of voids, as well as their individual properties. This will be useful for the latest machine learning applications [73, 168, 169] and in addition, these observations will allow us to verify some of our conclusions in observational studies and potentially in other biased tracers.

Bibliography

[1] C. L. Bennett, M. Halpern, G. Hinshaw, N. Jarosik, A. Kogut, M. Limon et al., *First-Year Wilkinson Microwave Anisotropy Probe (WMAP) Observations: Preliminary Maps and Basic Results*, ApJS **148** (2003) 1 [astro-ph/0302207].

[2] Planck Collaboration, N. Aghanim, Y. Akrami, F. Arroja, M. Ashdown, J. Aumont et al., *Planck 2018 results. I. Overview and the cosmological legacy of Planck*, Astron. Astrophys. **641** (2020) A1 [1807.06205].

[3] Y. B. Zeldovich, *Reprint of 1970A&A.....5...84Z. Gravitational instability: an approximate theory for large density perturbations.*, Astron. Astrophys. **500** (1970) 13.

[4] S. A. Gregory and L. A. Thompson, *The Coma/A1367 supercluster and its environs.*, Astrophys. J. **222** (1978) 784.

[5] M. Jõeveer, J. Einasto and E. Tago, *Spatial distribution of galaxies and of clusters of galaxies in the southern galactic hemisphere*, Mon. Not. Roy. Astron. Soc. **185** (1978) 357.

[6] R. P. Kirshner, J. Oemler, A., P. L. Schechter and S. A. Shectman, *A million cubic megaparsec void in Bootes ?*, Astrophys. J. **248** (1981) L57.

[7] I. B. Zeldovich, J. Einasto and S. F. Shandarin, *Giant voids in the Universe*, Nature **300** (1982) 407.

[8] E. Bertschinger, *The self-similar evolution of holes in an Einstein-de Sitter universe*, ApJS **58** (1985) 1.

[9] R. van de Weygaert and E. van Kampen, *Voids in Gravitational Instability Scenarios - Part One - Global Density and Velocity Fields in an Einstein - De-Sitter Universe*, Mon. Not. Roy. Astron. Soc. **263** (1993) 481.

[10] 6dF Galaxy Survey (http://www.6dfgs.net/).

[11] Baryon Oscillation Spectroscopic Survey (https://cosmology.lbl.gov/BOSS).

[12] Dark Energy Survey (https://www.darkenergysurvey.org).

[13] Dark Energy Spectroscopic Instrumen (https://www.desi.lbl.gov).

[14] Euclid (https://sci.esa.int/web/euclid).

[15] Nancy Grace Roman Space Telescope (https://roman.gsfc.nasa.gov).

[16] Rubin Observatory Legacy Survey of Space and Time (https://rubinobservatory.org/).

[17] Sloan Digital Sky Survey (http://www.sdss3.org/).

[18] SPHEREx (https://spherex.caltech.edu).

[19] VIMOS Public Extragalactic Redshift Survey (http://vipers.inaf.it).

[20] WiggleZ Dark Energy Survey (http://wigglez.swin.edu.au).

[21] A. G. Riess, A. V. Filippenko, P. Challis, A. Clocchiatti, A. Diercks, P. M. Garnavich et al., *Observational Evidence from Supernovae for an Accelerating Universe and a Cosmological Constant*, AJ **116** (1998) 1009 [astro-ph/9805201].

[22] S. Perlmutter, G. Aldering, G. Goldhaber, R. A. Knop, P. Nugent, P. G. Castro et al., *Measurements of* Ω *and* Λ *from 42 High-Redshift Supernovae*, Astrophys. J. **517** (1999) 565 [astro-ph/9812133].

[23] V. Springel, N. Yoshida and S. D. M. White, *GADGET: a code for collisionless and gasdynamical cosmological simulations*, New A **6** (2001) 79 [astro-ph/0003162].

[24] K. Dolag, E. Komatsu and R. Sunyaev, *SZ effects in the Magneticum Pathfinder simulation: comparison with the Planck, SPT, and ACT results*, Mon. Not. Roy. Astron. Soc. **463** (2016) 1797 [1509.05134].

[25] R. van de Weygaert and W. Schaap, *The Cosmic Web: Geometric Analysis*. Springer Berlin Heidelberg, 2009, 10.1007/978-3-540-44767-2_11.

[26] R. van de Weygaert, *Voids and the Cosmic Web: cosmic depression & spatial complexity*, in *The Zeldovich Universe: Genesis and Growth of the Cosmic Web* (R. van de Weygaert, S. Shandarin, E. Saar and J. Einasto, eds.), vol. 308, pp. 493–523, Oct., 2016, 1611.01222, DOI.

[27] A. Pisani, E. Massara, D. N. Spergel, D. Alonso, T. Baker, Y.-C. Cai et al., *Cosmic voids: a novel probe to shed light on our Universe*, BAAS **51** (2019) 40 [1903.05161].

[28] M. Moresco, L. Amati, L. Amendola, S. Birrer, J. P. Blakeslee, M. Cantiello et al., *Unveiling the Universe with emerging cosmological probes*, *Living Reviews in Relativity* **25** (2022) 6 [2201.07241].

[29] R. Biswas, E. Alizadeh and B. D. Wandelt, *Voids as a precision probe of dark energy*, Phys. Rev. D **82** (2010) 023002 [1002.0014].

[30] G. Lavaux and B. D. Wandelt, *Precision Cosmography with Stacked Voids*, Astrophys. J. **754** (2012) 109 [1110.0345].

[31] P. M. Sutter, G. Lavaux, B. D. Wandelt and D. H. Weinberg, *A First Application of the Alcock-Paczynski Test to Stacked Cosmic Voids*, Astrophys. J. **761** (2012) 187 [1208.1058].

[32] N. Hamaus, B. D. Wandelt, P. M. Sutter, G. Lavaux and M. S. Warren, *Cosmology with Void-Galaxy Correlations*, Phys. Rev. Lett. **112** (2014) 041304 [1307.2571].

[33] A. Pisani, P. M. Sutter, N. Hamaus, E. Alizadeh, R. Biswas, B. D. Wandelt et al., *Counting voids to probe dark energy*, Phys. Rev. D **92** (2015) 083531 [1503.07690].

[34] N. Hamaus, P. M. Sutter, G. Lavaux and B. D. Wandelt, *Probing cosmology and gravity with redshift-space distortions around voids*, JCAP **11** (2015) 036 [1507.04363].

[35] C. M. Correa, D. J. Paz, A. G. Sánchez, A. N. Ruiz, N. D. Padilla and R. E. Angulo, *Redshift-space effects in voids and their impact on cosmological tests. Part I: the void size function*, Mon. Not. Roy. Astron. Soc. **500** (2021) 911 [2007.12064].

[36] E. G. P. Bos, R. van de Weygaert, K. Dolag and V. Pettorino, *The darkness that shaped the void: dark energy and cosmic voids*, Mon. Not. Roy. Astron. Soc. **426** (2012) 440 [1205.4238].

[37] G. Verza, A. Pisani, C. Carbone, N. Hamaus and L. Guzzo, *The void size function in dynamical dark energy cosmologies*, JCAP **2019** (2019) 040 [1906.00409].

[38] N. Hamaus, P. M. Sutter and B. D. Wandelt, *Universal Density Profile for Cosmic Voids*, *Physical Review Letters* **112** (2014) 251302 [1403.5499].

[39] E. Ricciardelli, V. Quilis and J. Varela, *On the universality of void density profiles*, Mon. Not. Roy. Astron. Soc. **440** (2014) 601 [1402.2976].

[40] K. C. Chan, N. Hamaus and V. Desjacques, *Large-scale clustering of cosmic voids*, Phys. Rev. D **90** (2014) 103521 [1409.3849].

[41] F. Leclercq, J. Jasche, P. M. Sutter, N. Hamaus and B. Wandelt, *Dark matter voids in the SDSS galaxy survey*, JCAP **3** (2015) 047 [1410.0355].

[42] M. Cautun, Y.-C. Cai and C. S. Frenk, *The view from the boundary: a new void stacking method*, Mon. Not. Roy. Astron. Soc. **457** (2016) 2540 [1509.00010].

[43] C. Sánchez, J. Clampitt, A. Kovacs, B. Jain, J. García-Bellido, S. Nadathur et al., *Cosmic voids and void lensing in the Dark Energy Survey Science Verification data*, Mon. Not. Roy. Astron. Soc. **465** (2017) 746 [1605.03982].

[44] G. Pollina, N. Hamaus, K. Dolag, J. Weller, M. Baldi and L. Moscardini, *On the linearity of tracer bias around voids*, Mon. Not. Roy. Astron. Soc. **469** (2017) 787 [1610.06176].

[45] T. Chantavat, U. Sawangwit and B. D. Wandelt, *Void Profile from Planck Lensing Potential Map*, Astrophys. J. **836** (2017) 156 [1702.01009].

[46] Y. Fang, N. Hamaus, B. Jain, S. Pandey, G. Pollina, C. Sánchez et al., *Dark Energy Survey year 1 results: the relationship between mass and light around cosmic voids*, Mon. Not. Roy. Astron. Soc. **490** (2019) 3573 [1909.01386].

[47] S. Stopyra, H. V. Peiris and A. Pontzen, *How to build a catalogue of linearly evolving cosmic voids*, Mon. Not. Roy. Astron. Soc. **500** (2021) 4173 [2007.14395].

[48] J. Shim, C. Park, J. Kim and H. S. Hwang, *Identification of Cosmic Voids as Massive Cluster Counterparts*, Astrophys. J. **908** (2021) 211 [2012.03511].

[49] S. Tavasoli, *Void Galaxy Distribution: A Challenge for ΛCDM*, Astrophys. J. **916** (2021) L24 [2109.10369].

[50] P. Zivick, P. M. Sutter, B. D. Wandelt, B. Li and T. Y. Lam, *Using cosmic voids to distinguish f(R) gravity in future galaxy surveys*, Mon. Not. Roy. Astron. Soc. **451** (2015) 4215 [1411.5694].

[51] Y.-C. Cai, N. Padilla and B. Li, *Testing gravity using cosmic voids*, Mon. Not. Roy. Astron. Soc. **451** (2015) 1036 [1410.1510].

[52] A. Barreira, M. Cautun, B. Li, C. M. Baugh and S. Pascoli, *Weak lensing by voids in modified lensing potentials*, JCAP **8** (2015) 028 [1505.05809].

[53] B. Falck, K. Koyama, G.-B. Zhao and M. Cautun, *Using voids to unscreen modified gravity*, Mon. Not. Roy. Astron. Soc. **475** (2018) 3262 [1704.08942].

[54] T. Baker, J. Clampitt, B. Jain and M. Trodden, *Void lensing as a test of gravity*, Phys. Rev. D **98** (2018) 023511 [1803.07533].

[55] E. Paillas, M. Cautun, B. Li, Y.-C. Cai, N. Padilla, J. Armijo et al., *The Santiago-Harvard-Edinburgh-Durham void comparison II: unveiling the Vainshtein screening using weak lensing*, Mon. Not. Roy. Astron. Soc. **484** (2019) 1149 [1810.02864].

[56] C. T. Davies, M. Cautun and B. Li, *Cosmological test of gravity using weak lensing voids*, Mon. Not. Roy. Astron. Soc. **490** (2019) 4907 [1907.06657].

[57] E. L. D. Perico, R. Voivodic, M. Lima and D. F. Mota, *Cosmic voids in modified gravity scenarios*, Astron. Astrophys. **632** (2019) A52.

[58] C. Wilson and R. Bean, *Testing f (R) gravity with scale dependent cosmic void velocity profiles*, Phys. Rev. D **104** (2021) 023512 [2012.05925].

[59] A. Tamosiunas, C. Briddon, C. Burrage, A. Cutforth, A. Moss and T. Vincent, *Chameleon screening in cosmic voids*, JCAP **2022** (2022) 056 [2206.06480].

[60] B. Fiorini, K. Koyama and A. Izard, *Studying large-scale structure probes of modified gravity with COLA*, JCAP **2022** (2022) 028 [2208.01345].

[61] L. F. Yang, M. C. Neyrinck, M. A. Aragón-Calvo, B. Falck and J. Silk, *Warmth elevating the depths: shallower voids with warm dark matter*, Mon. Not. Roy. Astron. Soc. **451** (2015) 3606 [1411.5029].

[62] D. S. Reed, A. Schneider, R. E. Smith, D. Potter, J. Stadel and B. Moore, *The same with less: the cosmic web of warm versus cold dark matter dwarf galaxies*, Mon. Not. Roy. Astron. Soc. **451** (2015) 4413 [1410.1541].

[63] M. Baldi and F. Villaescusa-Navarro, *Cosmic degeneracies - II. Structure formation in joint simulations of warm dark matter and f(R) gravity*, Mon. Not. Roy. Astron. Soc. **473** (2018) 3226.

[64] E. Lester and K. Bolejko, *Imprints of decaying dark matter on cosmic voids*, Phys. Rev. D **104** (2021) 123540 [2111.11593].

[65] S. Arcari, E. Pinetti and N. Fornengo, *Got plenty of nothing: cosmic voids as a probe of particle dark matter*, JCAP **2022** (2022) 011 [2205.03360].

[66] E. Massara, F. Villaescusa-Navarro, M. Viel and P. M. Sutter, *Voids in massive neutrino cosmologies*, JCAP **11** (2015) 018 [1506.03088].

[67] A. Banerjee and N. Dalal, *Simulating nonlinear cosmological structure formation with massive neutrinos*, JCAP **11** (2016) 015 [1606.06167].

[68] C. D. Kreisch, A. Pisani, C. Carbone, J. Liu, A. J. Hawken, E. Massara et al., *Massive Neutrinos Leave Fingerprints on Cosmic Voids*, Mon. Not. Roy. Astron. Soc. (2019) 1877 [1808.07464].

[69] N. Schuster, N. Hamaus, A. Pisani, C. Carbone, C. D. Kreisch, G. Pollina et al., *The bias of cosmic voids in the presence of massive neutrinos*, JCAP **2019** (2019) 055 [1905.00436].

[70] G. Zhang, Z. Li, J. Liu, D. N. Spergel, C. D. Kreisch, A. Pisani et al., *Void halo mass function: A promising probe of neutrino mass*, Phys. Rev. D **102** (2020) 083537 [1910.07553].

[71] S. Contarini, F. Marulli, L. Moscardini, A. Veropalumbo, C. Giocoli and M. Baldi, *Cosmic voids in modified gravity models with massive neutrinos*, Mon. Not. Roy. Astron. Soc. **504** (2021) 5021 [2009.03309].

[72] A. E. Bayer, F. Villaescusa-Navarro, E. Massara, J. Liu, D. N. Spergel, L. Verde et al., *Detecting Neutrino Mass by Combining Matter Clustering, Halos, and Voids*, Astrophys. J. **919** (2021) 24 [2102.05049].

[73] C. D. Kreisch, A. Pisani, F. Villaescusa-Navarro, D. N. Spergel, B. D. Wandelt, N. Hamaus et al., *The GIGANTES Data Set: Precision Cosmology from Voids in the Machine-learning Era*, Astrophys. J. **935** (2022) 100 [2107.02304].

[74] D. Paz, M. Lares, L. Ceccarelli, N. Padilla and D. G. Lambas, *Clues on void evolution-II. Measuring density and velocity profiles on SDSS galaxy redshift space distortions*, Mon. Not. Roy. Astron. Soc. **436** (2013) 3480 [1306.5799].

[75] N. Hamaus, P. M. Sutter, G. Lavaux and B. D. Wandelt, *Testing cosmic geometry without dynamic distortions using voids*, JCAP **12** (2014) 013 [1409.3580].

[76] N. Hamaus, A. Pisani, P. M. Sutter, G. Lavaux, S. Escoffier, B. D. Wandelt et al., *Constraints on Cosmology and Gravity from the Dynamics of Voids*, *Physical Review Letters* **117** (2016) 091302 [1602.01784].

[77] Y.-C. Cai, A. Taylor, J. A. Peacock and N. Padilla, *Redshift-space distortions around voids*, Mon. Not. Roy. Astron. Soc. **462** (2016) 2465 [1603.05184].

[78] A. J. Hawken, B. R. Granett, A. Iovino, L. Guzzo, J. A. Peacock, S. de la Torre et al., *The VIMOS Public Extragalactic Redshift Survey. Measuring the growth rate of structure around cosmic voids*, Astron. Astrophys. **607** (2017) A54 [1611.07046].

[79] N. Hamaus, M.-C. Cousinou, A. Pisani, M. Aubert, S. Escoffier and J. Weller, *Multipole analysis of redshift-space distortions around cosmic voids*, JCAP **7** (2017) 014 [1705.05328].

[80] E. Massara and R. K. Sheth, *Density and velocity profiles around cosmic voids*, *arXiv e-prints* (2018) arXiv:1811.03132 [1811.03132].

[81] I. Achitouv, *New constraints on the linear growth rate using cosmic voids in the SDSS DR12 datasets*, Phys. Rev. D **100** (2019) 123513 [1903.05645].

[82] C. M. Correa, D. J. Paz, N. D. Padilla, A. G. Sánchez, A. N. Ruiz and R. E. Angulo, *Redshift-space effects in voids and their impact on cosmological tests - II. The void-galaxy cross-correlation function*, Mon. Not. Roy. Astron. Soc. **509** (2022) 1871 [2107.01314].

[83] E. Massara, W. J. Percival, N. Dalal, S. Nadathur, S. Radinović, H. A. Winther et al., *Velocity profiles of matter and biased tracers around voids*, Mon. Not. Roy. Astron. Soc. **517** (2022) 4458 [2206.14120].

[84] N. Schuster, N. Hamaus, K. Dolag and J. Weller, *Why cosmic voids matter: nonlinear structure & linear dynamics*, JCAP **2023** (2023) 031 [2210.02457].

[85] S. M. Carroll, *Spacetime and Geometry: An Introduction to General Relativity*. Addison Wesley, 2004.

[86] V. Mukhanov, *Physical Foundations of Cosmology*. Cambridge University Press, 2005.

[87] N. Hamaus, "Cosmic Voids" (https://wwwmpa.mpa-garching.mpg.de/~komatsu/lecturenotes/Nico_Hamaus_on_voids.pdf), last accessed: 17.08.2023.

[88] S. Dodelson and F. Schmidt, *Modern Cosmology*. 2020, 10.1016/C2017-0-01943-2.

[89] D. Baumann, *Cosmology*. Cambridge University Press, 2022, 10.1017/9781108937092.

[90] P. D. Group, R. L. Workman, V. D. Burkert, V. Crede, E. Klempt, U. Thoma et al., *Review of Particle Physics*, *Progress of Theoretical and Experimental Physics* **2022** (2022) 083C01.

[91] Planck Collaboration, N. Aghanim, Y. Akrami, M. Ashdown, J. Aumont, C. Baccigalupi et al., *Planck 2018 results. VI. Cosmological parameters*, Astron. Astrophys. **641** (2020) A6 [1807.06209].

[92] P. J. E. Peebles, *The large-scale structure of the universe*. Princeton University Press, 1980.

[93] J. M. Bardeen, J. R. Bond, N. Kaiser and A. S. Szalay, *The Statistics of Peaks of Gaussian Random Fields*, Astrophys. J. **304** (1986) 15.

[94] R. K. Sheth and R. van de Weygaert, *A hierarchy of voids: much ado about nothing*, Mon. Not. Roy. Astron. Soc. **350** (2004) 517 [astro-ph/0311260].

[95] E. Jennings, Y. Li and W. Hu, *The abundance of voids and the excursion set formalism*, Mon. Not. Roy. Astron. Soc. **434** (2013) 2167 [1304.6087].

[96] P. M. Sutter, G. Lavaux, N. Hamaus, A. Pisani, B. D. Wandelt, M. Warren et al., *VIDE: The Void IDentification and Examination toolkit*, *Astronomy and Computing* **9** (2015) 1 [1406.1191].

[97] M. C. Neyrinck, *ZOBOV: a parameter-free void-finding algorithm*, Mon. Not. Roy. Astron. Soc. **386** (2008) 2101 [0712.3049].

[98] E. Platen, R. van de Weygaert and B. J. T. Jones, *A cosmic watershed: the WVF void detection technique*, Mon. Not. Roy. Astron. Soc. **380** (2007) 551 [0706.2788].

[99] G. R. Blumenthal, L. N. da Costa, D. S. Goldwirth, M. Lecar and T. Piran, *The Largest Possible Voids*, Astrophys. J. **388** (1992) 234.

[100] T. Ronconi, S. Contarini, F. Marulli, M. Baldi and L. Moscardini, *Cosmic voids uncovered - first-order statistics of depressions in the biased density field*, Mon. Not. Roy. Astron. Soc. **488** (2019) 5075 [1902.04585].

[101] S. Contarini, T. Ronconi, F. Marulli, L. Moscardini, A. Veropalumbo and M. Baldi, *Cosmological exploitation of the size function of cosmic voids identified in the distribution of biased tracers*, Mon. Not. Roy. Astron. Soc. **488** (2019) 3526 [1904.01022].

[102] G. Verza, C. Carbone and A. Renzi, *The Halo Bias inside Cosmic Voids*, Astrophys. J. **940** (2022) L16 [2207.04039].

[103] P. M. Sutter, G. Lavaux, N. Hamaus, B. D. Wandelt, D. H. Weinberg and M. S. Warren, *Sparse sampling, galaxy bias, and voids*, Mon. Not. Roy. Astron. Soc. **442** (2014) 462 [1309.5087].

[104] F. Bernardeau and R. van de Weygaert, *A new method for accurate estimation of velocity field statistics*, Mon. Not. Roy. Astron. Soc. **279** (1996) 693 [astro-ph/9508125].

[105] P. J. E. Peebles, *Principles of Physical Cosmology*. Princeton University Press, 1993.

[106] M. Hirschmann, K. Dolag, A. Saro, L. Bachmann, S. Borgani and A. Burkert, *Cosmological simulations of black hole growth: AGN luminosities and downsizing*, Mon. Not. Roy. Astron. Soc. **442** (2014) 2304 [1308.0333].

[107] K. Dolag, B. M. Gaensler, A. M. Beck and M. C. Beck, *Constraints on the distribution and energetics of fast radio bursts using cosmological hydrodynamic simulations*, Mon. Not. Roy. Astron. Soc. **451** (2015) 4277 [1412.4829].

[108] L. K. Steinborn, K. Dolag, M. Hirschmann, M. A. Prieto and R.-S. Remus, *A refined sub-grid model for black hole accretion and AGN feedback in large cosmological simulations*, Mon. Not. Roy. Astron. Soc. **448** (2015) 1504 [1409.3221].

[109] A. F. Teklu, R.-S. Remus, K. Dolag, A. M. Beck, A. Burkert, A. S. Schmidt et al., *Connecting Angular Momentum and Galactic Dynamics: The Complex Interplay between Spin, Mass, and Morphology*, Astrophys. J. **812** (2015) 29 [1503.03501].

[110] S. Bocquet, A. Saro, K. Dolag and J. J. Mohr, *Halo mass function: baryon impact, fitting formulae, and implications for cluster cosmology*, Mon. Not. Roy. Astron. Soc. **456** (2016) 2361 [1502.07357].

[111] R.-S. Remus, K. Dolag and T. Hoffmann, *The Outer Halos of Very Massive Galaxies: BCGs and their DSC in the Magneticum Simulations*, *Galaxies* **5** (2017) 49 [1709.02393].

[112] T. Castro, M. Quartin, C. Giocoli, S. Borgani and K. Dolag, *The effect of baryons in the cosmological lensing PDFs*, Mon. Not. Roy. Astron. Soc. **478** (2018) 1305 [1711.10017].

[113] T. Castro, S. Borgani, K. Dolag, V. Marra, M. Quartin, A. Saro et al., *On the impact of baryons on the halo mass function, bias, and cluster cosmology*, Mon. Not. Roy. Astron. Soc. **500** (2021) 2316 [2009.01775].

[114] M. Angelinelli, S. Ettori, K. Dolag, F. Vazza and A. Ragagnin, *Mapping 'out-of-the-box' the properties of the baryons in massive halos*, Astron. Astrophys. **663** (2022) L6 [2206.08382].

[115] E. Komatsu, K. M. Smith, J. Dunkley, C. L. Bennett, B. Gold, G. Hinshaw et al., *Seven-year Wilkinson Microwave Anisotropy Probe (WMAP) Observations: Cosmological Interpretation*, ApJS **192** (2011) 18 [1001.4538].

[116] V. Springel, *The cosmological simulation code GADGET-2*, Mon. Not. Roy. Astron. Soc. **364** (2005) 1105 [astro-ph/0505010].

[117] A. M. Beck, G. Murante, A. Arth, R. S. Remus, A. F. Teklu, J. M. F. Donnert et al., *An improved SPH scheme for cosmological simulations*, Mon. Not. Roy. Astron. Soc. **455** (2016) 2110 [1502.07358].

[118] K. Dolag, E. Mevius and R.-S. Remus, *Distribution and Evolution of Metals in the Magneticum Simulations*, *Galaxies* **5** (2017) 35 [1708.00027].

[119] V. Springel, T. Di Matteo and L. Hernquist, *Modelling feedback from stars and black holes in galaxy mergers*, Mon. Not. Roy. Astron. Soc. **361** (2005) 776 [astro-ph/0411108].

[120] T. Di Matteo, V. Springel and L. Hernquist, *Energy input from quasars regulates the growth and activity of black holes and their host galaxies*, Nature **433** (2005) 604 [astro-ph/0502199].

[121] D. Fabjan, S. Borgani, L. Tornatore, A. Saro, G. Murante and K. Dolag, *Simulating the effect of active galactic nuclei feedback on the metal enrichment of galaxy clusters*, Mon. Not. Roy. Astron. Soc. **401** (2010) 1670 [0909.0664].

[122] S. Young, E. Komatsu and K. Dolag, *Testing the Sunyaev-Zeldovich-based tomographic approach to the thermal history of the Universe with pressure-density cross correlations: Insights from the Magneticum simulation*, Phys. Rev. D **104** (2021) 083538 [2105.15043].

[123] N. Gupta, A. Saro, J. J. Mohr, K. Dolag and J. Liu, *SZE observables, pressure profiles and centre offsets in Magneticum simulation galaxy clusters*, Mon. Not. Roy. Astron. Soc. **469** (2017) 3069 [1612.05266].

[124] V. Biffi, F. Mernier and P. Medvedev, *Enrichment of the Hot Intracluster Medium: Numerical Simulations*, Space Sci. Rev. **214** (2018) 123 [1811.01955].

[125] V. Biffi, K. Dolag and H. Böhringer, *Investigating the velocity structure and X-ray observable properties of simulated galaxy clusters with PHOX*, Mon. Not. Roy. Astron. Soc. **428** (2013) 1395 [1210.4158].

[126] A. Ragagnin, K. Dolag, L. Moscardini, A. Biviano and M. D'Onofrio, *Dependency of halo concentration on mass, redshift and fossilness in Magneticum hydrodynamic simulations*, Mon. Not. Roy. Astron. Soc. **486** (2019) 4001 [1810.08212].

[127] V. Biffi, K. Dolag, T. H. Reiprich, A. Veronica, M. E. Ramos-Ceja, E. Bulbul et al., *The eROSITA view of the Abell 3391/95 field: Case study from the Magneticum cosmological simulation*, Astron. Astrophys. **661** (2022) A17 [2106.14542].

[128] T. Naab and J. P. Ostriker, *Theoretical Challenges in Galaxy Formation*, ARA&A **55** (2017) 59 [1612.06891].

[129] P. Lustig, V. Strazzullo, R.-S. Remus, C. D'Eugenio, E. Daddi, A. Burkert et al., *Massive quiescent galaxies at z 3: A comparison of selection, stellar population, and structural properties with simulation predictions*, Mon. Not. Roy. Astron. Soc. **518** (2023) 5953 [2201.09068].

[130] M. Lotz, R.-S. Remus, K. Dolag, A. Biviano and A. Burkert, *Gone after one orbit: How cluster environments quench galaxies*, Mon. Not. Roy. Astron. Soc. **488** (2019) 5370 [1810.02382].

[131] L. K. Steinborn, K. Dolag, J. M. Comerford, M. Hirschmann, R.-S. Remus and A. F. Teklu, *Origin and properties of dual and offset active galactic nuclei in a cosmological simulation at z=2*, Mon. Not. Roy. Astron. Soc. **458** (2016) 1013 [1510.08465].

[132] M. Lotz, K. Dolag, R.-S. Remus and A. Burkert, *Rise and fall of post-starburst galaxies in Magneticum Pathfinder*, Mon. Not. Roy. Astron. Soc. **506** (2021) 4516 [2011.06602].

[133] V. Springel, S. D. M. White, G. Tormen and G. Kauffmann, *Populating a cluster of galaxies - I. Results at [formmu2]z=0*, Mon. Not. Roy. Astron. Soc. **328** (2001) 726 [astro-ph/0012055].

[134] K. Dolag, S. Borgani, G. Murante and V. Springel, *Substructures in hydrodynamical cluster simulations*, Mon. Not. Roy. Astron. Soc. **399** (2009) 497 [0808.3401].

[135] N. Hamaus, M. Aubert, A. Pisani, S. Contarini, G. Verza, M. C. Cousinou et al., *Euclid: Forecasts from redshift-space distortions and the Alcock-Paczynski test with cosmic voids*, Astron. Astrophys. **658** (2022) A20 [2108.10347].

[136] S. Contarini, A. Pisani, N. Hamaus, F. Marulli, L. Moscardini and M. Baldi, *Cosmological Constraints from the BOSS DR12 Void Size Function*, Astrophys. J. **953** (2023) 46 [2212.03873].

[137] G. Verza, C. Carbone, A. Pisani and A. Renzi, *DEMNUni: disentangling dark energy from massive neutrinos with the void size function*, *arXiv e-prints* (2022) arXiv:2212.09740 [2212.09740].

[138] S. Nadathur and S. Hotchkiss, *The nature of voids - II. Tracing underdensities with biased galaxies*, Mon. Not. Roy. Astron. Soc. **454** (2015) 889 [1507.00197].

[139] U. Seljak, N. Hamaus and V. Desjacques, *How to Suppress the Shot Noise in Galaxy Surveys*, Phys. Rev. Lett. **103** (2009) 091303 [0904.2963].

[140] N. Hamaus, U. Seljak, V. Desjacques, R. E. Smith and T. Baldauf, *Minimizing the stochasticity of halos in large-scale structure surveys*, Phys. Rev. D **82** (2010) 043515 [1004.5377].

[141] I. Achitouv, *Improved model of redshift-space distortions around voids: Application to quintessence dark energy*, Phys. Rev. D **96** (2017) 083506 [1707.08121].

[142] E. Paillas, Y.-C. Cai, N. Padilla and A. G. Sánchez, *Redshift-space distortions with split densities*, Mon. Not. Roy. Astron. Soc. **505** (2021) 5731 [2101.09854].

[143] D. Vallés-Pérez, V. Quilis and S. Planelles, *Void Replenishment: How Voids Accrete Matter Over Cosmic History*, Astrophys. J. **920** (2021) L2 [2109.08165].

[144] E. Paillas, C. D. P. Lagos, N. Padilla, P. Tissera, J. Helly and M. Schaller, *Baryon effects on void statistics in the EAGLE simulation*, Mon. Not. Roy. Astron. Soc. **470** (2017) 4434 [1609.00101].

[145] A. M. Rodríguez Medrano, D. J. Paz, F. A. Stasyszyn and A. N. Ruiz, *Imprints of the cosmic void evolution on the baryon processes inside galaxy haloes*, Mon. Not. Roy. Astron. Soc. **511** (2022) 2688 [2109.13378].

[146] D. Clowe, M. Bradač, A. H. Gonzalez, M. Markevitch, S. W. Randall, C. Jones et al., *A Direct Empirical Proof of the Existence of Dark Matter*, Astrophys. J. **648** (2006) L109 [astro-ph/0608407].

[147] D. Paraficz, J. P. Kneib, J. Richard, A. Morandi, M. Limousin, E. Jullo et al., *The Bullet cluster at its best: weighing stars, gas, and dark matter*, Astron. Astrophys. **594** (2016) A121 [1209.0384].

[148] P. M. Sutter, P. Elahi, B. Falck, J. Onions, N. Hamaus, A. Knebe et al., *The life and death of cosmic voids*, Mon. Not. Roy. Astron. Soc. **445** (2014) 1235 [1403.7525].

[149] R. Wojtak, D. Powell and T. Abel, *Voids in cosmological simulations over cosmic time*, Mon. Not. Roy. Astron. Soc. **458** (2016) 4431 [1602.08541].

[150] D. C. Pan, M. S. Vogeley, F. Hoyle, Y.-Y. Choi and C. Park, *Cosmic voids in Sloan Digital Sky Survey Data Release 7*, Mon. Not. Roy. Astron. Soc. **421** (2012) 926 [1103.4156].

[151] P. M. Sutter, G. Lavaux, B. D. Wandelt and D. H. Weinberg, *A Public Void Catalog from the SDSS DR7 Galaxy Redshift Surveys Based on the Watershed Transform*, Astrophys. J. **761** (2012) 44 [1207.2524].

[152] Q. Mao, A. A. Berlind, R. J. Scherrer, M. C. Neyrinck, R. Scoccimarro, J. L. Tinker et al., *A Cosmic Void Catalog of SDSS DR12 BOSS Galaxies*, Astrophys. J. **835** (2017) 161 [1602.02771].

[153] N. Hamaus, A. Pisani, J.-A. Choi, G. Lavaux, B. D. Wandelt and J. Weller, *Precision cosmology with voids in the final BOSS data*, JCAP **2020** (2020) 023 [2007.07895].

[154] M. Aubert, M.-C. Cousinou, S. Escoffier, A. J. Hawken, S. Nadathur, S. Alam et al., *The completed SDSS-IV extended Baryon Oscillation Spectroscopic Survey: growth rate of structure measurement from cosmic voids*, Mon. Not. Roy. Astron. Soc. **513** (2022) 186 [2007.09013].

[155] G. Pollina, N. Hamaus, K. Paech, K. Dolag, J. Weller, C. Sánchez et al., *On the relative bias of void tracers in the Dark Energy Survey*, Mon. Not. Roy. Astron. Soc. **487** (2019) 2836 [1806.06860].

[156] M. White and N. Padmanabhan, *Matched filtering with interferometric 21 cm experiments*, Mon. Not. Roy. Astron. Soc. **471** (2017) 1167 [1705.09669].

[157] T. Endo, H. Tashiro and A. J. Nishizawa, *The Alcock Paczynski test with voids in 21 cm intensity field*, Mon. Not. Roy. Astron. Soc. **499** (2020) 587 [2002.00348].

[158] C. W. Stark, A. Font-Ribera, M. White and K.-G. Lee, *Finding high-redshift voids using Lyman α forest tomography*, Mon. Not. Roy. Astron. Soc. **453** (2015) 4311 [1504.03290].

[159] A. Krolewski, K.-G. Lee, M. White, J. F. Hennawi, D. J. Schlegel, P. E. Nugent et al., *Detection of $z \sim 2.3$ Cosmic Voids from 3D Lyα Forest Tomography in the COSMOS Field*, Astrophys. J. **861** (2018) 60 [1710.02612].

[160] N. Porqueres, J. Jasche, G. Lavaux and T. Enßlin, *Inferring high-redshift large-scale structure dynamics from the Lyman-α forest*, Astron. Astrophys. **630** (2019) A151 [1907.02973].

[161] C. Ravoux, E. Armengaud, J. Bautista, J.-M. Le Goff, N. Palanque-Delabrouille, J. Rich et al., *First measurement of the correlation between cosmic voids and the Lyman-α forest*, *arXiv e-prints* (2022) arXiv:2203.11045 [2203.11045].

[162] D. J. Paz, C. M. Correa, S. R. Gualpa, A. N. Ruiz, C. S. Bederián, R. D. Graña et al., *Guess the cheese flavour by the size of its holes: a cosmological test using the abundance of popcorn voids*, Mon. Not. Roy. Astron. Soc. **522** (2023) 2553 [2212.06849].

[163] R. S. de Jong, O. Agertz, A. A. Berbel, J. Aird, D. A. Alexander, A. Amarsi et al., *4MOST: Project overview and information for the First Call for Proposals*, *The Messenger* **175** (2019) 3 [1903.02464].

[164] D. Spergel, N. Gehrels, C. Baltay, D. Bennett, J. Breckinridge, M. Donahue et al., *Wide-Field InfrarRed Survey Telescope-Astrophysics Focused Telescope Assets WFIRST-AFTA 2015 Report*, *arXiv e-prints* (2015) arXiv:1503.03757 [1503.03757].

[165] S. Contarini, G. Verza, A. Pisani, N. Hamaus, M. Sahlén, C. Carbone et al., *Euclid: Cosmological forecasts from the void size function*, Astron. Astrophys. **667** (2022) A162 [2205.11525].

[166] M. Bonici, C. Carbone, S. Davini, P. Vielzeuf, L. Paganin, V. Cardone et al., *Euclid: Forecasts from the void-lensing cross-correlation*, Astron. Astrophys. **670** (2023) A47 [2206.14211].

[167] S. Radinović, S. Nadathur, H. A. Winther, W. J. Percival, A. Woodfinden, E. Massara et al., *Euclid: Cosmology forecasts from the void-galaxy cross-correlation function with reconstruction*, *arXiv e-prints* (2023) arXiv:2302.05302 [2302.05302].

[168] M. C. Cousinou, A. Pisani, A. Tilquin, N. Hamaus, A. J. Hawken and S. Escoffier, *Multivariate analysis of cosmic void characteristics*, *Astronomy and Computing* **27** (2019) 53 [1805.07181].

[169] B. Y. Wang, A. Pisani, F. Villaescusa-Navarro and B. D. Wandelt, *Machine learning cosmology from void properties*, *arXiv e-prints* (2022) arXiv:2212.06860 [2212.06860].

Acknowledgements

This work has benefited from financial support by the Deutsche Forschungsgemeinschaft (DFG, German Research Foundation) – HA 8752/2-1 – 669764.

First of all, it is a great pleasure to thank both my advisors, Nico Hamaus and Jochen Weller. It has been an incredible journey with the two of you, starting with my first introduction to voids during my master thesis. I am beyond happy I got to continue my work in this fascinating field in more depth during the last three years, it's been amazing to be part of the 'Voidboyz'. I cannot be grateful enough for the support both of you provided me with during this time. You were always there when I needed advice, guidance and an open ear, as well as a relaxed beer after work, but you also provided me with the total freedom to pursue my own ideas. Moreover, I'm sorry for the massive amount of plots you had to endure during our meetings.

I am also grateful to the whole Physical Cosmology Group. To Angelo, Barbara, Giorgia, Jochen, Kerstin, Martin, Nico, Steffen and Sven: It has been an awesome time with you, both professionally and personally, and you are what makes this group so amazing! I highly enjoyed our fruitful scientific discussions, the various off topic conversations we've had, as well as our social events.

Furthermore, I would like to give my gratitude to Klaus Dolag for providing us with the `Magneticum` simulations and for all the helpful advice you've given me. In addition, an enormous thank you to Alice Pisani, Ben Wandelt and Rien Van De Weygaert for the great and insightful discussions we've shared, it's been a pleasure meeting you!

Special thanks to Dennis and Simon for reading parts of this thesis, your feedback helped me a lot and additional thanks for always letting me talk too much about voids.

Most importantly I am forever grateful to my parents and my family. You have supported me in every way possible during my studies, as well as the last few years. Without you and your support, I would not be where I am today, for which I cannot be grateful enough.